

Neutron and X-ray Scattering Studies of Strongly Correlated Electron Systems

Russell A. Ewings

A thesis submitted for the degree of Doctor of Philosophy



Linacre College
University of Oxford
Hilary Term 2008

Abstract

Neutron and X-ray Scattering Studies of Strongly Correlated Electron Systems

Russell A. Ewings, Linacre College, Oxford

DPhil Thesis, Hilary Term 2008

In this thesis results of x-ray scattering and neutron scattering experiments on several strongly correlated transition metal oxides are presented. The prototypical charge ordered cuprate $\text{La}_{1.48}\text{Nd}_{0.4}\text{Sr}_{0.12}\text{CuO}_4$ was investigated using polarised neutron scattering. The results show that several proposed schemes for the magnetic order in this class of materials may be ruled out, however the data are consistent with one-dimensional stripe-like magnetic order. X-ray diffraction was used to show that the charge order is insensitive to an applied magnetic field, but might be affected by the existence of superconductivity. The magnetic excitations were also studied, and at low energies a gap in the magnetic fluctuations was observed and there is tentative evidence that this is related to magnetic anisotropy. The spin state transition in LaCoO_3 was investigated using neutron inelastic scattering, and excitations reminiscent of those observed in ferromagnets above their critical temperatures were observed. The debate surrounding the nature of the excited spin state, $S = 1$ or $S = 2$, could not be resolved, however. The nature of the spin excitations in $\text{La}_{0.82}\text{Sr}_{0.18}\text{CoO}_3$ was investigated using polarised neutrons and it was found that at low energies the excitations take the form of spin-waves. At higher energies this mode becomes heavily damped, and several possible damping mechanisms for this are discussed. Finally, the multiferroic material DyMn_2O_5 was studied using x-ray resonant scattering. A complex, temperature dependent, magnetic structure was found using a Dy resonance, which reflects an underlying order of the Mn ions. The measurements were in agreement with a theory of multiferroics based on acentric spin-density waves.

Acknowledgements

There are many people I would like to thank, who have contributed in some way towards this thesis. Andrew Boothroyd, my supervisor, has provided insight and clear guidance throughout, and his support has been invaluable. The assistance of the instrument scientists at the Institut Laue-Langevin and the European Synchrotron Radiation Facility was especially important, so I am very grateful to Mechthild Enderle, Jiří Kulda, Anne Stunault, Martin Boehm, Paul Freeman, Danny Mannix, Stuart Wilkins, Valerio Scagnoli, Peter Bencok and Flora Yakhou. The assistance and discussions offered by my collaborators have been very helpful, and I therefore wish to thank Niels Christensen, Henrik Rønnow, Des McMorrow, Joel Mesot, Johan Chang, Helen Walker, Markus Braden, Paul Steffens, Peter Hatton, John Hill, and Tom Beale. None of this work would have taken place without samples, so I am very grateful to the crystal growers Prabhakaran Dharmalingam, Barbara Wanklyn, Naoki Momono, Masayuki Ido, and Migaku Oda.

There have been many people at the Clarendon laboratory who have provided help and good company, so thanks to Lucy Helme, Alexandra Olaya-Castro, Elisa Wheeler, Peter Baker, Rhiannon Jones, Heather Lewtas, Graeme Johnstone, Tom Huberman, Chiron Mukherjee, Dave Parfitt, Sasha Babkevich, Dave Keen, Roger Cowley, Steve Blundell, Bill Hayes and Fred Wondre.

Finally I would like to thank my family, and Lucy.

The most exciting happiness is the happiness generated by forces beyond your control.

Ogden Nash

Contents

1	Introduction	1
1.1	Single-Ion Interactions	2
1.1.1	Crystal Fields	2
1.2	Collective Interactions	3
1.2.1	Magnetism	3
1.2.2	Superconductivity	7
1.2.3	Charge Ordering	10
1.2.4	Orbital Ordering	10
1.2.5	Multiferroic Materials	11
1.3	Excitations	12
1.3.1	Spin Waves in Localised Magnets	12
1.3.2	Spin Excitations in Itinerant Magnets	13
1.4	Scope of this Thesis	14
1.5	Publications	16
2	Experimental Techniques	19
2.1	Neutron Scattering	19
2.1.1	Neutron Sources	19
2.1.2	Neutron Scattering Instruments	20
2.1.3	Neutron Scattering Cross Sections	23
2.1.4	Polarisation Analysis	29
2.2	X-ray Scattering	32
2.2.1	The Synchrotron Source	32
2.2.2	X-ray Scattering Instruments	35
2.2.3	X-ray Scattering Theory	38
2.3	Bulk Measurement Techniques	40
2.3.1	Magnetisation Measurements Using a SQUID	40
2.3.2	Heat Capacity Measurements Using a PPMS	41
3	Growth and Preparation of the Samples	44
4	Charge and Spin Order in $\text{La}_{1.48}\text{Nd}_{0.4}\text{Sr}_{0.12}\text{CuO}_4$	46
4.1	Introduction	46
4.1.1	Introduction to $\text{La}_{2-x}\text{Ba}_x\text{CuO}_4$	46
4.1.2	Introduction to $\text{La}_{2-x-y}\text{Nd}_y\text{Sr}_x\text{CuO}_4$	47
4.1.3	Recent Measurements of $\text{La}_{2-x}\text{Ba}_x\text{CuO}_4$	51
4.1.4	Motivations	52
4.2	Experimental details	53

4.2.1	Neutron Scattering	53
4.2.2	Synchrotron X-ray Scattering	54
4.2.3	Magnetisation Measurements	54
4.3	Results	55
4.3.1	Polarised Neutron Scattering Measurements	56
4.3.2	Unpolarised Neutron Scattering Measurements	60
4.3.3	X-ray Diffraction Measurements	63
4.4	Analysis and Discussion	66
4.4.1	Analysis of the Polarised Neutron Scattering Measurements	66
4.4.2	Discussion of the Polarised Neutron Scattering Measurements	71
4.4.3	Analysis and Discussion of the Unpolarised Neutron Scattering Measurements	74
4.4.4	Analysis and Discussion of the X-ray Diffraction Measurements	77
4.5	Conclusions	80
5	Neutron Scattering Measurements of LaCoO_3	84
5.1	Introduction	84
5.1.1	Motivations	87
5.2	Experimental details	88
5.3	Results	89
5.3.1	Polarised Neutron Scattering Measurements	89
5.3.2	Unpolarised Neutron Scattering Measurements	92
5.4	Analysis	93
5.5	Discussion	99
5.6	Conclusions	103
6	Polarised Neutron Scattering Measurements of $\text{La}_{0.82}\text{Sr}_{0.18}\text{CoO}_3$	107
6.1	Introduction	107
6.1.1	Motivations	112
6.2	Experimental details	112
6.3	Results	115
6.4	Analysis and Discussion	119
6.5	Conclusions	126
7	X-ray Resonant Scattering Measurements of Multiferroic DyMn_2O_5	129
7.1	Introduction	129
7.1.1	Bulk Properties	129
7.1.2	Previous Scattering Measurements	132
7.1.3	Analogies with TbMnO_3 : X-ray Resonant Scattering	134
7.2	Experimental details	135
7.3	Results	137
7.4	Discussion	143
7.5	Conclusions	147
A	Extra Terms in the Neutron Magnetic Scattering Cross-Section	150
B	Use of Pseudo-Cubic Notation for Rhombohedral Crystals	152
C	LaCoO_3 Structure Factor Calculation	154

List of Figures

1.1	A magnetic ion in an octahedral crystalline environment of oxygen ions. . . .	2
1.2	Overlap of d and p -orbitals in an octahedral environment	3
1.3	The effect of a Jahn-Teller distortion on the $3d$ energy levels of Mn^{3+}O_6 in an octahedral environment	3
1.4	The generic phase diagram of a cuprate superconductor	9
1.5	Schematic of a charge checkerboard for a half-doped $\text{La}_{2-x}\text{A}_x\text{MO}_4$ material. .	10
1.6	Schematic of orbital order in $\text{La}_{0.5}\text{Sr}_{1.5}\text{MnO}_4$	11
1.7	The split spin bands in a Fermi gas	14
1.8	The continuum of magnetic Stoner excitations	14
2.1	A schematic of a conventional triple-axis spectrometer.	20
2.2	The scattering triangle	23
2.3	Schematic of an undulator and a wiggler	33
2.4	The four-circle diffractometer	35
2.5	The six-circle diffractometer	36
2.6	A schematic of the principle of an x-ray polarisation analyser	36
2.7	A schematic of the layout of a real x-ray polarisation analyser.	37
2.8	The co-ordinate system for the x-ray resonant magnetic scattering matrices .	40
2.9	The pickup coils of the SQUID magnetometer.	41
2.10	Side view of the sample mount for heat capacity measurements using the PPMS	41
4.1	The crystal structure of LNSCO	48
4.2	A schematic of the charge order in a tetragonal unit cell proposed by the stripe model	49
4.3	A schematic of a single CuO_2 plane showing the spin ordering proposed in the stripe model.	50
4.4	A schematic of a checkerboard model.	50
4.5	Schematics of ‘0’-spirals and ‘ π ’-spirals	51
4.6	Long moment vs temperature in LNSCO	55
4.7	Elastic magnetic scattering at $\mathbf{Q} = (1/2, 0.62, 0)$, with $T = 1.7\text{K}$	56
4.8	The scattering plane used for polarised neutron diffraction measurements of LNSCO.	57
4.9	Polarisation analysed ω -scans with $T = 10\text{K}$ at $\mathbf{Q} = (0.5, 0.62, 0)$ and $\mathbf{Q} = (0.62, 0.5, 0)$	58
4.10	Polarisation analysed scans at $\mathbf{Q} = (-0.5, 1.38, 0)$ and $\mathbf{Q} = (-0.38, 1.5, 0)$. .	59
4.11	Polarisation analysed scans at $\mathbf{Q} = (1.5, -0.38, 0)$ and $\mathbf{Q} = (1.38, -0.5, 0)$. .	59
4.12	Fixed-energy wavevector scan over the $(0.5, 0.38, 0)$ position with $E = 1.5\text{meV}$	60
4.13	Fixed-energy wavevector scan over the $(0.5, 0.38, 0)$ position with $E = 4\text{meV}$	61

4.14	Peak minus background scattering at $\mathbf{Q} = (0.5, 0.38, 0)$ for $T = 2\text{ K}$, $T = 10\text{ K}$, and $T = 35\text{ K}$	61
4.15	The scattering planes used for the second measurement on the IN14 spectrometer.	62
4.16	The scattering at $\mathbf{Q} = (0.5, 0.38, 0)$ and $\mathbf{Q} = (0.5, 0.38, 4.5)$	62
4.17	Charge-order induced structural distortion peak in LNSCO, at $T=2\text{ K}$	63
4.18	Charge-order induced structural distortion peak in LBCO, at $T=2\text{ K}$	64
4.19	Temperature dependence charge order peak in LNSCO.	64
4.20	Temperature dependence charge order peak in LBCO.	65
4.21	Temperature dependence of the width of the charge order peak in LNSCO	65
4.22	Temperature dependence of the width of the charge order peak in LBCO	66
4.23	The sum of SF and NSF scattering, ruling out chiral magnetic order	67
4.24	Definitions of angles used in analysis of the polarised neutron diffraction data.	68
4.25	Angle definitions for analysis of polarised neutron data	69
4.26	Further angle definitions for analysis of polarised neutron data	70
4.27	‘Two- \mathbf{q} ’ magnetic ordering pattern	71
4.28	A coherent superposition of the two patterns shown would generate the π -spiral pattern.	72
4.29	A coherent superposition of two stripe domains	73
4.30	Schematics of vortex spin lattices	74
4.31	The in-plane and out-of-plane components of the spin fluctuations	77
5.1	The magnetic susceptibility of LaCoO_3 as a function of temperature.	85
5.2	Low energy Q-scans with $\mathbf{P} \parallel \mathbf{Q}$, showing the magnetic scattering at $T = 220\text{ K}$	90
5.3	Higher energy Q-scans with $\mathbf{P} \parallel \mathbf{Q}$, spin-flip, showing the magnetic scattering at $T = 220\text{ K}$	90
5.4	$\mathbf{P} \parallel \mathbf{Q}$ scans for both samples	91
5.5	Q-scans after polarisation analysis, showing the magnetic scattering at $T = 220\text{ K}$	91
5.6	Energy scans of the polarisation analysed magnetic scattering at $\mathbf{Q} = (1, 0, 0)$ and $\mathbf{Q} = (1, 0.5, 0.5)$	92
5.7	Energy scans at $\mathbf{Q} = (1, 0, 0)$ using unpolarised neutrons	92
5.8	Energy scans at $\mathbf{Q} = (1, 0.5, 0.5)$ using unpolarised neutrons	93
5.9	Q-scans at $E = 5\text{ meV}$ using unpolarised neutrons	94
5.10	Q-scans with $\mathbf{P} \parallel \mathbf{Q}$ spin-flip fitted to a damped-harmonic oscillator function.	96
5.11	Fits of unpolarised neutron Q-scans at $E = 5\text{ meV}$	98
5.12	The temperature dependence of Γ_0 and Γ_2	98
5.13	Fit of amplitude A vs temperature.	99
6.1	The double exchange mechanism	108
6.2	Magnetic susceptibility of $\text{La}_{1-x}\text{Sr}_x\text{CoO}_3$ as a function of temperature and doping x	109
6.3	Magnetic susceptibility and resistivity of $\text{La}_{1-x}\text{Sr}_x\text{CoO}_3$ as a function of applied magnetic field and doping x	109
6.4	The magnetic phase diagram of $\text{La}_{1-x}\text{Sr}_x\text{CoO}_3$	110
6.5	Raw data from a constant energy Q-scan at $E = 4\text{ meV}$, $T = 2\text{ K}$, using a fully polarised setup.	115
6.6	Colour map showing the magnetic scattering	116

6.7	Energy scans in the (non-magnetic) spin-flip channel showing the optic phonon.	116
6.8	Constant energy Q-scans of the magnetic scattering	117
6.9	Fits to fixed-wavevector energy scans, using a single Gaussian.	118
6.10	Fits to Q - and E -scans to determine a dispersion relationship.	118
6.11	Full width at half maximum (FWHM) in energy of the magnetic excitations as a function of wavevector.	119
6.12	Damped harmonic oscillator fit to the low energy spin-waves	120
6.13	Modified damped harmonic oscillator fit to the low energy spin-waves	121
6.14	Comparison of low energy excitations with zone boundary energy scans . . .	122
6.15	The magnon dispersion considering only nearest-neighbour terms, and with 4^{th} neighbour terms added.	123
6.16	Broadening of the dispersion due to a Gaussian distribution of nearest-neighbour exchange parameters.	124
6.17	Width of the spin excitations due to random disorder in the exchange parameter.	125
7.1	FE polarisation measured by Higashiyama <i>et al.</i>	130
7.2	The unit cell of DyMn_2O_5 , showing DyO_8 polyhedra	131
7.3	The DyMn_2O_5 unit cell showing Dy–O and Mn–O bonds.	132
7.4	The DyMn_2O_5 unit cell showing Mn^{3+}O_6 octahedra	132
7.5	The DyMn_2O_5 unit cell showing Mn^{4+}O_5 bi-pyramids	133
7.6	Magnetisation vs applied magnetic field at $T = 2\text{ K}$	137
7.7	The magnetisation of DyMn_2O_5 as a function of temperature.	138
7.8	Heat capacity of DyMn_2O_5 as a function of temperature.	138
7.9	(a) Intensity and (b) wavevector of AFM order vs temperature; (c) Energy resonance of Dy AFM order.	139
7.10	Temperature dependence of (a) intensity, and (b) and (c) wavevectors of Mn order in DyMn_2O_5	141
7.11	Energy resonance of induced Dy order.	142
7.12	Widths of diffraction peaks for different ordered phases.	142
7.13	Temperature dependence of non-resonant structural distortion peak.	143
B.1	The (non-primitive) unit cell of LaCoO_3	153

List of Tables

2.1	The Bessel function coefficients for the Cu^{2+} form factor	26
2.2	The matrix elements for different polarisation scattering events	29
4.1	Polarised inelastic neutron scattering intensities	60
5.1	Fit parameters obtained from polarised neutron Q-scans with $\mathbf{P} \parallel \mathbf{Q}$ spin-flip	96
5.2	Fit parameters obtained from polarisation-analysed Q-scans	97
5.3	Fit parameters from polarisation-analysed energy-scans	97
7.1	Allowed reflections for $Pbam$ and $Pb2_1m$ space groups	134

Chapter 1

Introduction

In this thesis strongly correlated electron systems are examined using neutron and x-ray scattering, together with complementary bulk measurements. Many different phenomena are covered by the term ‘correlated electron systems’. At one end of the spectrum of electronic interactions lie metals, in which the electrons may be considered to be virtually non-interacting, whereas at the other end of the spectrum there are insulators in which the electrons are strongly localised, bound to ion cores and also essentially devoid of interactions [1]. In between these two extremes lie many interesting and varied effects which arise due to interactions between electrons, and it is some of these phenomena which will be examined in this thesis.

Strong electron correlations are important because they lead directly to several physical phenomena which either are, or have the potential to be, of technological importance. For instance, high temperature superconductivity in cuprates is due to strong electron correlations, as is the phenomenon of colossal magnetoresistance.

Strongly correlated electron systems have proved to be rather difficult to understand, however. For example, so far no-one has been able to put forward a complete theory of high temperature superconductivity. Indeed, many phenomena associated with strong electron correlations have proved difficult to explain, in large part due to the fact that there are often several competing degrees of freedom in many of the technologically important classes of materials. The competition between different interactions can lead to quite complex phase diagrams, and any successful theory must be able to explain the physical properties of the system in all of these phases.

Faced with such a complicated set of problems physicists have sought to find model systems in which one kind of interaction dominates over the others. By gathering experimental data on such systems, and devising theoretical models to explain their behaviour, it is hoped that the understanding of more complicated materials can be improved upon iteratively.

In this chapter I will consider some of the interactions that are observed in solids. To begin, I will discuss the interactions of single ions, and will then move on to consider some of the plethora of ordered states that arise in multi-ion systems, such as different kinds of magnetic order, superconductivity, and multiferroicity. Some of the excitations of these ordered states will be considered, and finally the rest of the thesis will be outlined.

1.1 Single-Ion Interactions

To begin, let us recall that electrons are fermions and therefore obey the Pauli exclusion principle. This means that when electrons are placed in the potential well of a nucleus they cannot all have the same energy, but rather they occupy ‘shells’ for which there is a well defined angular momentum and energy. Each shell can accommodate a fixed number of electrons, so any further electrons added to the system must go into a shell with higher energy. Electrons in filled shells do not in general interact with the atom’s surroundings, so the electrons in unfilled shells will usually be discussed here.

1.1.1 Crystal Fields

When considering the properties of a magnetic ion in a solid, the crystalline environment of that ion will determine some of its properties. Of particular importance is the effect of Coulomb repulsion between the electron wavefunctions of the ion and its nearest neighbours. This interaction gives rise to eigenstates with different energy levels which depend on the symmetry of these wavefunctions and the symmetry of the crystalline environment. The effects of crystal fields are strong for d -electrons because their wavefunctions extend a relatively long way from the nucleus towards the surrounding ions, whereas f -electron wavefunctions are smaller and are partly shielded from Coulomb interactions with the surroundings by the s - and p -electrons in filled levels.

The crystal field levels in a material can be measured using several techniques. Neutron inelastic scattering can be used, whereby neutrons transfer energy to electrons in lower lying levels and excite them into the higher energy states. Such scattering is wavevector independent. Alternatively photons can be used to excite electrons between levels, with, for example, peaks in the infra-red absorption occurring at wavelengths corresponding to energy gaps between levels.

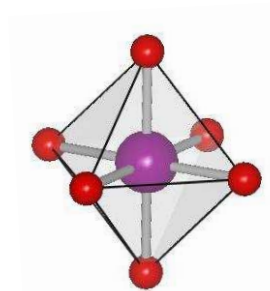


Figure 1.1: A magnetic ion (purple sphere) in an octahedral crystalline environment of oxygen ions (red spheres).

As an example, consider the octahedral environment MO_6 , shown in figure 1.1, in which the magnetic ion M has six nearest neighbour oxygen ions, with their p -electron wavefunctions extending towards M along the bonds. Figure 1.2 shows as an example the overlap between these p -orbitals, the d_{xy} orbitals and the $d_{x^2-y^2}$. There is more overlap between the oxygen electron wavefunctions in the latter compared to the former, resulting in an energy difference. In an octahedral environment the d_{xy} , d_{xz} and d_{yz} (t_{2g}) states will have lower energy than the $d_{x^2-y^2}$ and d_{z^2} (e_g) states.

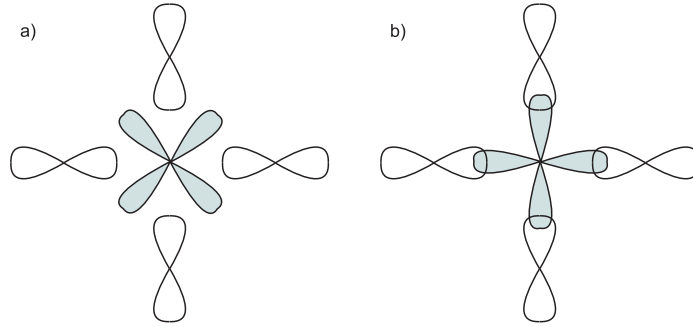


Figure 1.2: a) Overlap of magnetic d_{xy} orbitals (blue) with oxygen p orbitals (white) in an octahedral environment, b) Overlap of $d_{x^2-y^2}$ (blue) orbitals with p orbitals (white) in an octahedral environment.

Jahn-Teller Effect

There are six t_{2g} states and four e_g states, separated by an energy gap, that can be occupied in a $3d$ ion. The t_{2g} states are orbitally degenerate, as are the e_g states¹. In certain circumstances when these states are partially filled it may be energetically favourable for the lattice to distort spontaneously, thus lowering the degeneracy. This is known as the Jahn-Teller effect, and occurs because the energy gained by the system due to elastic strain may be outweighed by the energy lost by a lowering of the energy of the occupied orbitals. An illustration of this effect in a Mn^{3+}O_6 environment is shown in figure 1.3, where the distortion is a stretching of the octahedron along the z -axis.

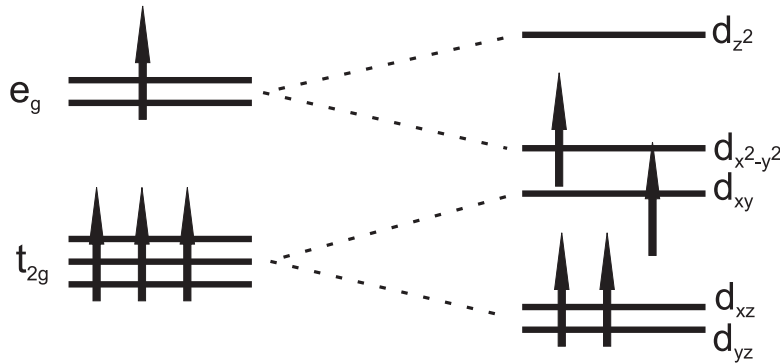


Figure 1.3: The $3d$ energy levels of Mn^{3+}O_6 in an octahedral environment before (left) and after (right) a Jahn-Teller distortion

1.2 Collective Interactions

1.2.1 Magnetism

Examples of magnetic phenomena have been known for many centuries. Thales of Miletus (625 to 547 BC) is the first person known to have considered magnetism, an account of which

¹Degeneracy is a requirement for the Jahn-Teller effect.

appears in Aristotle's *De Anima* [2]. Science has progressed somewhat in the intervening years, however fundamental magnetic phenomena are still providing a means for us to test the limits of our knowledge.

Diamagnetism, Paramagnetism, and Hund's Rules

Diamagnetism is a ubiquitous effect, although its strength is material dependent. It occurs only when a magnetic field is applied to the material, and acts to oppose the applied field, i.e. the magnetisation is antiparallel to the applied field. The diamagnetic susceptibility of an assembly of N identical ions in a volume V , each with Z electrons of mass m_e , is given by

$$\chi = -\frac{N e^2 \mu_0}{V 6m_e} \sum_{i=1}^Z \langle r_i^2 \rangle, \quad (1.1)$$

where r_i are the radii or electron orbitals in the material.

Paramagnetism also occurs only when a magnetic field is applied to a material, however the paramagnetic magnetisation will be parallel to the applied field. It arises due to the non-zero angular momentum (spin \mathbf{S} and/or orbital \mathbf{L}) of the electrons in unfilled shells in a material, and is due to an interaction between individual ions and the applied field. There are assumed to be no interactions between the ions. For a material in which the total angular momentum, J , of each ion is given by $J = 1/2$ the paramagnetic magnetisation, M , is given by

$$M = N\mu_B \tanh\left(\frac{\mu_B B}{k_B T}\right), \quad (1.2)$$

where N is the number of magnetic ions. In the general case, where $J \neq 0$,

$$M = Ng_J \mu_B J B_J(y), \quad (1.3)$$

where g_J is the Landé g-factor, $y = \frac{g_J \mu_B J}{k_B T}$, and $B_J(y)$ is the Brillouin function, which is given by

$$B_J(y) = \frac{2J+1}{2J} \coth\left(\frac{2J+1}{2J}y\right) - \frac{1}{2J} \coth\left(\frac{y}{2J}\right). \quad (1.4)$$

A set of empirical rules, known as Hund's rules, can be used to determine the angular momentum quantum numbers of the ground state of a magnetic system. They deal with the case where the energy of Coulomb repulsion is greater than that arising from spin-orbit interactions, i.e. the LS-coupling regime. Note that they only apply to the ground state – they cannot be used for excited states. The rules are as follows:

1. Maximise the spin. This means that, if we consider adding electrons to the shell, every electron added will increase S by $1/2$ until the shell is half-filled. Thereafter each

electron added will reduce S by $1/2$.

2. Maximise the orbital angular momentum, subject to the first rule. Suppose $l = 2$ (d -electrons), then as we add electrons to the shell the first one will have $m_l = 2$, the next $m_l = 1$, until we reach half-filling, where the m_l will have all cancelled out, and then we start the process again.
3. $J = |L - S|$ if the shell is less than half-full, and $J = |L + S|$ if the shell is more than half full.

Exchange Interactions

So far we have not considered any inter-site interaction terms in the Hamiltonian of the magnetic ions, and although this is a good approximation for a lot of materials, there are also many where the magnetic ions do interact. The exchange interaction arises due to Coulomb interactions arising from the overlap of electron wavefunctions in a material [3]. The Heisenberg Hamiltonian, \mathcal{H} , for exchange interaction terms is given by

$$\mathcal{H} = - \sum_{ij} J_{ij} \mathbf{S}_i \cdot \mathbf{S}_j, \quad (1.5)$$

where J_{ij} is the exchange constant between the i^{th} and j^{th} spins, with positive J corresponding to ferromagnetism and negative J corresponding to antiferromagnetism.

In a ferromagnet adjacent magnetic moments are aligned parallel, whereas in an antiferromagnet they are antiparallel along one or more directions. The periodicity of ferromagnetic order is equal to the separation of the magnetic moments, whereas for antiferromagnetic order the repeat period is doubled. There are many other magnetic structures that can arise, for a variety of reasons, where the periodicity is different. For example the magnetic moments may be helically ordered so that along a particular direction neighbouring moments are rotated by a fixed angle relative to their neighbours. Such order can be commensurate, where the period of the magnetic order is equal to an integer number of lattice units, or incommensurate where it is not.

The simplest case of exchange is direct exchange, where the amount of direct overlap between wavefunctions of neighbouring magnetic ions, and the resulting Coulomb energy, gives rise to the exchange interaction. More usually, and particularly in transition metal oxides, a non-magnetic ion such as oxygen is situated between pairs of magnetic ions whose wavefunctions do not directly overlap. In such cases interaction occurs through superexchange, where each magnetic ion wavefunction overlaps with the wavefunction of a mediating non-magnetic ion. It is usually, although not exclusively, an antiferromagnetic interaction. Considering an M–O–M bond, where M is a magnetic ion and O is non-magnetic, excited states can mix with the ground state for antiferromagnetic interactions, whereas for ferromagnetic interactions they cannot. In the antiferromagnetic case, then, the kinetic energy of the system is lowered and it is stable, whereas in the ferromagnetic case it is not.

The Goodenough-Kanamori-Anderson (GKA) rules are a set of guidelines for estimating the sign and relative magnitudes of superexchange interactions [4], and can be summarised as follows

1. Generally interactions in magnetic oxides will be antiferromagnetic.
2. The exchange between e_g electrons on different ions connected by a 180° bond is stronger than that between the t_{2g} electrons.
3. A small ferromagnetic coupling can occur for interaction between t_{2g} electrons separated by a 90° bond, or by e_g and t_{2g} electrons separated by a 180° bond.
4. Completely filled shells with an equal number of up and down spins do not contribute to the superexchange interaction.

Double exchange is in some respects similar to superexchange, but results in a ferromagnetic system. For example, consider a system containing Mn^{3+} ($3d^4$) and Mn^{4+} ($3d^3$) ions. In such a system e_g electrons can hop from site to site, however there are some constraints imposed by energy considerations of such a process. Crystal field splitting (discussed in section 1.1.1) will result in t_{2g} electrons lying at lower energies than the e_g states, and due to the first of Hund's rules the t_{2g} electrons will have parallel spins for both Mn^{3+} and Mn^{4+} ions. Any e_g electron that hops on to a neighbouring site must, for the same reason, have its spin aligned with the t_{2g} electrons of the site where it is hopping *to*, since a spin-flip in the hopping process costs energy. The e_g electron must also have been aligned parallel to the t_{2g} electrons on the site where it hopped *from*. In order to minimise the kinetic energy of the hopping process the ions must be ferromagnetically coupled.

Another kind of interaction, the Dzyaloshinskii-Moriya (DM) or anisotropic exchange interaction, arises due to spin-orbit coupling. In the case of superexchange there is a mixing of the ground state and excited state of the system due to the presence of a non-magnetic ion such as oxygen, whereas here the spin-orbit interaction can lead to the ground state of one magnetic ion interacting with the spin-orbit excited state of the other magnetic ion. The form of the DM Hamiltonian is:

$$\mathcal{H}_{\text{DM}} = \mathbf{D} \cdot (\mathbf{S}_i \times \mathbf{S}_j) \quad (1.6)$$

when acting between the i^{th} and j^{th} spins. The vector \mathbf{D} is non-zero provided that the crystal field acting on the two spins does not have an inversion symmetry at the half-way point of the vector joining the two spins. The effect of the DM interaction is for the spins to lie preferentially at right angles to one another, in a plane perpendicular to \mathbf{D} . If there are other interactions acting on the system then such a situation may not be realised, and instead the DM interaction may result, for example, in spins lying in the same plane and rotating slightly from site to site.

Itinerant Electron Magnetism

The descriptions of magnetic interactions have so far assumed that all of the magnetic ions were localised and therefore at fixed distances from each other. It is possible to envisage quite easily a situation in which this assumption is not valid, namely in a metal. Pauli paramagnetism is the paramagnetic response of an electron gas (i.e. a metal) to an applied magnetic field. Its physical origin is distinct from paramagnetism in ionic solids, discussed

above, in that it comes about due to splitting of bands with different spin state² in an applied magnetic field. The Pauli paramagnetic susceptibility is given by:

$$\begin{aligned}\chi_P &= \frac{M}{H} \approx \frac{\mu_0 M}{B} = \mu_0 \mu_B^2 g(E_F) \\ &= \frac{3N \mu_0 \mu_B^2}{2E_F}.\end{aligned}\tag{1.7}$$

It is also possible for spontaneous ferromagnetism to occur in metals under certain conditions. If electrons from one spin band are moved into another then in order to obey the Pauli exclusion principle they must gain kinetic energy, hence this is an unfavourable process. However the magnetisation caused by such a move gives rise to an effective magnetic field in the material. This effective field will be strong if there are strong Coulomb interaction in the metal, and it turns out that if the product of the density of states at the Fermi level and the Coulomb interaction energy is greater than unity, the system is unstable to ferromagnetism. This instability criterion is known as the Stoner criterion [5].

1.2.2 Superconductivity

Superconductivity below about 4K was first observed experimentally in mercury in 1911 by Kamerlingh Onnes [6]. There are a number of physical properties that are necessary conditions for a material to be said to be a superconductor, and which distinguish such a material from a perfect conductor. The most obvious property of a superconductor is that below a critical temperature, T_c , the material has zero electrical resistance. This does not, however, distinguish it from a perfect conductor. A superconductor additionally exhibits the Meissner effect, whereby magnetic flux is completely excluded from the material's interior³ and it becomes a perfect diamagnet, provided any applied magnetic field is not above the material's critical field H_c .

BCS Superconductivity

Following Onnes' initial discovery of superconductivity in mercury many more materials were found to superconduct, though it was not until 1957 that a theoretical understanding of the phenomenon was achieved, when Bardeen, Cooper, and Schrieffer [7] proposed what has come to be known as BCS theory.

Put simply, in BCS theory electrons become bound together by exchange of virtual phonons and form 'Cooper-pairs', decreasing their energy by doing so. These Cooper pairs are bosons and therefore the Pauli exclusion principle does not apply, so if one pair of

²The conduction band of a metal can be considered to be made up of two separate bands, one for each spin state.

³In fact magnetic flux does penetrate a short distance into the interior of a superconductor, although the flux decays exponentially with the distance from the surface. This finite penetration of flux can be phenomenologically explained using the London equations, which are themselves derived from Maxwell's equations. Note that the London equations do not encompass any microscopic information about the superconducting state.

electrons can save energy by becoming bound together, then other electrons are likely to do the same. Since Cooper pairs are Bosons there is no restriction on the number that exist in any particular quantum state. The binding energy (reduction in energy of the electron pair) is greatest if electrons with equal but opposite momentum become bound together.

Consider adding two electrons, with momenta \mathbf{k}_1 and \mathbf{k}_2 respectively, to a metal at zero temperature. If electron 1 emits a phonon with wavevector \mathbf{q} then $\mathbf{k}_1 \rightarrow \mathbf{k}_1 - \mathbf{q} = \mathbf{k}'_1$, and $\mathbf{k}_2 \rightarrow \mathbf{k}_2 + \mathbf{q} = \mathbf{k}'_2$, and by conservation of momentum $\mathbf{K} = \mathbf{k}_1 + \mathbf{k}_2 = \mathbf{k}'_1 + \mathbf{k}'_2$. Now the phonon has an energy $\sim \hbar\omega_{\text{Debye}} \ll E_F$, and in addition, because of the Pauli exclusion principle, $k_F \leq k'_1$ and $k'_2 \leq k_F + q$. The number of available states into which the electrons can be scattered is a maximum for $\mathbf{K} = 0$, i.e. $\mathbf{k}_1 = -\mathbf{k}_2$.

There are several physical properties exhibited by BCS superconductors which together can be used to identify them. There is an energy gap associated with the Cooper pairs, the energy saved by pair formation compared to the unpaired state, which can be probed using infra-red absorption. The peak in energy of the absorption will correspond to the energy gap. BCS theory predicts that the gap at zero temperature $\Delta(0)$, corresponding to the energy required to break up a Cooper pair, is related to T_c by

$$\frac{\Delta(0)}{k_B T_c} = 3.528. \quad (1.8)$$

Furthermore, BCS theory also predicts the so-called ‘isotope effect’, in which the critical temperature is found to depend on the isotope mass of the superconducting material. The fact that phonon modes are affected by isotope mass, and virtual phonon exchange is responsible for the superconductivity, makes it relatively straightforward to understand qualitatively why this is so.

Cuprate Superconductors

In 1986 Bednorz and Müller [8] made one of the most important discoveries in modern condensed matter physics when they found that La_2CuO_4 becomes superconducting when a certain amount of Ba^{2+} is substituted for La^{3+} . The unprecedentedly high critical temperature of the superconductivity was the most remarkable feature. This breakthrough quickly led to the discovery of other ‘high- T_c ’ cuprate superconductors such as $\text{YBa}_2\text{Cu}_3\text{O}_{6+x}$ [9]. The superconductivity in these cuprate compounds was found to be inconsistent with the well established BCS theory, which correctly explained the properties of the non-cuprate superconductors known at that point in time [10]. For example the critical temperatures of the cuprates were much larger than those generally compatible with BCS theory. Also the energy gaps observed in the cuprates suggested a moderate strength phonon interaction within the BCS framework, which was inconsistent with the very strong interaction needed to explain the high values of T_c . A new theoretical approach was therefore required to explain the physics of the cuprate superconductors, and in order for this to be formulated a large body of experimental data was needed.

Putting together the evidence from a large number of experiments allowed the phase diagrams relating the critical temperature to doping to be mapped out for many superconductors, and it has become clear that they display many similarities. Figure 1.4 shows a

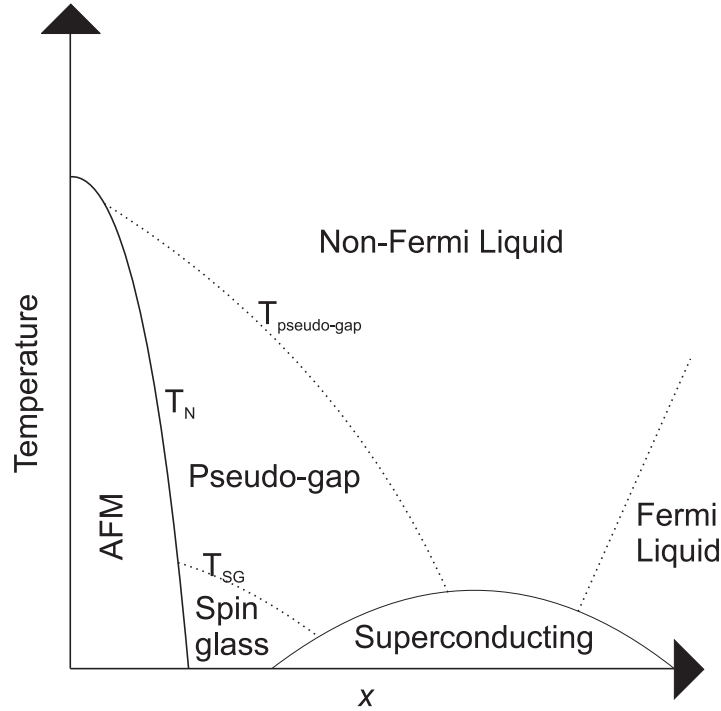


Figure 1.4: The generic phase diagram of a cuprate superconductor, showing the critical temperature T_c vs hole doping x .

generic phase diagram for a hole-doped superconductor⁴.

Considering the phase diagram with increasing doping, starting with the undoped case, a number of different phenomena occur. At the lowest doping the material is a Mott insulator and the spins order antiferromagnetically [11]. As x is increased the Néel temperature decreases, eventually reaching zero. If x is increased beyond this critical point the material enters either what is known as the spin-glass phase, or the pseudogap phase, at lower and higher temperatures respectively. The pseudogap phase is one in which certain physical properties show behaviour indicative of the existence of an energy gap. It seems that electrons are not totally forbidden from crossing the gap, however, and the symmetry of the gap has been shown to be that of d-wave electrons [12].

Further increases in the doping eventually lead to the material entering the superconducting phase⁵. Within this phase the critical temperature gradually increases with increasing x , until a maximum is reached whereupon T_c gradually reduces. A dip in T_c is also observed at $x = 1/8$, however it is too narrow to be shown in figure 1.4.

Eventually the doping x is increased enough that the superconducting transition temperature goes to zero. For higher doping than this critical level the material goes into the so-called Fermi liquid state. At low energies and temperatures we can consider a Fermi liquid state to consist of quasi-particles which separately contain the spin, charge and momentum of the fermions⁶, and are weakly interacting. A final phase exists at higher temperatures for

⁴There also exist superconductors doped with electrons.

⁵For doping lower than this lower critical level the material is said to be ‘underdoped’. Likewise for doping higher than the upper critical level the material is said to be ‘overdoped’.

⁶i.e. one set of quasi-particles contain the spin, another set the charge, and another set the momentum

a wide range of doping, the so-called non-Fermi liquid phase. In this phase the physics of a Fermi liquid appear to break down and the properties of the system cannot be explained either by independent electrons, or quasiparticles. The precise nature of the non-Fermi liquid phase is not yet understood.

1.2.3 Charge Ordering

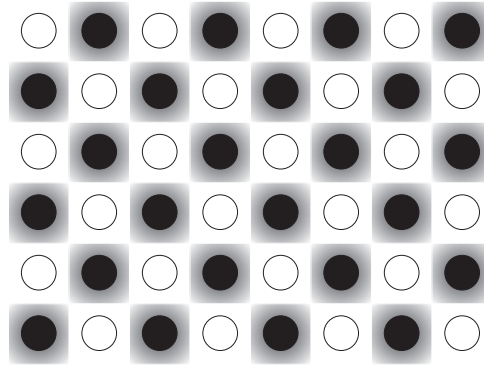


Figure 1.5: Schematic of a charge checkerboard for a half-doped $\text{La}_{2-x}\text{A}_x\text{MO}_4$ material, with circles representing ions on a square lattice and the shading representing localised charge.

Layered compounds isostructural to some cuprate superconductors, such as $\text{La}_{2-x}\text{A}_x\text{MO}_4$, with $\text{A} = \text{Sr}, \text{Ca}, \text{Ba} \dots$ (hole dopants), and $\text{M} = \text{Ni}, \text{Co} \dots$ [13] have been found to exhibit charge order, i.e. the localisation of the doped holes into periodic structures in the MO_2 planes. The spins of the M ions situated between the localised charges also tend to become ordered in periodic structures at the same time.

The details of the charge order structures depend somewhat on M, but there are many features common to all of the materials. Two models commonly used to describe the charge order are the checkerboard model and the stripe model. In the former, a good example of which is found in $\text{La}_{1.5}\text{Sr}_{0.5}\text{NiO}_4$, the charge forms into the checkerboard like that shown in figure 1.5 with alternate sites containing a hole, giving a periodicity of two lattice units. In $\text{La}_{5/3}\text{Sr}_{1/3}\text{NiO}_4$ the periodicity is three lattice units, and the charge structure is arranged into quasi-1D rivers (stripes) which run diagonally [14]. The presence of charge order can be detected directly using scanning tunnelling microscopy (STM) [15], or indirectly using neutrons or x-rays to probe periodic structural distortions caused by Coulomb interactions between the ordered charge and the ions in the lattice [20].

1.2.4 Orbital Ordering

As has already been mentioned in section 1.1, the electron wavefunctions in solids tend not to be spherically symmetric and their orientation can therefore be affected by the symmetry of the local crystalline environment. In some materials, then, the energy can be lowered by the orbitals arranging themselves into a periodic structure – termed orbital ordering.

of the fermions.

An example of a material in which orbital ordering occurs is $\text{La}_{0.5}\text{Sr}_{1.5}\text{MnO}_4$, which is, as with the charge ordered compounds discussed in section 1.2.3, isostructural to some cuprate superconductors [17]. In this material the $3d_{3z^2-r^2}$ orbitals of the e_g electrons on the Mn^{3+} sites form into zigzag chains in the ab -plane, shown schematically in figure 1.6. In general the orientation of electron orbitals in a material has a strong effect on the magnetic properties, because they affect the strength of the inter-atomic exchange. These effects are described by the GKA rules, already discussed in section 1.2.1.

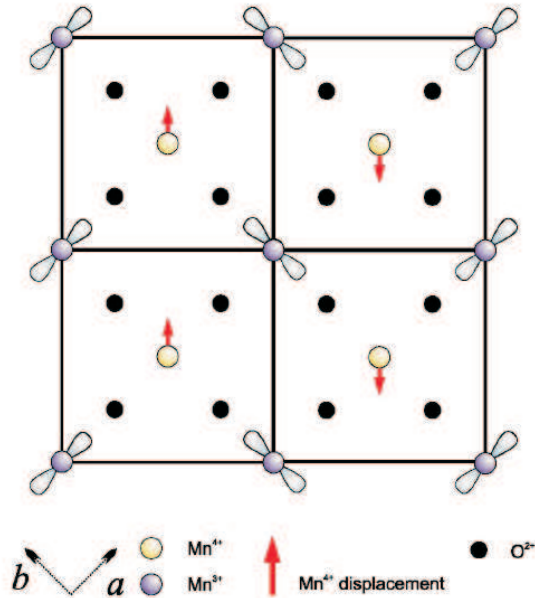


Figure 1.6: (After Wilkins *et al* [17], schematic of orbital order in $\text{La}_{0.5}\text{Sr}_{1.5}\text{MnO}_4$.

1.2.5 Multiferroic Materials

A multiferroic material is one in which there exists simultaneously more than one type of ‘ferroic’ order, such as magnetism, ferroelectricity, charge order, co-operative structural distortions etc. The term multiferroic is usually applied to materials in which there is a coupling or coexistence of magnetic and ferroelectric (FE) order, however. In recent years there has been an upsurge in research into such materials, although examples of this behaviour have been known for a long time [18]. The recent renaissance is due to discoveries of compounds in which the magneto-electric coupling is strong. Most of the renewed interest has centred around $R\text{MnO}_3$ and $R\text{Mn}_2\text{O}_5$ materials, where R is a member of the rare-earths⁷.

A common feature of the manganese oxide based compounds is a complex magnetic phase diagram, including magnetic order that is in turn antiferromagnetic, incommensurate and/or commensurate in wavevector [19]. Another common feature is the possibility to control FE polarisation by the application of a moderate magnetic field. This control can take the form of enhancing, creating, or switching the direction of the FE polarisation.

Several phenomenological theories, based on symmetry considerations, have been proposed to explain such phenomena [20, 21]. In these theories the free energy, calculated

⁷Many other materials have been found to have multiferroic properties, but they will not be discussed here.

using Ginzburg-Landau type continuum field theory, is minimised with respect to the FE polarisation. The coupling between FE polarisation \mathbf{P} and magnetisation \mathbf{M} is constrained by considerations of the behaviour of these two quantities under time reversal and spatial inversion. The physical origin of the magneto-electric coupling is not considered by these theories, rather the existence of such a coupling is assumed and the implications of this are then calculated. The main difference between the theory of Mostovoy [20] and that of Betouras *et al* [21] is that the former assumes a spatially homogeneous FE polarisation, whereas the latter allows spatial variation of \mathbf{P} within the material. However both theories predict that cycloidal magnetic order can create a non-zero FE polarisation.

The precise nature of the magnetoelectric coupling is not yet understood, however one possible candidate is the so-called ‘inverse Dzyaloshinskii-Moriya’ interaction [22, 23], where a structural distortion lowers the energy of a spiral chain when there is a DM exchange interaction between spins. The resulting FE polarisation has the form

$$\mathbf{P} \propto \mathbf{r}_{ij} \times (\mathbf{S}_i \times \mathbf{S}_j), \quad (1.9)$$

where \mathbf{r}_{ij} is the separation of spins i and j , which have spin \mathbf{S}_i and \mathbf{S}_j respectively. This result is strictly only valid for systems with just one magnetic ion per unit cell, and a magnetic propagation vector that is parallel to a lattice vector. Nevertheless, the underlying physics should be similar for more complicated systems. The same result is arrived at when spin supercurrents⁸ are considered [22].

Very recently Hu has provided an alternative microscopic theory of magneto-electric coupling in multiferroics [24], based on spin-orbit effects. The theory provides quantitative predictions for the strength of the magneto-electric coupling, provided that the material is a Mott insulator and the energy gap between the valence band and conduction band is known.

1.3 Excitations

1.3.1 Spin Waves in Localised Magnets

Spin waves are collective excitations of a system of ordered magnetic moments, and they can be visualised as single spins flipped from their ground state propagating through the system, which is parameterised by a dispersion relation. As a simple example consider a one-dimensional Heisenberg ferromagnet, i.e. a chain where all the spins are localised and parallel to the $+z$ -direction in the ground state, which is described by the eigenfunction $|0\rangle$.

The Heisenberg Hamiltonian, given in equation 1.5 is re-written as

$$\mathcal{H} = J \sum_i \left[S_i^z S_{i+1}^z + \frac{1}{2} (S_i^+ S_{i+1}^- + S_i^- S_{i+1}^+) \right], \quad (1.10)$$

where S_i^α is the α -component of the spin \mathbf{S}_i on site i , S_i^+ and S_i^- are the annihilation and

⁸A spin supercurrent is the flow of electron spin through a material. It is time even (time reversal causes a reversal of motion *and* spin polarisation), as opposed to the charge current which is time odd.

creation operators for a flipped spin on site i , and J is the exchange constant (negative for a ferromagnet). The ground state is defined so that $\mathcal{H}|0\rangle = E_0|0\rangle$, with $E_0 = NS^2J$, where N is the number of spins in the chain. An excitation in this ordered system is created by flipping a spin at site j , i.e. the excited state $|j\rangle = S_j^-|0\rangle$. Applying the Hamiltonian to this excited state gives

$$\mathcal{H}|j\rangle = (NS^2J - 2SJ)|j\rangle + SJ|j+1\rangle SJ|j-1\rangle. \quad (1.11)$$

Considering the Fourier transform $|q\rangle = \sum_j e^{iqr_j}|j\rangle$ then gives

$$\mathcal{H}|q\rangle = (E_0 + \hbar\omega)|q\rangle = \{NS^2J - 2JS[1 - \cos(qa)]\}|q\rangle, \quad (1.12)$$

where a is the lattice spacing, and the dispersion of the excitation is given by the expression $\hbar\omega = -2JS[1 - \cos(qa)]$, recalling that J is negative for a ferromagnet. It can be shown [25] that for a three dimensional ferromagnet with nearest neighbour interactions this becomes

$$\hbar\omega = 2JS[3 - \cos(q_x a) - \cos(q_y b) - \cos(q_z c)], \quad (1.13)$$

where q_α is the α -component of the wavevector and a, b, c are the lattice vectors in the directions specified by α . At small wavevectors $(q, 0, 0)$, for the simple case of a cubic system, this can be expanded in a Taylor series to give the spin-wave stiffness constant D

$$\hbar\omega = JSa^2q^2 = Dq^2. \quad (1.14)$$

1.3.2 Spin Excitations in Itinerant Magnets

As has already been discussed in section 1.2.1, there are many magnetic materials in which the electrons are not localised, i.e. in which they are itinerant. The excitations in such systems are somewhat different to the spin waves discussed in section 1.3.1, so I shall give a brief outline of them here.

In an metallic (itinerant electron) ferromagnet there exist spin-split Stoner bands, separated by a gap Δ . It is possible to excite an electron from one band to another provided that its spin is flipped during the excitation process, shown in figure 1.7. This can be achieved if the electron is excited using a neutron (neutron magnetic inelastic scattering), and the resulting magnetic excitation spectrum, shown by the shaded area in figure 1.8 is diffuse and isotropic.

There is also a line in figure 1.8 corresponding to dispersive excitations at energies and wavevectors below the threshold of the Stoner continuum. Such localised excitations have been observed in, for example iron [26], where outside the Stoner continuum spin-wave modes can still propagate.

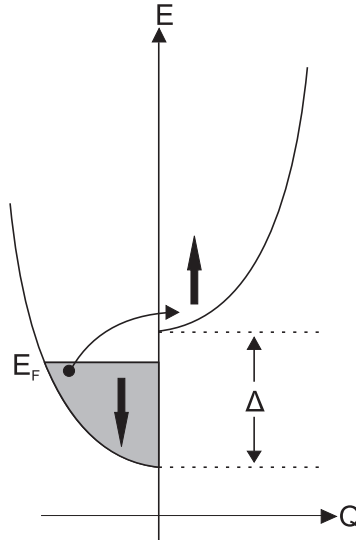


Figure 1.7: The split spin bands in a Fermi gas (metal), showing a single particle spin-flip excitation from one band to another. Arrows denote the spin state in each band.

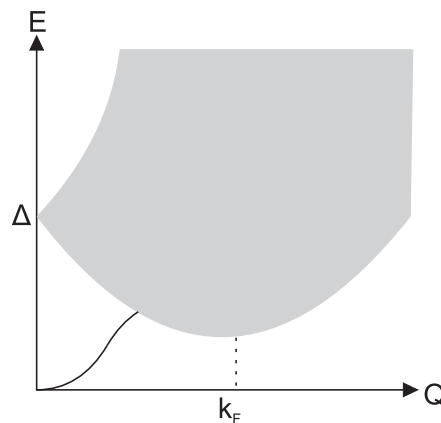


Figure 1.8: The continuum of magnetic excitations resulting from the spin flip processes shown in figure 1.7 (shaded area), and spin-wave modes that can still propagate below this continuum (solid line).

1.4 Scope of this Thesis

Studies of four different materials which display strong electron correlation will be presented in this thesis. Most of the work has been experimental, mainly utilising neutron scattering and x-ray scattering, with some bulk measurements. Neutron and x-ray scattering are microscopic probes and can be used to determine the atomic-scale order parameters in correlated electron systems. Furthermore, neutron inelastic scattering is the best probe of the fundamental excitations of such systems. In chapter 2 an introduction is given to the theory underpinning neutron and x-ray scattering, as well as some details of the practicalities of performing scattering measurements and bulk property measurements. In the following four chapters results of measurements of different materials are presented in turn.

Chapter 3: $\text{La}_{1.48}\text{Nd}_{0.4}\text{Sr}_{0.12}\text{CuO}_4$

$\text{La}_{1.48}\text{Nd}_{0.4}\text{Sr}_{0.12}\text{CuO}_4$ is a cuprate superconductor which is known to exhibit charge and spin ordering, and there exist several different theories to explain the nature of this order. Polarised neutron scattering was used to test these theories by probing the microscopic magnetic order. Neutron inelastic scattering was used to measure the magnetic excitations at low energies. Finally x-ray diffraction was used to study the charge order as a function of temperature and applied magnetic field.

Chapter 4: LaCoO_3

LaCoO_3 displays a transition from a non-magnetic ground state to a magnetic excited state when warmed to $T \geq 100$ K. The nature of this excited magnetic state is somewhat controversial, since there is conflicting theoretical work and conflicting experimental evidence. Polarised neutron inelastic scattering was used to measure the excitations of spins within this excited magnetic state.

Chapter 5: $\text{La}_{0.82}\text{Sr}_{0.18}\text{CoO}_3$

$\text{La}_{0.82}\text{Sr}_{0.18}\text{CoO}_3$ is a ferromagnetic metal which displays colossal magnetoresistance effects. Polarised neutron inelastic scattering was used to measure the dispersion of the ferromagnetic excitations at low temperature so that comparison may be drawn with similar data on other colossal magnetoresistive materials.

Chapter 6: DyMn_2O_5

DyMn_2O_5 is a multiferroic material where the microscopic magnetic order has been hard to measure due to the large neutron absorption cross-section of dysprosium. X-ray resonant magnetic diffraction was used to measure the static magnetic order in order to determine which theoretical model of multiferroics is appropriate for this compound, and also to compare the results with other rare-earth manganites.

1.5 Publications

The following publications relate to work presented in this thesis.

- *X-ray Resonant Scattering Study of Multiferroic $DyMn_2O_5$* , R. A. Ewings, A. T. Boothroyd, D. F. McMorrow, D. Mannix, H. C. Walker, and B. M. R. Wanklyn, Phys. Rev. B **77**, 104415 (2008).
- *Nature of the Magnetic Order in the Charge-Ordered Cuprate $La_{1.48}Nd_{0.4}Sr_{0.12}CuO_4$* , N. B. Christensen, H. M. Rønnow, J. Mesot, R. A. Ewings, N. Momono, M. Oda, M. Ido, M. Enderle, D. F. McMorrow, and A. T. Boothroyd, Phys. Rev. Lett. **98**, 197003 (2007).
- *X-ray Scattering Study of the Order Parameters in Multiferroic $TbMnO_3$* , D. Mannix, D. F. McMorrow, R. A. Ewings, A. T. Boothroyd, D. Prabhakaran, Y. Joly, B. Janousova, C. Mazzoli, L. Paolasini, and S. B. Wilkins, Phys. Rev. B **76**, 184420 (2007).

References

- [1] J. Singleton, *Band Theory and Electronic Properties of Solids*, Oxford University Press (2001).
- [2] Aristotle, *de Anima*, Book I, part II, Trans. H. Lawson-Tancred, Penguin Books (1986).
- [3] S. J. Blundell, *Magnetism in Condensed Matter*, Oxford University Press (1st edition), p.74.
- [4] J. B. Goodenough, Phys. Rev. **100**, 564 (1955); J. Kanamori, J. Phys. Chem. Solids **10**, 87 (1959); P. W. Anderson, Phys. Rev. **115**, 2 (1959).
- [5] P. Fazekas, *Lecture Notes on Electron Correlation and Magnetism*, World Scientific Publishing Co Pte Ltd (1999).
- [6] H. K. Onnes, ‘On the sudden change in the rate at which the resistance of mercury disappears’, Commun. Phys. Lab. Univ. Leiden **124c**, 1 (1911).
- [7] L. N. Cooper, Phys. Rev **104**, 1189 (1956); J. Bardeen, L. N. Cooper, and J. R. Schrieffer, Phys. Rev. **106**, 162 (1957); J. Bardeen, L. N. Cooper, and J. R. Schrieffer, Phys. Rev. **108**, 1175 (1957).
- [8] J. G. Bednorz, and K. A. Müller, Z. Phys. B **64**, 189 (1986).
- [9] P. A. Lee, N. Nagosa, and X. -G. Wen, Rev. Mod. Phys. **78**, 17 (2006).
- [10] J. R. Waldram, *Superconductivity of Metals and Cuprates*, Institute of Physics Publishing (1996).
- [11] D. Vaknin, S. K. Sinha, D. E. Moncton, D. C. Johnston, J. M. Newsam, C. R. Safinya, and H. E. King, Jr, Phys. Rev. Lett. **58**, 2802 (1987).
- [12] G. V. M. Williams, J. L. Tallon, E. M. Haines, R. Michalak, and R. Dupree, Phys. Rev. Lett. **78**, 721 (1997).
- [13] J. M. Tranquada, D. J. Buttrey, V. Sachan, and J. E. Lorenzo, Phys. Rev. Lett. **73**, 1003 (1994); I. A. Zaliznyak, J. P. Hill, J. M. Tranquada, R. Erwin, and Y. Moritomo, Phys. Rev. Lett. **85**, 4353 (2000).
- [14] H. Yoshizawa, T. Kakeshita, R. Kajimoto, T. Tanabe, T. Katsufuji, and Y. Tokura, Phys. Rev. B **61**, 854 (2000).
- [15] K. McElroy, D. -H. Lee, J. E. Hoffman, K. M. Lang, J. Lee, E. W. Hudson, H. Eisaki, S. Uchida, and J. C. Davis, Phys. Rev. Lett. **94**, 197005 (2005).

- [16] M. v. Zimmermann, A. Vigliante, T. Niemöller, N. Ichikawa, T. Frello, J. Madsen, P. Wochner, S. Uchida, N. H. Anderson, J. M. Tranquada, D. Gibbs, and J. R. Schneider, *Europhys. Lett.* **41**, 629 (1998).
- [17] S. B. Wilkins, P. D. Spencer, P. D. Hatton, S. P. Collins, M. D. Roper, D. Prabhakaran, and A. T. Boothroyd, *Phys. Rev. Lett.* **91**, 167205 (2003).
- [18] E. F. Bertaut and M. Mercier, *Mat. Res. Bull.* **6**, 907 (1971); I. E. Dzyaloshinskii, *Sov. Phys. JETP* **10**, 628 (1960); D. N. Astrov, *Sov. Phys. JETP* **11**, 708 (1960); G. T. Rado and V.J. Folan, *Phys. Rev. Lett.* **7**, 310 (1961); B. I. Al'shin and D. N. Astrov, *Sov. Phys. JETP* **17**, 809 (1963); C. Christov, I. Tsvetkov, and V. Kovachev, *Fiziologia na rasteniyata* **21**, 64 (1995); G. T. Rado, *Phys. Rev. Lett.* **13**, 335 (1964); E. Fischer, G. Gorodetsky, and R. M. Hornreich, *Solid State Commun.* **10**, 1127 (1972); L. M. Holmes, L. G. van Uitert, and G. W. Hull, *Solid State Commun.* **9**, 1373 (1971).
- [19] T. Kimura, T. Goto, H. Shintani, K. Ishisaka, T. Arima, and Y. Tokura, *Nature (London)* **426**, 55 (2003); T. Goto, T. Kimura, G. Lawes, A. P. Ramirez, and Y. Tokura, *Phys. Rev. Lett.* **92**, 257201 (2004); M. Kenzelmann, A. B. Harris, S. Jonas, C. Broholm, J. Schefer, S. B. Kim, C. L. Zhang, S. -W. Cheong, O. P. Vajk, and J. W. Lynn, *Phys. Rev. Lett.* **95**, 087206 (2005).
- [20] M. Mostovoy, *Phys. Rev. Lett.* **96**, 067601 (2006)
- [21] J. J. Betouras, G. Giovannetti, and J. van den Brink, *Phys. Rev. Lett.* **98**, 257602 (2007).
- [22] H. Katsura, N. Nagaosa, and A. V. Balatsky, *Phys. Rev. Lett.* **95**, 057205 (2005).
- [23] S. -W. Cheong, and M. Mostovoy, *Nature Materials* **6**, 13 (2007).
- [24] J. Hu, *Phys. Rev. Lett.* **100**, 077202 (2008).
- [25] W. Marshall and S. W. Lovesey, *Theory of Thermal Neutron Scattering*, Clarendon Press (1971), p.253.
- [26] J. W. Lynn, *Phys. Rev. B* **11**, 2624 (1975).

Chapter 2

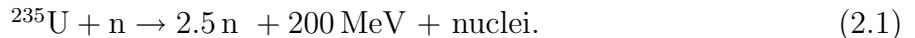
Experimental Techniques

This chapter gives a basic introduction to the experimental methods that were used for the measurements presented in the rest of this thesis. Section 2.1 outlines some details specific to the theory of neutron production and scattering, descriptions of neutron spectrometers, and a discussion of neutron polarisation analysis. Section 2.2 gives some background to the synchrotron x-ray source, details of the various kinds of diffractometer used for the work presented in this thesis, and a brief explanation of the technique of x-ray resonant scattering. Finally section 2.3 gives an overview of the SQUID magnetometer and the Quantum Design PPMS heat capacity measurement system.

2.1 Neutron Scattering

2.1.1 Neutron Sources

There are two methods currently employed to generate neutrons for use in scattering experiments, each with its pros and cons. The first method is nuclear fission, occurring in a traditional nuclear reactor with uranium as the fuel.



A reactor at a neutron scattering facility would be designed to produce an excess of neutrons beyond that required to maintain the chain reaction, and it is these excess neutrons which are used for scattering. Before reaching the scattering instruments the neutrons pass through a moderator which modifies their energy spectrum, the precise choice of moderator material and temperature determining the resulting spectrum. After this the neutrons pass through wave guides to the instruments. In order to avoid ‘fast’ (i.e. high energy) neutrons irradiating the sample the waveguides are actually oriented tangentially to the reactor core. Neutrons which undergo several scattering processes in the moderator tend to be more likely to enter such waveguides than unscattered fast neutrons, which are radiated radially from the reactor core. The main advantage of a reactor source is that it produces a high flux of neutrons at a steady rate.

The other method of generating neutrons for scattering is with a spallation source. Accelerated protons strike a heavy metal target, and the impact of the proton beam triggers a

nuclear reaction. The spallation process is the excitation and neutron emission of the target until it achieves a stable nuclear state. The spectrum of the neutrons is, as with a reactor source, modified by moderators. Such a source typically produces a much lower flux of neutrons than a reactor, however if the proton beam, and hence the neutron beam, is pulsed then so-called ‘time-of-flight’ instruments can be used which would be rather inefficient at a reactor source.

2.1.2 Neutron Scattering Instruments

There are many types of neutron scattering instrument. For inelastic scattering the two main types of instrument used are the time-of-flight (ToF) chopper spectrometer and the triple-axis spectrometer (TAS). The former are used at pulsed spallation neutron sources, as well as at continuous spallation or reactor sources, whereas the latter are most often used at reactor sources. For the research presented in this thesis all of the neutron scattering measurements were performed on triple-axis spectrometers, so only the details of these will be presented.

Triple-axis Spectrometer

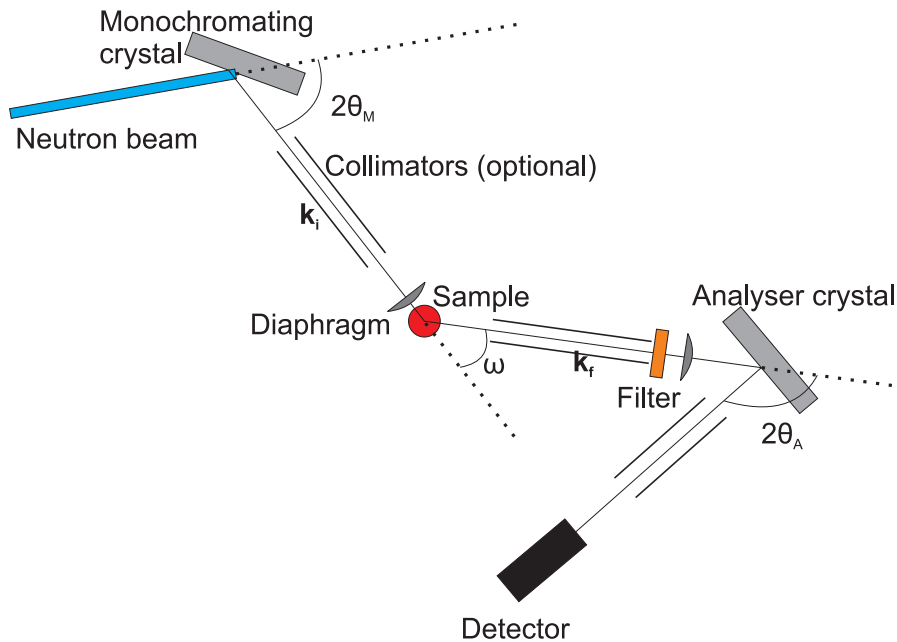


Figure 2.1: A schematic of a conventional triple-axis spectrometer.

The individual components of a TAS are as follows. The monochromator, typically made from pyrolytic graphite (PG), silicon or Heusler crystals, turns a polychromatic beam of neutrons into a monochromatic one by Bragg reflection (usually the 002 reflection for PG). Only neutrons of a given wavelength (energy) fulfil the Bragg condition. Collimators can be used to ensure that the beam does not diverge too much, and they typically take the form of parallel plates which are coated with a neutron-absorbing material such as boron or gadolinium. Despite this the width of the neutron beam is likely to be larger than the width

of the sample, so in order to improve the signal:noise ratio diaphragms are placed before and after the sample. Diaphragms are also placed in front of the analyser and detector in order to allow full illumination whilst reducing spurious scatter entering the detector, thus further improving the signal:noise ratio. The sample may be mounted in a standard orange cryostat, in a dilution refrigerator, or in a cryomagnet depending on the sample environment needed. The analyser crystals work in much the same way as the monochromator, e.g. one might use the (002) reflection from PG, or the (111) reflection from Si, depending on the choice of final neutron wavevector k_f .

More often than not the spectrometer is set up to use a fixed final wavevector k_f , meaning that in order to do inelastic scattering measurements it is only the magnitude of the incident wavevector that is varied. There are several reasons why this setup is chosen. One is that it offers a larger dynamic range that is available with fixed incident wavevector, in that a greater energy range and wavevector transfer is accessible within the geometric constraints of the spectrometer. Also, because the incident beam monitor efficiency is inversely proportional to k_i (discussed later) the neutron count rate normalised to the number of monitor counts is directly proportional to the response function $S(\mathbf{Q}, \omega)$ (defined in section 2.1.3). Moreover, by fixing the final wavevector it allows the use of a filter, the purpose of which is to remove so-called ‘ $\lambda/2, \lambda/3$ ’... noise, i.e. neutrons whose energy is such that their wavelength is an integer fraction of the desired wavelength so they also fulfil the Bragg condition at the analyser. This noise would result in spurious detector counts if filters were not used. The filters may be made from a variety of materials, dependent on the desired scattered wavevector. Typical choices might be cooled Beryllium for $k_i < 1.55 \text{ \AA}^{-1}$ or PG for $k_i = 2.66 \text{ \AA}^{-1}$ or 4.1 \AA^{-1} . These final wavevectors are chosen because they are values where the transmission is close to unity, but the transmission of the second, third and higher harmonics is close to zero.

For all of the work presented in this thesis thermal energy neutrons ($E_{\text{incident}} < 50 \text{ meV}$) were used, for which the filters one uses are ones based on Bragg scattering. For any given material there is a maximum wavelength (minimum energy) for which Bragg scattering can occur, which is given by twice the smallest lattice constant. For wavelengths shorter (energies higher) than this there is a steep decrease in the transmission. For example in a cooled Be filter¹ this change in transmission is rather sharp and occurs at about 5.2 meV. In a PG filter one can choose a neutron wavelength where the transmission of the beam is very high, and in addition the $\lambda/2$ and $\lambda/3$ neutrons are at wavelengths that are strongly Bragg scattered by the PG crystal², and hence have a very low probability of transmission through the filter.

One of the main advantages of neutrons is that they interact rather weakly with matter, and that their interaction with magnetic moments is not immeasurably weak. This does, however, present a problem when it comes to detecting scattered neutrons. Neutrons are not charged so they cannot be detected using radiation detectors which rely on direct gas ionisation. Instead the neutrons need to cause some other atom to emit charged particles which will ionise a gas and therefore be electronically detectable. The standard way of doing this is to use a chamber filled with ^3He gas, which then undergoes the following reaction:

¹The Be is cooled so that the population of phonons is very small, which means that the probability of phonon creation is very small, so neutrons with energies higher than 5.2 meV are less likely to lose energy through phonon scattering processes and pass through the filter.

²Note that the PG crystal has to be correctly oriented with respect to the beam scattered by the sample for this to work.



so that the charged decay products ionise the gas and give rise to a signal proportional to 0.77 MeV, which can be distinguished from signals at different energies arising from gamma rays entering the detector, for example. The ${}^3\text{H}$ nucleus eventually decays to form another ${}^3\text{He}$ nucleus and an electron, so the supply of helium in the detector does not need to be replenished.

It is important to know the flux of neutrons incident on the sample, especially given that this will vary depending on the value of the incident energy. The incident flux is measured using a monitor, which is simply a rather inefficient neutron detector. The monitor's efficiency is inversely proportional to the incident neutron wavevector, k_i , so that when detector counts are normalised to the monitor count rate and the final wavevector, k_f , is fixed, no correction for the k_f/k_i term in equation 2.24 is required. There are two main types of neutron monitor. The most common ones work on the same principle as the ${}^3\text{He}$ detector, but with a much lower gas pressure, which dramatically reduces the efficiency. Another kind of monitor is based on ${}^{235}\text{U}$ -doped sol-gel thin films. A small number of ${}^{235}\text{U}$ nuclei undergo fission when neutrons pass through the film, and the charged decay products are detected using scintillation detectors.

Polarised Neutron Scattering Instrument Components

A variation on the basic TAS is the polarised neutron TAS, which works on the same principles as the basic TAS but has a few modifications. The basic idea behind these is to produce an incident beam of neutrons whose spins all point in the same direction. This reduces the flux incident on the sample, however by analysing the change in polarization state of the neutrons after scattering it is possible to measure scattering which is solely magnetic in origin.

The first modification is to include a polarising monochromator. An example of such a monochromator would be an array of large single crystals of Heusler (Cu_2MnAl) alloy, arranged so that neutrons scatter off the (111) Bragg planes. The analyser would be made from the same material and works the same way. A magnetic field is applied parallel to the surface of the monochromator/analyser and the spins in the crystal align parallel to this. Because Heusler is a centrosymmetric crystal (i.e. the values for both the nuclear and magnetic structure factors are real) and the nuclear and magnetic structure factors are similar in value the two kinds of scattering can either constructively or destructively interfere, depending on the orientation of the applied field, resulting in very good (but not perfect) polarization. The precise details of this will be discussed later.

The next modification is the presence of guide fields around the neutron beam between the monochromator and the sample, and the sample and the analyser. These are basically shielded pipes inside which there is a uniform field of a few mT which serves to maintain the polarization state of the neutron beam. If the guide field was not there then electromagnetic noise would, over the course of the neutrons' path, destroy the polarization state.

The final modification is the insertion of 'flippers' upstream, or more usually downstream, of the sample. A flipper is a device which flips the neutron spin state from one eigenvalue

to another, i.e. from spin up to spin down. The flippers often used on a thermal neutron TAS are radio-frequency (RF) coil flippers. In an RF flipper a constant magnitude radio frequency magnetic field is applied parallel to the neutron beam while a static field applied perpendicular to the neutron beam varies in magnitude along the beam. For all neutron energies there will be some point in the flipper such that their Larmor frequency is equal to the radio frequency of the coil, thus resonance will occur and there will be a transition between the Zeeman split up and down states, i.e. a spin flip.

A spin-flip magnetic scattering event would work as follows: the monochromator polarises the beam so that the spins are up, then the spins are flipped in the sample by interaction with a spin-1/2 magnetic moment/excitation (parallel to the neutron spin) so that the neutrons are now spin down. The flipper then changes the spin state of the scattered beam so that the magnetically scattered neutrons are spin up again. The analyser is then set to Bragg-reflect only spin up, so almost all of the non-magnetically scattered neutrons are not reflected into the detector, while the scattering from magnetic moments/excitations make up the vast majority of the neutrons arriving at the detector.

2.1.3 Neutron Scattering Cross Sections

The derivation of the following results can be found in more detail in, for example, the book by Squires [1]. Here the important results are simply stated without their associated proofs.

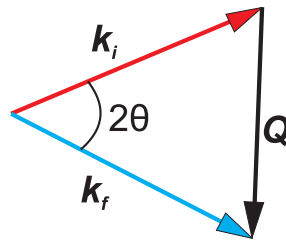


Figure 2.2: The scattering triangle, relating the incident and final wavevectors to the scattering wavevector

A neutron scattering event must conserve both momentum and energy, and these simple rules provide a starting point for the theory of neutron scattering. Energy conservation gives us

$$E_i - E_f = \frac{\hbar^2}{2m_N} (\mathbf{k}_i^2 - \mathbf{k}_f^2) = \hbar\omega, \quad (2.3)$$

where E_i and E_f are respectively the incident and final energies of the neutron, \mathbf{k}_i and \mathbf{k}_f are the incident and final neutron wavevectors and $\hbar\omega$ is the energy of excitation in the sample. Meanwhile momentum conservation gives us

$$\mathbf{Q} = \mathbf{k}_i - \mathbf{k}_f, \quad (2.4)$$

where \mathbf{Q} is the scattering wavevector. The process is shown schematically in figure 2.2.

Taken together equations 2.3 and 2.4 allow us to calculate from a given scattering event the wavevector and energy of the excitations (or static order if $\hbar\omega$ is zero) in the sample.

The quantity measured during a neutron scattering experiment is the double differential cross-section, which is defined as:

$$\frac{d^2\sigma}{d\Omega dE} = \frac{\text{total number of neutrons scattered per unit time into the solid angle } d\Omega \text{ in the direction } \theta, \phi \text{ with energy between } E \text{ and } E+dE}{dE d\Omega \Phi} \quad (2.5)$$

where the total incident neutron flux is given by Φ . For elastic scattering we do not include the dE term in the denominator, i.e. we are only interested in the differential cross-section $\frac{d\sigma}{d\Omega}$. This is because elastic scattering has a greater probability amplitude than inelastic scattering, rendering the differentiation with respect to energy redundant, as we assume scattering which is not in the elastic channel to be negligible. So in both nuclear and magnetic elastic scattering it is $\frac{d\sigma}{d\Omega}$ that is of interest.

Nuclear Elastic Scattering

The coherent nuclear elastic scattering cross section is given by

$$\frac{d\sigma}{d\Omega} = N \frac{(2\pi)^3}{V_0} |F_N(\mathbf{Q})|^2, \quad (2.6)$$

where N is the number of unit cells in the crystal, V_0 is the volume of the unit cell and F_N is the nuclear structure factor.

$$F_N(\mathbf{Q}) = \sum_j \bar{b}_j e^{i\mathbf{Q}\cdot\mathbf{r}_j} e^{-W_j(\mathbf{Q},T)}, \quad (2.7)$$

where the sum runs over all atoms j , \mathbf{r}_j is the position of the j^{th} atom, \bar{b}_j is the nuclear scattering length of the j^{th} atom and W_j is the Debye-Waller factor for the j^{th} atom, which takes account of the fluctuations of the atom due to finite temperature. Note that the cross section stated in equation 2.6 is that for coherent nuclear scattering. There is also an incoherent cross section which gives rise to an isotropic background scatter, which must be subtracted from any data before analysis is performed.

The Debye-Waller factor is included in equation 2.7 because the atoms are not frozen to their lattice sites, but rather they undergo a certain amount of thermal motion about an equilibrium position. As temperature increases this thermal motion also increases, and the result is that the intensity of the Bragg peaks decreases, this decrease being parameterised by the Debye-Waller factor. For a Bravais crystal the Debye-Waller factor is defined as

$$W_j(\mathbf{Q}, T) = \frac{1}{2} \langle (\mathbf{Q} \cdot \mathbf{u}_j(T))^2 \rangle, \quad (2.8)$$

where $\mathbf{u}_j(T)$ is the thermal displacement of atom j from its equilibrium position.

Magnetic Elastic Scattering

Let us now consider the scattering of neutrons by magnetic interactions. Neutrons have a magnetic moment given by

$$\boldsymbol{\mu}_n = -\gamma\mu_N\boldsymbol{\sigma}, \quad (2.9)$$

where μ_N is the nuclear magneton, γ is the gyromagnetic ratio (≈ 1.91) and $\boldsymbol{\sigma}$ is the Pauli spin operator with values ± 1 . The magnetic interaction potential operator $\hat{V}_M(\mathbf{r})$ between neutrons and the local magnetic field $\mathbf{B}(\mathbf{r})$ in a material (e.g. due to an unpaired electron) is given by

$$\hat{V}_M(\mathbf{r}) = -\boldsymbol{\mu}_n \cdot \mathbf{B}(\mathbf{r}). \quad (2.10)$$

The cross section must contain terms which are functions of wavevector \mathbf{Q} rather than spatial co-ordinate \mathbf{r} , so the Fourier transform of this, $\hat{V}_M(\mathbf{Q})$, is used. The local magnetic field can be related to the local magnetisation, so that

$$\hat{V}_M(\mathbf{Q}) = -\boldsymbol{\mu}_n \cdot \mathbf{B}(\mathbf{Q}). \quad (2.11)$$

Now $\mathbf{B}(\mathbf{r}) = \nabla \times \mathbf{A}$, where \mathbf{A} is the magnetic vector potential, given by

$$\mathbf{A}(\mathbf{r}) = \frac{\mu_0}{4\pi} \frac{\boldsymbol{\mu}_e \times \hat{\mathbf{r}}}{r^2}, \quad (2.12)$$

where $\hat{\mathbf{r}}$ is a unit vector in the direction of \mathbf{r} , the distance from the magnetic moment $\boldsymbol{\mu}_e$ which gives rise to the magnetic field and in this case is due to a single unpaired electron. Now

$$\nabla \times \left(\frac{\boldsymbol{\mu}_e \times \hat{\mathbf{r}}}{r^2} \right) = \frac{1}{2\pi^2} \int \hat{\mathbf{q}} \times (\boldsymbol{\mu}_e \times \hat{\mathbf{q}}) e^{i\mathbf{q}\cdot\mathbf{r}} d\mathbf{q}, \quad (2.13)$$

arises as a consequence of vector algebra³ so we can rewrite equation 2.11 as

$$\hat{V}_M(\mathbf{Q}) = -\mu_0\boldsymbol{\mu}_n \cdot \mathbf{M}_\perp(\mathbf{Q}), \quad (2.14)$$

where $\mathbf{M}_\perp(\mathbf{Q})$ is the component of the electron's magnetic moment (due to spin and orbital contributions) perpendicular to the scattering wavevector, such that

$$\mathbf{M}_\perp(\mathbf{Q}) = \hat{\mathbf{Q}} \times [\boldsymbol{\mu}_e(\mathbf{Q}) \times \hat{\mathbf{Q}}], \quad (2.15)$$

where $\hat{\mathbf{Q}}$ is a unit vector pointing in the direction of the scattering wavevector \mathbf{Q} .

³See appendix B of the book by Squires [1].

We must now consider the implications of the fact that the neutrons magnetically scattered by electrons will not necessarily consist of a spherical wave, so to formulate scattering cross sections that assume that the incident and scattered beams are plane-waves a correction factor must be applied. We make the dipole approximation so that rather than using the complicated form for the magnetisation $\mathbf{M}(\mathbf{Q})$ in equation 2.14 we are able to use the dipole moment of the scattering electrons $\boldsymbol{\mu}$. For a $3d$ ion the total angular momentum J is often not a good quantum number because the orbital angular momentum L is quenched. Under such circumstances the magnetisation can be written as

$$\mathbf{M}(\mathbf{Q}) = -g\mu_B f(\mathbf{Q})\mathbf{S} = f(\mathbf{Q})\boldsymbol{\mu}. \quad (2.16)$$

where \mathbf{S} is the spin quantum number, and $f(\mathbf{Q})$ is the magnetic form factor. If we denote the normalised spin density by \mathcal{S} , then the form factor is defined, for the spin-only case, as the Fourier transform of \mathcal{S} , i.e.

$$f(\mathbf{Q}) = \int d^3\mathbf{r} e^{i\mathbf{Q}\cdot\mathbf{r}} \mathcal{S}(\mathbf{r}). \quad (2.17)$$

The derivation of the explicit form of the form factor $f(\mathbf{Q})$ is rather complicated and is omitted here for brevity. For a full derivation see the work of Freeman [2].

In fact $f(\mathbf{Q})$ can be approximated analytically using Bessel functions, which can themselves be approximated in terms of sums of exponentials with suitable coefficients. These coefficients have been found by experiment [3]. If we define s as

$$s = \frac{\sin \theta_s}{\lambda} = \frac{|\mathbf{Q}|}{4\pi}, \quad (2.18)$$

where θ_s is the Bragg angle at the sample, and λ is the wavelength of the incident neutrons, then the analytic approximations for the expectation values of the Bessel functions are

$$\begin{aligned} \langle j_0(s) \rangle &= Ae^{-as^2} + Be^{-bs^2} + Ce^{-cs^2} + D \\ \langle j_{n>0}(s) \rangle &= (Ae^{-as^2} + Be^{-bs^2} + Ce^{-cs^2} + D)s^2. \end{aligned} \quad (2.19)$$

As an illustration the coefficients for Cu^{2+} are given in table 2.1

n	A	a	B	b	C	c	D
0	0.0232	34.969	0.4023	11.564	0.5882	3.843	-0.0137
2	1.5189	10.478	1.1512	3.813	0.2981	1.398	0.0017
4	-0.3914	14.740	0.1275	3.384	0.2548	1.255	0.0103

Table 2.1: The Bessel function coefficients for the Cu^{2+} form factor

Finally, we end up with an expression for the magnetic form factor for a pure $(x^2 - y^2)$ orbital⁴:

⁴See reference [4] for a derivation of this.

$$f(\mathbf{Q}) = \langle j_0(\mathbf{Q}) \rangle - \frac{5}{7}(1 - 3 \cos^2 \beta) \langle j_2(\mathbf{Q}) \rangle + \frac{9}{56} \left(1 - 10 \cos^2 \beta + \frac{35}{3} \cos^4 \beta \right) \langle j_4(\mathbf{Q}) \rangle, \quad (2.20)$$

where β is the angle between the scattering wavevector and the axis perpendicular to the $x^2 - y^2$ orbital plane. Note that for a spherical charge density (i.e. $L = 0$, so spin-only) this simplifies considerably to

$$f(\mathbf{Q})_{\text{spherical}} = \langle j_0(\mathbf{Q}) \rangle. \quad (2.21)$$

For magnetic elastic scattering:

$$\frac{d\sigma}{d\Omega} = N \frac{(2\pi)^3}{V_{\text{mag}}} \left(\frac{\gamma r_0}{2} \right)^2 \sum_{\alpha\beta} (\delta_{\alpha\beta} - \hat{Q}_\alpha \hat{Q}_\beta) \langle F^{(\alpha)}(-\mathbf{Q}) \rangle \langle F^{(\beta)}(\mathbf{Q}) \rangle, \quad (2.22)$$

where N is the number of magnetic unit cells, V_{mag} is the volume of the magnetic unit cell, $\gamma = 1.91$ is the gyromagnetic ratio, $r_0 = 2.8 \times 10^{-15} \text{m}$ is the classical electron radius and the sum over α and β is a sum over all combinations of two cartesian axes (i.e. xx , xy , xz , ...). \hat{Q}_α is a unit vector parallel to the α component of the scattering wavevector, and $\delta_{\alpha\beta}$ is the Kronecker delta. $F^{(\alpha)}(\mathbf{Q})$ is the α component of the magnetic unit cell structure factor. It is given by

$$F^{(\alpha)}(\mathbf{Q}) = \sum_j \mu_j^{(\alpha)} f_j^{(\alpha)} e^{i\mathbf{Q}\cdot\mathbf{r}_j} e^{-W_j(\mathbf{Q}, T)}, \quad (2.23)$$

where the sum runs over all atoms, $\mu_j^{(\alpha)}$ is the α component of the magnetic moment of the j^{th} atom, and $f_j^{(\alpha)}$ is the α component of the magnetic form factor of the j^{th} atom.

Magnetic Inelastic Scattering

Let us consider now the case of an inelastic scattering process, i.e. one in which the neutron gains or loses energy during the scattering process. The cross section for magnetic inelastic scattering, in the dipole approximation for the case of spin-only scattering, is given by

$$\frac{d^2\sigma}{d\Omega dE} = \left(\frac{\gamma r_0}{2} \right)^2 f^2(\mathbf{Q}) e^{-2W(\mathbf{Q}, T)} \frac{k_f}{k_i} S(\mathbf{Q}, \omega), \quad (2.24)$$

where $S(\mathbf{Q}, \omega)$ is the response function which is given by

$$S(\mathbf{Q}, \omega) = \sum_{\alpha\beta} (\delta_{\alpha\beta} - \hat{Q}_\alpha \hat{Q}_\beta) S^{\alpha\beta}(\mathbf{Q}, \omega), \quad (2.25)$$

and the $S^{\alpha\beta}$ are the space and time Fourier transforms of the time dependent spin-spin correlation functions, given by

$$S^{\alpha\beta}(\mathbf{Q}, \omega) = \frac{1}{2\pi\hbar} \int_{-\infty}^{+\infty} \sum_{jj'} e^{i\mathbf{Q}\cdot(\mathbf{r}_j - \mathbf{r}_{j'})} e^{-i\omega t} \langle S_{j'}^\alpha(0) S_j^\beta(t) \rangle dt, \quad (2.26)$$

where $S_j^\beta(t)$ is the β -component of the spin at site j at time t , and $\langle \dots \rangle$ denotes an average over the initial states of the system. This expression can be considerably simplified if we consider a system where the excitations are out of the ground state only⁵. The ground state has wavefunction $|0\rangle$ and energy E_0 , and the spin-spin correlation function is given by

$$S^{\alpha\alpha}(\mathbf{Q}, \omega) = \sum_{\lambda} |\langle \lambda | S^\alpha(\mathbf{Q}) | 0 \rangle|^2 \delta(\hbar\omega - E_0 - E_\lambda), \quad (2.27)$$

where the sum is over all eigenstates $|\lambda\rangle$ of the final state of the system with energy E_λ . $S^\alpha(\mathbf{Q})$ is the Fourier transform of the α -component of the spin S_j^α .

Principle of Detailed Balance

The principle of detailed balance relates the response function for neutron energy loss and neutron energy gain processes with equal and opposite wavevector. It accounts for the fact that at any given temperature there will be a fraction $e^{-\hbar\omega/k_B T}$ fewer excitations already extant for neutrons to scatter from, compared to the number of excitations that can be created by the neutron. Mathematically this is given by

$$S(\mathbf{Q}, \omega) = e^{\hbar\omega/k_B T} S(-\mathbf{Q}, -\omega). \quad (2.28)$$

Fluctuation Dissipation Theorem

The fluctuation dissipation theorem relates the imaginary part of the dynamic susceptibility $\chi''(\mathbf{Q}, \omega)$ to the response function $S(\mathbf{Q}, \omega)$. Mathematically this relationship is given by

$$S(\mathbf{Q}, \omega) = [1 + n(\omega)] \frac{1}{\pi} \chi''(\mathbf{Q}, \omega), \quad (2.29)$$

where $n(\omega)$ is the Bose population factor

$$n(\omega) = \frac{1}{e^{\hbar\omega/k_B T} - 1}. \quad (2.30)$$

Also note the sum rule that relates the imaginary part of the dynamic susceptibility to the bulk susceptibility:

⁵Strictly speaking this means a system at zero temperature, however for non-zero temperatures the simplification described is still a good approximation provided that the excited state lies at an energy greater than $k_B T$ above the ground state

$$\chi_{\text{Bulk}} = \lim_{Q \rightarrow 0} \int_{-\infty}^{+\infty} \frac{\chi''(Q, \omega)}{\pi\omega} d\omega. \quad (2.31)$$

2.1.4 Polarisation Analysis

Spin-flip (SF) refers to when the spin state of the neutron is flipped from up to down, or vice versa, and non-spin-flip (NSF) refers to when the spin state of the neutron remains unchanged during scattering⁶. In general the scattering cross section is given by

$$\frac{d^2\sigma}{d\Omega dE} \propto |\langle k_f S_f | \hat{V} | k_i S_i \rangle|^2, \quad (2.32)$$

where the initial and final neutron states are labelled by their wavevectors k_i and k_f , and their spin states S_i and S_f respectively. \hat{V} is the scattering potential, which contains contributions from both nuclear and magnetic potentials.

The coherent nuclear cross section is proportional to

$$\langle S_f | \hat{V}_{\text{nuc}}^{\text{coh}}(\mathbf{Q}) | S_i \rangle = \hat{V}_{\text{nuc}} \langle S_f | S_i \rangle, \quad (2.33)$$

where $\langle S_f | S_i \rangle = 0$ for spin flip scattering ($S_i \neq S_f$), or $\langle S_f | S_i \rangle = 1$ for non-spin-flip scattering ($S_i = S_f$). Therefore all coherent nuclear scattering is in the non-spin-flip channel.

Recall equation 2.14, which gives the Fourier transform of the magnetic scattering potential. Writing out the dot product explicitly

$$\hat{V}_{\text{M}}(\mathbf{Q}) = \sum_{\alpha} \mu^{\alpha} M_{\perp}^{\alpha}(\mathbf{Q}). \quad (2.34)$$

We define the quantisation direction as z and calculate the matrix elements involving $\hat{V}_{\text{M}}(\mathbf{Q})$ for the various different spin-flip states as follows.

Transition	Matrix element
$ \uparrow\rangle \rightarrow \uparrow\rangle$	$\langle S_f \hat{V}_{\text{M}}(\mathbf{Q}) S_i \rangle = M_{\perp}^z(\mathbf{Q})$
$ \downarrow\rangle \rightarrow \downarrow\rangle$	$\langle S_f \hat{V}_{\text{M}}(\mathbf{Q}) S_i \rangle = M_{\perp}^z(\mathbf{Q})$
$ \uparrow\rangle \rightarrow \downarrow\rangle$	$\langle S_f \hat{V}_{\text{M}}(\mathbf{Q}) S_i \rangle = M_{\perp}^x(\mathbf{Q}) + iM_{\perp}^y(\mathbf{Q}),$
$ \downarrow\rangle \rightarrow \uparrow\rangle$	$\langle S_f \hat{V}_{\text{M}}(\mathbf{Q}) S_i \rangle = M_{\perp}^x(\mathbf{Q}) - iM_{\perp}^y(\mathbf{Q})$

Table 2.2: The matrix elements for different polarisation scattering events

The equations in table 2.2 allow us to determine what component of the magnetic scattering can be observed with a given flipper channel and polarisation direction. These rules can be summarised as follows:

⁶Neutrons are spin- $\frac{1}{2}$ fermions and thus have only two spin states, $|\uparrow\rangle$ and $|\downarrow\rangle$, otherwise known as spin $+\frac{1}{2}$ and spin $-\frac{1}{2}$, or spin-up and spin-down respectively.

1. No component of spin parallel to \mathbf{Q} may be detected.
2. In the SF channel only those components of spin perpendicular to the polarisation \mathbf{P} , subject to (1), may be detected.
3. In the NSF channel only those components of spin parallel to \mathbf{P} may be detected, subject to (1).

This then allows us to calculate the component of a static spin or a fluctuating spin in the three possible orthogonal directions. Let us define N as the coherent nuclear scattering arising from structural Bragg peaks, phonons etc. This scattering does not depend on neutron spin polarisation and does not flip the neutron spins, so it is divided equally between the three orthogonal NSF polarisation channels. Next we define B_{SF} and B_{NSF} as the backgrounds in the SF and NSF channels respectively. The background will be different in the two flipper channels because they contain different contributions from the nuclear spin incoherent scattering. Finally we define \mathcal{M} as the magnetic moment of the sample's constituents squared⁷, μ^2 . Let the superscripts x , y and z be the directions of the polarisation parallel to \mathbf{Q} , perpendicular to \mathbf{Q} but lying in the scattering plane, and perpendicular to the scattering plane respectively. Then we get:

$$\begin{aligned}
I_{\text{SF}}^x &= B_{\text{SF}} + \mathcal{M}_y + \mathcal{M}_z, \\
I_{\text{SF}}^y &= B_{\text{SF}} + \mathcal{M}_z, \\
I_{\text{SF}}^z &= B_{\text{SF}} + \mathcal{M}_y, \\
I_{\text{NSF}}^x &= B_{\text{NSF}} + \frac{N}{3}, \\
I_{\text{NSF}}^y &= B_{\text{NSF}} + \frac{N}{3} + \mathcal{M}_y, \\
I_{\text{NSF}}^z &= B_{\text{NSF}} + \frac{N}{3} + \mathcal{M}_z.
\end{aligned} \tag{2.35}$$

By subtracting the measured scattering in the different polarisation channels from one another it is possible to be left with the scattering that is solely magnetic in origin. This is the great strength of polarised neutron scattering.

Production of a Polarised Neutron Beam

For all of the experiments described in this thesis where polarised neutrons were used, a Heusler monochromator was used, so discussion of polarised beam production will be restricted to this method. The total coherent neutron scattering cross section from any crystal is a sum of the nuclear and magnetic parts, i.e.

$$\frac{d\sigma}{d\Omega} = \{AF_{\text{Nuclear}} + BF_{\text{Magnetic}}\}^2, \tag{2.36}$$

⁷ $\mathcal{M} \propto \mu^2$ is only valid for elastic scattering. For inelastic scattering $\mathcal{M} \propto S^{\alpha\alpha}(\mathbf{Q}, \omega)$, where $S^{\alpha\alpha}(\mathbf{Q}, \omega)$ is the spin-spin correlation function.

where A and B are constants which depend on the details of the scatterer, and F_{Nuclear} is the nuclear structure factor and F_{Magnetic} is the magnetic structure factor. Since the nuclear scattering length can be either negative or positive, it is possible for the two terms in equation 2.36 to combine destructively or constructively.

Suppose we have a crystal where the scattering Bragg plane has a magnetic field \mathbf{B} applied parallel to its surface so that the spins line up parallel to \mathbf{B} . Each incident neutron has a polarisation \mathbf{P} either parallel or antiparallel to the spins in the monochromator. This means that for \mathbf{P} antiparallel to the spins in the monochromator

$$\frac{d\sigma}{d\Omega} = \{|AF_{\text{Nuclear}}| + |BF_{\text{Magnetic}}|\}^2, \quad (2.37)$$

whereas for \mathbf{P} parallel to the monochromator spins

$$\frac{d\sigma}{d\Omega} = \{|AF_{\text{Nuclear}}| - |BF_{\text{Magnetic}}|\}^2. \quad (2.38)$$

If a material is chosen such that $|AF_{\text{Nuclear}}|$ is equal to $|BF_{\text{Magnetic}}|$ then in one case neutrons are strongly Bragg reflected and in the other they not reflected at all. Heusler alloy is just such a material, which is why it is used to make polarising monochromators. Analysers for polarised neutron scattering instruments work on exactly the same principles.

One might think, given the above, that polarised neutrons would be used as a matter of course for all experiments involving magnetic materials. There are, however, some disadvantages to the use of a polarised setup. The main disadvantage is the reduction in neutron flux with polarised neutrons compared to unpolarised neutrons. The polarisation process necessarily rejects 50% of the neutrons incident on the monochromator, however the reflectivity of Heusler crystals is about a factor of two worse than for PG or Si crystals. Finally, with Heusler crystals it is more difficult to focus the neutrons on to the sample than it is with PG or Si, and even at the best polarised spectrometers this accounts for a further factor of two loss in intensity.

Flipping Ratios

In a real experiment the polarisation is not perfect, and nor are the spin-flippers. It is possible to correct for these imperfections, however, by measuring the flipping ratios. The flipping ratio f is defined as follows when measuring the scattering that is purely non-magnetic⁸.

$$f = \frac{\text{NSF}_{\text{meas}}}{\text{SF}_{\text{meas}}}. \quad (2.39)$$

The true spin-flip and non-spin-flip scattering is therefore

⁸For a purely magnetic signal the flipping ratio would be the reciprocal of this.

$$\text{NSF}_{\text{true}} = \left(\frac{f}{f-1}\right) \text{NSF}_{\text{meas}} + \left(\frac{1}{f-1}\right) \text{SF}_{\text{meas}}, \quad (2.40)$$

$$\text{SF}_{\text{true}} = \left(\frac{f}{f-1}\right) \text{SF}_{\text{meas}} + \left(\frac{1}{f-1}\right) \text{NSF}_{\text{meas}}. \quad (2.41)$$

This means that in a polarised scattering experiment both flipping channels should be measured for any given polarisation so that this correction can be made.

2.2 X-ray Scattering

2.2.1 The Synchrotron Source

An excellent description of the function of synchrotron light sources, as well as scattering theory for x-rays, may be found in the book by J. Als-Nielsen and D. McMorrow [5]. The following is an outline of the most important pieces of technology and theory for this thesis.

The X-ray experiments were carried out at the European Synchrotron Radiation Facility (ESRF) in Grenoble, France. The basic principle of a synchrotron light source is very simple – a beam of electrons (although they could be any charged particles) is accelerated in a linear accelerator and then again in a circular accelerator to near light speeds ($\sim 6\text{GeV}$) and is then injected into a storage ring (circumference 844m at ESRF) and allowed to travel at constant speed around an approximately circular path. The acceleration of the electrons as they travel on their curved path results in emission Bremsstrahlung x-rays.

Bending Magnets

In reality the circular path is made up of many straight sections, and at the end of each one there is a magnetic field which bends the electrons into the next straight section, the so-called bending magnet. The bending magnet is simply a static magnetic field that deflects the electron path (describing a circular arc) due to the Lorentz force. Upon bending the electrons are accelerated and therefore emit radiation in the form of Bremsstrahlung, and these X-rays are emitted in the forward direction (parallel to the electron beam, with a small divergence of about 0.08mrad) due to the relativistic Döppler effect.

Following the convention of Nielsen and McMorrow [5], let us define the energy of an electron in the synchrotron storage ring as ξ_e . The radius of curvature ρ , for the (useful) units shown in square brackets is given by

$$\rho [\text{m}] = \frac{3.3\xi_e [\text{GeV}]}{B [\text{T}]}, \quad (2.42)$$

where B is the constant magnetic field applied by the bending magnet. The characteristic energy, $\hbar\omega_c$, of the emitted electrons, i.e. the energy at which the flux is greatest, is given by

$$\hbar\omega_c [\text{keV}] = 0.665\xi_e^2 [\text{GeV}] B [\text{T}] \quad (2.43)$$

and the radiated power, P , is given by

$$P [\text{kW}] = 1.266\xi_e^2 [\text{GeV}] B^2 [\text{T}^2] L [\text{m}] I [\text{A}], \quad (2.44)$$

where L is the length of the section over which the electron experiences a magnetic field, and I is the current of electrons in the storage ring.

Insertion Devices

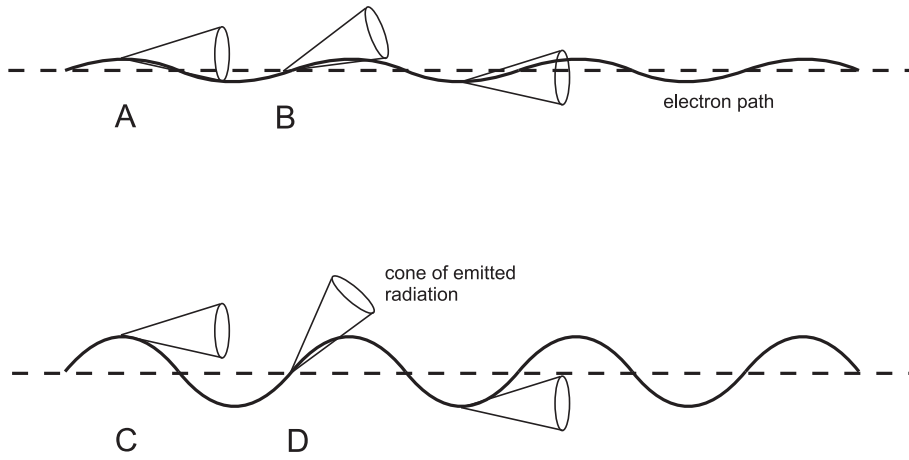


Figure 2.3: A schematic of an undulator (upper figure) and a wiggler (lower figure) insertion device. The cones shown at various points along the electron path show the direction of the emitted radiation.

Synchrotron light may be also emitted by passing the electron beam through ‘wiggles’ or ‘undulators’ in the straight sections. A wiggler is a periodic array of alternating magnetic fields which cause the electron paths to bend (describing a circular arc) in alternate directions (wiggling), so essentially it is a series of alternating bending magnets. The electrons undergo the same process as with a bending magnet, but several times, so that the emerging radiation is the incoherent sum of $2n$ bending magnets, if the wiggler has n magnet periods⁹. The period of the magnetic fields ‘seen’ by the electrons is affected by relativistic Lorentz length contraction, so that for an array of n magnetic periods with overall length L the electrons see an array of magnets of length L/γ , with a period of $L/n\gamma$, where the relativistic Lorentz factor is given by

$$\gamma = \frac{1}{\sqrt{1 - \frac{v_e^2}{c^2}}}, \quad (2.45)$$

⁹there are two wiggles per period.

where v_e is the speed of the electrons in the storage ring. In the laboratory frame this transforms to approximately $L/2n\gamma$ if $v_e \sim c$. The wavelength of the synchrotron light generated is of the same order of magnitude as the relativistic period of the wiggler magnets as seen in the laboratory frame. The angular divergence of the beam is $\sim 1/\gamma$.

An undulator is similar to a wiggler but works in a slightly different way. Figure 2.3 shows schematically the main difference. At points like C on the electron path, radiation is emitted along the electron beam tube and will be incident on the sample, whereas at points like D it will not. For an undulator radiation is emitted along the beam tube on to the sample at both of the corresponding points A and B. The result of this is that the overall intensity of radiation arriving at the sample, rather than striking the walls of the electron beam pipe, is higher for an undulator. In addition the radiation cones from the undulator interfere constructively so that the spectral weight is concentrated around just a few wavelengths (the fundamental and its harmonics), which further increases the available monochromated intensity. All of the experiments presented in this thesis that were performed at insertion device beamlines were performed on undulator beamlines, so detailed discussion of the expected x-ray spectrum from insertion devices is restricted to the case of undulators.

Let us define the magnetic field applied to the electrons, perpendicular to the plane of the undulations, as

$$B_z = B_0 \sin(2\pi s/\lambda_u), \quad (2.46)$$

where s is the spatial co-ordinate in the direction of the unbent electron path, λ_u is the period of the magnetic field, and B_0 is the maximum applied field. Define the dimensionless parameter K as

$$K = \frac{e}{2\pi mc} \lambda_u B_0 = 0.934 \lambda_u [\text{cm}] B_0 [\text{Tesla}], \quad (2.47)$$

where the right-hand term gives the value in the most useful units. The frequency of emitted radiation from an undulator as a function of off-axis angle θ is given by

$$\omega_{\text{und}}(\theta) = \frac{4\pi c \gamma^2 M}{\lambda_u} \left(\frac{1}{1 + K^2/2 + \gamma^2 \theta^2} \right), \quad (2.48)$$

where M represents the number of the harmonic, and λ_u is the wavelength of the electron undulation. Note that on-axis, where $\theta = 0$, only odd harmonics are produced.

For all of the x-ray experiments described in this thesis linearly polarised incident x-rays were used. X-rays from bending magnets, undulators, and wigglers are linearly polarised in the horizontal plane if the x-rays are incident on a point that is in the plane of orbit of the electrons. The proof for this is rather complex so I simply state the result here – further details may be found in reference [6].

2.2.2 X-ray Scattering Instruments

From both an insertion device and a bending magnet x-ray source one should also place a monochromator between the magnet and the sample. The need for this is obvious for a bending magnet, however even a well controlled undulator does not produce a single wavelength but rather a range. For all of the experiments detailed in this thesis where synchrotron x-rays were used a monochromatic beam was required. On both the ID20 and XMaS beamlines at ESRF that were used for experiments presented in this thesis Si (111) Bragg reflections are used for monochromation. Downstream of the monochromator the beam is guided using mirrors. The x-rays are then incident on the sample, which for the diffraction experiments presented here were placed on either four-circle or six-circle diffractometers.

The Four-Circle and Six-Circle Diffractometers

The two standard diffractometers used in the work detailed in this thesis are the four-circle and six-circle diffractometers. These diffractometers have been extensively detailed by Busing and Levy [7], and by Lohmeier and Vlieg [8] respectively. Their diagrams showing all of the angles are reproduced below.

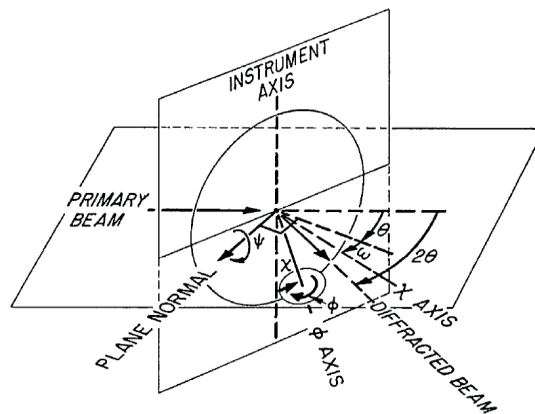


Figure 2.4: After Busing and Levy. All of the angles shown here for the four-circle diffractometer are in their first quadrant.

Looking at figure 2.4 we see that for the four-circle diffractometer θ and 2θ are coupled, whereas ω is coaxial to these but is an independent rotation. ψ is the angle of rotation about the normal to the reflecting surface of the sample. Changes in this angle are achieved through a combination of ω , ϕ and χ rotations. χ is a rotation about the circle which is in a plane perpendicular to the scattering plane. The ϕ circle is perpendicular to this, with the ϕ shaft attached to the χ circle.

Looking at figure 2.5 we see that there are additional degrees of freedom compared to the four-circle diffractometer. The δ , ω and ϕ circles are coaxial in the zero angle setting. δ is a rotation of the detector arm, ω is a rotation of the sample mount, including χ circle, while the ϕ circle is a rotation of just the sample about the axis normal to its reflecting plane. The γ circle is for out-of-plane rotations of the detector. The α circle is a rotation of the whole diffractometer about the x-axis (vertical). Finally the χ circle is a rotation about an axis perpendicular to the ω circle.

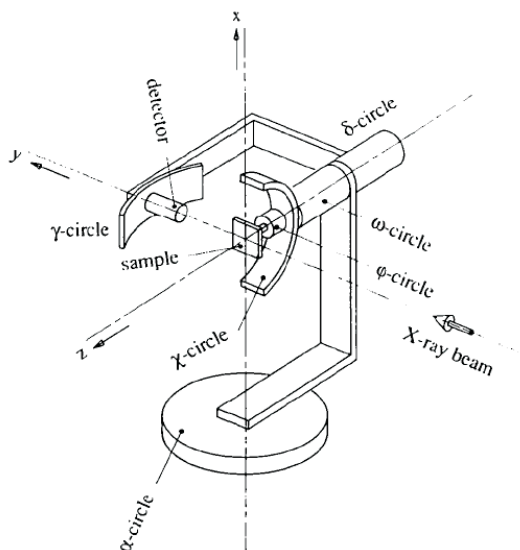


Figure 2.5: After Lohmeier and Vlieg. All of the angles shown here for the six-circle diffractometer are set in the zero position (for clarity). The diffractometer shown has a horizontal scattering plane.

X-ray Polarisation Analysis

It is often the case that one wishes to analyse the polarisation state of the scattered x-ray beam. For the case of linearly polarised x-rays this can be done using a polarisation analyser (PA) crystal. To understand how this works let us first consider a single electron with an oscillating electric field applied to it, shown schematically in figure 2.6.

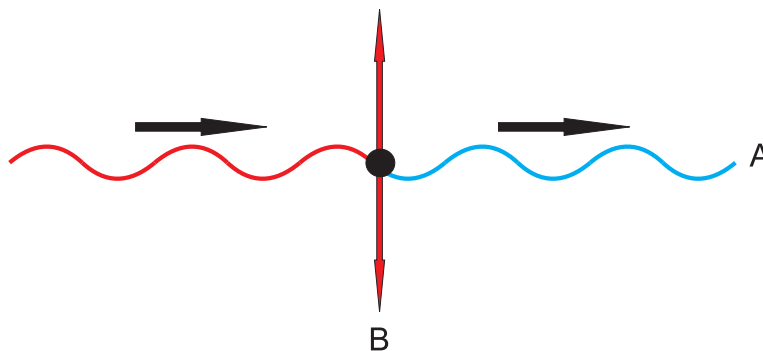


Figure 2.6: A schematic of the principle of an x-ray polarisation analyser

The electron, shown by the black circle, oscillates in phase with the oscillating applied electric field of the incident photon, denoted by the red wavy line. The electron emits photons over a range of angles. In figure 2.6 the electron is oscillating vertically so no photons are emitted in this direction, and the maximum number of photons are emitted in the horizontal plane. Consider now a collection of electrons in, for example, a crystal. They will clearly behave in the same way, such that no photons are scattered vertically and in the horizontal plane lots of photons will be scattered. If the electrons are in a crystal such that the Bragg angle of one of the planes is 45° then for one orientation, where the scattered beam is at 90° to the incident beam but is still in the horizontal plane, lots of photons will be scattered,

whereas for another orientation, where the outgoing beam is vertical, hardly any photons are scattered.

Figure 2.7 shows schematically how this effect would be utilised to analyse the polarisation state of x-rays. The polarisation analysis (PA) crystal is chosen such that the scattered beam from a particular Bragg plane is perpendicular to the incident beam. In the two orientations shown for the PA and detector either photons polarised in the horizontal plane (σ), or photons polarised in the vertical plane (π) will be detected.

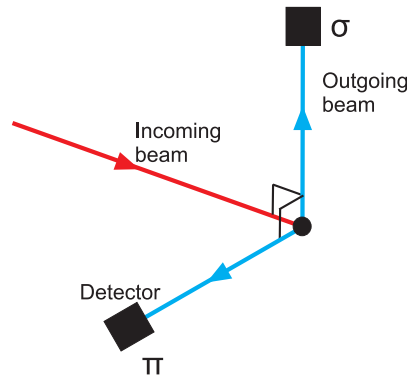


Figure 2.7: A schematic of the layout of a real x-ray polarisation analyser.

X-ray Detectors

Let us now consider how to detect x-rays from a synchrotron source. For the kind of single crystal diffraction measurements that will be described in this thesis the detector consisted of a single pixel that can be scanned in order to characterise the intensity and lineshape of a particular scattering peak. This is as opposed to a position sensitive detector that is held stationary and many peaks are measured, but with a lower sensitivity to the exact intensity and lineshape – the crudest example of which would be photographic film in a Laue camera.

The older sort of detector used, for the experiments on ID20 and for fluorescence measurements on XMaS, is a Bicon NaI scintillator. In such a detector a NaI crystal scintillates (i.e. fluoresces photons of a lower energy than the x-rays that are incident on it) when it is exposed to x-rays. The fluorescence from the NaI strikes a cathode which emits electrons due to the photoelectric effect. These electrons are then multiplied in a vacuum chamber by a succession of increasing electric fields so that a cascade is created. At the final electrode there is a sharp electronic signal, which is recorded by the counting electronics.

The newer kind of detector, which was used for scattering measurements on XMaS, is a silicon drift diode detector. X-ray photons incident on the Si crystal generate electron-hole pairs, which can be separated if a sufficiently large electric field is applied to the Si crystal. The electrons and holes are then collected at the electrodes. By measuring the amount of charge that arrives at the electrode at a given time (near simultaneous arrival of charge is assumed to be due to the same photon) the energy of the photon that caused the electrons and holes to be separated can be calculated. This means that an electronic bandpass can be set so that the measuring computer only registers x-rays that are in the expected energy range of the experiment, thus reducing noise.

2.2.3 X-ray Scattering Theory

For all x-ray scattering processes, the scattering cross-section is related to the form factor, f as follows:

$$\frac{d\sigma}{d\Omega} \propto |f|^2. \quad (2.49)$$

The form factor is made up of non-resonant and resonant contributions, which arise from the scattering of electrons by the electron clouds of atoms (charge scattering, non-resonant), the scattering of electrons by both spin and orbital magnetic moments (non-resonant and resonant) and more besides. I will detail here the simplest, and most relevant, contributions.

Non-resonant Scattering

Non-resonant scattering occurs when the incident x-ray energy is far from any absorption edges of species in the sample. In such cases the x-rays are scattered by the electrons of the atoms in the material. The intensity of scattering, I , from a single electron is given by

$$\begin{aligned} I &= I_0 \left(\frac{\mu_0}{4\pi} \right)^2 \left(\frac{e^4}{m^2 r^2} \right) \left(\frac{1 + \cos^2(2\theta)}{2} \right) \\ &= I_0 \frac{r_0^2}{r^2} \left(\frac{1 + \cos^2(2\theta)}{2} \right) \end{aligned} \quad (2.50)$$

where m is the mass of an electron, 2θ is the angle between the incident and scattered beam, I_0 is the intensity of the incident beam, and r_0 is termed the Thomson scattering length, and is equal to $0.282 \times 10^{-4} \text{ \AA}$.

When considering the scattering from a large number of electrons, e.g. in an atom, we must consider the electron density $\rho(\mathbf{r})$. The atomic form factor, which is an amplitude envelope function for the scattering, has the form

$$f_0(\mathbf{Q}) = \int \rho(\mathbf{r}) e^{i\mathbf{Q}\cdot\mathbf{r}} d^3\mathbf{r}. \quad (2.51)$$

where \mathbf{r} is the radial co-ordinate from the atomic nucleus. If we assume a spherical charge density, then

$$f_0(Q) = \int_0^\infty 4\pi r^2 \rho(r) \frac{\sin(Qr)}{Qr} dr, \quad (2.52)$$

where Q is the magnitude of the scattering wavevector \mathbf{Q} . If we assume that $\rho(r)$ decays exponentially and isotropically with characteristic distance $a/2$ then the form factor is

$$f_0(Q) \sim \frac{1}{[1 + (Qa/2)^2]}. \quad (2.53)$$

X-ray Resonant Scattering

The technique of x-ray resonant scattering (XRS) relies, for the purposes of magnetic scattering, on an enhancement of the magnetic scattering cross-section when the incident energy is tuned through an absorption edge of the magnetic ion. The effect was first observed in the form of a large increase in signal upon tuning through the L_3 absorption edge in holmium [9]. When combined with polarisation analysis and azimuthal scans of the sample it allows the direction of the ordered moment of a specific ion in a material to be determined. This is useful when, for example, there is more than one species of magnetic ion present in a sample. In a neutron scattering measurement the neutron is sensitive only to the average moment of the system, that is to say that if there is more than one magnetic ion present the neutron cannot distinguish between their magnetic order. It is the fact that XRS is species specific that is its main strength.

The resonant enhancement process is in principle quite simple. When an incident photon's energy is tuned to the binding energy of one of the electron shells of one of the constituents of the sample one can visualise that it will excite that electron into a vacancy in a higher energy shell. The electron will then relax back down into the hole created in that shell, emitting a photon with the same energy as the incident x-ray. This process allows information about the magnetic order, charge order, orbital order etc. of the outer shell electrons to be passed to the emitted photon. This picture must be taken with a pinch of salt, however, because in reality the resonant process is a virtual process and does not occur in the two discrete steps described. Nor is it possible to remove the excited virtual electron from the material, that is to say that the transition occurs in a closed loop.

The dominant resonant processes are generally from dipole-dipole (E1E1) transitions, although there do also exist quadrupole-quadrupole (E2E2) transitions and other more complex transitions. An example of an E1E1 process would be the $2p_{3/2} \rightarrow 5d_{1/2}$ transition in Holmium at the L_3 edge.

The resonant magnetic scattering cross-sections for E1E1 (and E2E2) transitions are derived in the paper of Hill and McMorow [10], and I simply state the results here. The E1E1 resonant contribution from a magnetic ion to the total coherent elastic scattering amplitude is given by

$$\begin{aligned} f_{nE1}^{XRS} &= \begin{pmatrix} \sigma \rightarrow \sigma' & \sigma \rightarrow \pi' \\ \pi \rightarrow \sigma' & \pi \rightarrow \pi' \end{pmatrix} \\ &= F_{E1}^{(1)} \begin{pmatrix} 0 & z_1 \cos\theta + z_3 \sin\theta \\ z_3 \sin\theta - z_1 \cos\theta & -z_2 \sin 2\theta \end{pmatrix} \end{aligned} \quad (2.54)$$

where the magnetic moment \mathbf{z} is resolved into three components, parallel to the principal axes which define the scattering geometry. The constant $F_{E1}^{(1)}$ is related to the atomic properties of the ions from which resonant scattering occurs. σ and π denote the linear polarisation

state of the incident beam, whereas σ' and π' relate to the scattered beam. The scattering geometry is shown schematically in figure 2.8 for a vertical scattering plane.

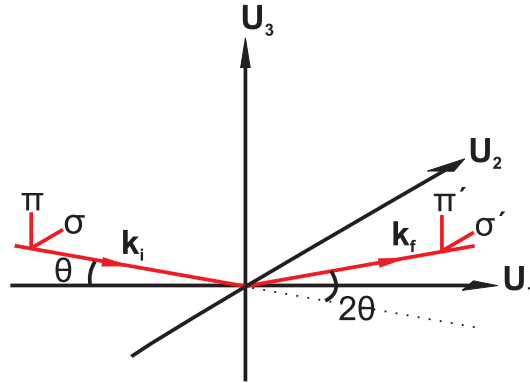


Figure 2.8: The coordinate system used for defining the scattering plane and the components of magnetic moments in the resonant scattering cross sections. π and σ are the components of the polarization parallel and perpendicular to the scattering plane respectively.

2.3 Bulk Measurement Techniques

2.3.1 Magnetisation Measurements Using a SQUID

The magnetisation measurements presented in this thesis were all taken using a Quantum Design MPMS XL magnetometer. This magnetometer works using a superconducting quantum interference device (SQUID) coil [11]. The sample environment is a Helium flow cryostat, which can be cooled to a base temperature of 1.6 K. A magnetic field is applied in the vertical direction by a superconducting magnet, which has a practical range of about ± 5 T. All of the measurements are computer controlled using software which was designed specifically for this magnetometer by Quantum Design Inc.

For a measurement of the magnetic susceptibility the sample is typically mounted inside a plastic straw of diameter ~ 5 mm, the diamagnetic moment of which is very small. It can be secured inside this straw in a variety of ways. The two that were most often used for the work presented here were, 1) to place the sample inside a plastic capsule, packed tight with cotton wool and sealed with kapton tape, itself inserted into the plastic straw; 2) to wedge the sample between two folded over straws inserted into the plastic straw. The method chosen depended on the particular geometry of the sample and the crystallographic direction in which the field needed to be applied.

The principle of operation of the apparatus is shown schematically in figure 2.9. The plastic straw containing the sample is translated vertically between three superconducting coils, in which a current proportional to the sample magnetisation is induced. These coils lead to two coupled inductors, which then leads to another pair of inductors, between which a SQUID is placed. Thus small changes in the sample magnetisation are measured as small current changes, which are converted into small changes in magnetic field near the SQUID.

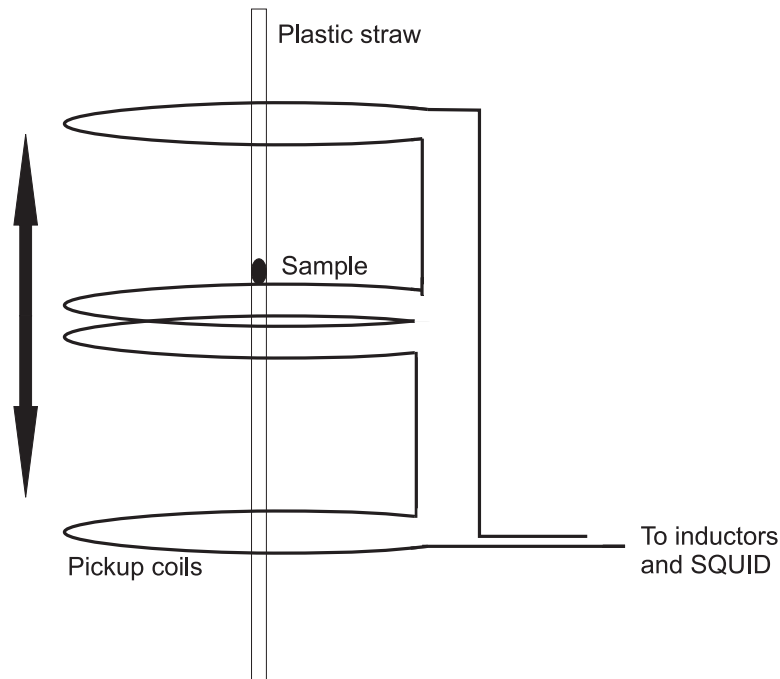


Figure 2.9: The pickup coils of the SQUID magnetometer.

2.3.2 Heat Capacity Measurements Using a PPMS

The heat capacity measurements presented in this thesis were all performed using a Quantum Design Physical Properties Measurement System (PPMS) [12]. The PPMS can measure a variety of physical properties (resistivity, AC susceptibility, etc), however the heat capacity option is the only one that was utilised for the work presented in this thesis.

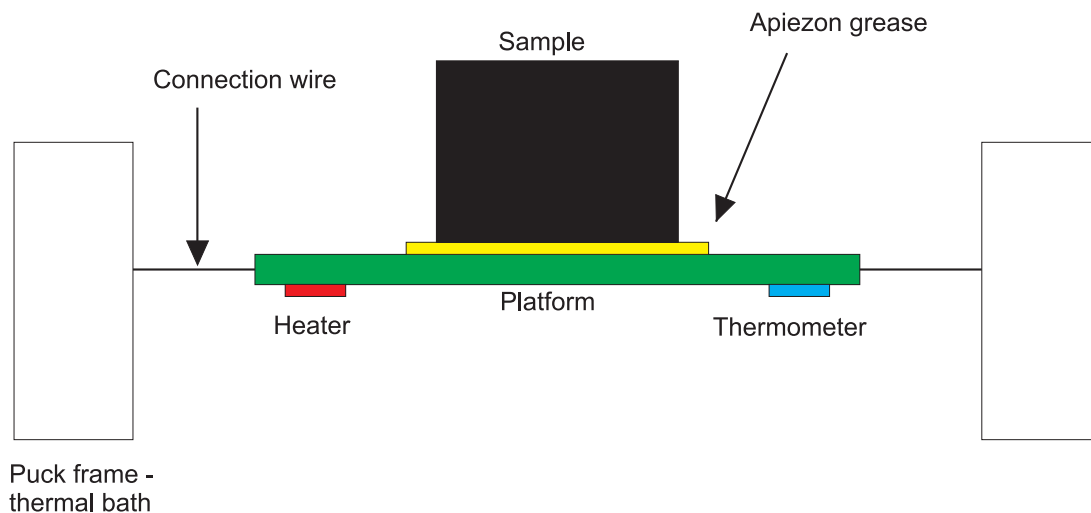


Figure 2.10: Side view of the sample mount for heat capacity measurements using the PPMS

A schematic of the sample mount, known as the puck, is shown in figure 2.10. The platform is connected to the support frame of the puck, which acts as a heat sink, by thin wires, which also serve as electrical contacts for the heater and resistance thermometer. A good thermal contact between the bottom surface of the sample and the platform is ensured

by using Apiezon grease. The whole apparatus is controlled by computer, using bespoke software.

In order to make a measurement the heater supplies a fixed amount of power $P(t)$ for a length of time t , and is then turned off. The temperature of the sample/platform/grease assembly rises as the heat is applied, whereas the thermal bath remains at constant temperature, and then cools through radiation and conduction through the wires when the heater is turned off. The software monitors the temperature throughout this, and the heat transfer is modelled by the differential equation

$$C_{\text{total}} \frac{dT}{dt} = -K_w \{T(t) - T_b\} + P(t), \quad (2.55)$$

where C_{total} is the heat capacity of the sample and platform together, K_w is the thermal conductivity of the wires, and T_b is the fixed temperature of the thermal bath. By solving this differential equation the heat capacity is calculated from the exponential decay constant of the sample temperature. In order to find the heat capacity of the sample the heat capacity of the puck and platform must be subtracted, so the behaviour of this quantity as a function of temperature is calibrated before the experiment takes place.

If the thermal contact between the platform and sample is not very good a more complicated model is used which accounts for the behaviour of the two separately.

$$C_{\text{platform}} \frac{dT_p}{dt} = P(t) - K_w \{T_p(t) - T_b\} + K_g \{T_s(t) - T_p(t)\} \quad (2.56)$$

$$C_{\text{sample}} \frac{dT_s}{dt} = -K_g \{T_s(t) - T_p(t)\}, \quad (2.57)$$

where K_g is the thermal conductivity of the grease, and the temperature of the sample and platform is given by T_s and T_p respectively.

References

- [1] G. L. Squires, *Introduction to the Theory of Thermal Neutron Scattering*, Dover Publications Inc, Mineola, New York, (1996).
- [2] A. J. Freeman, *Acta Cryst.* **12**, 261 (1959).
- [3] http://www.ill.eu/fileadmin/users_files/static/ccsl/html/ccsldoc.html
- [4] S. Shamoto, M. Sato, J. M. Tranquada, B. J. Sternlieb, and G. Shirane, *Phys. Rev. B* **48**, 13817 (1993).
- [5] J. Als-Nielsen and D. F. McMorrow, *Elements of Modern X-Ray Physics*, John Wiley and Sons Ltd, Chichester, West Sussex, (2001).
- [6] J. Baruchel, J. L. Hodeau, M. S. Lehmann, J. R. Regnard, and C. Schlenker, *Neutron and Synchrotron Radiation for Condensed Matter Studies*, Vol. 1, p. 55, Springer Verlag, (1993).
- [7] W. R. Busing and H. A. Levy, *Acta Cryst.* **22**, 457 (1967).
- [8] M. Lohmeier and E. Vlieg, *J. Appl. Cryst.* **26**, 706 (1993).
- [9] D. Gibbs, D. R. Harshmann, E. D. Isaacs, D. B. McWhan, D. Mills and C. Vettier, *Phys. Rev. Lett.* **61**, 1241 (1988).
- [10] J. P. Hill and D. F. McMorrow, *Acta Cryst. A* **52**, 236 (1996).
- [11] A. Barone, *Principles and Applications of Superconducting Quantum Interference Devices*, World Scientific, (1992).
- [12] Quantum Design Inc. *PPMS Manual*, 11th edition (2004).

Chapter 3

Growth and Preparation of the Samples

In this chapter I give a brief outline of how the various samples that were measured as part of this thesis were grown.

The samples used for the measurements detailed in this thesis were grown in several locations and at several different times. To summarise, the $\text{La}_{1.48}\text{Nd}_{0.4}\text{Sr}_{0.12}\text{CuO}_4$ samples were grown at the University of Hokkaido, Japan, in the group of Dr. Naoki Momonol; the $\text{La}_{1.88}\text{Ba}_{0.12}\text{CuO}_4$ samples were grown by Dr. Genda Gu at Brookhaven National Laboratory, USA; the LaCoO_3 and $\text{La}_{0.82}\text{Sr}_{0.18}\text{CoO}_3$ samples were grown by Dr. Prabhakaran Dharmalingam at Oxford; and the DyMn_2O_5 samples were grown by Dr. Barbara Wanklyn at Oxford (in 1970!).

The $\text{La}_{1.48}\text{Nd}_{0.4}\text{Sr}_{0.12}\text{CuO}_4$, $\text{La}_{1.88}\text{Ba}_{0.12}\text{CuO}_4$ [I THINK], LaCoO_3 and $\text{La}_{0.82}\text{Sr}_{0.18}\text{CoO}_3$ samples were all grown using the floating zone technique [REFERENCE VARIOUS CRYSTAL GROWTH PAPERS HERE TO SHOW THIS]. In this method a powdered version of the sample is made first, and this powder is then compressed to make two rod-shaped pellets. The tips of the two rods are brought into contact with each other in an image furnace such that at the contact point the pellets melt. The pair of rods are translated relative to the ‘hot spot’ so that soon after melting the material cools in a single crystalline phase. By slow and careful movement of the ‘hot spot’ along the rods a single crystal rod may be grown which may be several centimetres long.

The DyMn_2O_5 samples were grown using the flux method [REFERENCE THE 1972 PAPER]. NEED TO DESCRIBE HERE HOW THIS METHOD WORKS.

Chapter 4

Charge and Spin Order in $\text{La}_{1.48}\text{Nd}_{0.4}\text{Sr}_{0.12}\text{CuO}_4$

Polarised neutron scattering measurements, both elastic and inelastic, of the charge ordered cuprate $\text{La}_{1.48}\text{Nd}_{0.4}\text{Sr}_{0.12}\text{CuO}_4$ are presented, along with x-ray diffraction measurements. The neutron diffraction measurements rule out a number of proposed ordering schemes for the Cu^{2+} spins, and it is shown that only three models can account for the data. Of these, one is the so-called ‘stripe’ model, whereas the other two are more complicated patterns associated with charge checkerboards. The preliminary polarised inelastic scattering measurements can be more readily reconciled with the stripe model. Unpolarised neutron inelastic scattering measurements show that there is a gap in the low energy magnetic excitations, and that this gap is in part due to anisotropy. X-ray scattering was used to probe structural distortions associated with charge ordering, and the temperature and magnetic field dependence of these distortions was measured. It was found that these distortions, and by inference the charge order which causes them, are unaffected by the presence of a vortex lattice.

4.1 Introduction

4.1.1 Introduction to $\text{La}_{2-x}\text{Ba}_x\text{CuO}_4$

$\text{La}_{2-x}\text{Ba}_x\text{CuO}_4$ (hereafter referred to as LBCO) was the first high- T_c cuprate superconductor to be discovered [1], and very little time elapsed after this initial discovery before the main features of the phase diagram as a function of doping were known. These follow the generic features described in section 1.2.2. Of particular interest is the very strong suppression of superconductivity near to $x = 1/8$. This suppression of T_c has been seen in all cuprates, however in certain materials, of which LBCO is one example, T_c decreases almost to zero. This contrasts with, for example, $\text{La}_{2-x}\text{Sr}_x\text{CuO}_4$, where the suppression of T_c is only a few percent [2, 3].

The crystal structure of LBCO is different to most cuprates, because on cooling to low temperatures ($T \leq 50\text{K}$) it changes from orthorhombic to tetragonal [4], whereas most other cuprates tend to remain in an orthorhombic structural phase. Measurements of the resistivity [5] parallel to the CuO_2 planes show that in the normal state there is a sharp increase in resistivity on cooling to about 50 K and then a further more gradual increase in

resistivity with decreasing temperature, indicating that the mobile charge carriers become localised below 50 K. Such measurements do not, however, provide any information about the spatial distribution of these localised carriers (holes).

It would be natural to investigate whether the difference in the low temperature structure of LBCO compared to other cuprates is relevant to the strong suppression of superconductivity and the concomitant localisation of the charge carriers. The most obvious way to do this would be to perform x-ray diffraction and neutron scattering measurements in order to probe the order parameters in the tetragonal state. Unfortunately the necessary large single crystals of LBCO have proved somewhat difficult to grow, and it has only been in recent years that such measurements have been possible.

Faced with this difficulty other materials were sought which displayed similar characteristics, and it was noticed quite quickly that substitution of a certain amount of Nd for La in $\text{La}_{2-x}\text{Sr}_x\text{CuO}_4$ stabilised a tetragonal phase at low temperatures [6]. It was found that the material $\text{La}_{2-x-y}\text{Nd}_y\text{Sr}_x\text{CuO}_4$ (LNSCO) with $y = 0.4$ and $x = 1/8$ had many similarities with $x = 1/8$ LBCO, with the advantage that the crystals were easier to grow.

4.1.2 Introduction to $\text{La}_{2-x-y}\text{Nd}_y\text{Sr}_x\text{CuO}_4$

$\text{La}_{2-x-y}\text{Nd}_y\text{Sr}_x\text{CuO}_4$, with $y = 0.4$ and $x = 0.12$, (LNSCO)¹, is a superconductor with a relatively low critical temperature compared to other hole-doped layered cuprates. Below about 5 K it becomes a superconductor, evidenced in the magnetic susceptibility by the appearance of a Meissner state [7]. Neutron scattering measurements [8] led to a belief that LNSCO becomes charge ordered below about 70 K. Resistivity measurements showed, as with LBCO, that the mobile charge carriers become localised at lower temperatures [9, 10].

LNSCO is structurally different to its much-studied parent superconductor $\text{La}_{2-x}\text{Sr}_x\text{CuO}_4$ (LSCO) – the crystal structure of the latter is orthorhombic whereas the former, exhibits two structural phase transitions, similar to LBCO. On cooling to $T \approx 70\text{K}$ LNSCO undergoes a transition from a low-temperature orthorhombic (LTO) to a low-temperature tetragonal (LTT) structural phase [11], the latter of which is shown in figure 4.1. In the LTO phase the b -axis is $\sim 0.05\text{\AA}$ longer than the a -axis. Concomitant with transition into the LTT phase is the appearance of satellite peaks in the neutron diffraction at $(H, 0, L) \pm (\delta, 0, 0)$ and $(H, 0, L) \pm (0, \delta, 0)$, where $\delta = 2x = 0.25$, H is an integer, and L is any real number [8, 12, 13]. These peaks have been interpreted as arising from the formation of a charge ordered state [8, 12], the nature of which will be discussed later. This contrasts with the behaviour of LSCO, where these satellite peaks are not observed in the elastic scattering channel but are seen in inelastic channels, although the signals are rather weak [14, 15, 16, 17, 18]. It has also been noted that in the LTT phase the CuO_6 octahedra in the $z=0$ layer are rotated along the \mathbf{a} -direction, and the octahedra at the $z=0.5$ layer are rotated along the \mathbf{b} -direction.

Neutrons cannot measure the ordered charge directly, since neutrons do not scatter from localised charge, however the small ionic displacements brought about by electrostatic interactions between the localised charge and the ions in the crystal can be probed. It is these displacements, which have the same periodicity as the charge order, which are observed as

¹these doping fractions will be assumed in all of the following discussion. Note that x is not quite equal to $1/8$.

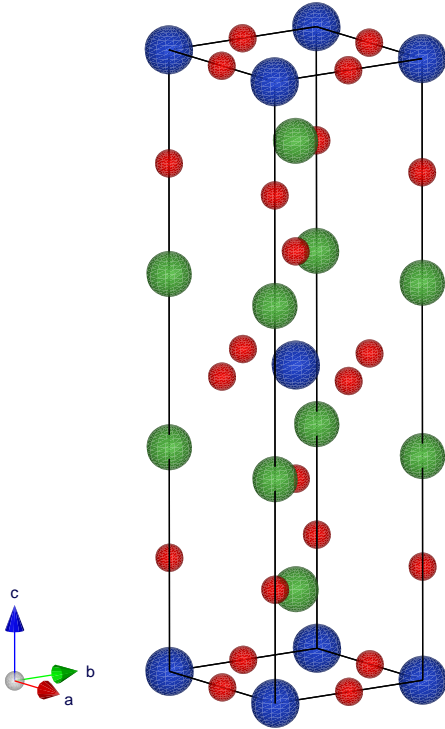


Figure 4.1: The crystal structure of LNSCO [19]. Blue spheres represent Cu^{2+} ions, red spheres O^{2-} ions, and green spheres La^{3+} , Nd^{3+} and Sr^{4+} ions. The space group is $P4_2/nm$.

satellites around the structural Bragg peaks. It appears that the structural transition from orthorhombic to tetragonal is important for the formation of a charge-ordered state because the appearance of the charge order peaks occurs at the same temperature as the onset of the LTT structural phase, i.e. $T_{\text{CO}} = T_{\text{LTO-LTT}} \approx 70$ K. Similar measurements of the structural distortion have been made using high energy x-rays [20], where it was found that half-integer values of L give rise to the strongest peak intensity, which was attributed to a 90° rotation of the charge stripes between adjacent CuO_2 planes along the c -axis.

Magnetic Bragg peaks at $(\frac{1}{2}, \frac{1}{2} \pm \varepsilon, 0)$ and $(\frac{1}{2} \pm \varepsilon, \frac{1}{2}, 0)$, with $\varepsilon = x = 0.12$, appear below a Néel temperature of $T_{\text{N}} \approx 50$ K [13]². The origin of these peaks is a subject of some debate, with various different models of the ordered moments proposed to explain their existence. The details of these models will be discussed later.

At very low temperatures, $T_{\text{Nd}} \leq 3$ K, the Nd ions become statically ordered [12]. The Nd ordering has the same wavevector as the magnetic satellite peaks corresponding to Cu ordering at higher temperatures. An important difference is that the Nd moments point along the c -axis, whereas the Cu spins are thought to lie in the ab -plane. The ordering of the Nd moments is due to a combination of interactions between Nd ions due to exchange between them, and an interaction between the Nd and the already fully ordered Cu moments. The Nd – Cu interaction is rather weak so that at higher temperatures it is very hard to observe, since the moments fluctuate quite a lot. The Nd – Nd interaction is also very weak, and is restricted to low temperatures (i.e. below about 3 K). However the Nd moments are

²Muon spin relaxation measurements indicate that $T_{\text{N}} \approx 30$ K [21]. This may be because muons measure on a longer time scale, and the neutrons have finite energy resolution and might pick up fluctuations of the magnetic moments.

quite large so the scattering arising from these ordered moments is relatively strong.

In order to explain the existence of the two sets of satellite peaks, arising from spin and charge order, in LNSCO and other similar materials, several different models have been proposed. The ‘stripe’ model, which was described briefly in section 1.2.3, and is shown schematically in figures 4.2 and 4.3 describes a situation where the nearest-neighbour Cu^{2+} spins in the ab -plane are antiferromagnetically coupled, with stripes of localised charge coming every four lattice spacings. Across the charge stripe the interaction between Cu^{2+} spins is also antiferromagnetic, i.e. the localised charge acts as an antiphase domain boundary between two *different* blocks of antiferromagnetic spins. The periodicity of the domains of spins is therefore twice that of the localised charge, that is to say eight lattice spacings, so it is this periodicity which gives rise to the satellite peaks around the $(\frac{1}{2}, \frac{1}{2}, 0)$ type magnetic peaks. Because of the tetragonal symmetry there is an equal population of orthogonal domains, with stripes running either parallel to the a -axis or parallel to the b -axis, giving rise to the four charge satellite peaks observed. The maximum intensity of the charge peaks with half-integer L [20] can be explained by considering a stripe model in which the stripes in adjacent planes (i.e. the CuO_2 planes at $z=0$ and $z=0.5$ in the unit cell) are perpendicular, because in the LTT phase the CuO_6 octahedra in the $z=0$ layer are rotated along the \mathbf{a} -direction, and the octahedra at the $z=0.5$ layer are rotated along the \mathbf{b} -direction. This would stabilise stripes parallel to the \mathbf{b} -direction and \mathbf{a} -direction in the $z=0$ and $z=0.5$ layers respectively. Coulomb interactions then cause the stripes at the $z=1$ layer to be shifted two unit cells to one side, which gives an overall periodicity of two unit cells, and hence the value of $L = 0.5$

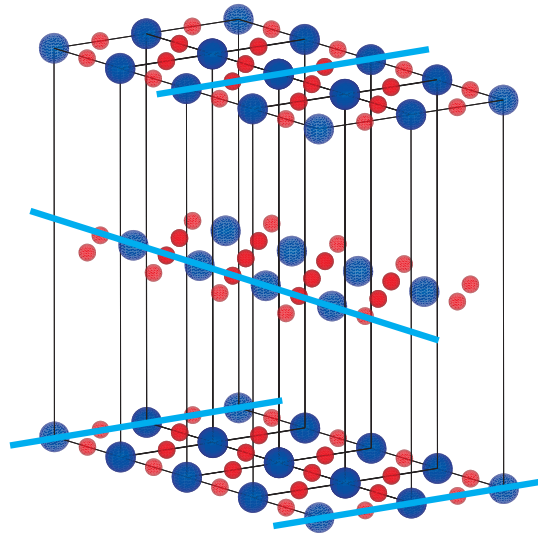


Figure 4.2: A schematic of the charge order in a tetragonal unit cell proposed by the stripe model

There have also been several other models proposed to explain the charge and spin order which fall under the loose heading of ‘checkerboard’ ordering [22, 23, 24]. In all of

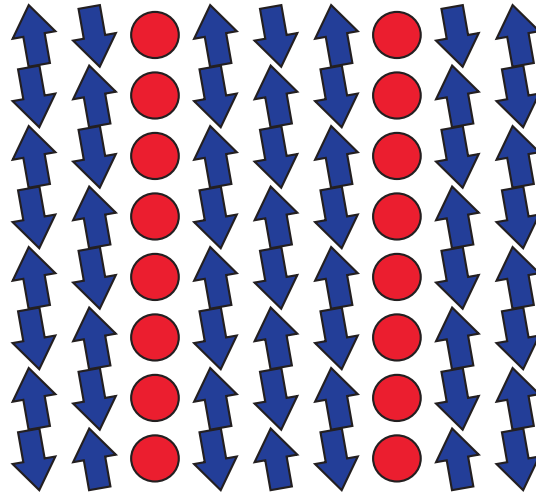


Figure 4.3: A schematic of a single CuO_2 plane showing the spin ordering proposed in the stripe model.

these models there exists only one domain type of ordered charge, i.e. a single CuO_2 plane contains all of the information needed to realise all four of the charge satellite peaks seen in neutron and x-ray measurements. The simplest of such models, shown schematically in figure 4.4, is simply a superposition of the charge of the two possible stripe domains. In more complicated models the charge does not form into one-dimensional ‘rivers’, but rather is localised in a periodic lattice within the CuO_2 plane.

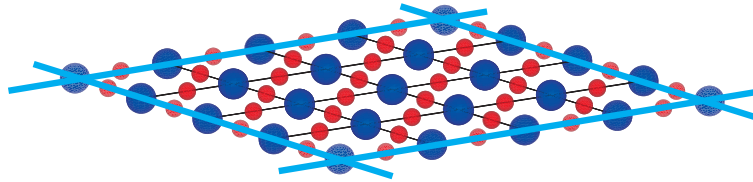


Figure 4.4: A schematic of a checkerboard model.

Some models do not explicitly discuss the nature of the charge order, but rather focus on the nature of the ordered spins and propose various different kinds of spiral ordering patterns [25, 26]³. Lindgård [25] considers a spiral structure where there are two possible domains, where in each one there is a spiral with wavevector parallel to one of the principal axes, and spins are modulated antiferromagnetically perpendicular to this wavevector. Silva-Neto [26] proposes an ordering based on so-called ‘ π -spirals’, which is similar to the model of Lindgård but in adjacent lines of spins the sense of rotation is opposite. Figure 4.5 shows a schematic of both of these models.

³Such models, like the stripe model, require two orthogonal domains to explain the existence of four magnetic satellite peaks.

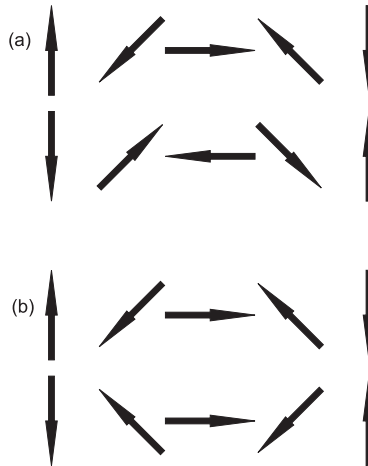


Figure 4.5: (a) The spiral structure proposed by Lindgård [25]; (b) The ‘ π -spiral’ structure proposed by Silva-Neto [26]

The magnetic excitations in LNSCO have been investigated by Ito *et al* using neutron inelastic scattering [27]. The excitations at low energy ($E \leq 5\text{meV}$) were found to decrease in incommensurability with increasing temperature, i.e. ε decreased for the peaks at $(0.5 \pm \varepsilon, 0.5, 0)$ etc, concomitant with an increase in their width. The fluctuations were found to persist well above T_N and even above T_{CO} , and were attributed to so-called ‘slowly fluctuating stripes’ [28]. Unlike in other superconducting materials at higher energies no resonance was observed, suggesting that the presence of static stripes has a direct bearing on the superconducting properties of the material. Ito *et al* suggested that this is because the material is divided into hole-rich and hole-poor regions and this somehow changes the interactions felt by the superconducting quasiparticles.

The magnetic field dependence of the charge order has been investigated using x-ray diffraction [29]. On measuring the charge order peaks as a function of temperature for several different magnetic fields applied parallel to the c -axis (after zero field cooling) it was found that within experimental error the charge order peaks are unaffected by an applied magnetic field.

4.1.3 Recent Measurements of $\text{La}_{2-x}\text{Ba}_x\text{CuO}_4$

Neutron scattering measurements have recently been performed on LBCO with $x \approx 1/8$ (see for example reference [30], and the references therein), now that it has lately become possible to grow large enough single crystal samples. These experiments have shown that there exist peaks arising from charge and spin ordering at the same wavevectors as in LNSCO, demonstrating that the underlying physics of these two systems is very similar. The neutron scattering measurements of LBCO will not be of direct concern for the work presented here, however. Rather, there is more interest in x-ray measurements of the charge order, so it is these studies that will be focussed on now.

Jungho Kim *et al* [31] measured the charge superlattice reflections using x-rays, and found that just below the LTO-LTT transition the correlation length of the charge order was much shorter than at lower temperatures, with long range order, characterised by the maximal correlation length, not setting in until $T \leq 40\text{K}$. Furthermore they noticed that there was a

small decrease in correlation length of the charge order peaks below about 15 K, which they attributed to the onset of superconductivity, suggesting that the charge ordered state is in competition with the superconducting state. No second or third harmonic reflections of the charge order were observed, leading the authors to conclude that the charge order is actually a sinusoidal charge density wave.

Young-June Kim *et al* [32] also used x-rays to measure the charge superlattice reflections, however their measurements instead mostly focussed on the very low temperature range around $T \sim 2$ K. They found that the application of increasingly large magnetic fields, up to 10 T perpendicular to the CuO_2 planes, caused a small increases in the correlation length of the charge order peaks. This was again interpreted as evidence of competition between charge order and superconductivity, with the applied field reducing the superconducting correlations and the charge order correlations increasing as a result. Similarly to Jungho Kim *et al* they found that in zero applied magnetic field the charge order correlation length reduced below ~ 12 K.

Abbamonte *et al* [33] have used soft x-ray resonant scattering (i.e. low energy x-rays, with $E < 1$ keV, tuned to an absorption edge of the material) to probe the charge order directly, rather than the associated structural distortions. By scanning the incident x-ray energy over the oxygen K-edge and the Cu L_3 -edge they attempted to measure the location in real space of the charge order, and found that there existed resonances at both energies. This suggests that simple models of localised charge on either the Cu–O bonds or on the Cu sites do not fully capture the physics of the charge ordered state.

4.1.4 Motivations

There exist several different theories for the ordering of spins in stripe / checkerboard ordered materials, and in order for progress to be made in the field experiments are required to determine which of these models are realistic. Polarised neutron scattering is a technique that can distinguish between the proposed models, because the magnetic scattering can be completely separated from the non-magnetic scattering. Furthermore some of the different proposed ordering schemes would give rise to quite different magnetic scattering, e.g. some would give rise to a nuclear-magnetic interference term in the magnetic cross-section that can only be precisely determined when polarised neutrons are employed. LNSCO was chosen for such a measurement because it is considered by many to be the archetypal charge ordered cuprate, and it is also relatively easier to grow large samples, which are a definite requirement for polarised neutron scattering experiments. Once an understanding of the static order of is obtained the next natural step is to consider the excitations, and for this neutron inelastic scattering measurements are the most obvious tool.

The competition postulated to exist between a charge ordered state and a superconducting state can be tested by measuring the charge order whilst tuning the superconductivity, either with temperature or applied magnetic field. Such measurements have already been performed on LBCO using x-ray scattering, so if similar results could be reproduced in LNSCO then it would go some way towards proving whether charge order and superconductivity compete in the general case.

4.2 Experimental details

4.2.1 Neutron Scattering

All of the polarised neutron scattering measurements described in this chapter were made on the IN20 thermal neutron triple-axis spectrometer (TAS) at ILL. All of the unpolarised neutron scattering measurements were performed on the IN14 cold neutron TAS at ILL. The outline of a generic TAS was detailed in section 2.1.2, as are some of the details of the equipment needed for polarised neutron scattering.

For this particular experiment on IN20 a standard polarised neutron setup was used, i.e. Heusler monochromator and analyser, a flipper in the scattered beam, etc. The polarising field at the sample was provided by electromagnetic Helmholtz coils which could be rotated coaxially with the sample. A pyrolytic graphite (PG) filter was placed in the scattered beam in order to suppress higher harmonic contamination. The sample environment was the standard orange cryostat, with ^4He used as the cryogen.

All of the polarised measurements detailed below were performed at fixed final neutron wavevector $k_f = 4.1 \text{ \AA}^{-1}$. This was chosen for two reasons. First was because even the elastic scattering was found to be rather weak, and so it was decided that increasing the resolution volume of the spectrometer, and hence the count rate, was necessary in order to make the experiment possible in the allowed time frame. Second was that in order to access magnetic reflections outside the first Brillouin zone a final wavevector larger than 2.662 \AA^{-1} was needed for the scattering angle not to be inconveniently large for the specific geometry of the spectrometer⁴.

The unpolarised measurements on IN14 were made with a fixed final wavevector of $k_f = 1.5 \text{ \AA}^{-1}$. This wavevector was chosen in order to optimise flux from the cold source at IN14, whilst still allowing the use of a cooled beryllium filter in order to cut off scattering from higher harmonic neutrons.

The sample used for the polarised neutron scattering measurements, and some of the unpolarised neutron measurements, consisted originally of a single cylindrical rod about 3 cm long, with a diameter of about 0.7 cm and a mass of 3.2 g. It was grown at Hokkaido university using the floating zone technique [6, 34]. Unfortunately, after the first unpolarised neutron measurement, the upper third of the rod split. The effect of this was, despite the two pieces being tied together with aluminium wire, a slight misalignment between the two parts of the crystal. This could clearly be seen in scans of the sample angle ω , where instead of a single peak there were two peaks, one larger than the other, separated by about 1° . The presence of the two peaks made fitting the data more complex, however ultimately it was possible provided the ratio of the peak intensities could be fixed at each reciprocal lattice vector. The procedure for doing this is described later in this chapter.

This sample was mounted in the cryostat with the $(0, 0, 1)$ -axis vertical, so the scattering plane was the $(H, K, 0)$ -plane. The wavevectors of interest were the spin-superstructure satellites to the antiferromagnetic (AFM) wavevector $\mathbf{Q}_{\text{AFM}} = (1/2, 1/2, 0)$, i.e. $\mathbf{Q} = (1/2 \pm q, 1/2, 0) + \mathbf{G}$ and $\mathbf{Q} = (1/2, 1/2 \pm q, 0) + \mathbf{G}$, where \mathbf{G} is a reciprocal lattice vector.

⁴A k_f of 2.662 \AA^{-1} would have resulted in the detector crashing into the walls of the experiment zone, but $k_f = 4.1 \text{ \AA}^{-1}$ avoided this problem.

The first unpolarised measurement was made, as stated above, using the same crystal as the polarised measurements, with the same scattering plane, before one of the pieces became broken and misaligned. The second unpolarised measurement was made on an array of four crystals with a combined mass of ~ 8 g that were aligned to give a scattering plane $(H, H, 0)/(0, 0, L)$ when the cryostat was vertical. In order to access the satellite reflection at $(0.5, 0.38, L)$ the cryostat was then tilted off vertical using the goniometer whose axis was parallel to the $(0, 0, L)$ direction.

4.2.2 Synchrotron X-ray Scattering

For the x-ray measurements the ID20 beamline at the ESRF in Grenoble was used. This beamline is situated on an undulator source, the generic details of which are given in section 2.2.1, and consequently has a very high flux over energy range used, in this case 8.5 keV. This incident photon energy does not correspond to the absorption edge of any materials in the compound, so the scattering was not resonantly enhanced. This is because the structural distortion peaks to be measured exhibit no resonant enhancement. Also if the energy of the x-rays is tuned to an absorption edge of an element in the material being studied there is a considerable increase in the background due to fluorescence. It was therefore appropriate for the experiments detailed in this chapter to use an energy where the flux from the undulator is maximal, but where there are no elemental absorption edges nearby which could cause an increase in the background.

This particular experiment was conducted using a vertical-field magnet with a maximum field of 10 T. Since such magnets cannot be tilted a horizontal scattering geometry was used, and rather than using a χ rotation there was a different rotation, γ , whose axis is perpendicular to 2θ , the (horizontal) scattering angle. This essentially corresponds to the six-circle diffractometer discussed in section 2.2.2 and shown in figure 2.5, albeit with a slightly different scattering plane.

The LNSCO sample, which was from the same batch as that used for the neutron scattering measurements, was cut and polished so that the surface was parallel to the $(1, 0, 2)$ -planes, so that Bragg reflections that are some multiple of this (specular) wavevector would be relatively strong compared to equivalent wavevectors off-specular. Experiments were performed during the same x-ray beamtime at ID20 on a sample of $\text{La}_{1.88}\text{Ba}_{0.12}\text{CuO}_4$ (LBCO) which was cut and polished in the same way. This sample was grown at the Brookhaven National Laboratory, and was taken from the same batch as other samples on which neutron scattering measurements have been reported [8, 12]. The stick on which samples are mounted to go into the cryomagnet on ID20 has two slots in which samples can sit, one above the other, making it possible to move one sample out of the beam and the other into it without warming up and venting the sample chamber. Both samples were cut so that the c -axis would be parallel to the axis of the magnet, thus establishing a two dimensional vortex lattice within the CuO_2 planes.

4.2.3 Magnetisation Measurements

Magnetometry measurements were performed in a Quantum Design SQUID magnetometer, the principles of operation of which were described in section 2.3.1. The sample used was

a small piece from the same growth batch as those used for the neutron and x-ray measurements. It was cooled in zero field (ZFC) and then its magnetisation as a function of temperature was determined whilst warming, with an applied magnetic field of 500 Oe. The same procedure was also followed but with field cooling (FC) with 500 Oe. The crystal was mounted using the plastic capsule method, described in section 2.3.1, in such a way that the applied field was parallel to the ab -plane.

4.3 Results

The sample's longitudinal moment⁵ which was used to determine the superconducting properties of the LNSCO sample, is shown in figure 4.6, and the entry into the Meissner state can clearly be seen at about 7K in the ZFC data. Above the critical temperature the long moment displays a Curie-Weiss type behaviour, which can be attributed to the disordered (i.e. paramagnetic) Nd moments, which are much larger than the ordered Cu moments and therefore dominate. This is best seen in the magnified FC data, shown in figure 4.6(a).

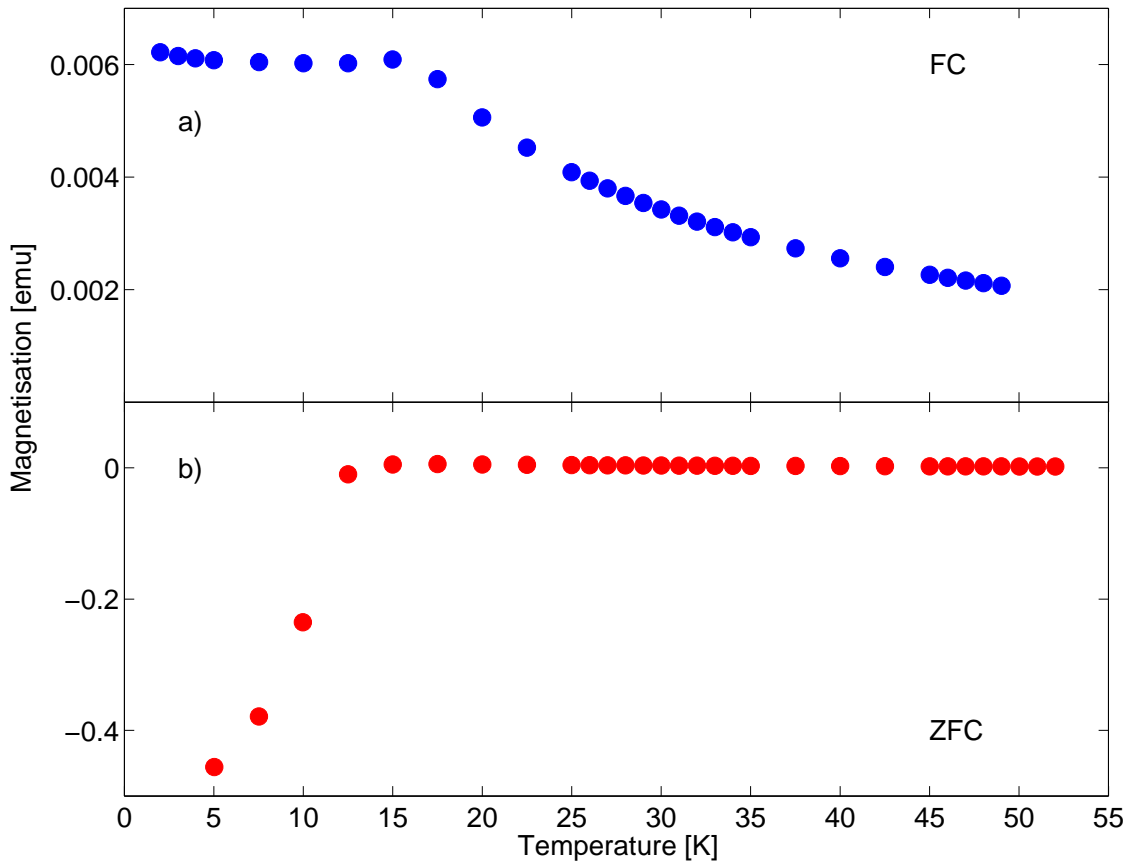


Figure 4.6: (a) FC measurement of the long moment. (b) ZFC measurement of the long moment. The applied magnetic field was 500 Oe in the ab -plane.

⁵which is proportional to its magnetisation.

4.3.1 Polarised Neutron Scattering Measurements

The results of the polarised neutron scattering measurements presented are the same as those published in reference [35]. All of the scattering was corrected for imperfect polarisation – a flipping ratio of 14 was measured at the purely non-magnetic Bragg peak $\mathbf{Q}_{\text{nuc}} = (1, 1, 0)$.

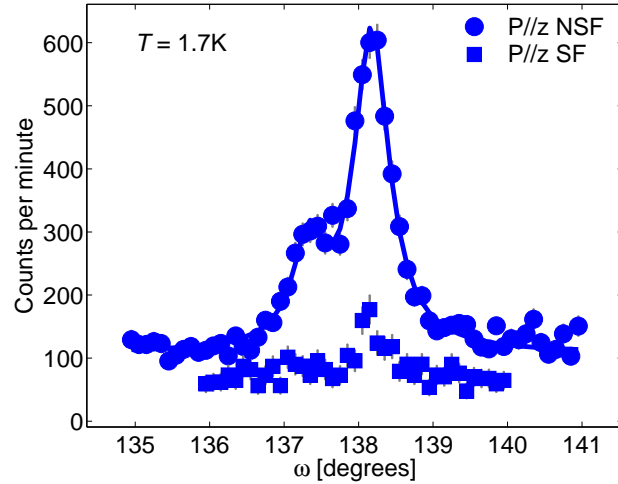


Figure 4.7: Measurements of the scattering with \mathbf{P} perpendicular to the scattering plane at $\mathbf{Q} = (1/2, 0.62, 0)$, with $T = 1.7\text{K}$. The non-spin-flip (NSF) channel is sensitive to the component of the ordered moment pointing out of the plane (parallel to the polarisation), whereas the spin-flip (SF) channel is sensitive to components of the ordered moment that are in-plane. The NSF data are fitted to two Lorentzians. The scan angle ω corresponds to a rotation of the sample about the $(0, 0, 1)$ -axis.

Figure 4.7 shows the scattering at $\mathbf{Q} = (1/2, 0.62, 0)$ with $T = 1.7\text{K}$, which was the base temperature of the cryostat used for this experiment. As noted in the section 4.1.2, previous experiments with unpolarised neutrons in zero field [12] and in an applied magnetic field [29] have concluded that the Nd^{3+} moments align perpendicular to the Cu-O planes below $T_{\text{N}}^{\text{Nd}} \approx 3\text{K}$. The Cu^{2+} have two nearest-neighbour La/Nd ions along the c -axis, each connected via a single oxygen ion (see fig. 4.1). Coupling between the ordered Nd^{3+} and Cu^{2+} spins results in the latter rotating out of the plane as the temperature is lowered and the ordered Nd moment grows. It is a combination of the ordered Cu^{2+} and Nd^{3+} moments that are detected in the neutron scattering measurements at low temperature.

The wavevector of the low-temperature magnetic order is the same as that of the spin stripes observed at higher temperatures. This is because just above T_{N}^{Nd} the Nd^{3+} moments are entrained to the order of the Cu^{2+} . As the sample is then cooled through T_{N}^{Nd} it costs more energy for the Nd^{3+} moments to change their ordering wavevector than it does for them just to, in effect, amplify the order of the Cu^{2+} spins.

As stated in section 2.1.4, equations 2.36, the diffraction in the non-spin-flip (NSF) channel with $\mathbf{P} \parallel \mathbf{z}$ is sensitive to the component of the ordered moment that is also parallel to \mathbf{z} , which in this case is the c -axis, plus some background. Conversely the spin-flip (SF) channel with this polarisation is sensitive to moments that lie in the scattering plane and are perpendicular to \mathbf{Q} . It is immediately obvious from the data shown in figure 4.7, that the ordered moment points almost entirely along the c -axis. The NSF data were fitted using

two Lorentzians - this peak function was used simply because it was the one provided the best fit, quantified by having the smallest χ^2 .

The presence of a strong signal at low temperatures due to this ordering of the Nd^{3+} moments was actually quite helpful for the purposes of this experiment. The strength of the signal meant that it was easy to characterise without using prohibitively long counting times. Because the Nd-ordering had the same wavevector as the Cu-ordering it was possible to use these well characterised scans to determine accurately the position in sample angle, ω , of the two peaks (resulting from the two slightly misaligned crystals) at any given wavevector. Furthermore the relative intensity of the two peaks was purely due to the profile of the two crystals seen by the neutron beam, so by fitting these low temperature data it was possible to fix this relative intensity in the higher temperature data fitting. In addition the widths of the two peaks at any given wavevector were determined by the resolution of the spectrometer at that position, so the low temperature fits could be used to constrain this parameter for the higher temperature fits. Finally, because full polarisation analysis was performed at each wavevector, the ‘pure’ magnetic signal was determined. This meant that the background could be constrained to zero, and could hence be fixed when the higher temperature data were fitted. The result of all of these constraints meant that for any given fit of the higher temperature data only one parameter was free to be varied by the fitting program, resulting in much more reliable fitting.

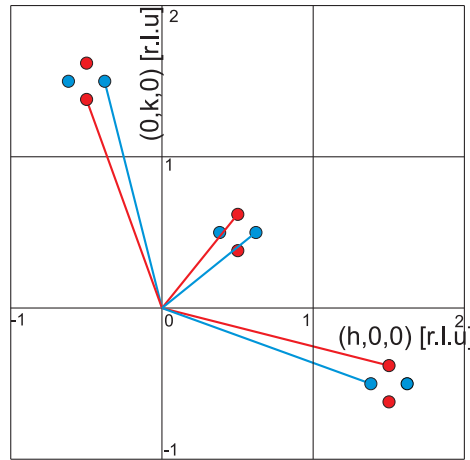


Figure 4.8: The scattering plane, showing the positions of the satellite peaks around the AFM wavevectors in several Brillouin zones. The wavevectors with lines drawn to them from the origin are the ones at which measurements were made.

Figure 4.8 shows the scattering plane in which the measurements presented below were made. The spin superstructure peaks are shown as red and blue filled circles, depending on whether they arise from spins modulated along the b - or a -axis respectively. The red and blue solid lines from the origin to some of these positions indicate at which wavevectors measurements of the scattering were made. I will adopt the convention of denoting scattering resulting from in-plane moments lying perpendicular to the scattering wavevector as M_y .

Figures 4.9 to 4.11 show the polarisation analysed magnetic scattering at the six wavevectors shown in figure 4.8 for $T = 10\text{K}$. At this temperature the Nd^{3+} spins are in a disordered paramagnetic state, so the scattering arises entirely from the ordered Cu^{2+} moments.

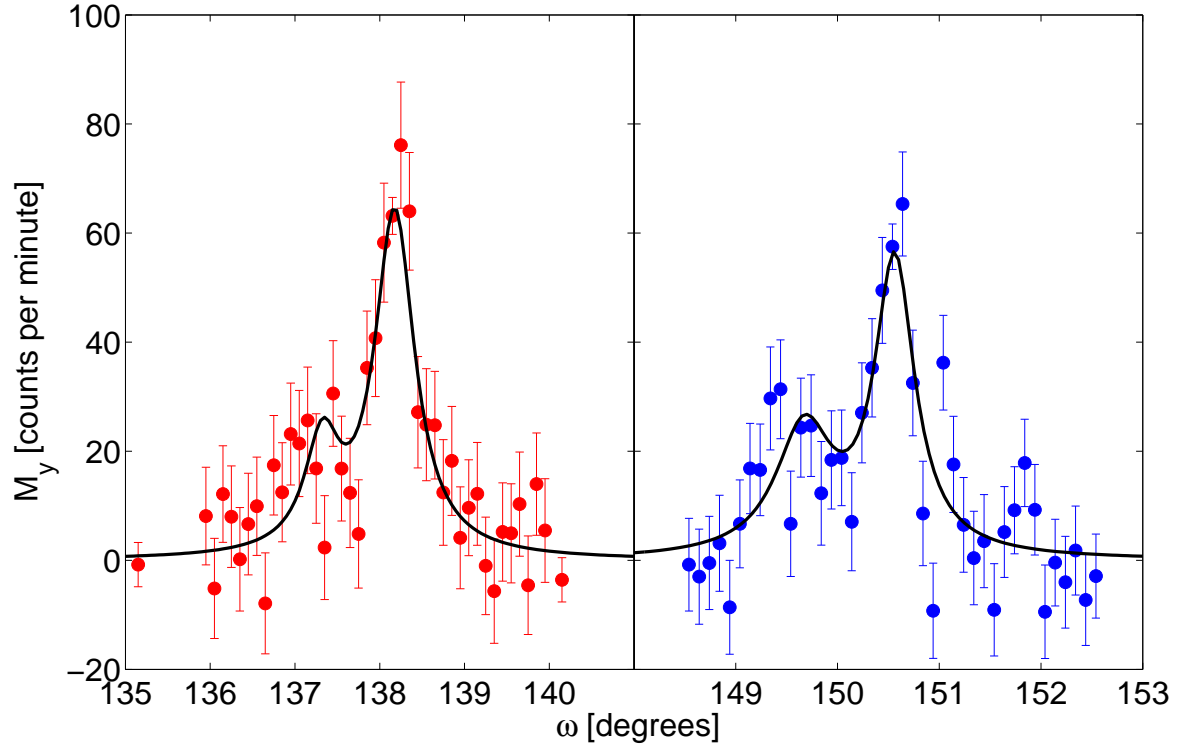


Figure 4.9: Polarisation analysed ω -scans with $T = 10\text{K}$ at $\mathbf{Q} = (0.5, 0.62, 0)$ and $\mathbf{Q} = (0.62, 0.5, 0)$, denoted by red and blue circles respectively. The y-axis corresponds to the magnetic signal arising from ordered moments that are in-plane and perpendicular to the scattering wavevector. The black line represents a fit to the data, described in the text.

The main feature to notice is that the intensities of the scattering at the two positions around the $(0.5, 0.5, 0)$ position (fig. 4.9) are almost equal. This contrasts with the measurements at the satellite peaks of $(-0.5, 1.5, 0)$ and $(1.5, -0.5, 0)$, figs. 4.10 and 4.11 respectively, where the signals resulting from modulation of the spins along either the a - or b -axis have substantially different intensities. For the satellite peaks around $(-0.5, 1.5, 0)$ it is the magnetic signal arising from spins modulated along the b -axis that is stronger, whereas for the peaks around $(1.5, -0.5, 0)$ it is the signal arising from spins modulated along the a -axis that is stronger.

Table 4.1 shows the inelastic scattering intensities for two different wavevectors at an energy transfer of 5meV with $T = 10\text{K}$. Polarisation analysis allowed the ‘pure’ spin-spin correlations to be measured, with S_y denoting components perpendicular to \mathbf{Q} but in the scattering plane, and S_z denoting components perpendicular to the scattering plane. The measurements of the six polarisation channels were made at a point in the middle of the peak position, determined from the elastic scattering, and at two points at the background level either side of this peak⁶. A full scan in wavevector space (i.e. a linear \mathbf{Q} -scan or an ω -scan) would have been preferable in order to determine the line-shape accurately, however the intensity of the scattering was very weak that this was not feasible. Indeed three-point scans at these two wavevectors with sufficiently long counting times for the results to have statistical significance took a total of 44 hours.

⁶Unpolarised neutron inelastic scattering measurements, shown later, have shown that the spin excitations are non-dispersive at low energies.

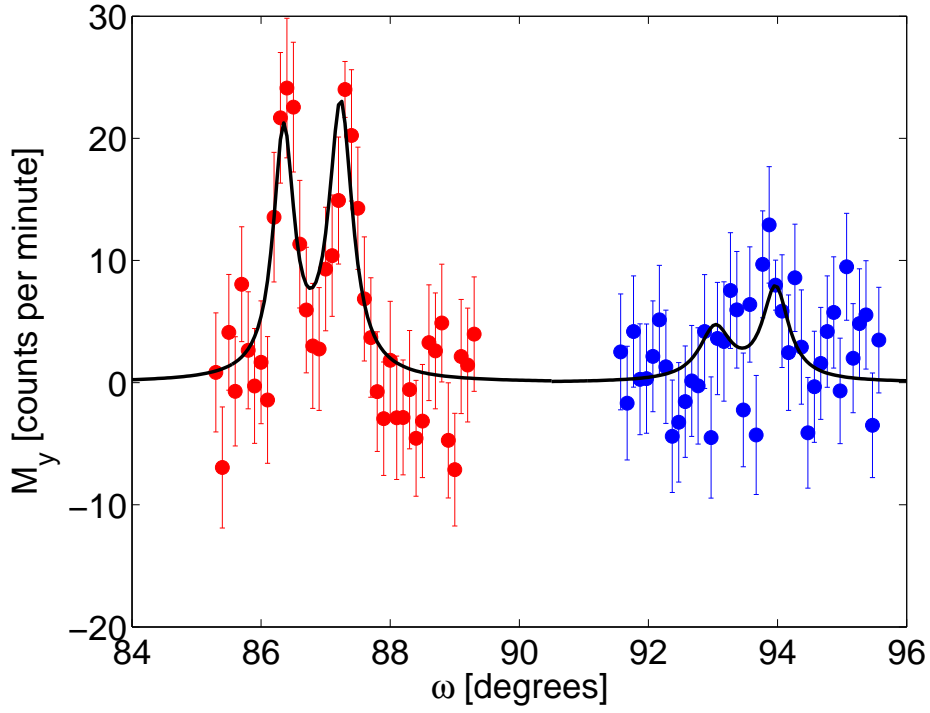


Figure 4.10: The scans at $\mathbf{Q} = (-0.5, 1.38, 0)$ and $\mathbf{Q} = (-0.38, 1.5, 0)$ (red and blue circles respectively) corresponding to the scans shown in figure 4.9. The black line is a fit to the data, described in the text.

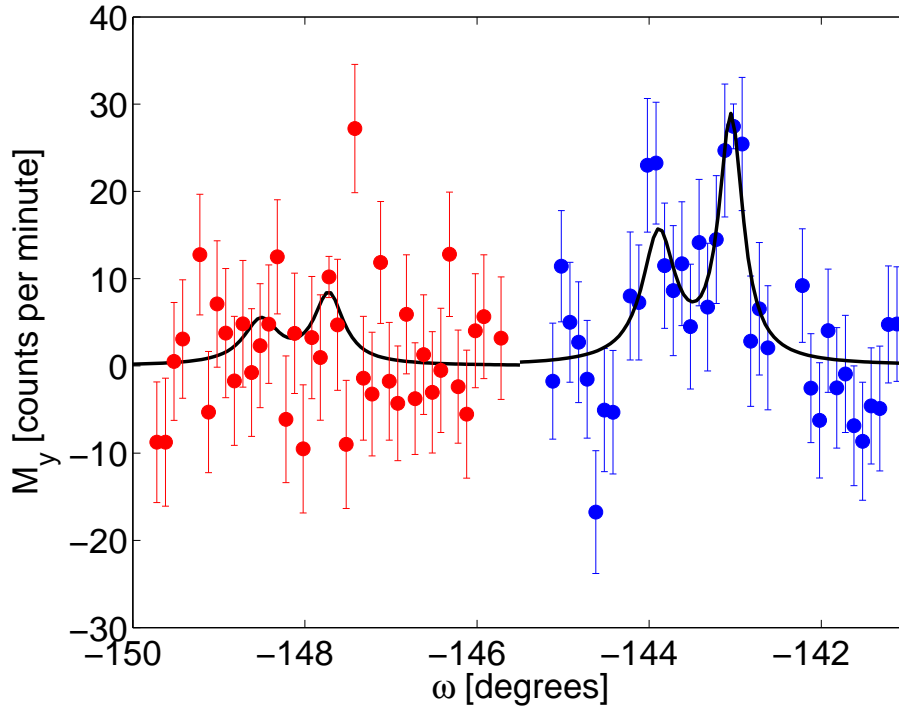


Figure 4.11: The scans at $\mathbf{Q} = (1.5, -0.38, 0)$ and $\mathbf{Q} = (1.38, -0.5, 0)$ (blue and red circles respectively) corresponding to the scans shown in figures 4.9 and 4.10. The black line represents a fit to the data, described in the text.

Wavevector \mathbf{Q}	Magnetic fluctuation component	Intensity
(-0.38,1.5,0)	S_y	7.4 ± 1.3
(-0.38,1.5,0)	S_z	9.9 ± 1.4
(1.38,-0.5,0)	S_y	2.4 ± 1.1
(1.38,-0.5,0)	S_z	7.6 ± 1.1

Table 4.1: The inelastic scattering intensities of the transverse in-plane and out-of-plane spin fluctuations, for $E = 5$ meV, and $T = 10$ K.

It is clear that whilst the two components of the spin fluctuations that were measured at $\mathbf{Q} = (-0.38, 1.5, 0)$ are quite close in magnitude, the two components are very different at $\mathbf{Q} = (1.38, -0.5, 0)$.

4.3.2 Unpolarised Neutron Scattering Measurements

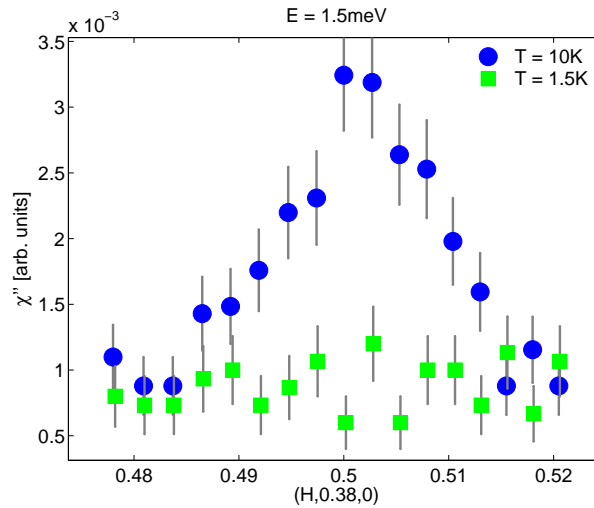


Figure 4.12: Fixed-energy wavevector scan over the $(0.5, 0.38, 0)$ position with $E = 1.5$ meV, showing the scattering at $T = 1.5$ K and $T = 10$ K.

The spin excitations at the wavevectors $\mathbf{Q} = (0.5 \pm \delta, 0.5, 0)$ and $\mathbf{Q} = (0.5, 0.5 \pm \delta, 0)$, with $\delta = 0.12$, were measured at low energies using unpolarised neutrons from a cold source on the IN14 TAS. The excitations measurable in the first Brillouin zone with the spectrometer setup described (see section 4.2.1) were found not to disperse, and nor did they change in width as a function of energy or temperature, shown by the fixed-energy \mathbf{Q} -scans at $E = 1.5$ meV and $E = 4$ meV shown in figure 4.12 and figure 4.13 respectively. This therefore meant that subsequent fixed wavevector energy scans could be performed more quickly by measuring three points at each energy without losing information about the signal, like with the polarised inelastic measurements described in section 4.3.1.

The first set of measurements used a single crystal sample with a $(H, 0, 0)/(0, H, 0)$ scattering plane. Figure 4.14 shows energy scans of the signal minus the background, corrected

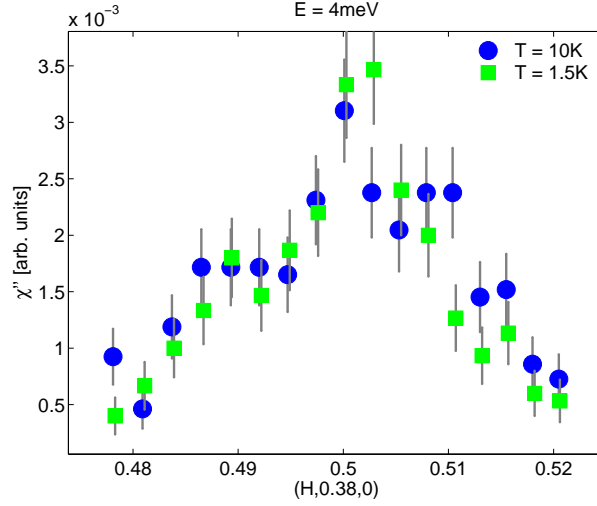


Figure 4.13: Fixed-energy wavevector scan over the $(0.5, 0.38, 0)$ position with $E = 4$ meV, showing the scattering at $T = 1.5$ K and $T = 10$ K.

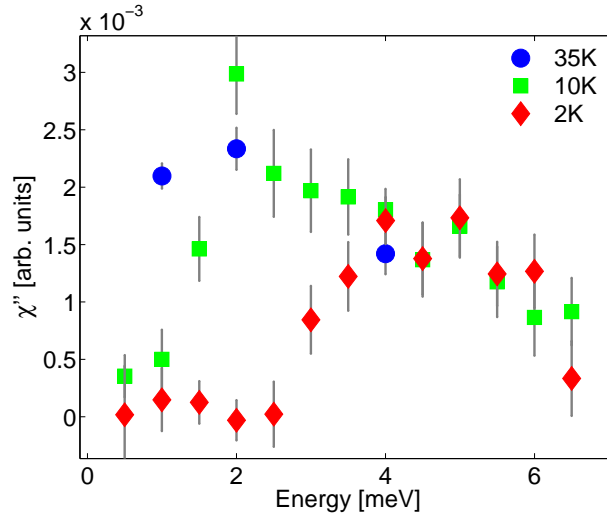


Figure 4.14: The peak minus background scattering at $\mathbf{Q} = (0.5, 0.38, 0)$ for $T = 2$ K, $T = 10$ K, and $T = 35$ K.

for the Bose-Einstein population factor, for $T = 2$ K, $T = 10$ K, and $T = 35$ K. The scan at 2 K shows a clear gap of about 3 meV, whereas at 10 K the gap has reduced to about 1 meV. The scan at 35 K consists of only three points, but it is clear that after correcting for the Bose factor the signal at 4 meV is the same as it is at the other two temperatures. It also appears that the scattering is more intense at lower energies, because at 1 meV the dynamic susceptibility, χ'' , at 35 K is a factor of 5 stronger than the same energy with $T = 10$ K and is a factor of 10 stronger than at $T = 2$ K.

The second set of measurements on IN14 were made on a four-crystal sample with a scattering plane defined by the vectors $(H, H, 0)$ and $(0, 0, L)$, with a small goniometer tilt required to access magnetic satellite peaks. Figure 4.15 shows a schematic of the two wavevectors at which measurements were made. The angles θ_1 and θ_2 are 37.23° and 82.06° respectively. Thus the measurements at $L = 0$ measure spin fluctuations perpendicular to the ab -plane and perpendicular to $(0.5, 0.38, 0)$, whereas the measurements at $L = 4.5$ measure

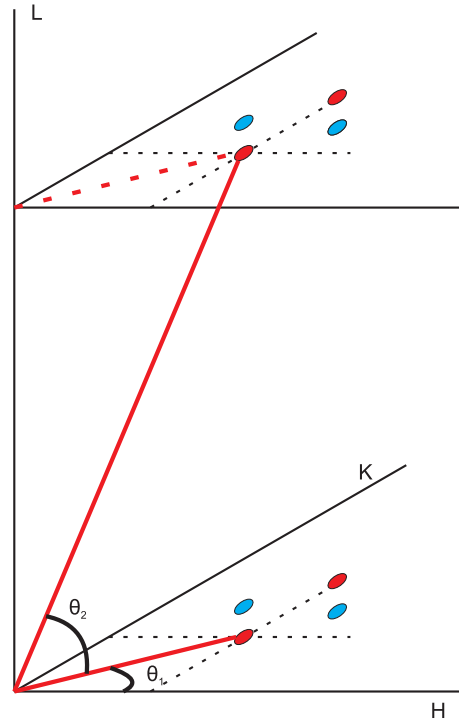


Figure 4.15: The scattering planes used for the second measurement on the IN14 spectrometer.

a much smaller fraction of the out-of-plane component and almost all of the fluctuations in the ab -plane.

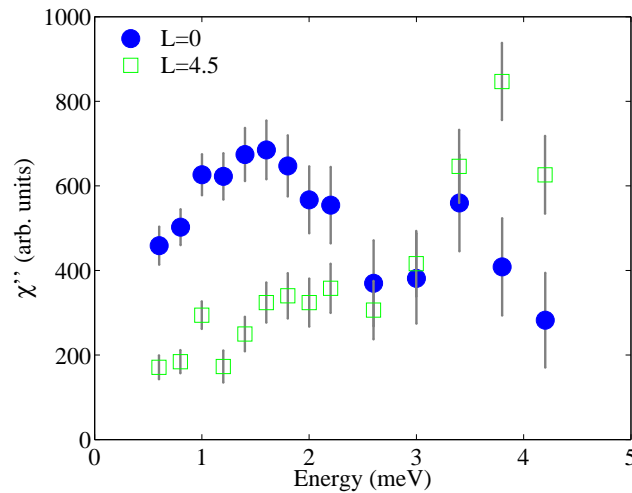


Figure 4.16: The scattering at $\mathbf{Q} = (0.5, 0.38, 0)$ and $\mathbf{Q} = (0.5, 0.38, 4.5)$, $L = 0$ and $L = 4.5$ respectively, with $T = 35$ K

Figure 4.16 shows data taken using the four-crystal array sample. The measurements here were made at $T = 35$ K, which was chosen because the absolute count rate arising from the magnetic excitations was greater at this temperature than at lower temperatures due to the Bose population factor. This meant that better quality data, i.e. higher counts, could be collected in a shorter period of time, giving rise to smaller error bars on the data and also

faster data collection.

The data shown were obtained, as with the first experiment, by measuring three points at each energy - one peak and two background. The scattering at $(0.5, 0.38, 4.5)$ is less intense than that at $(0.5, 0.38, 0)$ at the lowest energies. Its intensity then increases less sharply with increasing energy, and reaches a maximum at 4meV. The scattering at $(0.5, 0.38, 0)$ reaches a maximum at 1.5meV and then decreases steadily with increasing temperature. The behaviour as a function of temperature of the scattering at $(0.5, 0.38, 0)$ is consistent with the three points measured on a different sample, shown in figure 4.14.

4.3.3 X-ray Diffraction Measurements

Figure 4.17 shows a typical scan along the $(H, 0, 0)$ -direction of LNSCO over the wavevector $\mathbf{Q} = (2.24, 0, 4.5)$, i.e. $\mathbf{Q} = (2, 0, 4) + (0.24, 0, 0.5)$, probing a structural modulation, induced by a similarly modulated charge ordering pattern. As was noted in section 4.1, $\text{La}_{2-x}\text{Ba}_x\text{CuO}_4$ (LBCO), with $x \approx 1/8$, shows similar behaviour. In figure 4.18 the same kind of scan for LBCO as was shown in figure 4.17 for LNSCO is presented for comparison. This measurement was also made on ID20 with the exact same setup of the apparatus during the same beamtime allocation. Note that although the measurements discussed in the rest of this section relate to these peaks at $\mathbf{Q} = (2.24, 0, 4.5)$, there was an observable signal at the other satellites of the $(2, 0, 4)$ Bragg peak. The $(2.24, 0, 4.5)$ was chosen simply for experimental convenience⁷.

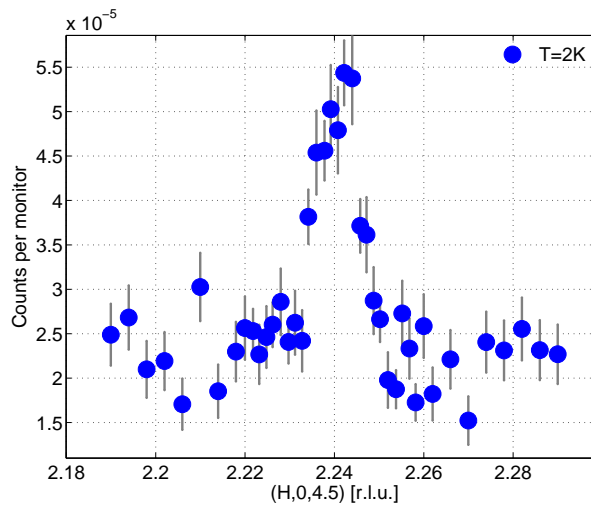


Figure 4.17: Scan of charge-order induced structural distortion peak in LNSCO, at $T=2\text{K}$ in zero applied field.

The temperature dependence of the peak intensity in both materials is shown in figures 4.19 and 4.20. The peaks were fitted with a Lorentzian-squared lineshape, since of the simple peak functions (Gaussian, Lorentzian etc.) this provided the best overall fit. The intensity was then calculated from this using the product of the amplitude and the width.

In both materials the intensity of the charge peak decreases monotonically above about 20 K. In LNSCO the peak disappears at about 70 K, which is the same temperature as the

⁷The specular direction of the sample used was $(1, 0, 2)$.

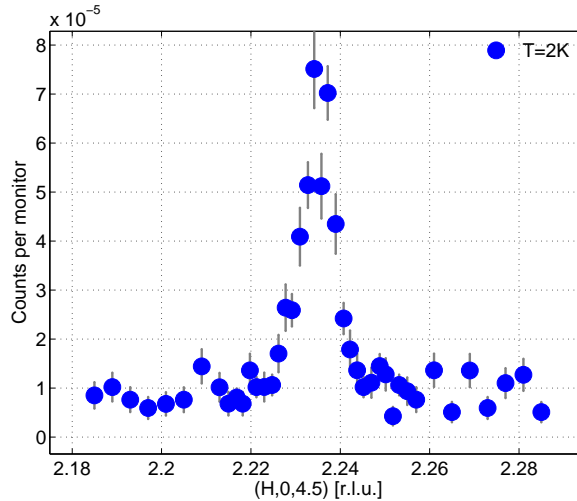


Figure 4.18: Scan of charge-order induced structural distortion peak in LBCO, at $T=2$ K in zero applied field.

LTT-LTO structural transition. In LBCO the peak disappears above 50 K, which is similarly around the temperature of a structural transition.

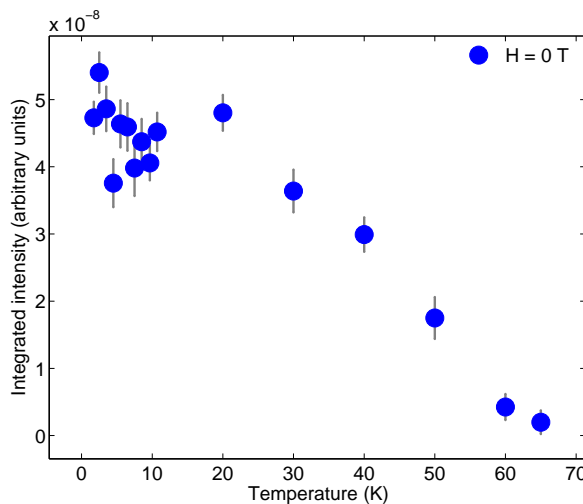


Figure 4.19: The temperature dependence of the integrated intensity of the charge order induced structural peak at $\mathbf{Q} = (2.24, 0, 4.5)$ in LNSCO.

It is possible that the correlation length of the charge order may change, depending on the presence or absence of superconductivity. The fits also provide information about this, and the width in zero field in LNSCO is shown in figure 4.21. This clearly shows that the width does not deviate significantly over the range $2 \leq T \leq 60$ K (above 60 K the fit for the width is so large that to plot it on the same axes would not be sensible).

A similar measurement was conducted for LBCO, measuring the charge order peak in zero applied field, and then the same peak after field cooling in applied field of $H = 10$ T. Figure 4.22 shows that the peak does broaden at higher temperatures, just below the charge ordering transition temperature. The measurement in an applied field is not discernibly different from the zero-field measurement, so it appears that the charge order is unaffected by the presence of an applied magnetic field.

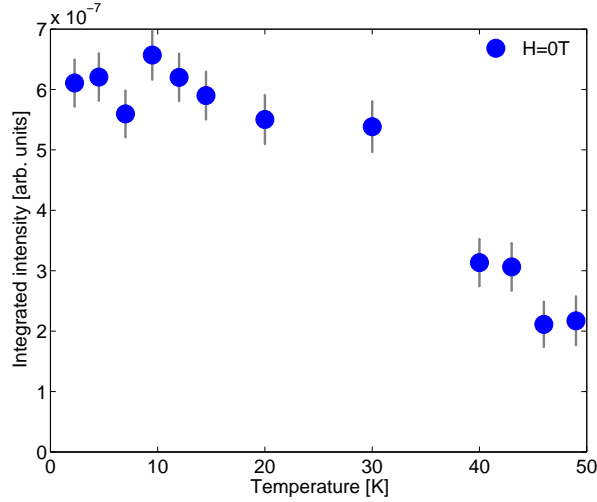


Figure 4.20: The temperature dependence of the integrated intensity of the charge order induced structural peak at $\mathbf{Q} = (2.24, 0, 4.5)$ in LBCO.

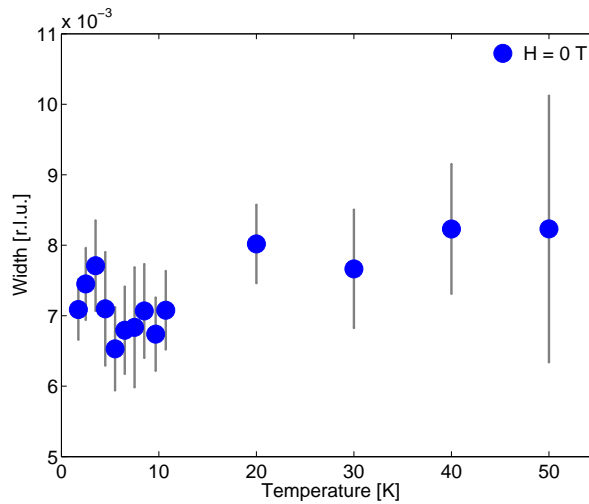


Figure 4.21: The temperature dependence of the width of the charge order peak in LNSCO in zero applied magnetic field

To test further the result from LBCO, that an applied magnetic field does not affect charge order, the LNSCO sample was field cooled from 100 K (well above the stripe-order and superconducting transition temperatures) and then the charge order peaks were measured as function of temperature. As with the zero field data, the peaks were fitted with a Lorentzian-squared lineshape. It was found, within the error bars of the fits, that there is no difference between the zero-field intensity and the field cooled intensities for applied fields of up to 9 T. Furthermore, the charge order peak's width did not change compared to the zero field measurement when magnetic fields were applied.

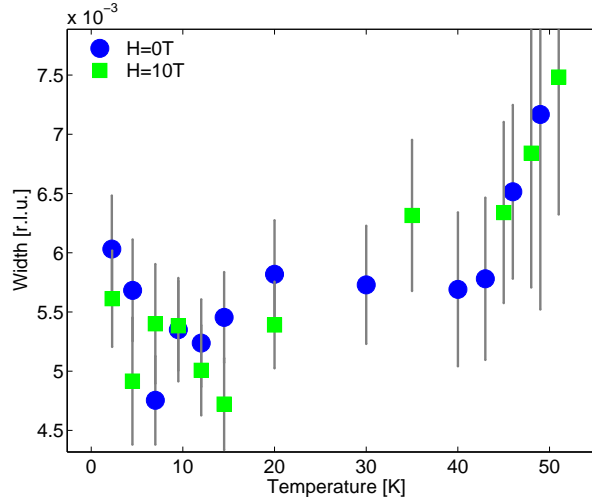


Figure 4.22: The temperature dependence of the width of the charge order induced structural peak at $\mathbf{Q} = (2.24, 0, 4.5)$ in LBCO with zero applied magnetic field, and an applied field of 10 T.

4.4 Analysis and Discussion

4.4.1 Analysis of the Polarised Neutron Scattering Measurements

For chiral magnetic structures there are extra terms in the magnetic inelastic scattering cross-section that were neglected, for brevity, in the general introduction to scattering theory presented in section 2.1. The relevant part of the full cross-section is instead given in appendix A.

Referring to equations A.5 and A.6, note that the imaginary part of \mathbf{M}_\perp contains the information about the phase of the magnetic order. For non-chiral structures $\mathbf{M}_\perp = \mathbf{M}_\perp^*$, so that $\mathbf{M}_\perp \times \mathbf{M}_\perp^* = 0$. Therefore measuring the scattering in both channels, spin-flip and non-spin-flip, for each polarisation allows one to determine whether or not there exists chiral magnetic order. If chiral order exists then the sum of the two channels for the different polarisations would be different, whereas if there were no chiral order the sum of NSF and SF scattering would be the same for each polarisation. Figure 4.23 shows the differences in the values of the sum of SF and NSF scattering at $\mathbf{Q} = (-0.5, 1.38, 0)$ and $\mathbf{Q} = (-0.38, 1.5, 0)$ for all three polarisations. It is clear that the sum of the two channels is the same, within the error on the measurement, for all three polarisations at each wavevector. This means that chiral ordering is completely ruled out by these measurements.

Analysis based on Landau theory considerations [36] shows that if there is a non-spiral spin order at wavevectors \mathbf{Q}_1 and \mathbf{Q}_2 then there will be charge order at wavevectors of the form $\mathbf{Q}_1 + \mathbf{Q}_2$, as well as at $2\mathbf{Q}_1$ and $2\mathbf{Q}_2$, however the former set of peaks have never been observed experimentally, ruling out spin-checkerboard type models.

Let us now make the ansatz that the stripe model provides an adequate description of the spin order in LNSCO, and calculate whether the data are consistent with this ansatz, and if so what further information may be obtained about the ordered spins.

When manipulating the data they were first corrected for the differences in magnetic

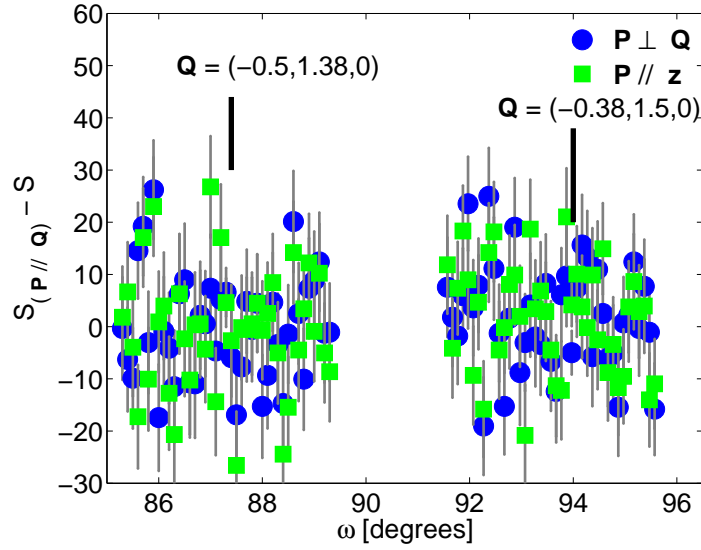


Figure 4.23: The scans at $\mathbf{Q} = (-0.5, 1.38, 0)$ and $\mathbf{Q} = (-0.38, 1.5, 0)$, showing the sum of NSF and SF for $\mathbf{P} \parallel \mathbf{Q}$ minus the sum of NSF and SF for $\mathbf{P} \perp \mathbf{Q}$ and $\mathbf{P} \parallel \mathbf{Q}$. Black vertical lines show the main peak position for each wavevector.

form factor at different wavevectors. There exist tabulated coefficients for the analytical approximation of the form factor for various magnetic ions [37] which can be used to calculate the form factor at the various different wavevectors. However in many solids there may be extra effects which cause the analytical approximations to break down, so correcting the data for form factor in this way is somewhat risky. It was therefore considered safer for this material to compare the integrated intensities of the signals of peaks in the same group of magnetic satellites (e.g. only compare the signal from a peak at $(-0.38, 1.5, 0)$ with other satellites around the $(-0.5, 1.5, 0)$ position). This meant that when the data were being fitted the integrated intensities of pairs of peaks were compared, but peaks in different magnetic zones were not compared. During the analysis the only fitting parameter required for the pair of peaks at each wavevector was an overall intensity scale factor, since the widths, background and intensity ratio was fixed by the low temperature data fits (see section 4.3.1).

The integrated intensity of a particular spin signal is proportional to the square of the ordered moment in that direction (see section 2.1.4), so for each pair of wavevectors the ratio of the intensities will determine a unique spin direction relative to the principal axes for the case of spins ordered in the stripe model. In such a model there is an equal population of orthogonal domains of spins and stripes, due to the tetragonal symmetry of the crystal, but these domains do not contribute to the same satellite peak. However the spin direction relative to the b -axis for the $(0.12, 0, 0)$ satellites will be the same, due to the tetragonal symmetry, as the spin direction relative to the a -axis for the $(0, 0.12, 0)$ satellites.

The angle of the spin to the wavevector for the $(0.12, 0, 0)$ -type peaks is given by

$$\alpha = (90 - \theta_1) + \phi, \quad (4.1)$$

where ϕ is the angle of the spin to the b -axis, α is the angle of the spin to the scattering wavevector, and θ_1 is the angle of the wavevector to the a -axis.

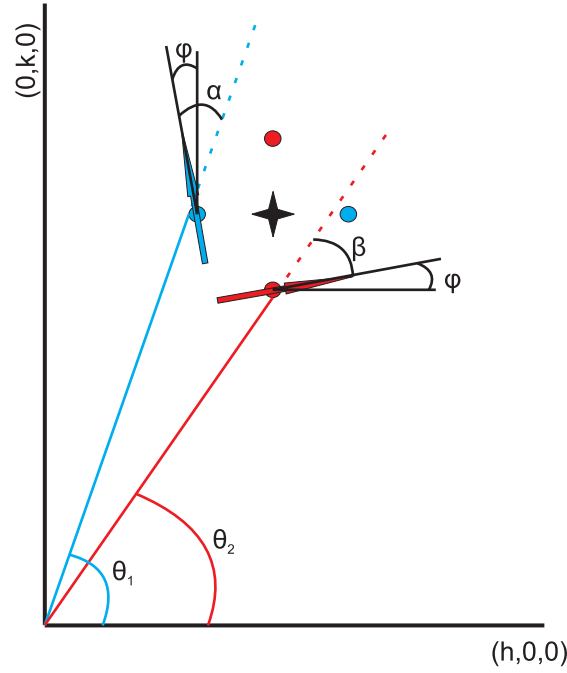


Figure 4.24: Definitions of angles used in analysis of the polarised neutron diffraction data.

The same angle, relative to the a -axis for the $(0, 0.12, 0)$ peaks results in

$$\beta = \theta_2 - \phi, \quad (4.2)$$

where β is the angle of the spin relative to the scattering wavevector and θ_2 is the angle of this wavevector to the b -axis. The ratio, R , of the scattering at the two wavevectors arising from the component of the spin perpendicular to the wavevector is then given by

$$R = \frac{\sin^2(\alpha_+) + \sin^2(\alpha_-)}{\sin^2(\beta_+) + \sin^2(\beta_-)}, \quad (4.3)$$

where α_+ and α_- represent the α calculated in equation 4.1 with $+\phi$ and $-\phi$ respectively, and β_+ and β_- are defined similarly⁸.

The results of these fits which, to reiterate, were magnetic zone independent, gave rise to slightly different values for the angle between the spins and the principal axes. For the wavevectors $\mathbf{Q} = (0.62, 0.5, 0)$ and $\mathbf{Q} = (0.5, 0.62, 0)$ the symmetry of the system means that the angle between the spins and the principal axes cannot be determined. Irrespective of the angle ϕ chosen the ratio of intensities will always be the same, which can be seen immediately on inspection of equations 4.1 and 4.2. The pair of satellite peaks of $(0.5, 0.5, 0)$ chosen for these measurements were symmetric about a line at 45° to the principal axes. This means that $(90 - \theta_1) = \theta_2$, and if we allow an equal number of spins to be at $+\phi$ and $-\phi$, which we must given the tetragonal symmetry, then the ratio given in equation 4.3 will always be unity. Hence this pair of peaks provide no information about the orientation of

⁸Due to symmetry there is no difference in energy between a spin lying at $+\phi$ and $-\phi$ to a principal axis, so there will be an equal population of both.

the spins in the stripes.

The other magnetic zones in which measurements were made do, however, provide information on the arrangement of the spins. The ratio of intensities of the peaks at $\mathbf{Q} = (-0.38, 1.5, 0)$ and $\mathbf{Q} = (-0.5, 1.38, 0)$ was found to be $R_1 = 0.35 \pm 0.06$, which in turn gives $\phi = 27.8 \pm 2.4^\circ$. The ratio of intensities of the peaks at $\mathbf{Q} = (1.38, -0.5, 0)$ and $\mathbf{Q} = (1.5, -0.38, 0)$ was found to be $R_2 = 2.77 \pm 0.68$, which would give rise to an angle of $\phi = 28.2 \pm 4^\circ$. Calculating the weighted mean and weighted error of these two values gives $\phi = 28.0 \pm 1.5^\circ$. It is the fits that give this result that are shown as the solid lines in figures 4.9, 4.10, and 4.11.

The information shown in table 4.1 can be readily interpreted in terms of the stripe model. The low energy of the excitation examined (5 meV) means that the fluctuations can be simply interpreted as arising from semi-classical spin-waves. When spins are statically correlated then such fluctuations should be predominantly perpendicular to the direction of the ordered moment. If the spin waves are isotropic then both of the two components of the excitations that are perpendicular to the ordered moment direction should be non-zero and equal. This contrasts with the component that is longitudinal to the spin ordering direction, which one would expect to be very small, or even zero. As with measurements of the static magnetic moments, detailed above, it is only the components of the spin excitations that are perpendicular to the scattering wavevector that can be measured.

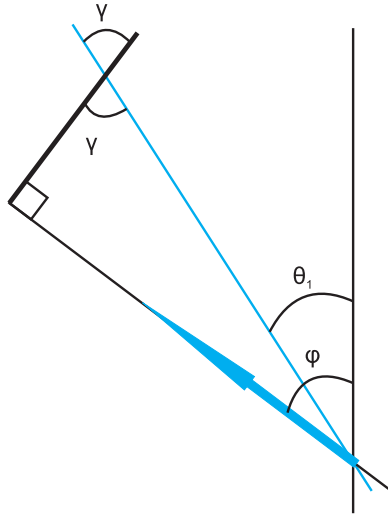


Figure 4.25: Definitions of the first set of angles used in analysis of the polarised neutron inelastic scattering data.

Examining the inelastic scattering at $\mathbf{Q} = (-0.38, 1.5, 0)$ first, and defining the angle between the b -axis and \mathbf{Q} as θ_1 , the angle between the ordered moment and the b -axis as ϕ , and the angle between \mathbf{Q} and the transverse component of the spin wave as γ (as in figure 4.25) we see that

$$\begin{aligned}\gamma_+ &= 90^\circ + \theta_1 - \phi, \\ \gamma_- &= 90^\circ + \theta_1 + \phi,\end{aligned}\tag{4.4}$$

where the + and - subscripts take into account the assumed equal population of spins oriented at angles $+\phi$ and $-\phi$ to the b -axis. This means that the in-plane transverse component of the inelastic scattering, which is labelled S_y in table 4.1 will be related to the out of plane component S_z by

$$S_y = \frac{S_z}{2} (\sin^2(\gamma_+) + \sin^2(\gamma_-)). \quad (4.5)$$

If we put $\gamma = 28^\circ$ then we find that $S_y = 0.75S_z$. Looking at table 4.1 we see that $S_z = 9.9 \pm 1.4$, which means that the calculated value is $S_y^{\text{calc}} = 7.4 \pm 1.1$. This is in excellent agreement with the measured value $S_y^{\text{meas}} = 7.3 \pm 1.3$.

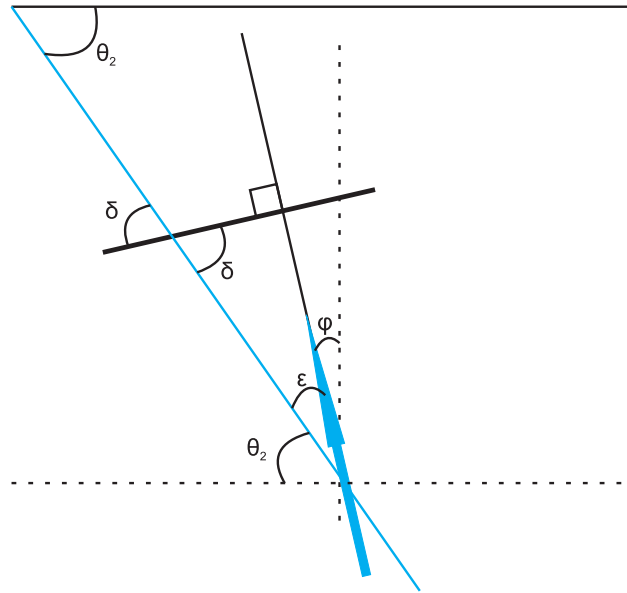


Figure 4.26: Definitions of the second set of angles used in analysis of the polarised neutron inelastic scattering data.

Following the same procedure for the polarised inelastic scattering at $\mathbf{Q} = (1.38, -0.5, 0)$, where this time the angle between the in-plane transverse component of the scattering and the wavevector is δ , and the wavevector makes an angle θ_2 with the a -axis, we find that

$$\epsilon = 90^\circ - (\phi + \theta_2), \quad (4.6)$$

$$\delta_+ = 90^\circ - \epsilon$$

$$= \phi + \theta_2,$$

$$\delta_- = \theta_2 - \phi, \quad (4.7)$$

and calculating S_y in the same way as before we find that $S_y^{\text{calc}} = 0.29 \cdot S_z = 2.17 \pm 0.31$. Again this is in excellent agreement with $S_y^{\text{meas}} = 2.4 \pm 1.1$.

4.4.2 Discussion of the Polarised Neutron Scattering Measurements

The main result presented in this chapter concerns the polarised diffraction data taken at $T = 10\text{K}$, which corresponds to the ordering of the Cu^{2+} moments. Although it has been shown that the data can be fitted quite well by assuming a stripe ordering model, it is useful to consider qualitatively several of the other proposed models of the spin-ordering in charge ordered materials such as LNSCO, and what polarised neutron diffraction features they predict.

Consider first the single domain of helically ordered spins shown in figure 4.5(a), corresponding to the spiral order proposed by Lindgård, which are described by a single wavevector $\mathbf{q} = (0.12, 0, 0)$. A pattern of spins orthogonal to the one shown, and with an orthogonal wavevector, is equally likely so the population of these two domains in a bulk sample should be the same. The measurements at $\mathbf{Q} = \mathbf{G} + (0.5, 0.5, 0) + (0.12, 0, 0)$, where \mathbf{G} is a reciprocal lattice vector, should all give rise to scattering of the same intensity (after form factor corrections). This is manifestly not the case for the data presented here. Furthermore, assuming the population of the two orthogonal domains was the same, all of the satellite peaks in any given magnetic zone should also have the same magnitude, which is also not observed. This means that such a pattern of ordered spins may be ruled out by the measurements presented here.

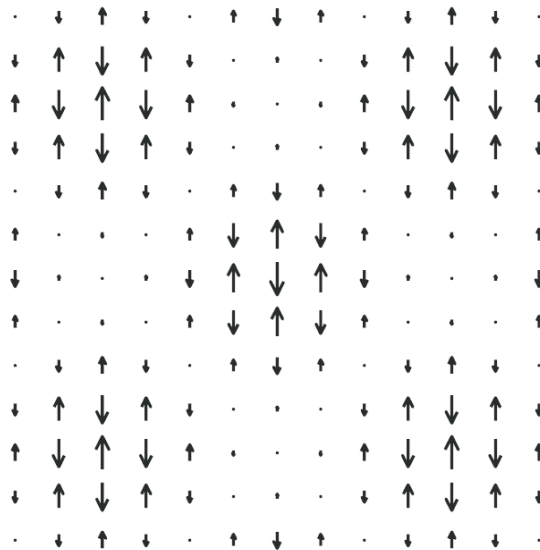


Figure 4.27: ‘Two- \mathbf{q} ’ magnetic ordering pattern, proposed by Fine [24].

Figure 4.27 shows another proposed ordering pattern of the spins, proposed by Fine [24], a collinear ‘two- \mathbf{q} ’ arrangement. In this case only a single domain is required to produce all four satellite peaks, because the pattern shown has the required periodicity in both the \mathbf{a} and \mathbf{b} directions. In this case one needs to consider pairs of measurements made in the same magnetic zone. For example let us consider the measurements at $\mathbf{Q} = (-0.38, 1.5, 0)$ and $\mathbf{Q} = (-0.5, 1.38, 0)$. The angle between these two scattering wavevectors is 5.7° , so the direction of the spins relative to the measurement wavevector is almost the same for both cases. Since there is only one domain the two wavevectors are measuring the same spins, and if the angle between the wavevectors is almost the same the angle between the spins

and the wavevector in each case is almost the same. This would give rise to almost equal intensity of the magnetic scattering, but for the wavevectors considered here the scattering is clearly much more intense at one wavevector than the other, and this observation means that we can immediately rule out this proposed spin ordering pattern.

Now consider the so-called π -spirals proposed by Silva-Neto [26], shown in figure 4.5(b). In this model the alternating rows of spins rotate alternately clockwise and anticlockwise, which is distinct from the model of Lindgård [25] where there is only one sense of rotation of the spins. The ordering pattern proposed by Lindgård provides peaks at the correct positions, $\mathbf{Q} = (1/2, 1/2) \pm (\delta, 0)$ and $\mathbf{Q} = (1/2, 1/2) \pm (0, \delta)$, provided there are two orthogonal chiral domains. If one were then to superpose another ordering pattern on this model then it should be possible to produce the π -spiral pattern. The required superposition is shown in figure 4.28. The wavevector of the upper structure is $\mathbf{Q}_1 = (1/2, 1/2) \pm (\delta, 0)$, whereas the lower structure has $\mathbf{Q}_2 = (1/2, 1/2) \pm (2\delta, 0)$. This gives four possible wavevectors, $Q_{A,B} = (1/2, 0) \pm (\delta, 0)$ and $Q_{C,D} = \pm(\delta, 0)$. In other words, if the π -spiral structure were correct then there would be additional magnetic Bragg peaks at these positions. Scans were performed using unpolarised neutrons at the $(0.38, 1)$ position, which corresponds to \mathbf{Q}_B , and there was no signal. This measurement proves that the π -spiral model cannot describe the ordering of spins in LNSCO.

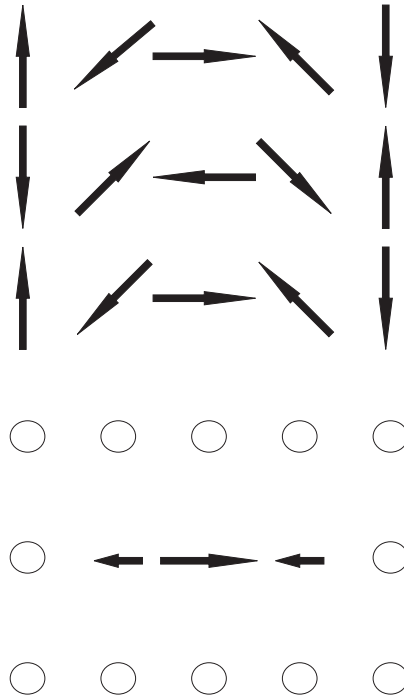


Figure 4.28: A coherent superposition of the two patterns shown would generate the π -spiral pattern. Circles denote zero spin, and the central spin is twice as large as the other two shown.

The qualitative inspection and quantitative analysis of the data presented thus far rule out all but three possibilities for the pattern of the spins in this material. The first model that is not ruled out is the stripe model, with the proviso that there exist an equal population of orthogonal domains. To reiterate a point that was made in section 4.1, it has been proposed that these orthogonal domains exist in adjacent CuO_2 planes, that is to say that the stripes are stacked orthogonally along the c -axis. Another model with which the data are consistent

is one particular kind of checkerboard order, shown in figure 4.29, which is in fact a coherent superposition of the two orthogonal stripe domains. Such a model has the interesting feature of a 90° rotation of spins across the charge domain wall. The interaction between spins across the domain wall would certainly not have a simple form for such an ordering pattern to arise. A third model has been proposed [23], subsequent to the publication of the results described here [35], to describe these data. It bears many similarities to the second model, however in this model the nature of the charge order is very different, so that the magnetic domain walls described above do not exist. Instead of stripes or checkerboards of charge, the charge is localised at single points in the CuO_2 planes, and the spins are then organised in a so-called ‘vortex lattice’. Two such vortex lattices are shown in figure 4.30, describing situations where the charge is centred on Cu sites or on Cu-O bonds respectively. This model is in fact another possible result of a coherent superposition of an equal number of domains of orthogonal stripes, but with the difference that the charge stripes shown in figure 4.29 are assumed not to exist.

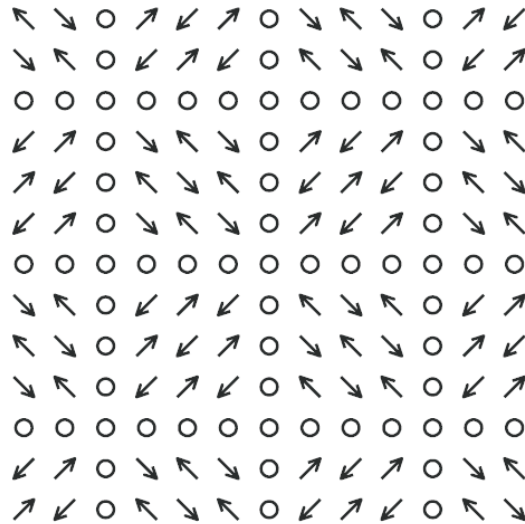


Figure 4.29: A coherent superposition of two stripe domains, which would give an equivalent diffraction pattern.

The diffraction data cannot provide any further information that would allow one to distinguish between these three models, since they must give rise to the same diffraction features because they are all superpositions of the stripe model. Indeed the inelastic scattering data, taken at face value, cannot provide any further clues as to which model is likely to be correct, since the inelastic scattering in all three models would also be a coherent superposition of two stripe domains. One can, however, consider the plausibility of the simple spin wave model used to analyse effectively the inelastic scattering data. For the stripe model, with nearest neighbour spins that are arranged antiferromagnetically, simple spin waves would seem to be the most obvious way for the system to be excited and the data bear out such an interpretation. Such a simple interpretation may not, however, be applicable to the more complicated ordering patterns shown in the other two models. However, no stronger statement than this may be made in the absence of further evidence and/or theoretical predictions of the microscopic properties (including the magnetic excitations) of

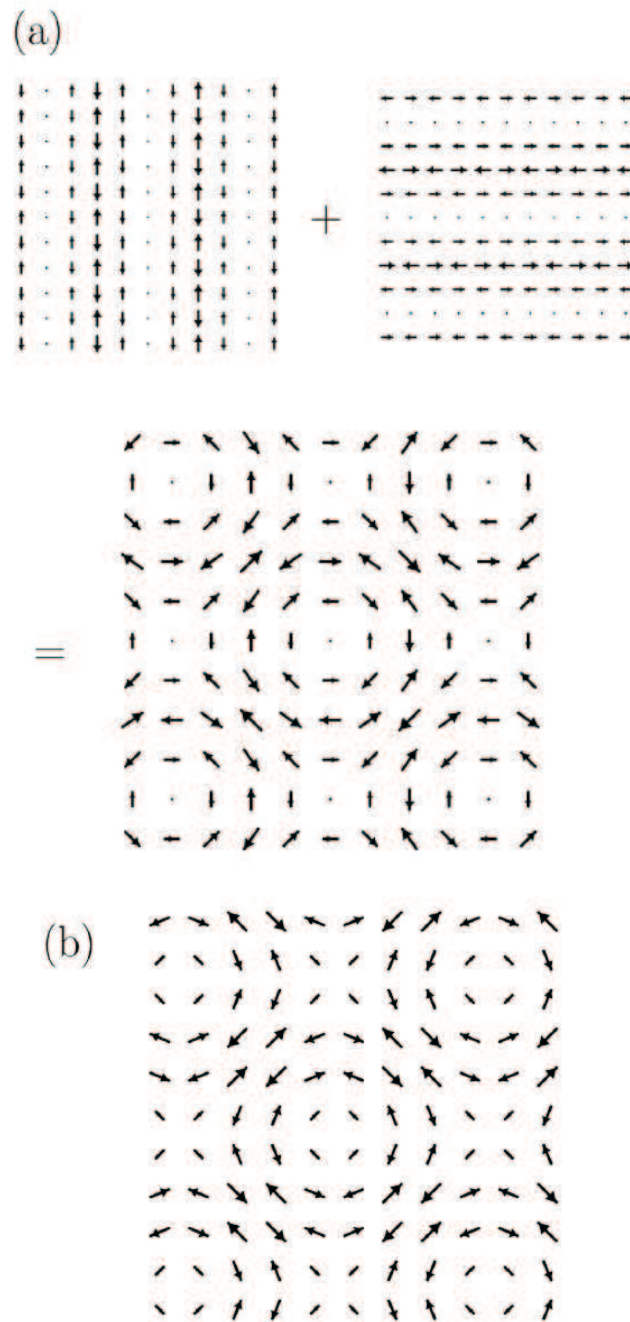


Figure 4.30: (a) Site centred charge with a vortex spin lattice, (b) Bond centred charge with a vortex spin lattice, as proposed by B.V. Fine [23].

the non-stripe models.

4.4.3 Analysis and Discussion of the Unpolarised Neutron Scattering Measurements

The measurement at $\mathbf{Q} = (0.5, 0.38, 0)$ with $T = 2\text{ K}$ shows that there is an energy gap in the excitations of the spins in LNSCO. The size of this gap seems to be temperature dependent,

reducing from 3meV to 1meV as the temperature is increased from 2 K to 10 K. At 35 K the gap is lower than 1meV, but because there are no measurements at sufficiently low energies for this temperature it is not possible to say by how much it has reduced, or even whether it has disappeared.

The cause of the gap, and its temperature dependence, are not immediately obvious. However one possible explanation is that the spin fluctuations are anisotropic. It is common in strongly correlated electron systems for different components of the spin fluctuations to have different energy gaps (so-called anisotropy gaps). This is because of single-ion anisotropy, which arises due to quenching of the orbital moments by the crystal field, which has the same symmetry as the lattice. The effect is felt by the spin excitations due to spin-orbit coupling, resulting in magnetic moments that preferentially lie along a particular direction, and which must be supplied with a fixed amount of energy before they can support spin waves. Another possible cause of the gap is that there is some coupling between the excited Cu^{2+} spins and the Nd^{3+} spins which are introduced into the material in order to stabilise the LTT crystallographic phase below 70 K. The polarised neutron diffraction measurements described in section 4.3.1 showed that the Nd moments order at low temperature ($T \leq 3$ K) such that the moments point along the c -axis. This magnetic anisotropy could cause the excitations parallel to the c -axis to be more favourable at low temperatures than excitations in the ab -plane.

The most straightforward way to test the hypothesis of an anisotropy-related gap would be to conduct a polarised neutron inelastic scattering experiment, and repeat the fixed- \mathbf{Q} energy scans at several temperatures. Polarisation analysis would allow the various components of the fluctuations to be determined individually and the anisotropy measured. Such a measurement was the original intention of the polarised neutron measurements described in this chapter, however it was soon realised that the counting times required to do the experiment with polarised neutrons would be prohibitively long due to the much-reduced flux of the polarised neutron spectrometer IN20 compared to unpolarised neutron instruments.

By using two different crystal orientations in an unpolarised neutron scattering experiment, it is possible to resolve partially the spin fluctuation components of the scattering. This can be done because the magnetic part of the unpolarised cross-section is not sensitive to any component of an excitation parallel to the scattering wavevector. As stated in section 4.3.2 scattering at $\mathbf{Q} = (0.5, 0.38, 4.5)$ is largely sensitive to the components of the spin fluctuations in the ab -plane, whereas scattering at $\mathbf{Q} = (0.5, 0.38, 0)$ is sensitive to the out-of-plane component of the spin fluctuations, plus the in-plane component perpendicular to \mathbf{Q} .

A qualitative inspection of the data suggests that there is some degree of anisotropy, simply because the shape of the fixed- \mathbf{Q} energy scans at different wavevectors behave so differently as a function of energy. A more quantitative approach can be made by assuming that the statically ordered moments are oriented according to the results of the polarised neutron diffraction analysis. The scattering at $\mathbf{Q} = (0.5, 0.38, 0)$ ($L = 0$), shown in figure 4.16, comprises components of the fluctuations that are perpendicular to \mathbf{Q} , i.e. along unit vectors \mathbf{v}_1 and \mathbf{v}_2 which are parallel to $(0, 0, 1)$ and $(0.38, -0.5, 0)$ respectively. If we assume that in the low energy regime the fluctuations are purely transverse to the ordered moment direction (semi-classical spin-waves), and we know the direction of the ordered moment, then we also know two vectors perpendicular to it - one of which is out of the plane (we are free to choose this) and the other is in the plane. The polarisation of the spin fluctuations can

be completely described by these two vectors, and hence the projection of these two vectors on to \mathbf{v}_1 and \mathbf{v}_2 can be calculated. It is the sum of these two projections that is measured by the unpolarised magnetic scattering cross-section.

Explicitly, for the case of $L = 0$:

$$\mathbf{S} = (-\sin 28, \cos 28, 0)S_{\text{in-plane}} + (0, 0, 1)S_z, \quad (4.8)$$

and the quantity measured in the inelastic scattering measurements is

$$\frac{d\sigma}{d\Omega} \propto ((\mathbf{S} \cdot \mathbf{v}_1)^2 + (\mathbf{S} \cdot \mathbf{v}_2)^2). \quad (4.9)$$

For the $L = 0$ case the terms in equation 4.9 are given by

$$(\mathbf{S} \cdot \mathbf{v}_1)^2 = S_z^2, \quad (4.10)$$

$$(\mathbf{S} \cdot \mathbf{v}_2)^2 = 0.985S_{\text{in-plane}}^2. \quad (4.11)$$

However there is also an equal population of spins at an angle of -28° to the principal axis. The vector describing these spins is given by

$$\mathbf{S}_- = (\sin 28, \cos 28, 0)S_{\text{in-plane}} + (0, 0, 1)S_z, \quad (4.12)$$

so performing the same analysis for this group of spins and averaging the two intensities we finally arrive at

$$\frac{d\sigma}{d\Omega}_{L=0} \propto 0.566S_{\text{in-plane}}^2 + S_z^2. \quad (4.13)$$

For the case of $L=4.5$, we get, following the same procedure

$$\frac{d\sigma}{d\Omega}_{L=4.5} \propto 0.992S_{\text{in-plane}}^2 + 0.031S_z^2. \quad (4.14)$$

Equations 4.13 and 4.14 can be solved simultaneously for $S_{\text{in-plane}}^2$ and S_z^2 . The result of manipulating the data accordingly is shown in figure 4.31. This measurement seems to suggest that above about 2.5meV the in-plane component of the fluctuations becomes much larger than the out-of-plane component. The out-of-plane component apparently tends to zero for $E \geq 3\text{meV}$. This cannot be reconciled with the results of the polarised inelastic measurements, shown in table 4.1 – indeed those measurements appear to give almost the opposite result! The most obvious reason for the discrepancy is that the three-point method used to calculate the peak intensity did not work. For example if a small amount of spurious scatter was present in the background signals for the higher energies at $L = 0$ then the signal there might be anomalously low and result in the effect seen in figure 4.31.

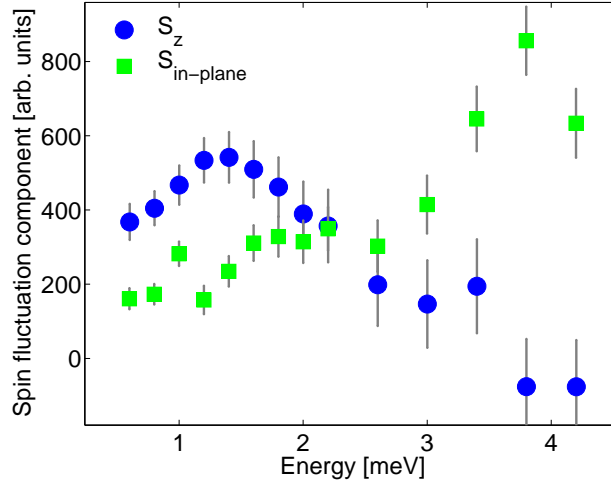


Figure 4.31: The in-plane and out-of-plane components of the spin fluctuations, determined from unpolarised neutron scattering. $T = 35$ K.

4.4.4 Analysis and Discussion of the X-ray Diffraction Measurements

In section 4.3.3 non-resonant x-ray diffraction measurements of a superlattice which is present in both LNSCO and LBCO were presented. The existence of this superlattice has been attributed to a periodic structural distortion of the crystal lattice which is induced by a periodic modulation of the charge density within the CuO_2 planes. In section 4.1 the possibility that this charge order may be influenced by superconductivity and/or the existence of a vortex lattice was mooted. The measurements presented in section 4.3.3 clearly demonstrate, however, that the charge order is not affected by the presence of a vortex lattice.

In a superconductor in the vortex phase magnetic flux penetrates the bulk of the sample, however this flux is quantised and forms a so-called flux line lattice. The flux quantum is given by

$$\Phi = \frac{h}{2e} = 2.068 \times 10^{-15} \text{ Wb}, \quad (4.15)$$

so that the flux density penetrating the sample is $B = N\Phi$, where N is the number of fluxoids per unit area. Now if the flux forms a triangular lattice comprising equilateral triangles of side L then it is obvious that

$$\begin{aligned} \frac{\sqrt{3}}{4}L^2 &= \frac{1}{N} = \frac{\Phi}{B} = \frac{h}{2eB}, \\ L &= \left(\frac{h}{eB} \frac{2}{\sqrt{3}} \right)^{1/2}. \end{aligned} \quad (4.16)$$

For an applied magnetic field of 10 T this gives $N = 4.836 \times 10^{15} \text{ m}^{-2}$, i.e. $L = 219 \text{ \AA}$. For the case of LNSCO and LBCO this translates as $L \approx 58$ unit cells. This can be compared

with the widths of the charge order peaks shown in fig. 4.17 and fig. 4.18, which correspond to the inverse correlation length of the charge order. For the case of LBCO, the peak width is 0.012 r.l.u, giving a correlation length of 315 Å or about 83 unit cells. This tells us that in the highest applied field there is, on average, at least one flux-line penetrating each domain of correlated charge so that if there was an interaction between this flux-line and the charge then x-ray diffraction could in principle be used to measure it.

Theoretical studies [38, 39] have shown that the existence of a vortex core causes nearby stripe order to be stabilised, both in terms of the spin order and the charge order. Neutron scattering experiments by Chang *et al* [40] on the spin stripe peaks in $\text{La}_{2-x}\text{Sr}_x\text{CuO}_4$ (LSCO) at different doping fractions have shown that the presence of a large enough magnetic field gives rise to the appearance of static spin order, where in the absence of an applied field the spins were not ordered in such a pattern. These results would seem to tie in with the theoretical predictions mentioned above, so that fluctuating stripes become statically correlated. In the same neutron scattering study Chang *et al* present similar measurements on LNSCO. There it was found that an applied field of up to 15 T had no effect on the spin stripe order at $T = 15$ K, unlike in LSCO. If one takes the degree of spin stripe order and the degree of charge stripe order to be inherently connected then this result would tie in with the measurements presented here, that the stripes are not affected by the presence of an applied magnetic field.

A possible explanation for this lies in the theoretical prediction that vortex cores stabilise stripes. The theory assumes that any other interactions that might drive the formation of stripes are not sufficiently strong to give rise to static stripes in the absence of vortex cores, which would be an accurate description of the situation in LSCO. However in LNSCO there *are* stripes in zero applied field, indeed they are correlated over quite a long range, so although the interaction that makes vortex cores stabilise stripes may still exist in this material, its effect is not seen because stripes exist already. The vortex interaction may, perhaps, cause stripes to be correlated over a slightly longer range. Indeed this could well explain the results of Jungho Kim *et al* [31] who observe a very slight narrowing of the charge order peaks in their sample of LBCO in an applied field of 10 T. However if the correlation length of the stripe order is already determined in zero field by intrinsic properties of the material such as impurities or oxygen stoichiometry, then the presence of the vortex cores may well make the stripe phase more stable but the effect would not be measurable. It is this latter situation, therefore, that probably accounts for the measurements presented in this work, on both the LBCO and the LNSCO samples.

The effect of superconductivity on charge order is less clear. In figures 4.21 and 4.22 it appears that in the lower temperature range, where for these particular samples superconductivity was extant, the charge order might become correlated over a slightly longer range, evidenced by a very small reduction in the peak width. This change of width is, however, smaller than the error bars on the measurements so it is not possible to be entirely certain that the effect is real and not just due to statistics. Indeed, if the charge order were to become correlated over a longer range one might expect the intensity of the scattering to increase, and figures 4.19 and 4.20 show that, within the error bars, this does not occur. Indeed the intensity at temperatures below $T_c \approx 10$ K may actually be somewhat lower than that at higher temperatures, e.g. around 20 K.

This result is somewhat surprising, because one might expect that when superconductivity occurs the charge carriers would become paired and delocalised. If, just above T_c , all

of the charge is localised in stripes, say, then it would seem logical that just below T_c some of the charge would be removed from these stripes and hence the order would extend over a shorter length scale, resulting in a lower peak intensity and an increased peak width. This is at variance with what is actually observed. A possible alternative explanation might be that in the stripe phase the localised charges experience Coulomb repulsion from the surrounding localised charges. The energy of such an interaction may not be high enough to destabilise the stripe phase. On cooling below T_c some charge is removed from the stripes so the Coulomb repulsion energy would be lowered, resulting in a more stable stripe phase with a longer correlation length. The intensity of the structural distortion peak is proportional to the Coulomb interaction between the stripes and the lattice, so if charge is removed from the stripes then this Coulomb interaction would be weaker, resulting in a reduction in intensity.

4.5 Conclusions

In conclusion the results presented here have provided new information on several different aspects of the charge and magnetic order, and dynamics in two copper-oxide superconductors at 1/8 doping.

The spin order found in LNSCO using polarised neutrons was consistent with stripe order, but ruled out several more exotic types of chiral order. There remain two possible structures not ruled out by the data – a coherent superposition of two orthogonal stripe domains, and a checkerboard model in which there is a periodic vortex-like arrangement of spins centred on localised charge.

Unpolarised neutron measurements of LNSCO show that there is a gap in the low energy spin excitations, the magnitude of which decreases with increasing temperature. Polarised neutron measurements were unable to shed light on the nature of any anisotropies in the fluctuations due to very low neutron count rates. Unpolarised neutron scattering measurements with the crystal in different orientations showed that the in-plane fluctuation spectrum is different to that of the out-of-plane spectrum.

X-ray measurements of the structural distortions induced by the presence of a periodic charge order were performed on LNSCO and LBCO. In both materials no change was observed in either the intensity of the scattering, or width of the peaks, at low temperatures when a magnetic field was applied parallel to the c -axis, establishing a vortex lattice. This can be explained if the length scale over which charge order exists is already limited by other effects, because theoretical studies have suggested that the presence of a vortex lattice should help to stabilise charge stripe order. There is circumstantial evidence that superconductivity has a small effect on the charge order, which might be explained by some of the localised charge becoming delocalised when it participates in superconductivity.

There are several possibilities for future measurements on LNSCO and LBCO. Soft x-ray measurements could be performed on both materials in order to measure directly the charge order and establish its symmetry. Anisotropies in the excitation spectrum of LNSCO could be investigated further, either by performing careful absorption corrections whilst using the same sample as before, or by growing a larger series of samples with similar shapes and repeating the existing measurements.

References

- [1] J. G. Bednorz, and K. A. Müller, *Z. Phys. B* **64**, 189 (1986).
- [2] A. R. Moodenbaugh, Y. Xu, M. Suenaga, T. J. Folkerts, and R. N. Shelton, *Phys. Rev. B* **38**, 4596 (1988).
- [3] P. G. Radaelli, D. G. Hinks, A. W. Mitchell, B. A. Hunter, J. L. Wagner, B. Dabrowski, K. G. Vandervoort, H. K. Viswanathan, and J. D. Jorgensen, *Phys. Rev. B* **49**, 4163 (1994).
- [4] Yimei Zhu, A. R. Moodenbaugh, Z. X. Cai, J. Taftø, M. Suenaga, and D. O. Welch, *Phys. Rev. Lett.* **73**, 3026 (1994).
- [5] J. -S. Zhou, and J. B. Goodenough, *Phys. Rev. B* **56** 6288 (1997).
- [6] Y. Nakamura and S. Uchida, *Phys. Rev. B* **46**, 5841 (1992)
- [7] Y. Liu, and X. G. Li, *J. Appl. Phys.* **99**, 053903 (2006).
- [8] J. M. Tranquada, B. J. Sternlieb, J. D. Axe, Y. Nakamura and S. Uchida, *Nature (London)* **375**, 561 (1995).
- [9] T. Noda, H. Eisaki, and S. -I. Uchida, *Science* **286**, 265 (1999).
- [10] R. Saito, N. Tsujia, T. Katoa, T. Machidaa, T. Noguchia, and H. Sakata, *Physica C* **460**, 878 (2007).
- [11] B. Büchner, M. Breuer, M. Cramm, H. Micklitz, W. Schlabitz and A. P. Kampf, *J. Low Temp. Phys.* **95**, 285 (1994).
- [12] J. M. Tranquada, J. D. Axe, N. Ichikawa, Y. Nakamura, S. Uchida and B. Nachumi, *Phys. Rev. B* **54**, 7489 (1996).
- [13] J. M. Tranquada, N. Ichikawa and S. Uchida, *Phys. Rev. B* **59**, 14712 (1999).
- [14] T. R. Thurston, R. J. Birgeneau, M. A. Kastner, N. W. Preyer, G. Shirane, Y. Fujii, K. Yamada, Y. Endoh, K. Kakurai, M. Matsuda, Y. Hidaka and T. Murakami, *Phys. Rev. B* **40**, 4585 (1989).
- [15] S. -W. Cheong, G. Aeppli, T. E. Mason, H. Mook, S. M. Hayden, P. C. Canfield, Z. Fisk, K. N. Clausen and J. L. Martinez, *Phys. Rev. Lett.* **67**, 1791 (1991).
- [16] T. R. Thurston, P. M. Gehring, G. Shirane, R. J. Birgeneau, M. A. Kastner, Y. Endoh, M. Matsuda, K. Yamada, H. Kojima and I. Tanaka, *Phys. Rev. B* **46**, 9128 (1992).

- [17] T. E. Mason, G. Aeppli and H. A. Mook, *Phys. Rev. Lett.* **68**, 1414 (1992).
- [18] K. Yamada, C. H. Lee, K. Kurahashi, J. Wada, S. Wakimoto, S. Ueki, H. Kimura, Y. Endoh, S. Hosoya, G. Shirane, R. J. Birgeneau, M. Greven, M. A. Kastner and Y. J. Kim, *Phys. Rev. B* **57**, 6165 (1998).
- [19] J. D. Axe and M. K. Crawford, *J. Low Temp. Phys.* **95**, 271 (1994).
- [20] M. v. Zimmermann, A. Vigliante, T. Niemöller, N. Ichikawa, T. Frello, J. Madsen, P. Wochner, S. Uchida, N. H. Anderson, J. M. Tranquada, D. Gibbs, and J. R. Schneider, *Europhys. Lett.* **41**, 629 (1998).
- [21] B. Nachumi, Y. Fudamoto, A. Keren, K. M. Kojima, M. Larkin, N. Ichikawa, M. Goto, H. Takagi, S. Uchida, M. K. Crawford, E. M. McCarron, D. E. MacLaughlin, and R. H. Heffner, *Phys. Rev. B* **58**, 8760 (1998).
- [22] H. -D. Chen, J. -P. Hu, S. Capponi, E. Arrigoni and S. -C. Zhang, *Phys. Rev. Lett.* **89**, 137004 (2002).
- [23] B. V. Fine, *Phys. Rev. B* **75**, 060504 (2007).
- [24] B. V. Fine, *Phys. Rev. B* **70**, 224508 (2004).
- [25] P Lindgård, *Phys. Rev. Lett.* **95**, 217001 (2005).
- [26] M. B. Silva Neto, *Phys. Rev. B* **76**, 033103 (2007).
- [27] M. Ito, Y. Yasui, S. Iikubo, M. Soda, M. Sato, A. Kobayashi, and K. Kakurai, *J. Phys. Soc. Jpn.* **72**, 1627 (2003); M. Ito, Y. Yasui, S. Iikubo, M. Soda, A. Kobayashi, M. Sato, K. Kakurai, C. -H. Lee, and K. Yamada, *J. Phys. Soc. Jpn.* **73**, 991 (2004).
- [28] S. A. Kivelson, I. P. Bindloss, E. Fradkin, V. Oganesyan, J. M. Tranquada, A. Kapitulnik, and C. Howald, *Rev. Mod. Phys.* **75**, 1201 (2003).
- [29] S. Wakimoto, R. J. Birgeneau, Y. Fujimaki, N. Ichikawa, T. Kasuga, Y. J. Kim, K. M. Kojima, S. -H. Lee, H. Niko, J. M. Tranquada, S. Uchida, and M. v. Zimmermann, *Phys. Rev. B* **67**, 184419 (2003).
- [30] M. Fujita, H. Goka, K. Yamada, J. M. Tranquada, and L. P. Regnault, *Phys. Rev. B* **70**, 104517 (2004).
- [31] J. Kim, A. Kagedan, G. D. Gu, C. S. Nelson, T. Gog, D. Casa, and Y. -J. Kim, *cond-mat/0703265* (2007).
- [32] Y. -J. Kim, G. D. Gu, T. Gog, and D. Casa, *Phys. Rev. B* **77**, 064520 (2008).
- [33] P. Abbamonte, A. Rusydi, S. Smadici, G. D. Gu, G. A. Sawatzky, and D. L. Feng, *Nature Physics* **1**, 155 (2005).
- [34] *Phase Transformations in Metals and Alloys*, D. A. Porter, and K. E. Easterling, CRC Press (1992).

- [35] N. B. Christensen, H. M. Rønnow, J. Mesot, R. A. Ewings, N. Momono, M. Oda, M. Ido, M. Enderle, D. F. McMorrow, and A. T. Boothroyd, *Phys. Rev. Lett.* **98**, 197003 (2007).
- [36] J. A. Robertson, S. A. Kivelson, E. Fradkin, A. C. Fang, and A. Kapitulnik, *Phys. Rev. B* **74**, 134507 (2006).
- [37] http://www.ill.eu/fileadmin/users_files/static/ccsl/html/ccsl/doc.html
- [38] M. Ichioka, M. Takigawa, and K. Machida, *J. Phys. Soc. Jpn.* **70**, 33 (2001).
- [39] Y. Chen, H. Y. Chen, and C. S. Ting, *Phys. Rev. B* **66**, 104501 (2002).
- [40] J. Chang, Ch. Niedermayer, R. Gilardi, N. B. Christensen, H. M. Rønnow, D. F. McMorrow, M. Ay, J. Stahn, O. Sobolev, A. Hiess, S. Pailhes, C. Baines, N. Momono, M. Oda, M. Ido, and J. Mesot, *cond-mat/07122181* (2007).

Chapter 5

Neutron Scattering Measurements of LaCoO_3

Neutron scattering measurements were performed on LaCoO_3 in order to probe the nature of its thermally excited spin state. Very broad dispersive magnetic excitations were found to be extant throughout the Brillouin zone, reminiscent of those observed in ferromagnets above their critical temperatures. Analysis of these excitations allowed an upper limit on a possible ferromagnetic interaction strength to be determined. Analysis of the temperature dependence of the excitations was unable to differentiate between proposed models of the excited spin state.

5.1 Introduction

LaCoO_3 is a semiconductor that has been of interest for many years due to its peculiar magnetic properties. The ground state, measured at low temperatures, is non-magnetic however as the material is warmed the magnetic susceptibility steadily increases, reaching a maximum at about 100 K. As the temperature is increased further the susceptibility gradually decreases following a Curie law type behaviour. The behaviour of the susceptibility then deviates from this above about 400 K, becoming slightly larger than expected from the Curie law alone. The magnetic susceptibility, as measured by English *et al* [1] is shown in figure 5.1.

This behaviour is somewhat surprising, because the Co^{3+} ions have the $3d^6$ configuration, for which Hund's rules predict a ground state with $S = 2$. It is therefore clear that this is a material in which the competition between the intra-atomic exchange and the crystal field determines the magnetic properties. The general principles to explain the unusual magnetism observed in LaCoO_3 are broadly agreed upon – the Co^{3+} ions have a ground state with $S = 0$, and there is an energy gap between this state and excited states that have $S \neq 0$. As the material is warmed the magnetic excited state(s) are thermally populated, so that increasing temperature leads to an increased number of magnetic ions. However there is a trade-off between the increase in susceptibility that results from this thermal population, and the thermally induced fluctuations of the ions in the magnetic state that act to reduce the susceptibility according to the Curie law. It is this trade-off which results in the susceptibility rising to a maximum before decreasing again on warming.

Measurements of the electrical resistivity show that this decreases with increasing temperature [1], and its behaviour is consistent with a semiconducting gap of about 38 meV for

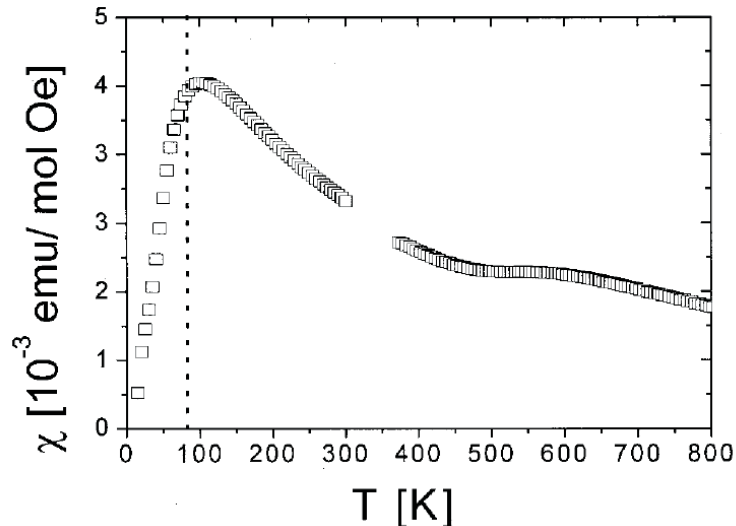


Figure 5.1: After English *et al* [1], the magnetic susceptibility of LaCoO_3 as a function of temperature. Van-Vleck and impurity contributions to the susceptibility have been subtracted from these data.

$T \leq 80$ K, and a larger gap of about 146 meV for $T \geq 120$ K. These energy gaps correspond to temperatures of 440 K and 1700 K respectively. Measurements of the optical conductivity [2] have shown that the indirect semiconducting gap is about 1.1 eV, however the transition is rather broad in energy, with a noticeable rise in the conductivity as low as 0.1 eV.

LaCoO_3 crystallises in the rhombohedral space group $R\bar{3}c$, in which its lattice parameter $a \approx 5.43$ Å and lattice angle $\alpha \approx 60.8^\circ$. The lattice can be regarded as a slightly distorted cubic lattice, with pseudo-cubic¹ lattice parameters $a \approx 3.8$ Å and $\alpha = 90^\circ$, and the crystalline environment of the Co^{3+} ions is therefore very close to being octahedral. An octahedral crystal field would split the $3d$ orbitals into t_{2g} and e_g states, with the former at a lower energy [3]. In the non-magnetic state the Co^{3+} is in the t_{2g}^6 configuration, whereas in the magnetic state one or more electrons are excited into the e_g states.

The delicate balance of the various interactions in LaCoO_3 means that the nature of the magnetic excited state is not immediately obvious. A simple view is that there exists competition between the crystal field and the L-S coupling (parameterised by Hund's rules), which would mean that the excited state has $S = 2$. Indeed this view prevailed for many years after the physical properties of LaCoO_3 were first measured. For example Raccah and Goodenough [4] were able to model successfully the behaviour with temperature of the conductivity, magnetic susceptibility and structural parameters assuming a high-spin (HS, $S = 2$) model.

More recently, however, such interpretation has been cast into doubt. LDA+U calculations by Korotin *et al* [5] predict an excited state with $S = 1$, which has been called intermediate-spin (IS). The IS state is favoured by the LDA+U calculation because there is a strong hybridisation between the Co e_g levels and the O $2p$ levels which lowers the IS energy relative to that of the HS state. Subsequently measurements of susceptibility, thermal expansion [6, 7], photoemission spectroscopy, x-ray absorption spectroscopy [8], and infra-red spectroscopy [9] were all interpreted using models with an IS excited state, where

¹See appendix B.

at higher temperatures a HS state is thermally populated, or the orbital degeneracy of the IS state increases, to account for the semiconductor-metal transition.

Several predictions were made by the calculations of Korotin *et al* [5], in addition to the existence of the IS state. The IS state was predicted to be metallic and the HS state semiconducting, at variance with experimental observations. It was suggested that this may be an artifact of the calculation, because the existence of long-range spin order was assumed. It was also predicted that an orbitally ordered state is energetically favoured in the IS state.

The low-spin (LS) non-magnetic ground state is not Jahn-Teller active because it is orbitally non-degenerate [10]. The proposed IS and HS states, however, do possess orbital degeneracy and therefore would be Jahn-Teller active. X-ray diffraction measurements on powder and single crystal samples [11] in the temperature range $95 \leq T \leq 295$ K have shown lattice distortions attributed to Jahn-Teller distortions, in agreement with measurements of the susceptibility [6] and infra-red spectroscopy [9] which find that the thermally excited spin states are orbitally non-degenerate.

Neutrons can probe magnetism on an atomic scale, so neutron scattering is an obvious choice of technique to investigate the interplay of effects that determine the spin state in LaCoO_3 . The simplest experiment to confirm the existence of a HS or IS first excited state would be to use inelastic scattering to excite electrons directly from the LS state, since the HS state would preclude such transitions whereas the IS would not, provided that the LS-IS scattering matrix element is non-zero. Evidence for such a transition, from the LS to IS state at $T = 8$ K, was presented by Kobayashi *et al* [12], who used unpolarised neutrons and therefore had to perform quite complicated corrections to their data in order to subtract the non-magnetic scattering from the signal. The energy gap between the LS and IS state determined by this method was found to give rise to a broad peak centred around 20 meV at the ferromagnetic wavevector $\mathbf{Q}_{FM} = (1, 0, 0)$ in pseudo-cubic notation. Recently, however, measurements using polarised neutrons [13] have failed to confirm these results, indeed finding no magnetic signal at either ferromagnetic or antiferromagnetic wavevectors at low temperature. This has cast doubt on the background subtraction procedure used by Kobayashi *et al*, and it seems that a direct transition from the ground state is not observable, which would suggest either that the first excited state is high-spin, or that the LS-IS transition matrix element is too small to make the transition observable.

Neutrons can also be used to probe the magnetism within the excited spin state, and several studies have already been performed to examine different aspects of this. An early measurement by Asai *et al* [14] used polarised and unpolarised neutrons to measure the diffuse quasi-elastic scattering around the pseudo-cubic wavevector $(1, 0, 0)$, the scattering corresponding to short range ferromagnetic correlations. They found reasonable agreement between the local moment calculated from susceptibility measurements and the intensity of the scattering as a function of temperature. A later work by Asai *et al* [15] measured the same scattering at higher temperatures, and found a gradual decrease in intensity at the ferromagnetic wavevector above about 300 K, with no abrupt changes near 500 K, the temperature at which anomalies have been observed in the bulk susceptibility and conductivity. Plakhty *et al* [16] conducted detailed polarised neutron diffraction measurements on a single crystal in an applied magnetic field of 5.8 T in order to determine the local moments on the Co^{3+} ions. They found that their measurements were consistent with an IS first excited state, although the uncertainty on some of the fit parameters used was quite high.

Two groups have used unpolarised neutrons to examine the low energy excitations in LaCoO₃ [17, 18], using powder samples. Both studies found that there exists an excitation at $E \approx 0.6$ meV in the temperature range $25 < T < 100$ K, however the interpretations differed. Phelan *et al* [17] performed measurements on a single crystal and a powder sample, and found that the 0.6 meV excitation could be discerned for $T > 100$ K at both ferromagnetic $Q_{FM} = (0, 0, 1.1)$ and antiferromagnetic $Q_{AFM} = (0, 0.5, 0.5)$ wavevectors². They interpreted their data as showing that there exists an orbital contribution to the magnetic correlations within an IS state. Podlesnyak *et al* [18] measured the 0.6 meV excitation in a powder sample only, however they additionally measured the neutron inelastic scattering with an applied magnetic field of 6 T. The latter measurement showed a shift in the excitation energy to $E \approx 1.5$ meV which was consistent with a g -factor of about 3, which is interpreted as arising either from a HS triplet excited state with a weak splitting due to small trigonal distortions from cubic symmetry³, or a IS triplet excited state with a much larger trigonal distortion.

The suggestion by Phelan *et al* [17] of orbital correlations in LaCoO₃ is based on an analogy with LaMnO₃, which has the spin state $t_{2g}^3 e_g^1$. This spin state is Jahn-Teller active and orbital ordering of the e_g states results, in turn giving rise to A-type antiferromagnetic order, which corresponds to ferromagnetic coupling within the ab -plane, and antiferromagnetic coupling between planes. Phelan *et al* argue that similar orbital ordering occurs in LaCoO₃, but that this order is not static, and hence leads to dynamic magnetic correlations with a short range.

Both of these neutron scattering experiments are consistent with an electron spin resonance (ESR) measurement by Noguchi *et al* [19], who found a g -factor of 3.35 and a uniaxial crystal field splitting of 0.6 meV. They point out that such a g -factor is almost identical to that of Fe²⁺ in MgO, which is a $3d^6$ paramagnetic system in a HS state within an octahedral crystal field environment [20].

Subsequent to all of the bulk and microscopic measurements described thus far, soft x-ray absorption spectroscopy and magnetic circular dichroism measurements have been interpreted as arising from a HS first excited state [21], provided that the gap between the ground state and the excited states is temperature dependent.

5.1.1 Motivations

Despite many experimental and theoretical studies, there remains much controversy surrounding the excited spin states of LaCoO₃. Until now it has not been possible to use polarised neutrons to examine this material, other than to use diffraction to determine that there is no static magnetic order. Recent improvements to the IN20 spectrometer, together with the high neutron flux available at the ILL [22], mean that it is now possible to measure the magnetic excitations. This offers the possibility of probing the dynamic magnetic correlations, and possibly determine the strength and type of coupling between spins in the excited state. This can, in turn, be used to shed light on the nature of the excited spin state.

²The offset was used at the FM wavevector to avoid contamination of the unpolarised signal by the tail of the structural Bragg peak.

³A trigonal distortion of an octahedron from cubic symmetry is one which preserves the 3-fold symmetry.

5.2 Experimental details

In order to measure the magnetic scattering in LaCoO_3 definitively, something that has not yet been done, polarised neutrons must be used in order to separate out the magnetic and non-magnetic scattering. We chose to use the IN20 polarised triple-axis spectrometer (TAS) at ILL for these measurements due to the fact that it has the highest flux of any polarised spectrometer in the world. Additional measurements were subsequently performed on the IN8 unpolarised thermal neutron TAS.

The IN20 spectrometer was used in the standard fully polarised mode (i.e. Heusler monochromator and analyser, Helmholtz coils at the sample position, etc.), a description of which is given in section 2.1.2. On the IN8 spectrometer a silicon monochromator was used, with a graphite analyser and a PG filter in the scattered beam between the sample and the analyser. On both spectrometers the samples were mounted in a standard orange cryostat.

The experiments used both $k_f = 2.662 \text{ \AA}^{-1}$ and $k_f = 4.1 \text{ \AA}^{-1}$, the former being used in preference for its better resolution in wavevector-energy space, although the latter was used for higher excitation energies where constraints of the scattering geometry made its use necessary.

Two different samples were used for the measurements detailed in this chapter. One sample was grown in Oxford by Dr. D. Prabhakaran using the floating zone technique, and the other was grown using the same method in Cologne [23]. For one of the IN20 experiments, and for the IN8 experiment, the rod-shaped Oxford sample was used (mass=18.25 g, length 40.6 mm and diameter 8.6 mm), aligned so that the scattering plane was $(0, 1, 1) - (1, 0, 0)$ ⁴ with the cylindrical crystal's axis tilted about 30° from vertical. For the other two experiments on IN20 the Cologne sample was used. This consisted of six co-aligned rods with a combined mass of ~ 17 g. These were mounted with the same scattering plane as the Oxford sample. The rods had been grown in such a way that their cylindrical axes were in the scattering plane, which meant that for certain orientations of the spectrometer the crystals were all parallel either to the incident beam or the scattered beam. In such configurations there was a measurable decrease in the count rate, so such configurations were avoided if possible. In a few situations it was impossible to avoid such configurations, so in order to correct for this effect a scan was made of the incoherent elastic scattering as a function of sample angle. The reduced transmission when the crystals lay nearly parallel to the incident or scattered beam could therefore be quantified and the data were subsequently corrected.

Calculations of the phonon scattering intensities, which at low energies have a similar form to the structure factor, detailed in appendix C, revealed that the phonon scattering would be weakest near the $(1, 0, 0)$ pseudo-cubic position in reciprocal space. This was then verified by measuring several structural Bragg peaks and phonons at the start of the experiment.

⁴These wavevectors are in pseudo-cubic notation, detailed in appendix B, which will be used for all of this chapter.

5.3 Results

The results of neutron scattering measurements of the magnetic scattering in LaCoO₃ will be presented in this section. The first set of measurements were performed using polarised neutrons, and these enabled us to determine unequivocally the character of the magnetic inelastic scattering. It is clear from these measurements that the magnetic scattering is rather broad and diffuse. In order to characterise further the magnetic scattering unpolarised neutron inelastic scattering measurements were performed in an energy range where the nuclear scattering is minimal.

As detailed in section 5.2, two different samples were used. For one of the polarised neutron scattering measurements, and the unpolarised neutron scattering measurement, the sample grown in Oxford was used. For the other polarised neutron scattering measurement the sample grown in Cologne was used.

5.3.1 Polarised Neutron Scattering Measurements

Polarisation analysis, as described in section 2.1.4, was performed on these data in order to separate the magnetic from the non-magnetic scattering. The magnetic fluctuation components along the $(0, 1, 1)$ and $(0, \bar{1}, 1)$ directions could be determined⁵, and it was found that these two components were indistinguishable, i.e. that the magnetic scattering at all energies and temperatures shown was isotropic.

Figures 5.2 and 5.3 show fixed-energy Q-scans for a range of energies at $T = 220$ K, for the $\mathbf{P} \parallel \mathbf{Q}$ channels. Measurements were made using only one polarisation because the counting times required to measure all polarisation channels would have been prohibitively long⁶. Nevertheless, for this polarisation the non-spin-flip (NSF) channel shows only non-magnetic scattering whereas the spin-flip (SF) channel shows magnetic scattering plus some background, so it is possible to distinguish magnetic from non-magnetic scattering. Indeed, a peak appears in the SF channel, but not in the NSF, showing that the excitations being probed are magnetic. Note that the scans for $E \geq 12$ meV were taken with $k_f = 4.1 \text{ \AA}^{-1}$, as opposed to $k_f = 2.662 \text{ \AA}^{-1}$, due to constraints on the spectrometer geometry. The magnetic signal appears to disperse from the ferromagnetic $(1, 0, 0)$ position with increasing energy, becoming broader and less intense as it does so.

Figure 5.4 shows scans in the SF and NSF channels with $\mathbf{P} \parallel \mathbf{Q}$ at $E = 4$ meV. The blue circles (filled for SF, open for NSF) show measurements made on the Oxford-grown sample, whereas the green squares show measurements made on the Cologne-grown samples. When the data are rescaled to account for the different counting times used, it is clear that they are equivalent and that the measurements are reproducible and sample independent.

Figure 5.5 shows similar fixed-energy Q-scans to figures 5.2 and 5.3. In this case the measurements were made in all six polarisation channels. This meant that, by performing the analysis described in section 2.1.4, the scattering that is purely magnetic in origin could

⁵These wavevectors are in the scattering plane and perpendicular to \mathbf{Q} , and perpendicular to the scattering plane respectively.

⁶The counting times required were longer than usual because of a problem, which was not known about at the time of the experiment, with the Heusler monochromator on IN20.

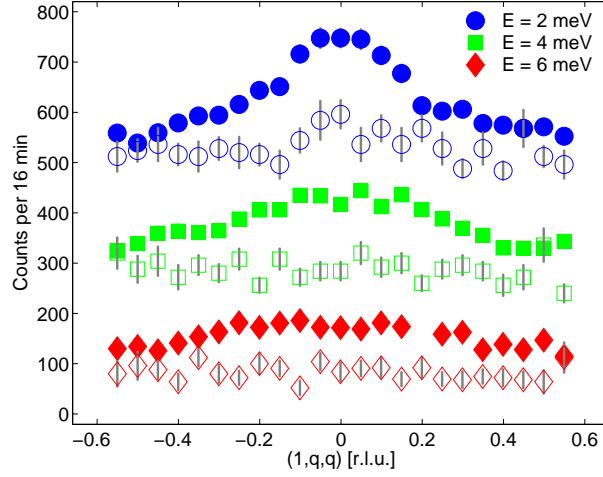


Figure 5.2: Fixed-energy Q-scans for $\mathbf{P} \parallel \mathbf{Q}$, spin-flip (filled symbols) and non-spin-flip (open symbols), showing the magnetic scattering at $T = 220$ K with energies in the range $2 \leq E \leq 6$ meV. Scans at successive energies are offset by 200. The Oxford-grown sample was used for these measurements.

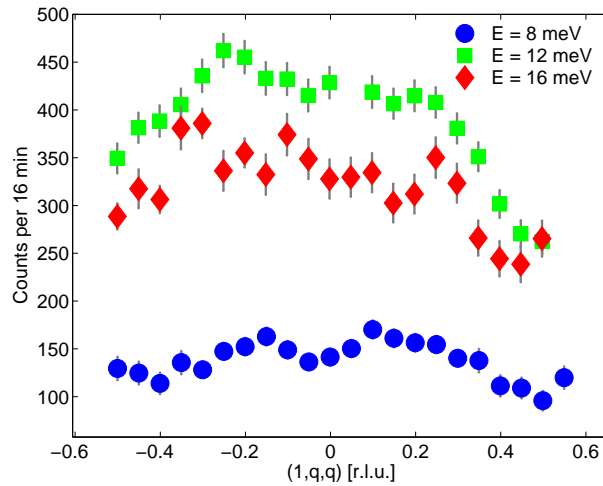


Figure 5.3: Fixed-energy Q-scans for $\mathbf{P} \parallel \mathbf{Q}$, spin-flip, showing the magnetic scattering at $T = 220$ K with energies in the range $8 \leq E \leq 16$ meV. Note that the 8 meV scan was with $k_f = 2.662 \text{ \AA}^{-1}$, whereas the scans at 12 meV and 16 meV were with $k_f = 4.1 \text{ \AA}^{-1}$. The non-spin-flip is not shown because the data are very noisy due to the shorter counting times used to measure this channel. Note that successive scans are *not* offset. The Oxford-grown sample was used for these measurements.

be separated from all other contributions. It is this ‘pure’ magnetic signal that is shown in figure 5.5. Note that the Cologne grown sample was used for these measurements. It is clear that the dispersion is not a feature of the background, which was a possibility, albeit a remote one, for the data showing only the $\mathbf{P} \parallel \mathbf{Q}$ channel.

Figure 5.6 shows fixed wavevector energy scans at $\mathbf{Q} = (1, 0, 0)$ and $\mathbf{Q} = (1, 0.5, 0.5)$, i.e. the magnetic zone centre and the magnetic zone boundary, that have been polarisation analysed to give just the magnetic scattering. The lines shown are fits to these data, and will be described later. It is clear that the magnetic scattering does not go to zero at the

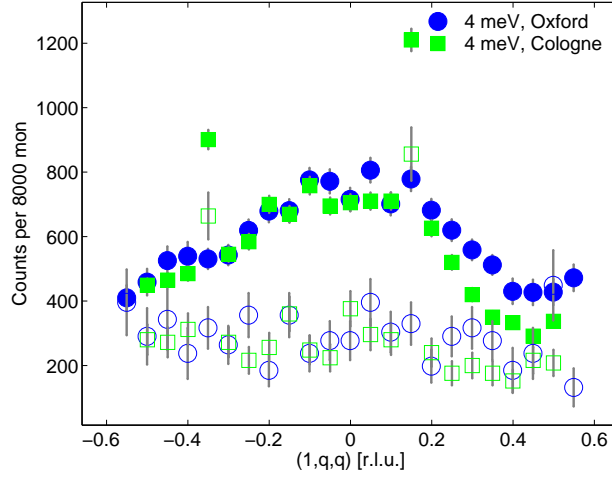


Figure 5.4: $\mathbf{P} \parallel \mathbf{Q}$ SF and NSF (closed and open symbols respectively) Q-scans at 4 meV for both samples, showing that both display the same effects. The raw data from the Cologne sample are contaminated slightly by spurious scatter, but this is eliminated in the polarisation analysis in other figures showing data from this sample. The data have been scaled to the same monitor count, which corresponded to 16 minutes for the experiment on the Oxford sample, and 12 minutes for the experiments on the Cologne sample.

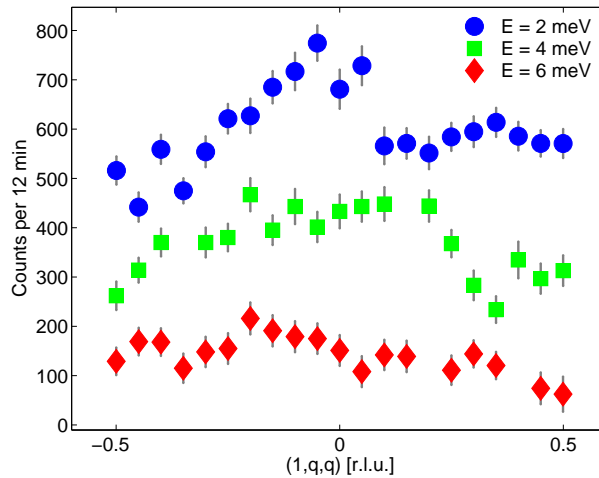


Figure 5.5: Fixed-energy Q-scans after polarisation analysis, showing the magnetic scattering at $T = 220$ K for $2 \leq E \leq 6$ meV. Successive scans have been offset by 200 for clarity. The Cologne-grown sample was used for these measurements.

zone boundary, i.e. the magnetic scattering is spread over the whole Brillouin zone.

In summary, the polarised neutron inelastic scattering measurements presented here show that the magnetic scattering is very diffuse in wavevector and energy. Q-scans show features that are reminiscent of spin-wave dispersion, namely two symmetric peaks which move further apart at higher excitation energies. The fixed-wavevector energy scans, do not, however, show a peak indicative of such a mode.

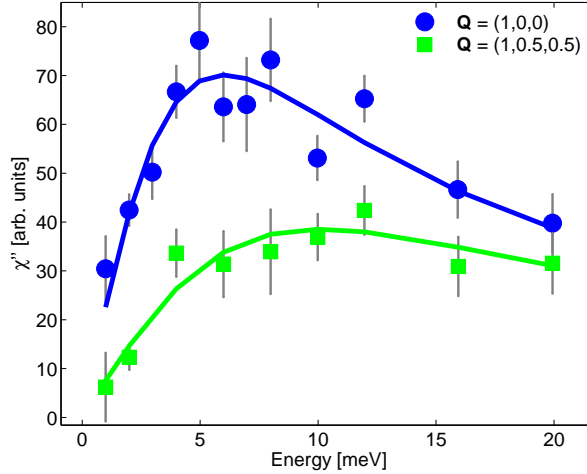


Figure 5.6: Fixed wavevector energy scans of the polarisation analysed magnetic scattering, at $\mathbf{Q} = (1, 0, 0)$ and $\mathbf{Q} = (1, 0.5, 0.5)$, at $T = 220$ K. Solid lines are fits to the data, described in the text. The Cologne-grown sample was used for these measurements.

5.3.2 Unpolarised Neutron Scattering Measurements

The Oxford-grown sample was used for all of the unpolarised neutron scattering measurements.

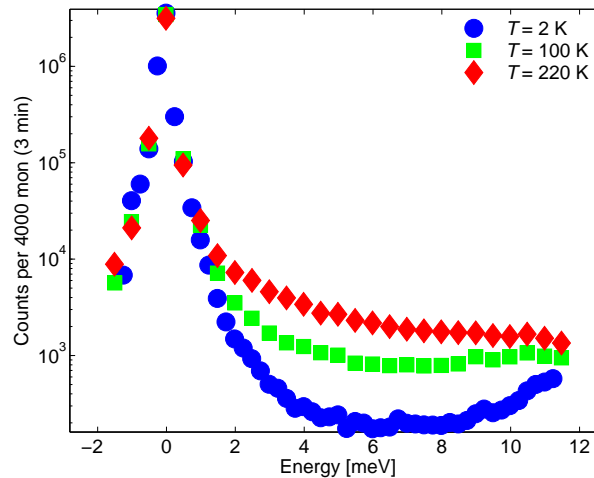


Figure 5.7: Fixed- \mathbf{Q} energy scans at $\mathbf{Q} = (1, 0, 0)$ using unpolarised neutrons, showing scans at $T = 2, 100,$ and 220 K on a logarithmic scale.

When using unpolarised neutrons a major concern is non-magnetic background scatter, particularly for a material such as LaCoO_3 where, as the polarised neutron measurements have shown, the magnetic scattering is very weak and broad in reciprocal space. To this end the first concern for these measurements was to select positions in (\mathbf{Q}, E) -space where the non-magnetic scattering was minimal. The structure factor at $\mathbf{Q} = (1, 0, 0)$ is very small, as has been mentioned, but it was also important to consider over which energy range the non-magnetic scatter was lowest. Energy scans were performed at $\mathbf{Q} = (1, 0, 0)$ and $\mathbf{Q} = (1, 0.5, 0.5)$, the magnetic zone centre and zone boundary respectively, at low temperature where the material is in the LS state and hence all the scattering is non-

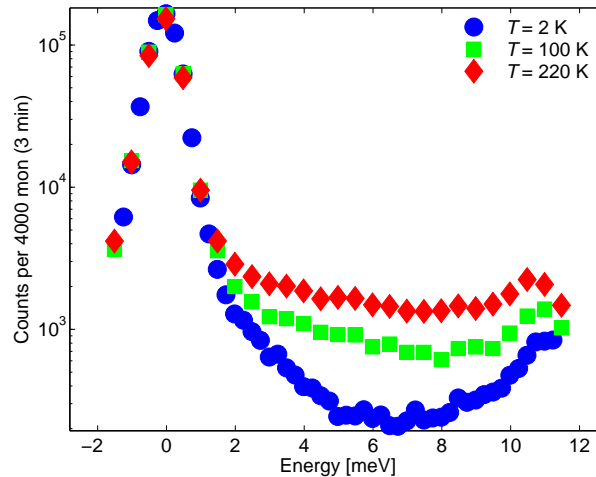


Figure 5.8: Fixed-Q energy scans at $\mathbf{Q} = (1, 0.5, 0.5)$ using unpolarised neutrons, showing scans at $T = 2, 100,$ and 220 K on a logarithmic scale.

magnetic. The blue circles in figures 5.7 and 5.8 show that there are no non-magnetic features between 5 meV and 7 meV, so for fixed energy Q-scans energies within this range would be the easiest to analyse.

The energy scans shown in figures 5.7 and 5.8 also display some other features. At about 11 meV there is an optic mode phonon, which is easier to see in figure 5.8 because the overall intensity is lower and hence the phonon is more apparent on the logarithmic scale used. The tail of this phonon is apparent down to an energy of about 8 meV. The nuclear Bragg peak at $(1, 0, 0)$ is also obvious in fig. 5.7, and it appears to broaden at higher temperatures, which might be due to the presence of quasi-elastic ferromagnetic scattering. The elastic line in fig. 5.8 is, of course, much weaker since it corresponds to just the incoherent elastic scatter.

Figure 5.9 shows examples of the raw data from the unpolarised scattering measurement of fixed energy Q-scans, at $E = 5$ meV. The energy was fixed at 5 meV because, as mentioned above, the level of non-magnetic scatter at this level is the lowest and is also the easiest to subtract off. It is clear that at $T = 2$ K there are no features in the scan, apart from a few pieces of spurious scatter. As the temperature is increased to 100 K a pair of peaks, the same as those seen in fig. 5.2, appear. Concomitant with this the background scattering also increases. As the temperature is increased further to 220 K the peaks become more distinct and the overall intensity continues to increase. As the temperature is increased above about 150 K, the peaks gradually move closer to the origin.

5.4 Analysis

The polarised neutron scattering data can be fairly straightforwardly treated, since the non-magnetic background scattering has either been subtracted off, in the case of fully polarisation analysed scans, or can be modelled using a straight line for the case of single polarisation scans. The treatment of the unpolarised neutron scattering data is somewhat more complicated, because both the non-magnetic background scattering and the magnetic scattering are temperature dependent.

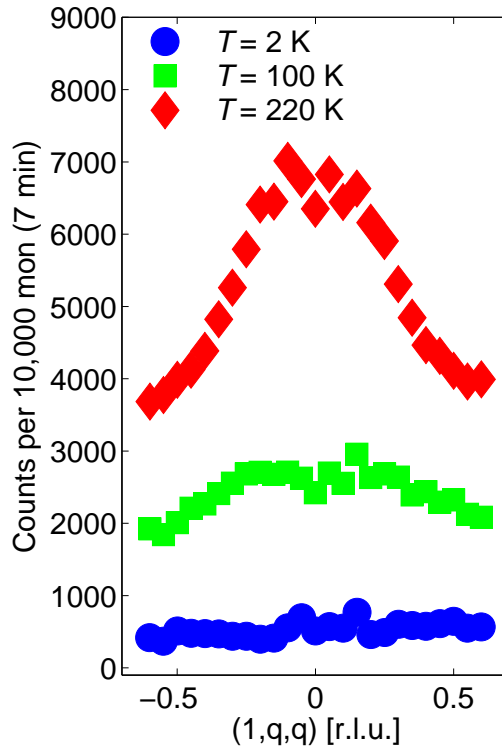


Figure 5.9: Typical fixed-energy Q-scans at $E = 5$ meV using unpolarised neutrons, showing scans at $T = 2, 100,$ and 220 K. Note that the scans are *not* offset from one another.

Fortunately the way in which the non-magnetic background behaved as a function of temperature could be determined from the polarised neutron measurements. This is because the scattering in the $\mathbf{P} \parallel \mathbf{Q}$ non-spin-flip channel has no magnetic contributions, so by combining all of the measurements in this channel at a range of temperatures the behaviour of the non-magnetic background with temperature could be interpolated

The energy-scans made with unpolarised neutrons, shown in figures 5.7 and 5.8, display several features which must be considered in the analysis. Whilst it is clear that the non-magnetic scattering around $E = 5$ meV is quite low and simple to model, the other features such as the optic phonon and the quasi-elastic scattering are not. In principle the optic phonon should scale simply as the Bose factor, however in reality there are likely to be multi-phonon scattering events whose behaviour with temperature cannot be simply modelled with the data available here. The nuclear elastic scattering is so strong in comparison to the magnetic scattering at low energies that subtraction of the former to give the latter is rather risky given the size of the error bars that would result. It was therefore decided that only the Q-scans at $E = 5$ meV could be reliably analysed, and that the energy-scans could not be used to draw quantitative conclusions.

The unpolarised neutron scattering measurements, specifically the Q-scans at $E = 5$ meV, also feature a few pieces of spurious scattering. These are temperature independent, and do not change position in wavevector or energy, and must be subtracted from all data sets before any other corrections relating to temperature dependent background are made. Since the measurements at $T = 2$ K contain no magnetic scattering, scans taken at this temperature could be subtracted from all higher temperature data sets in order to remove these so-called ‘spurions’.

The non-magnetic background subtraction procedure was thus as follows:

- Only consider measurements where there is little non-magnetic scattering, e.g. Q-scans at $E = 5$ meV.
- Subtract data at $T = 2$ K in order to remove temperature-independent spurions.
- Next scale the next highest temperature set of data ($T = 20$ K) according to the interpolation of the temperature-dependent non-magnetic scattering deduced from polarised neutron scattering measurements, and subtract this from all higher temperature scans.
- Finally scale all measurements to the Bose thermal population factor, detailed in section 2.1.3, $n(\omega) + 1 = 1 + 1/(e^{\hbar\omega/k_B T} - 1)$.

For the analysis of the data presented there are several considerations for the model to be employed. The first is that when analysing the temperature dependence of the unpolarised scattering data the function should obey the sum rule relating the response function and the bulk susceptibility (see equation 2.31). In addition the model must account for the experimental observation that the spin excitations are rather weak and broad in reciprocal space. The electrons thermally excited into the e_g level must have a finite lifetime, which is rather short. In other words the number density and lifetime of magnetic ions is finite and temperature dependent. For a magnetic excitation to propagate through a material magnetic ions must be near to each other for a timescale comparable to the lifetime of the excitation. If there are a large number of non-magnetic ‘gaps’ between magnetic ions when an excitation is created then that excitation will be very short ranged and will have rather a short lifetime. Conversely if the number of non-magnetic gaps is smaller, because more electron have been thermally excited into the e_g levels and the interval where any given ion is in the non-magnetic state is shorter, then excitations will on average be able to propagate further and live longer. The natural choice of function to describe the behaviour of such local excitations is the damped harmonic oscillator function,

$$\chi''(q, \omega) \propto \frac{\Gamma(q)\omega}{\Gamma^2(q) + \omega^2}, \quad (5.1)$$

where ω is the energy of the spin excitation, and $\Gamma(q)$ is the q -dependent damping. The precise details of this q -dependence will be determined by the best fits to the data⁷. It has been found in studies of materials with short range magnetic correlations [24] that equation 5.1 will not alone capture all of the physics – an additional term needs to be included in the form of a Lorentzian in q -space, which leads to the response function

$$\chi''(q, \omega) = \frac{A}{T} \cdot \frac{\kappa^2}{\kappa^2 + q^2} \cdot \frac{\Gamma(q)\omega}{\Gamma^2(q) + \omega^2}, \quad (5.2)$$

where κ parameterises the Lorentzian width. Various different functional forms for $\Gamma(q)$ were tried, and it was found that the best fits were obtained when $\Gamma(q) = \Gamma_0 + \Gamma_2 q^2$. The

⁷Various different forms of q -dependence have been observed, especially in magnetic materials above their critical temperatures. See reference [24] for some examples.

scaling amplitude, A , is divided by temperature, T , in equation 5.2 because measurements of the bulk susceptibility [6] found that it could be modelled by a Curie law. This means that $A \propto \mu_{\text{eff}}$, the effective local moment, so that the temperature dependence of A directly reflects that of the microscopic magnetism.

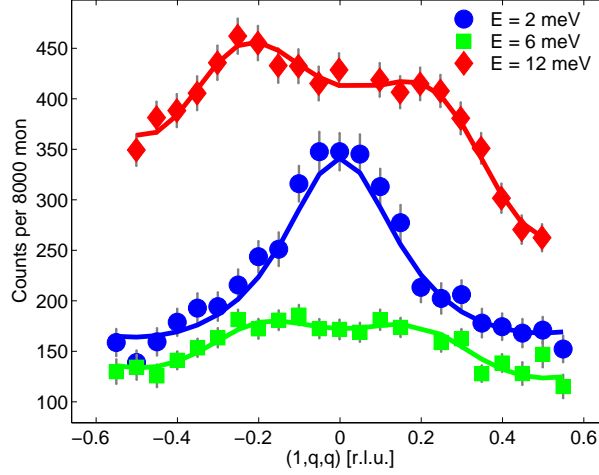


Figure 5.10: Fits to equation 5.2, plus a sloping background since the data were not fully polarisation-analysed, of fixed energy Q-scans with $\mathbf{P} \parallel \mathbf{Q}$ spin-flip, taken with the Oxford sample on IN20 at $T = 220$ K. Note that the data at $E = 12$ meV was taken with $k_f = 4.1 \text{ \AA}^{-1}$, whereas the other two scans were with $k_f = 2.662 \text{ \AA}^{-1}$.

Figure 5.10 shows fits to Q-scans, with data taken in the polarised scattering channel $\mathbf{P} \parallel \mathbf{Q}$ spin-flip. In order to account for the fact that this channel includes some background contributions, an additional term was included in equation 5.2 in the form of a linearly sloping background. Similar fitting was performed on Q-scans which had been fully polarisation-analysed to give solely the magnetic signal, such as the data shown in figure 5.5, but without a background contribution since the polarisation analysis should remove such terms.

Energy (meV)	A (arb. units)	Γ_0 (meV)	Γ_2 (meV r.l.u. ⁻²)	κ (r.l.u.)
2	130000 ± 4000	2 ± 14	0.25 ± 0.27	0.17 ± 0.01
4	68000 ± 2000	4 ± 300	73 ± 11	0.17 ± 0.005
6	58000 ± 2000	3.7 ± 0.2	65 ± 7	0.23 ± 0.005
8	48000 ± 2000	2.9 ± 0.1	130 ± 12	0.23 ± 0.006
12	36000 ± 1000	12.0 ± 1.1	118 ± 13	0.28 ± 0.002

Table 5.1: Fit parameters obtained by fitting equation 5.2 to polarised neutron Q-scans with $\mathbf{P} \parallel \mathbf{Q}$ spin-flip at $T = 220$ K. The fit for the data at $E = 12$ meV was scaled down by a factor of 4 because a larger k_f was used – the scale factor was determined experimentally by measuring a Q-scan at 8 meV with both $k_f = 2.662 \text{ \AA}^{-1}$ and $k_f = 4.1 \text{ \AA}^{-1}$.

The resulting parameters of fits to equation 5.2 of the magnetic scattering obtained with polarised neutrons are given in tables 5.1 and 5.2. The amplitude steadily decreases with increasing energy for the $\mathbf{P} \parallel \mathbf{Q}$ spin-flip data shown in table 5.1. This is actually what would be expected for a constant amplitude in equation 5.2 because these data were *not* corrected for the Bose thermal population factor as they contain a non-zero background. The fit parameters presented in table 5.2 are the results of fits to data that *have* been corrected for

Energy (meV)	A (arb. units)	Γ_0 (meV)	Γ_2 (meV r.l.u. ⁻²)	κ (r.l.u.)
2	32000 ± 2000	1.0 ± 0.2	6.8 ± 3.1	0.19 ± 0.01
4	27000 ± 2000	4 ± 133	120 ± 37	0.29 ± 0.02
6	28700 ± 1900	6.1 ± 35	71 ± 26	0.33 ± 0.02

Table 5.2: Fit parameters obtained by fitting equation 5.2 to polarised neutron Q-scans analysed to give the ‘pure’ magnetic scattering at $T = 220$ K.

the Bose factor, because the polarisation analysis removes background contributions to the scattering. It can be seen here that the data can be fitted with a constant amplitude for all energies.

The fit to the $\mathbf{P} \parallel \mathbf{Q}$ spin-flip data at 2 meV suggests that Γ_2 is negligible. However this may be because of a feature in the background, and indeed the fit to the fully polarised scan gives a larger value for Γ_2 at 2 meV, however it is still not consistent with the results of the other fits. One problem with the fit parameters is that they are all interconnected, in that the heights and widths of the peaks are determined by A , Γ_0 , Γ_2 and κ together, and not by a single parameter. This in turn means that the errors on the fit parameters are interconnected, so that if for a given fit the error on A is large, the error on Γ_0 , say, is likely to be smaller.

Temp. (K)	\mathbf{Q} (r.l.u.)	A (arb. units)	Γ (meV)	κ_0 (r.l.u.)
150	(1, 0, 0)	25300 ± 1500	6.8 ± 0.8	N/A
150	(0.5, 0.5, 0.5)	26200 ± 3000	6.9 ± 1.2	0.34 ± 0.12
220	(1, 0, 0)	41000 ± 1300	6.0 ± 0.6	N/A
220	(1, 0.5, 0.5)	43000 ± 4000	10.1 ± 1.0	0.34 ± 0.09
300	(1, 0, 0)	21600 ± 1300	5.8 ± 0.6	N/A
300	(0.5, 0.5, 0.5)	21200 ± 2000	8.8 ± 0.9	0.39 ± 0.11

Table 5.3: Fit parameters from polarised energy-scans of the polarisation-analysed, taken at the magnetic zone centre and zone boundary over a range of temperatures.

Table 5.3 shows fit parameters derived from fitting the magnetic signal in fixed-wavevector energy-scans at three temperatures – sample fits for $T = 220$ K are shown in figure 5.6. The analysis performed so far has shown that κ appears to vary slightly with energy, with κ becoming larger at higher excitation energies. However when fitting the energy-scans various different functional forms for κ were tried, and none of them improved the quality of the fits. Indeed in most cases they appeared to cause the Γ parameter to become inconsistent with that obtained from the Q-scans, so in the end a constant value for κ was assumed. The values of Γ obtained from the energy-scans at the magnetic zone boundary, $\mathbf{Q}_{\text{AFM}} = (1, 0.5, 0.5)$ are consistent with those obtained from Q-scans⁸. However the values of Γ obtained for the energy scans at $\mathbf{Q}_{\text{FM}} = (1, 0, 0)$ are larger than expected, and do not appear to be consistent with the results of the fits of Q-scans.

Figure 5.11 shows typical fits to Q-scans at 5 meV taken with unpolarised neutrons, after the data have been processed by subtracting the temperature dependent background and then correcting for the Bose thermal population factor. When equation 5.2 was used then the average ‘goodness of fit’ parameter for all of the fits was $\chi^2 = 6.4$ when the functional

⁸A single Γ was used because the scans were performed at fixed wavevector.

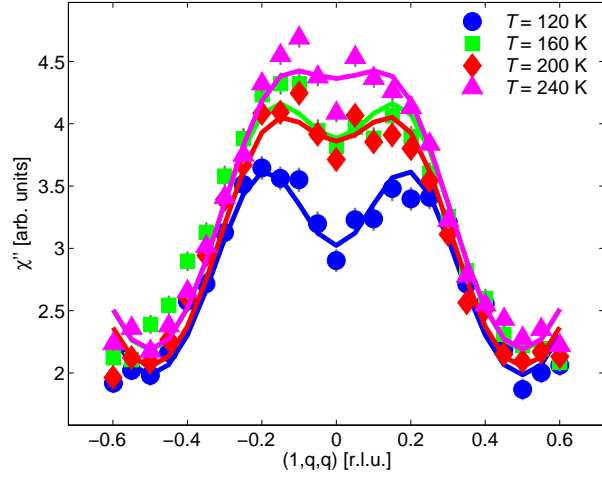


Figure 5.11: Fits to equation 5.2 for unpolarised neutron Q-scans at $E = 5$ meV, after correction for the Bose factor.

form $\Gamma(q) = \Gamma_0 + \Gamma_2 q^2$ was used. Other functions to describe the damping gave fits with larger values of χ^2 .

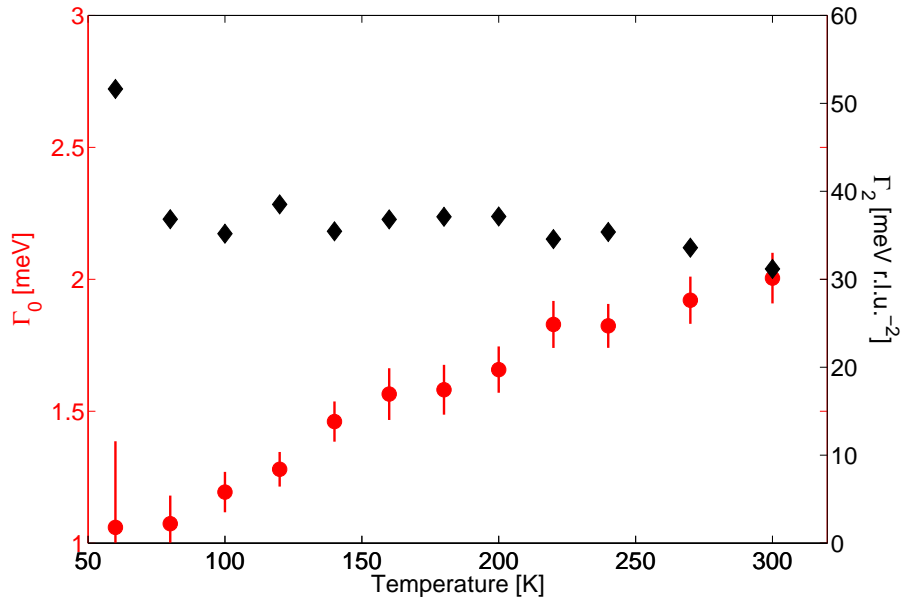


Figure 5.12: The temperature dependence of Γ_0 (red circles, left-hand axis) and Γ_2 (black diamonds, right-hand axis), determined from fits of unpolarised Q-scans at 5 meV using equation 5.2.

Figure 5.12 shows how the values of Γ_0 and Γ_2 vary with temperature. The value of Γ_0 increases almost linearly with increasing temperature, whereas Γ_2 remains more or less constant. The value of κ was also allowed to vary in the fits, but was found to be constant with temperature at $\kappa = 0.28$ r.l.u. This corresponds to a correlation length of about 3.5 lattice units, or about 14\AA . The values of Γ_0 and Γ_2 are generally consistent with those obtained from fits of the polarised neutron data.

The Bleaney-Bowers equation, which gives the susceptibility of a spin system in which there is a non-magnetic singlet ground state and a magnetic multiplet excited state is

$$\chi_{B-B}(T) = \frac{N_A g^2 \mu_B^2}{3k_B T} \cdot \frac{\nu S(S+1)(2S+1)e^{-\Delta/T}}{1 + \nu(2S+1)e^{-\Delta/T}} \quad (5.3)$$

where Δ is the gap between the ground state and the first excited state, ν is the orbital degeneracy of the first excited state, and all other symbols have their usual meanings. The second term on the right-hand side is a measure of the occupation number of the magnetic excited state. This equation was used by Zobel *et al* [6] to model the behaviour of the bulk susceptibility, and it was found that their data were fitted well when $S = 1$, $\Delta = 15.5$ meV, and $\nu = 1$; this represents an IS excited state which is orbitally non-degenerate.

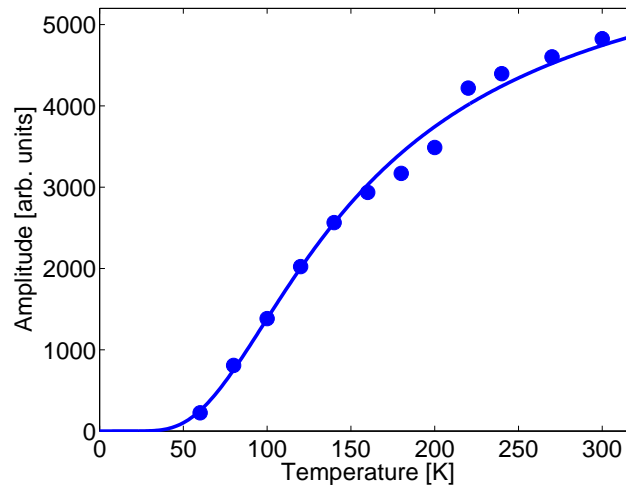


Figure 5.13: Fit of amplitude A , defined in equation 5.2, determined from fits to equation 5.3 (multiplied by T) of unpolarised Q-scans at 5 meV. At many points the errorbars are smaller than the points themselves.

Figure 5.13 shows a fit of the amplitude of the scattering arising from correlations in the magnetic state, which is proportional to the occupation number in equation 5.3. The fit parameters for this are $\Delta = 23.9 \pm 0.5$ meV and the best fit was obtained when $\nu = 1$ and $2S + 1 = 3$ (fixed), so the energy gap between the ground state and thermally populated excited state does not agree with that determined by bulk measurements, but the orbital degeneracy and spin state do agree.

5.5 Discussion

The main points that should be taken from the data analysis presented in section 5.4 are:

1. The data can be modelled well by a damped harmonic oscillator function.
2. The magnetic excitations appear to disperse.
3. The correlation length of the magnetic excitations might be slightly energy dependent, with shorter correlation lengths for higher energy excitations.

4. The results of fits to the magnetic scattering in fixed wavevector energy scans are not fully consistent with the results of fits of the Q-scans from both polarised and unpolarised neutron scattering experiments.
5. The amplitude, which reflects the effective local moment, μ_{eff} , is temperature dependent and can be modelled quite well by the Bleaney-Bowers equation (5.3). However the parameters which give the best fit are not consistent with those determined from measurements of the bulk susceptibility.

Once these points have been addressed there are some further more general points for discussion, namely:

1. The physical origins of the damping, and the possible reasons for its dependence on temperature.
2. Whether these data can shed any light on the nature (IS or HS) of the excited magnetic state.

Let us first address the point that the data are fitted well by the damped harmonic oscillator function, given by equation 5.2. In fact it is possible to get a fit that is just as good using two Lorentzians to model the magnetic scattering from the Q-scans. However, such a model does not contain as much physical information as the damped harmonic oscillator model. The appropriateness of the latter function demonstrates that the excitations are indeed rather localised and tend to be short-lived, as was hypothesised.

The appearance of dispersion of the magnetic excitations has been noted in other materials which bear some similarities to LaCoO_3 . In particular measurements of the magnetic excitations in ferromagnetic Fe and Ni above their critical temperatures [25] showed what were termed ‘persistent spin-waves’. However it was subsequently realised that these features, which were found in Q-scans, were not actually due to spin-waves because there did not exist a corresponding peak in fixed-wavevector energy-scans [26].

Equation 5.2 has poles at non-zero values of q when the energy ω is held constant, and these poles move to larger q as ω is increased. There are, however, also poles in equation 5.2 when q is held constant and ω is varied, which is different to the case of the metallic ferromagnets Fe and Ni. This suggests, then, that spin-waves do exist in the magnetic state of LaCoO_3 , but that they are strongly localised due to the inhomogeneous nature of the excited spin state.

The peaks in the constant energy Q-scans disperse outwards with increasing energy when κ is held constant in equation 5.2, so the variation observed in κ with energy does not itself give rise to the dispersion-like features. However it appears that κ does increase with increasing energy, corresponding to a reduction in the correlation length of the excitations at higher energies. It is not clear why this occurs, and the effect is rather small, with the correlation length varying between about 11 \AA and 25 \AA for high and low energies respectively (see tables 5.1 and 5.2). Furthermore, the quality of fits to the energy-scans was actually reduced when κ was allowed to vary as a function of energy, so if the effect does occur it is indeed rather small.

Consider now the fits to the energy scans, the results of which are presented in table 5.3. Whilst the fits to the scans at $\mathbf{Q}_{\text{AFM}} = (1, 0.5, 0.5)$ produce parameters which are consistent with those obtained from Q-scans, the fits of scans at $\mathbf{Q}_{\text{FM}} = (1, 0, 0)$ do not. Specifically the values of Γ obtained from these latter fits, which should reflect just Γ_0 since $q = 0$, are somewhat larger than expected. Even considering the finite resolution of the neutron spectrometer, which would allow a certain contribution of the Γ_2 term, this is rather hard to reconcile with the rest of the data. These data have been polarisation-analysed to give solely the magnetic scattering. One problem with this, however, is that the errorbars become quite large compared to the signal when the necessary subtractions are performed, so it is possible that the fits are not as well constrained as they might be. The result of this is that the fit is particularly sensitive to individual data points, which may then skew the fits.

We have established, then, by measuring their fluctuations, that the ions in the excited magnetic state are coupled. There is a significant body of literature concerning the magnetic fluctuations of ferromagnets above their critical temperatures – see for example the review article by Endoh and Böni [24] and the references therein. It is common for the magnetic neutron inelastic scattering from such systems to be modelled using a damped harmonic oscillator function, with a q -dependent damping $\Gamma(q)$.

The precise details of $\Gamma(q)$ are not, however, universal. In materials that are insulators where the magnetic moments are localised and ferromagnetically aligned below T_C , the spin fluctuations above T_C are well described by a damped harmonic oscillator like equation 5.2. The damping is given by dynamical scaling⁹ as

$$\Gamma_{\text{paramag}} = \Gamma_{\text{p}} q^{2.5} f(\kappa/q), \quad (5.4)$$

where Γ_{p} is a constant, κ is defined the same as in eq. 5.2 and $f(\kappa/q)$ is the dynamical scaling function, which in ferromagnetic semiconductors such as EuO is the Résibois-Piette function [28]. In addition κ is temperature dependent and has the form

$$\kappa = \kappa_0 \left(\frac{T - T_C}{T_C} \right)^m, \quad (5.5)$$

where κ_0 is the correlation length of the fluctuations at $T = 2T_C$ and m is a constant which is material dependent. The Résibois-Piette dynamical scaling function does not have a simple analytical form, but at T_C $f(\kappa/q) = 1$, and with increasing temperature it first decreases and then increases again as $\sqrt{\kappa/q}$.

In metallic systems it has been found that the damping of spin fluctuations increases more rapidly with increasing temperature, since additional damping by the conduction electrons occurs [29, 30]. The general functional form for the damping in this case is

$$\Gamma_{\text{metallic}} = \Gamma_{\text{m}} q (q^2 + \kappa^2), \quad (5.6)$$

where Γ_{m} is a constant and κ has the same temperature dependence as before, given by eq. 5.5. At the temperatures under consideration in this study LaCoO₃ is not metallic, and

⁹Scaling laws in general relate the critical exponents of static order parameters. Dynamical scaling is an extension of this to non-equilibrium, dynamic, phenomena. See reference [27] for further details.

indeed when this equation was used to analyse the data the quality of the fit was poor.

In contrast equation 5.4 is in best agreement with the data if $f \sim \sqrt{(\kappa/q)}$, i.e. if LaCoO₃ is like a local moment ferromagnetic material at $T \gg T_C$. Additional credence is provided by noticing that Γ_2 , which corresponds to $\Gamma_p \cdot f(\kappa/q)$ in equation 5.4, is constant with temperature, as is κ .

In order to provide the best fit, however, an additional q -independent damping term, Γ_0 , was required. This additional damping increases approximately linearly with increasing temperature. A clue to the origin of this extra damping term might be found in considerations of the spin fluctuations observed in nearly-ferromagnetic semiconductors such as FeSi [31, 32], and theoretical descriptions thereof [33]. In such materials the magnetic fluctuations are the result of correlations between electrons thermally excited into the conduction band, however since the electrons are never statically ferromagnetically correlated the fluctuations are similar to those seen in metallic ferromagnets above T_C .

It has already been noted in section 5.1 that LaCoO₃ is a semiconductor, and that even for energies well below the band gap the optical conductivity is non-zero, suggesting that a small number of electrons are excited into the conduction band even at temperatures where $k_B T \ll E_{\text{gap}}$. These electrons might act to damp the magnetic excitations, in much the same way as conduction electrons in metallic or semiconducting ferromagnets do. Since the number of conduction electrons increases with increasing temperature the damping will concomitantly increase, in agreement with the measurements presented here.

Returning to equation 5.4, it has been noted [24] that in many ferromagnets the constant Γ_p is often very close in value to the spin-wave stiffness, albeit in many cases slightly lower. It has been determined here that in LaCoO₃ $\Gamma_2 \approx 35 \text{ meV r.l.u.}^{-2}$, and considering equation 5.4 this leads to

$$\Gamma_2 = \Gamma_p \cdot \sqrt{\kappa}, \quad (5.7)$$

which means that $\Gamma_p \approx 66 \text{ meV r.l.u.}^{-2.5}$, or $\Gamma_p \approx 19.4 \text{ meV \AA}^{2.5}$. The spin-wave stiffness for a cubic lattice can be related to the nearest-neighbour Heisenberg exchange constant (see equation 1.14) by

$$D = 2JSa^2, \quad (5.8)$$

where J is the exchange constant, S is the spin, a is the lattice constant, and the factor of 2 is included because the scans were along the $(0, q, q)$ direction. Assuming an IS state this gives upper limits on the exchange parameters of $J_{\text{IS}} = 0.65 \text{ meV}$, and alternatively assuming a HS state we get $J_{\text{HS}} = 0.33 \text{ meV}$.

Let us now consider the behaviour with temperature of the scaling amplitude A , shown in figure 5.13, that is a measure of the size of the effective local magnetic moment. As has already been mentioned, the bulk susceptibility was successfully modelled with an energy gap of $\sim 15.5 \text{ meV}$ between the ground state and an IS excited state that is orbitally non-degenerate [6]. The amplitude dependence found in this study was consistent with an orbitally non-degenerate IS excited state. The gap was found to be somewhat larger, however. There are several possible explanations of this discrepancy.

The first is that we have assumed that the neutron magnetic inelastic scattering spectrum is entirely modelled by equation 5.2, and that integrating this over all energies at zero wavevector gives the bulk susceptibility. However it is conceivable that there are other magnetic excitations, for example at higher energies than were studied here, that will also contribute to the bulk susceptibility.

Another possibility is that the model of Zobel *et al* [6] is not correct – in order to fit the susceptibility they required a Landé g -factor of 2, whereas ESR and neutron inelastic scattering studies [19, 18] have shown that a g -factor of 3 is appropriate. Haverkort *et al* [21] were able to obtain agreement between their soft x-ray absorption and magnetic circular dichroism with the bulk susceptibility by making the gap between the LS and HS states temperature dependent, varying from about 20 meV at 70 K up to 80 meV for $T \geq 450$ K. Furthermore, the measurements presented here suggest that there exist ferromagnetic correlations between magnetic ions, whereas the model used by Zobel *et al* to describe the bulk susceptibility assumes that the magnetic ions are completely paramagnetic, i.e. that they are uncorrelated.

Without a functional form for the temperature dependence of the gap it is not possible to analyse the data presented here in terms of the model proposed by Haverkort *et al*. It was found, however, that by choosing a simple function to describe the temperature dependence of the gap, e.g. $\Delta(T) = \Delta_0 + \alpha T$ with α a constant, that fits with a slightly better χ^2 of 3.85 were obtained, as opposed to 3.89 with constant Δ and $\nu = 1$. However using such a functional form meant that the spin and orbital degeneracy of the excited state could not be determined – indeed a model that includes an energy gap with a linear temperature dependence is equivalent to equation 5.3. This does not, then, allow us to say whether the excited state is IS or HS.

5.6 Conclusions

In conclusion, the thermally excited spin state of LaCoO₃ has been investigated using neutron inelastic magnetic scattering. Ferromagnetic spin fluctuations which are rather weak and broad in reciprocal space were observed, the behaviour of which was found to be very similar to those of the magnetic fluctuations in ferromagnets above their critical temperatures. It seems, therefore, that LaCoO₃ is a strange kind of nearly-ferromagnetic material, since most other nearly-ferromagnetic materials are itinerant electron systems. In addition the behaviour whereby ferromagnetic correlations are thermally activated and increase in size up to a given temperature before declining again is seemingly unique.

The nature of the excited spin state, IS or HS, could not be definitively determined from the measurements presented here. It is hoped that these results will stimulate further theoretical work that may solve this riddle.

There are several further scattering experiments that could be performed on this material. The present measurements could be extended further to higher temperatures, up to and above the insulator–metal transition at 450 K. Once the material becomes metallic the spin excitations would almost certainly change, and the way they change might shed some light on the spin state both above and below this transition temperature. In the future, when polarised neutron time-of-flight instruments with sufficiently high neutron flux are available,

a broader survey of reciprocal space could be made, which would determine if there are any additional excitations that have not been observed by the measurements presented here. Such measurements would also give the magnetic scattering in absolute units, which means that the amplitude of the fluctuations would convey information about the nature of the excited spin state.

References

- [1] G. Thornton, B. C. Tofield, and D. E. Williams, *Solid State Commun.* **44**, 1213 (1982); V. G. Bhide, D. S. Rajoria, G. R. Rao and C. N. R. Rao, *Phys. Rev. B* **6**, 1021 (1972); S. R. English, J. Wu, and C. Leighton, *Phys. Rev. B* **65**, 220407 (2002).
- [2] S. Yamaguchi, Y. Okimoto, and Y. Tokura, *Phys. Rev. B* **54**, 11022 (1996).
- [3] S. J. Blundell, *Magnetism in Condensed Matter*, Oxford University Press (2001).
- [4] P. M. Raccah, and J. B. Goodenough, *Phys. Rev.* **155**, 932 (1967).
- [5] M. A. Korotin, S. Yu. Ezhov, I. V. Solovyev, V. I. Anisimov, D. I. Khomskii, and G. A. Sawatzky, *Phys. Rev. B* **54**, 5309 (1996).
- [6] C. Zobel, M. Kriener, D. Bruns, J. Baier, M. Grüniger, T. Lorenz, P. Reutler, and A. Revcolevschi, *Phys. Rev. B* **66**, 020402 (2002).
- [7] K. Asai, A. Yoneda, O. Yokokura, J.M. Tranquada, G. Shirane, and K. Kohn, *J. Phys. Soc. Jpn.* **67**, 290 (1998).
- [8] T. Saitoh, T. Mizokawa, A. Fujimori, M. Abbate, Y. Takeda, and M. Takano, *Phys. Rev. B* **55**, 4257 (1997)
- [9] S. Yamaguchi, Y. Okimoto, and Y. Tokura, *Phys. Rev. B* **55**, 8666 (1997).
- [10] I. B. Beruker, *The Jahn Teller Effect*, Cambridge University Press (2006).
- [11] G. Maris, Y. Ren, V. Volotchaev, C. Zobel, T. Lorenz, and T. T. M. Palstra, *Phys. Rev. B.* **67**, 224423 (2003).
- [12] Y. Kobayashi, T. S. Naing, M. Suzuki, M. Akimitsu, K. Asai, K. Yamada, J. Akimitsu, P. Manuel, J. M. Tranquada, and G. Shirane, *Phys. Rev. B* **72**, 174405 (2005).
- [13] M. Cwik, M. Braden, M. Kriener, and K. Schmalzl, I.L.L. Experimental Report CRG 1126, (2005).
- [14] K. Asai, P. Gehring, H. Chou, and G. Shirane, *Phys. Rev. B* **40**, 10982 (1989).
- [15] K. Asai, O. Yokokura, N. Nishimori, H. Chou, J. M. Tranquada, G. Shirane, S. Higuchi, Y. Okajima, and K. Kohn, *Phys. Rev. B* **50** 3025 (1994).
- [16] V. P. Plakhty, P. J. Brown, B. Grenier, S. V. Shiryaev, S. N. Barilo, S. V. Gavrilov, and E. Ressouche, *J. Phys. Condens. Matter* **18**, 3517 (2006).

- [17] D. Phelan, Despina Louca, S. Rosenkranz, S. -H. Lee, Y. Qiu, P. J. Chupas, R. Osborn, H. Zheng, J. F. Mitchell, J. R. D. Copley, J. L. Sarrao and Y. Morimoto, *Phys. Rev. Lett.* **96**, 027201 (2006).
- [18] A. Podlesnyak, S. Streule, J. Mesot, M. Medarde, E. Pomjakushina, K. Conder, M. W. Haverkort, and D. I. Khomskii, *Phys. Rev. Lett.* **97**, 247208 (2006).
- [19] S. Noguchi, S. Kawamata, K. Okuda, H. Nojiri, and M. Motokawa, *Phys. Rev. B* **66**, 094404 (2002).
- [20] A. Abragam, and B. Bleaney, *Electron Paramagnetic Resonance of Transition Ions*, Clarendon Press, Oxford (1970).
- [21] M. W. Haverkort, Z. Hu, J. C. Cezar, T. Burnus, H. Hartmann, M. Reuther, C. Zobel, T. Lorenz, A. Tanaka, N. B. Brookes, H. H. Hsieh, H. -J. Lin, C. T. Chen, and L. H. Tjeng, *Phys. Rev. Lett.* **97**, 176405 (2006).
- [22] <http://neutron.neutron-eu.net/FILES/ILL-dec-2001.pdf>
- [23] M. Kriener, C. Zobel, A. Reichl, J. Baier, M. Cwik, K. Berggold, H. Kierspel, O. Zabara, A. Freimuth, and T. Lorenz, *Phys. Rev. B* **69**, 094417 (2004).
- [24] Y. Endoh and P. Böni, *J. Phys. Soc. Jpn.* **75**, 111002 (2006).
- [25] J. Lynn, *Phys. Rev. B* **11**, 2624 (1975); J. Lynn and H. Mook, *Phys. Rev. B* **23**, 198 (1981).
- [26] J. P. Wicksted, P. Böni, and G. Shirane, *Phys. Rev. B* **30**, 3655 (1984).
- [27] B. I. Halperin and C. Hohenberg, *Phys. Rev.* **177**, 952 (1969).
- [28] P. Résibois, and C. Piette, *Phys. Rev. Lett.* **24**, 514 (1970).
- [29] G. G. Lonzarich, and L. Taillerfer, *J. Phys. C* **18**, 4339 (1985).
- [30] T. Moriya, *Physica B* **91**, 235 (1977).
- [31] G. Shirane, J. E. Fischer, Y. Endoh, and K. Tajima, *Phys. Rev. Lett.* **59**, 351 (1987).
- [32] K. Tajima, Y. Endoh, J. E. Fischer, and G. Shirane, *Phys. Rev. B* **38**, 6954 (1988).
- [33] Y. Takahashi, *J. Phys. Condens. Matter* **9**, 2593 (1997).

Chapter 6

Polarised Neutron Scattering Measurements of $\text{La}_{0.82}\text{Sr}_{0.18}\text{CoO}_3$

‘Half polarised’ neutron inelastic scattering measurements of the ferromagnetic spin-waves in $\text{La}_{0.82}\text{Sr}_{0.18}\text{CoO}_3$ are described in this chapter. The dispersion of these spin-waves was well defined at low energies, allowing a spin-wave stiffness constant of $D = 216 \pm 14 \text{ meV \AA}^2$ to be measured. At higher energies the spin-waves became heavily damped. Several possible damping mechanisms are suggested, however it was not possible to determine unequivocally which of them was responsible for the observed effects.

6.1 Introduction

The materials with the general formula $\text{La}_{1-x}\text{Sr}_x\text{CoO}_3$ (LSCO)¹ are an interesting group of materials to study because they display many of the characteristics typical of the colossal magnetoresistance (CMR) perovskites [1, 2], and also share some similarities with giant magnetoresistance (GMR) heterostructures [3]. The latter materials are artificial structures in which ferromagnetic metallic sections are placed in a matrix of non-magnetic material, and have been extremely important for the development of efficient hard disk drives. Similar so-called ‘phase separation’ of ferromagnetic and non-magnetic media, occurring naturally rather than being engineered, has been observed in CMR materials. An example of such heterogeneity would be the formation of ‘islands’ of magnetically ordered ions surrounded by a region of the material that is non-magnetic. The most studied CMR perovskites to date have the general formula $\text{La}_{1-x}\text{A}_x\text{MnO}_3$, where A is a hole dopant such as Sr^{2+} , Ca^{2+} , Ba^{2+} , etc. The CMR effect is observed to be greatest near the critical temperature for the onset of bulk magnetic order [1].

There does not yet exist a complete theoretical understanding of the mechanisms which give rise to CMR. A good deal of progress has nevertheless been made and it is possible to outline some of the underlying physics of this effect. The phenomenon of double exchange (DE), introduced in section 1.2.1 and shown schematically in figure 6.1, whereby ferromagnetic alignment of adjacent ions where one has a single e_g electron and a half filled set of t_{2g} levels, and the other does not have the e_g electron, turns out to be important. The ferromagnetism is driven by the energy saving caused by hopping of the e_g electron, so mag-

¹LSCO would be a more obvious choice of acronym, however it is already commonly used to denote $\text{La}_{2-x}\text{Sr}_x\text{CuO}_4$, so LSCO is used to avoid confusion.

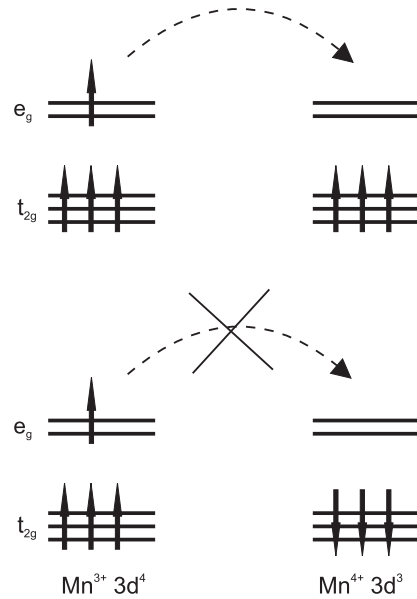


Figure 6.1: The double exchange mechanism. In the upper half the ferromagnetic case is shown, where electron hopping is possible. In the lower half of the figure the antiferromagnetic case is shown, where hopping is not possible

netoresistance can be explained by such a model, because application of a magnetic field will tend to align the t_{2g} cores and hence give rise to an increased amount of electron hopping, meaning a lower resistivity.

The mechanism described above does not fully explain CMR, however. The DE model would only give rise to a relatively small change in resistivity, whereas the CMR effect is too big to be explained by this alone. Millis *et al* [4] have proposed a possible mechanism for the enhancement of the magnetoresistance which is based on the existence of a strong electron–phonon coupling. This strong coupling results in a localisation of the conduction electrons, that is to say that the carriers should be considered as ‘polarons’ rather than electrons. It is proposed that this effect weakens as the material is cooled towards its critical temperature, so that the actual CMR results from the fact that the non-magnetic state would have a higher than expected resistivity. This qualitatively agrees with the fact that the largest CMR is observed near to the critical temperature – the application of a field is able to drive the system from a state in which there are polarons into the ferromagnetic metallic state. At lower temperatures the material would already be somewhat metallic so the change in resistivity would be smaller.

Bulk measurements of the magnetic and transport properties of LSCoO show dramatic changes with doping [5, 6]. Susceptibility measurements, shown in figure 6.2, show that the $x = 0$ material is non-magnetic, but as doping is increased the size of the moment increases rapidly, with a transition into a true ferromagnetic state at $x = 0.18$. The Curie temperature at $x = 0.18$ is 150 K, and T_C increases with further increase in doping. These measurements have been interpreted as arising from the growth of ferromagnetic clusters, the number and size of which increase as doping is increased, until percolation to a bulk ferromagnetic state occurs at $x = 0.18$.

As is shown in the left-hand panel of figure 6.3, in the ferromagnetic phase the hysteresis

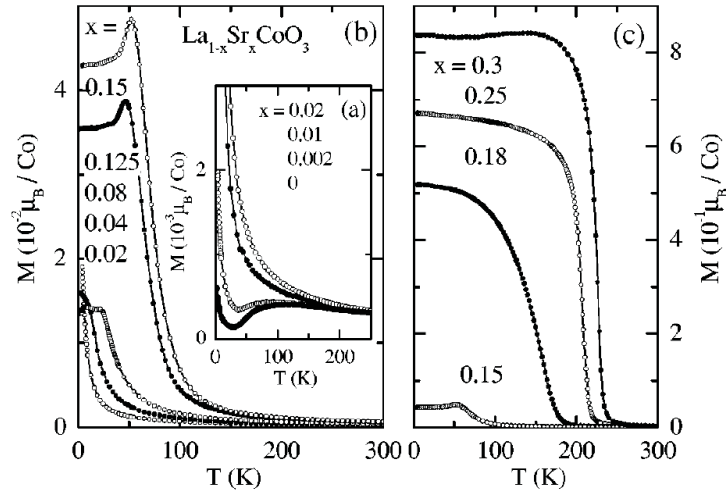


Figure 6.2: (After Kriener *et al* [5]) Magnetic susceptibility of $\text{La}_{1-x}\text{Sr}_x\text{CoO}_3$ as a function of temperature and doping x .

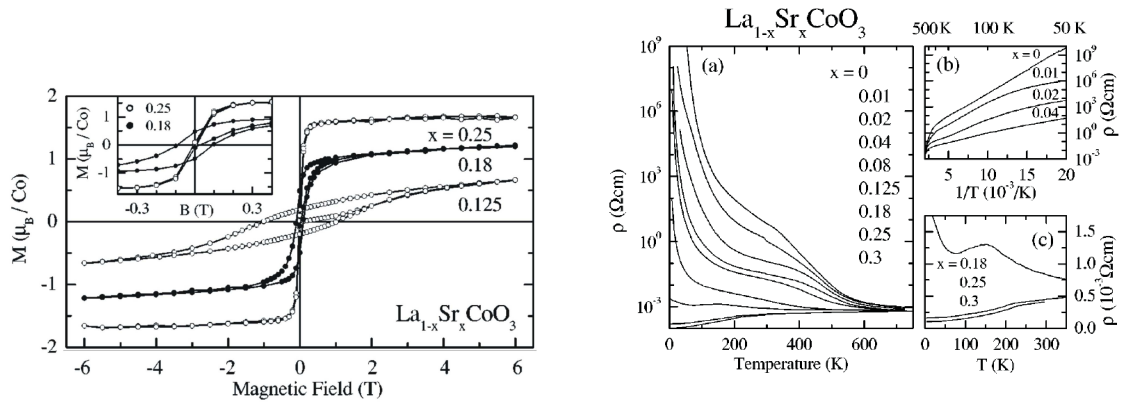


Figure 6.3: Left-hand panel (after Kriener *et al* [5]), magnetic susceptibility of $\text{La}_{1-x}\text{Sr}_x\text{CoO}_3$ as a function of applied magnetic field and doping x . Right-hand panel (after Kriener *et al* [5]), resistivity of $\text{La}_{1-x}\text{Sr}_x\text{CoO}_3$ as a function of temperature and doping x .

of the magnetisation with applied field decreases, as does the applied field necessary to reach saturation, with increasing doping above $x = 0.18$. The magnetic easy axis has been found to be the $(1, 0, 0)$ -direction in the rhombohedral unit cell [7], which corresponds to the $(1, 1, 0)$ -direction in pseudo-cubic notation. See appendix B for a general discussion on the use of pseudo-cubic notation for rhombohedral crystal structures.

The behaviour of the resistivity with temperature, shown in the right-hand panel of figure 6.3, is also found to vary as a function of doping [5, 6]. At $x = 0$ the material is a semiconductor, but the resistivity steadily decreases as holes are doped into the material. These measurements show that as the material tends towards ferromagnetism it also becomes increasingly metallic, i.e. the magnetism resides on itinerant rather than localised electrons. This aspect of LSCO bears many similarities to the behaviour of the CMR manganites.

Of perhaps the greatest importance are measurements of the magnetoresistance of LSCoO as a function of doping [8]. These show that for higher dopings, when the material is in a ferromagnetic metallic phase, the magnetoresistance is just a few percent. However when the doping reaches the critical level of $x = 0.18$ the MR becomes around 30%, and as the doping is decreased further the MR increases such that for $x = 0.09$ the resistivity drops by as much as 90% at low temperatures.

In the region of doping $0 < x \leq 0.18$ the material displays behaviour which is in some respects like that of a spin glass. In a true spin glass dilute spins in a solid are randomly distributed, however there exist interactions between spins that act to freeze them into a metastable state with short range magnetic order [9]. The spin glass phase in LSCoO has been investigated by Wu *et al* [6] for $x = 0.15$ by cooling the material in a magnetic field, removing the field and observing the evolution of the magnetisation and resistivity over time. They found that the material appears to relax, with magnetisation decreasing and resistivity increasing, as time passes, behaviour typical of a spin glass. The interpretation of these measurements is that as holes are doped into the material clusters of metallic ferromagnetic regions form, these clusters becoming more numerous and larger as doping is increased. At the ferromagnetic-metallic phase transition at $x = 0.18$ these clusters percolate to form a bulk metallic ferromagnet. Below this phase transition the inter-cluster interactions are what give rise to the spin-glass-like behaviour, whereas the intra cluster interactions give rise to the decreasing resistivity and increasing magnetic moment. Co NMR [10] and small-angle neutron scattering measurements [11] have demonstrated the veracity of the cluster model, and have furthermore shown that the nature of the correlations within the clusters is the same as those in the bulk metallic ferromagnetic phase.

Giblin *et al* [12] have proposed, based on μSR measurements on the $x = 0.03$ material, that in addition the ferromagnetic clusters interact with the underlying ‘matrix’ of LaCoO_3 . A neutron inelastic scattering study on very lightly doped LSCoO ($x = 0.002$) by Podlesnyak *et al* [13], which was performed on a powder sample at low temperatures, found that the presence of even a small number of holes appears to induce a spin-state transition in the Co^{3+} ions in the surrounding matrix of LaCoO_3 from a non-magnetic ground state to an excited magnetic state. This measurement ties in quite well with the μSR measurements described above.

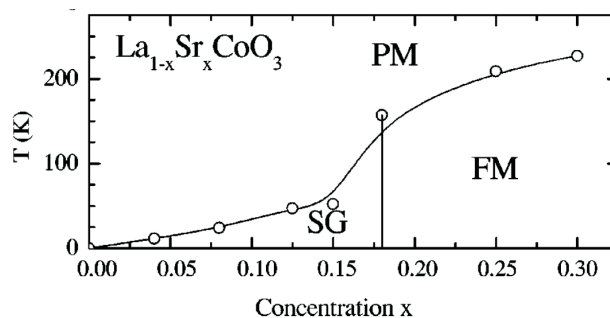


Figure 6.4: (After Kriener *et al* [5]) The magnetic phase diagram of $\text{La}_{1-x}\text{Sr}_x\text{CoO}_3$, showing the spin glass (SG), paramagnetic (PM), and ferromagnetic (FM) phases.

LSCoO crystallises in the rhombohedral space group $R\bar{3}c$. The specific material studied in this work had $x = 0.18$, and previous work [7] shows that the rhombohedral lattice parameters are $a = 5.371\text{\AA}$ and $\alpha = 60.758^\circ$. This lattice can be regarded as a slightly

distorted cubic lattice, with pseudo-cubic² lattice parameters $a \approx 3.8$ and $\alpha = 90^\circ$.

There have already been several neutron scattering studies of the magnetic correlations in LSCoO [7, 13, 14, 15]. Caciuffo *et al* [7] conducted a powder diffraction study for a range of different dopings, and were able to observe enhancement of weak Bragg peaks (where the nuclear structure factor was very small, or indeed zero) due to the onset of ferromagnetism. They found that this enhancement was very large for $x \geq 0.2$ but was still non-negligible for $x < 0.18$, i.e. below the ferromagnetic percolation threshold, supporting the idea that ferromagnetic clusters form below the critical doping level. Phelan *et al* [14] measured the undoped material and then the doped material using single crystal and powder samples. The excitation at the ferromagnetic $(0, 0, 1)$ -position (in pseudo-cubic notation) at about 0.6 meV found in the undoped material (see section 5.1) has vanished by $x = 0.1$, concomitant with an increase in intensity of the ferromagnetic Bragg peak. This is interpreted as follows: on doping there occurs the formation of Co^{4+} ions with $S = 1/2$ in the t_{2g}^5 configuration, and these interact with the surrounding Co^{3+} to induce a $S = 1$, $t_{2g}^5 e_g^1$ state. Hopping between these ions then mediates the conductivity, i.e. double exchange, which means that as the clusters of Co^{4+} ions become bigger the conductivity should increase. In a different study Phelan *et al* [15] observe a superstructure in the neutron diffraction from single crystals. The intensity of the scattering from this superstructure is greatest at a doping just below the transition to the bulk ferromagnetic state. The origin of this superstructure is tentatively proposed to arise from local distortions induced by the clustering.

Manganite compounds with the formula $\text{A}_{1-x}\text{B}_x\text{MnO}_3$, where A are rare-earth and B are alkaline-earth ions, are well known for their CMR properties. There exists a much greater body of literature concerning neutron scattering experiments on these materials [16, 17, 18, 19, 20, 21, 22], so it is instructive to review it.

Ye *et al* [17] show that for many of the CMR manganites there exists a softening of the magnon modes near to the zone boundary, which can be fitted using a Heisenberg ferromagnetic Hamiltonian with nearest neighbour and 4th-nearest neighbour interactions, the ratio of which seems to be Curie temperature-independent. This latter observation would appear to rule out on-site disorder, double exchange, coupling with optic-mode phonons, and orbital fluctuations, as giving rise to zone-boundary softening of the magnon modes. It does not appear that this behaviour is universal, however, since the magnon spectrum of $\text{La}_{0.7}\text{Pb}_{0.3}\text{MnO}_3$ is found to be adequately described by a simple Heisenberg model with only nearest neighbour coupling.

In any case recent work [19] has cast doubt on some of the measurements described above. Many of the previous neutron scattering experiments were performed with unpolarised neutrons, whereas theirs, which used a polarised neutron setup, showed that the softening of the magnon modes was much less dramatic in $\text{La}_{0.7}\text{Ca}_{0.3}\text{MnO}_3$ than had been previously reported. Moussa *et al* [23] have very recently performed a very extensive study of $\text{La}_{1-x}(\text{Ca}_{1-y}\text{Sr}_y)_x\text{MnO}_3$ using unpolarised neutrons. They showed that the magnon dispersion crosses phonon dispersions at several different points between the zone centre and zone boundary, and the softening and broadening of spin-wave modes observed previously was actually an artifact of the proximity of the magnon and phonon dispersions. The data were satisfactorily described by 4th-nearest neighbour interactions, but there is some broadening of the spin-wave modes near the magnetic zone boundary, which was attributed to random

²See appendix B.

fluctuations in the values of the exchange parameters.

The holes in the CMR manganite $\text{La}_{1-x}\text{Ca}_x\text{MnO}_3$ are known to form clusters within a hole poor matrix (which is magnetic) [24] for $0.05 < x < 0.125$, similar to the effect observed in LSCoO . Neutron scattering measurements by Hennion *et al* [25] on the $x = 0.17$ and $x = 0.2$ materials have shown that there exist standing-wave spin excitations at discrete energy levels. Analysis of the exchange coupling within these clusters show that in fact they correspond to standing spin-waves within hole-poor clusters, embedded within a hole-rich matrix. This analysis was rendered somewhat easier because both the hole-rich and hole-poor regions are magnetic, so with very low and very high doping it had been possible to characterise these regions independently. In LSCoO it is less clear whether or not the hole-poor regions are magnetic, and hence whether such a scenario could occur in this material as well.

6.1.1 Motivations

There are several motivations for performing a neutron scattering experiment on LSCoO . Whilst there exists a large body of literature on neutron scattering experiments on the CMR manganites, comparatively little has been done with the cobaltites, which also display CMR effects. Comparison between the magnetic scattering data of manganites and cobaltites might then shed some light on the similarities and differences between the origin of the CMR in these two classes of materials.

One major difference is the nature of the undoped parent compounds, which for the manganites is magnetic whereas for the cobaltites is non-magnetic, and this difference may be evidenced in the spin excitation spectra. Another clear difference relates to the spin states of the two classes of materials. The Mn^{3+} and Mn^{4+} ions have $t_{2g}^3 e_g^1$ and t_{2g}^3 configurations respectively, whereas the Co^{3+} ions are in the $t_{2g}^6 e_g^0$, $t_{2g}^5 e_g^1$, or $t_{2g}^4 e_g^2$ states, and the Co^{4+} is in the t_{2g}^5 configuration. The manganites are therefore orbitally ordered, whereas the degeneracy of the spin states in the cobaltites is greater. This difference may also contribute to differences in the CMR properties, and also in the neutron magnetic scattering spectra.

6.2 Experimental details

In order to measure the ferromagnetic fluctuations (ferromagnons) in LSCoO , with $x = 0.18$, using polarised neutrons the ferromagnetic domains into which the material would be divided in zero applied field needed to be aligned. In order to align as many domains as possible the sample was field cooled from room temperature to 2 K in an applied field of 3.5 T. Once the temperature had stabilised at 2 K the field was ramped down slightly to 1 T. Inspection of the $M - H$ curve of LSCoO shown in the left-hand panel of figure 6.3 shows that the reduction in magnetisation, and hence domain alignment, only decreases by about 10% on decreasing the applied field from 3.5 T to 1 T. A smaller applied field than 3.5 T makes the experiment easier to conduct, as it makes it easier to correct for stray fields at the flipper which would otherwise prevent its proper operation.

The magnetic field was applied using an Oxford Instruments cryomagnet with a horizontal magnetic field. The field in such an instrument is provided by four oppositely poled 10 T

vertical magnets, giving a region in the centre of the bore of the cryostat where the non-uniformity of field was at worst just 3% [26]. There were a few ‘dead zones’ on the cryostat where there were support structures for the vertical magnets, however the positions of these were checked so that situations where the incident or scattered beam lay close to such zones were avoided.

For a polarised neutron inelastic scattering measurement with a magnetic field applied to the sample the cross-section is somewhat modified, in that the magnetic field affects the neutron polarisation as well as the moments in the sample. In particular the polarisation state of the scattered beam will be modified. Note that a full derivation of the following is given in the book of Marshall and Lovesey [27].

For the case of a Heisenberg ferromagnet the polarisation of the scattered beam, \mathbf{P}' , when there is creation (+) or annihilation (−) of a magnon is given by

$$\begin{aligned} \mathbf{P}'_{\pm} = & \left[-2\hat{\mathbf{Q}}(\hat{\mathbf{Q}}\cdot\hat{\boldsymbol{\eta}}) \left\{ (\hat{\mathbf{Q}}\cdot\mathbf{P})(\hat{\mathbf{Q}}\cdot\hat{\boldsymbol{\eta}}) \mp 1 \right\} - \mathbf{P} \left\{ 1 - (\hat{\mathbf{Q}}\cdot\hat{\boldsymbol{\eta}})^2 \right\} + 2\boldsymbol{\eta}_{\perp} \times (\mathbf{P}_{\perp} \cdot \boldsymbol{\eta}_{\perp}) \right] \\ & \times \left\{ 1 + (\hat{\mathbf{Q}}\cdot\hat{\boldsymbol{\eta}})^2 \mp 2(\hat{\mathbf{Q}}\cdot\mathbf{P})(\hat{\mathbf{Q}}\cdot\hat{\boldsymbol{\eta}}) \right\}^{-1} \end{aligned} \quad (6.1)$$

where the unit vector parallel to the wavevector is denoted by $\hat{\mathbf{Q}}$, \mathbf{P} denotes the polarisation of the incident neutron beam, $\boldsymbol{\eta}$ defines the direction of the spins (and hence applied field), and the \perp subscripts refer to the component of a variable which is perpendicular to the scattering wavevector. For an unpolarised incident beam ($\mathbf{P} = 0$) this simplifies to

$$\mathbf{P}'_{\pm} = \frac{\pm 2\hat{\mathbf{Q}}(\hat{\mathbf{Q}}\cdot\hat{\boldsymbol{\eta}})}{1 + (\hat{\mathbf{Q}}\cdot\hat{\boldsymbol{\eta}})^2} \quad (6.2)$$

meaning that if the spins are perpendicular to the scattered wavevector then the scattered beam is unpolarised, and hence there is no way of distinguishing magnetic from non-magnetic scattering. Such a case would occur if a vertical magnetic field were used with a horizontal scattering plane. On the other hand if a horizontal magnetic field is used and scans are performed where the field direction and the wavevector are kept parallel, then $\hat{\mathbf{Q}} \parallel \hat{\boldsymbol{\eta}}$, and the final polarisation state is parallel to the scattering wavevector. A non-magnetic signal would not polarise the scattered beam, so magnetic and non-magnetic signals can be separated in this way if a horizontal field with scans parallel to the field direction are used.

In the case where the incident beam is polarised, considering now only magnon creation for simplicity, the final polarisation state is given by the somewhat more complicated equation 6.1. For a horizontal applied magnetic field we have $\hat{\mathbf{Q}} \parallel \hat{\boldsymbol{\eta}}$, and in addition $\hat{\boldsymbol{\eta}} \parallel \mathbf{P}$ or $\hat{\boldsymbol{\eta}}$ is antiparallel to \mathbf{P} , if a flipper is placed in the incident beam and is off or on respectively. Inspecting equation 6.1 we get

$$\mathbf{P}'_{\text{parallel}} = 0 \quad (6.3)$$

$$\mathbf{P}'_{\text{antiparallel}} = \hat{\mathbf{Q}} \quad (6.4)$$

which means that of the four possible combinations of flipper states, only one will show a signal arising from the magnon.

There are, then, two options for measuring ferromagnons when using a horizontal magnetic field. For almost all of the work presented in this chapter an unpolarised incident neutron beam was used. This is because it was found that preventing stray fields from interfering with the operation of both flippers simultaneously was practically impossible. In addition the so-called ‘half polarised’ (i.e. unpolarised incident beam, polarisation analysed scattered beam) setup does have some advantages over the fully polarised setup: it is easier to find a configuration of the spectrometer where stray fields do not affect the performance of the flipper very much, and the incident flux from a Si monochromator is significantly higher than that from a Heusler monochromator. The disadvantage is that non-magnetic and magnetic scattering are mixed together, even in the channel which shows the magnetic scattering, hence making weak signals harder to measure above the background.

Prevention of stray fields affecting the one remaining flipper (in the scattered beam) was important to maintain the possibility of polarisation analysis. Therefore an electromagnet, whose current could be varied from the instrument control computer, was placed in front of the flipper so that an opposite ‘compensation’ field could be applied to make the environment of the flipper free from unwanted magnetic fields. The stray fields at the flipper were strongly dependent on the orientation of the spectrometer, specifically the angle of the sample relative to the incident beam (ω) and the scattering angle minus this ($2\theta - \omega$), so the current in the electromagnet had to be adjusted for every data point. Calibrations for the current variation with spectrometer configuration were done using germanium, a material from which the scattering is purely nuclear in origin, with a negligible magnetic contribution. The required currents to give optimum flipping ratio were recorded and then interpolated for every spectrometer configuration.

Often sections of scans during the experiment were found to require a linear variation of the flipper currents, so that rather than constructing each scan from a discrete set of points the scans could be broken into several sections with flipper currents as a linear scan variable. The best achievable flipping ratios were still dependent on the orientation of the magnetic field with respect to the flipper, however on average the flipping ratio was about 8 for $k_f = 4.1 \text{ \AA}^{-1}$ and about 17 for $k_f = 2.662 \text{ \AA}^{-1}$.

For this experiment the spectrometer was set to give fixed final wavevector of either $k_f = 2.662 \text{ \AA}^{-1}$ or $k_f = 4.1 \text{ \AA}^{-1}$, depending on the energy of the excitation being measured. A pyrolytic graphite (PG) filter was placed in the scattered beam in order to reduce contamination of the signal by scattering from higher harmonic scattering. The sample was mounted with the pseudo-cubic $(1, 0, 0) - (0, 1, 1)$ plane horizontal (i.e the scattering plane) and hence the $(0, \bar{1}, 1)$ -direction vertical. The sample used for this experiment was grown using the floating zone method [5], and its mass was 8.76 g. The sample comprised a single cylindrical rod about 4cm long with a diameter of about 0.8cm, and was mounted on an aluminium bracket, with a small amount of GE varnish and secured additionally with aluminium wires. When mounted inside the cryostat the sample was encased in a bag made from thin aluminium foil so that if the sample was forced off the mount by magnetic forces it would not be lost to the bottom of the cryostat.

In the horizontal field the ferromagnons around the $(0\ 1\ 1)$ Bragg peak were measured. This was because it has been found that the Co^{4+} moments order along the $(0, 1, 1)$ -direction

[7] and thus with the constraint of using a horizontal field scans had to be performed with the field (and therefore the wavevector) along this direction, i.e. scans of the form $(0, 1 + H, 1 + H)$. This is not the optimum setup as far as possible contamination of the signal by non-magnetic scattering is concerned because, after calculating the structure factors (see appendix C) and checking them on the instrument itself, for a pseudo-cubic lattice of this type the $(1\ 0\ 0)$ -type positions, and the low energy acoustic phonons dispersing out of them, have a much smaller structure factor. It was therefore imperative to set up the flippers carefully so that the best possible flipping ratio could be obtained at all energies, but particularly at higher energies, where $k_f = 4.1\ \text{\AA}^{-1}$ was required and the magnons may be weaker but phonons comparatively stronger.

6.3 Results

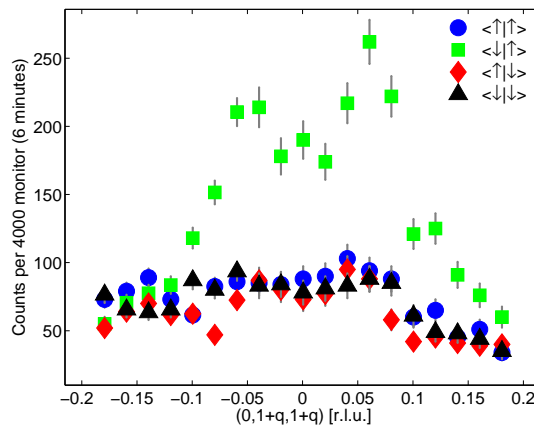


Figure 6.5: Raw data from a constant energy Q -scan at $E = 4\ \text{meV}$, $T = 2\ \text{K}$, using a fully polarised setup.

Figure 6.5 shows a sample scan from a slightly different experimental setup from the one described. One fixed-energy Q -scan was performed using a fully polarised setup, i.e. with a Heusler monochromator so that the incident beam was polarised with flippers in the incident and scattered beams. In order to prove beyond doubt the existence of ferromagnetic spin excitations in this material the scattering should appear in just one channel, and this is indeed the case since it appears in the channel where the incident beam flipper was on but the scattered beam flipper was off, i.e. one of the true spin flip (magnetic) channels.

The rest of the data presented in this chapter were taken using the half-polarised setup. Figure 6.6 shows all of the polarisation-analysed scans, i.e. non-spin-flip (flipper off) minus spin-flip (flipper on) channel, combined. The colours, representing intensity, have been smoothed by interpolation, so the figure is for the purpose of illustration only. The black dots show points in (\mathbf{Q}, E) -space where the scattering was measured, so special care should be taken when considering colours on this map far from any such dots, because the interpolation in such regions is a less reliable indicator of the true intensity there³. This figure shows us several features which will guide our understanding of the physics of LSCoO. First is

³Note that the data have been symmetrised, e.g. data taken at the wavevector $(0, 1.4, 1.4)$ are shown on this figure at $(0, 0.6, 0.6)$ because they are symmetrically equivalent once they have been corrected for the magnetic form factor.

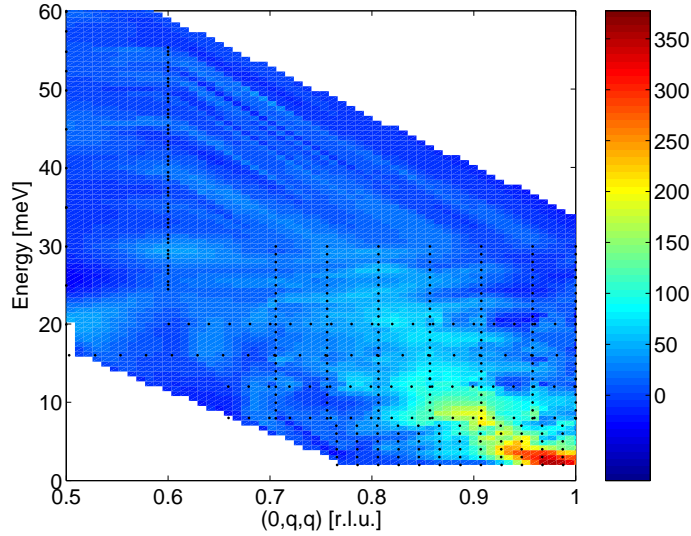


Figure 6.6: Colour map showing the magnetic scattering (NSF–SF), all scans combined and symmetrised. $T = 2\text{ K}$.

that at low energy there are well defined spin-waves which disperse from the ferromagnetic wavevector $(0, 1, 1)$. Close to the origin these spin-waves can be approximated by a quadratic, and the fitting of these scans will allow the calculation of the spin-wave stiffness constant for this material. Second is that above about 12 meV the spin-waves broaden in both energy and wavevector quite significantly, and above about 20 meV the magnetic scattering is very diffuse and hence very hard to characterise accurately.

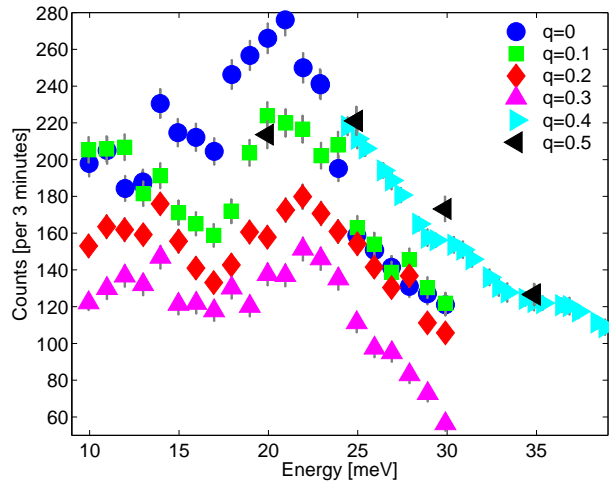


Figure 6.7: Energy scans in the (non-magnetic) spin-flip channel showing the optic phonon. q is defined such that the measurements were taken at $\mathbf{Q} = (0, 1 - q, 1 - q)$. $T = 2\text{ K}$.

Figure 6.7 shows scattering in the spin-flip (non-magnetic) channel at a range of wavevectors across the magnetic Brillouin zone, showing the presence of an optic mode phonon around 20 meV. Note that for $0.4 \leq q \leq 0.5$ the scattering was actually measured at the symmetrically equivalent⁴ wavevector $(0, 1 + q, 1 + q)$, due to geometrical constraints of the

⁴I adopt the convention of denoting the actual wavevector used for the measurement as $(0, Q, Q)$, and the wavevector relative to $(0, 1, 1)$ as $(0, q, q)$. So for $\mathbf{Q} = (0, 1.4, 1.4)$, $\mathbf{q} = (0, 0.4, 0.4)$.

spectrometer. At larger wavevectors the phonon structure factor is generally larger, which would explain why the background and the phonon signal are larger for $q = 0.4$ and 0.5 . Due to the fact that there were only two polarisation channels, both of which contain some non-magnetic scattering, one would expect the error of the subtraction measurements to determine the magnetic signal to be higher in the vicinity of this phonon, and hence the magnons would be more difficult to measure here. For example, if the subtraction giving the magnetic signal was $(25 \pm 5) - (9 \pm 3) = 16 \pm 6$ in a region with little non-magnetic scattering, then a magnetic signal of the same magnitude near a large non-magnetic signal would have a much bigger error $-(125 \pm 11) - (109 \pm 10) = 16 \pm 15$. This means that scans which pass over the vicinity of 20 meV required longer counting times in order to reduce the errors.

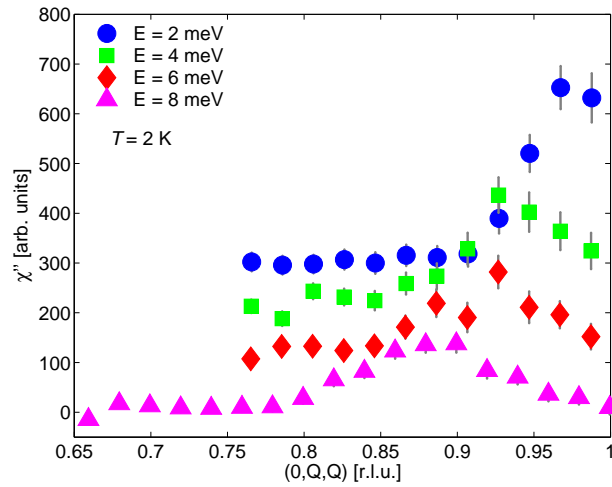


Figure 6.8: Constant energy Q-scans of the magnetic scattering (NSF-SF). $T = 2$ K. Successive scans are displaced by 100 for clarity.

Figure 6.8 shows several fixed-energy Q-scans in the magnetic scattering channel, for relatively low energies. At these low energies it was possible to use $k_f = 2.662 \text{ \AA}^{-1}$, at which final wavevector the flipping ratio was significantly better and hence the cross-contamination of non-magnetic scattering into the magnetic scattering channel was much lower. A clear dispersion from the origin is visible, accompanied by a decrease in the intensity of the scattering. These data, and the data from similar scans taken at other nearby energies, can be fitted fairly easily and the results compared with the predictions of linear spin-wave theory.

Figure 6.9 shows fits (solid lines) to the magnetic signal, offset by +1, from fixed-wavevector energy scans at a range of wavevectors on a logarithmic scale. A single Gaussian function, with a flat background that was fixed to zero, was used as the fitting function. The fits show that as the wavevector moves away from the ferromagnetic zone centre, the excitation disperses out to a higher energy. The fits also illustrate that the energy width of the excitation increases markedly at higher energies and wavevectors.

Figure 6.10 shows the results of fits to the constant-energy Q-scans (red circles with horizontal error bars), and constant-wavevector energy-scans (blue circles with vertical error bars). The Q-scans were fitted with two Lorentzians, which were constrained to be centred at symmetrically equivalent wavevectors relative to the ferromagnetic zone centre, and also to have the same width. The energy scans were fitted, as described above, using a single

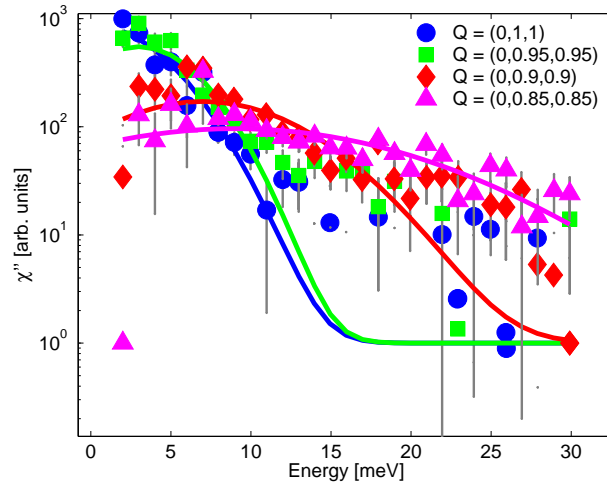


Figure 6.9: Fits to fixed-wavevector energy scans, using a single Gaussian. $T = 2$ K. Note that all of the data points and fits have been offset by +1 so that a logarithmic scale can be used.

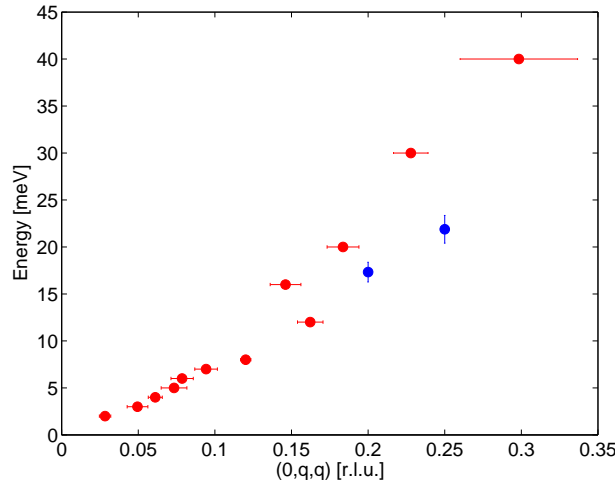


Figure 6.10: Fits to Q - and E -scans to determine a dispersion relationship. Red filled circles with horizontal errorbars are determined from Q -scans, blue filled circles with vertical errorbars are from E -scans.

Gaussian. Note that only the higher energy fits are shown because for lower energies the centre positions of the Gaussians were fixed to values determined from the fits to the Q -scans.

It is immediately obvious that not all of the scans provide consistent results, particularly for $E > 10$ meV, where for most wavevectors the Q -scans appear to overestimate the energy of the dispersive mode compared to the results of fitting energy scans. In some cases this may be due to choice of fitting function – if the line shape of the data are not well fitted by the Gaussian or Lorentzian functions, e.g. because they are asymmetric, then the value of the centre of the fit may not be correct. There is also the question of the error bars, which seem to underestimate the error on the measurement somewhat. This again could be due to the line shape of the data compared to the fit function – if the value of $\chi^2 \gg 1$ then the error on the resulting fit will be given by the fitting program as being unrealistically small⁵.

⁵The errors are only meaningful if $\chi^2 \approx 1$, because the error on a particular variable is calculated by

It is also possible that, due to a combination of the line shape of the excitations and the shape of the resolution ellipsoid, that the maximum co-ordinates given by a cut along the energy axis are not the same as those given by a cut along the $(0, q, q)$ axis.

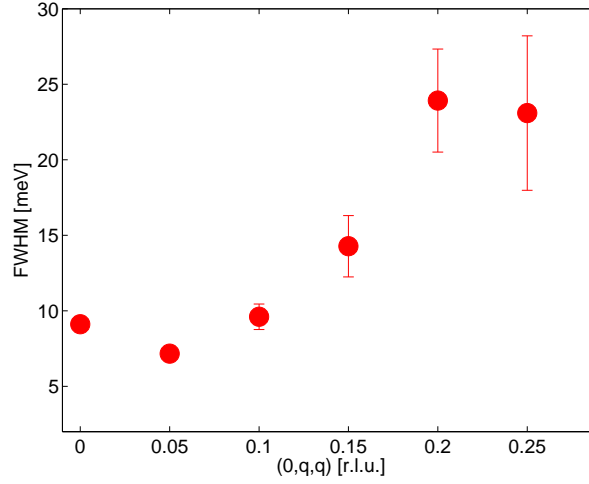


Figure 6.11: Full width at half maximum (FWHM) in energy of the magnetic excitations as a function of wavevector.

Figure 6.11 shows the FWHM of the energy scans, determined from the Gaussian fits already described, as a function of wavevector. It is clear that for lower energy excitations the width is relatively constant, however it increases markedly above about 10 meV ($q = 0.15$) becoming close to the energy of the excitations themselves.

6.4 Analysis and Discussion

The low energy data ($E \leq 7$ meV) were fitted using a quadratic dispersion of the form

$$E_0 = \Delta + Dq^2 \quad (6.5)$$

where E_0 is the energy of the spin-wave, D is the spin-wave stiffness constant and Δ is an energy gap. If the spin-waves are damped then the intensity of the scattering I can be described using a damped harmonic oscillator model, i.e.

$$I \propto \frac{4\Gamma E E_0}{(E^2 - E_0^2)^2 + 4\Gamma^2 E^2} \quad (6.6)$$

where Γ is the damping constant. This function has a maximum, which corresponds to a spin-wave peak, when $\frac{dI}{dE} = 0$. Using the quotient rule, this is when

$$E_{\max}^2 = \frac{-(4\Gamma^2 - 2E_0^2) \pm \sqrt{(4\Gamma^2 - 2E_0^2)^2 + 12E_0^4}}{6} \quad (6.7)$$

varying that parameter from its optimum value until $\Delta\chi^2 = 1$.

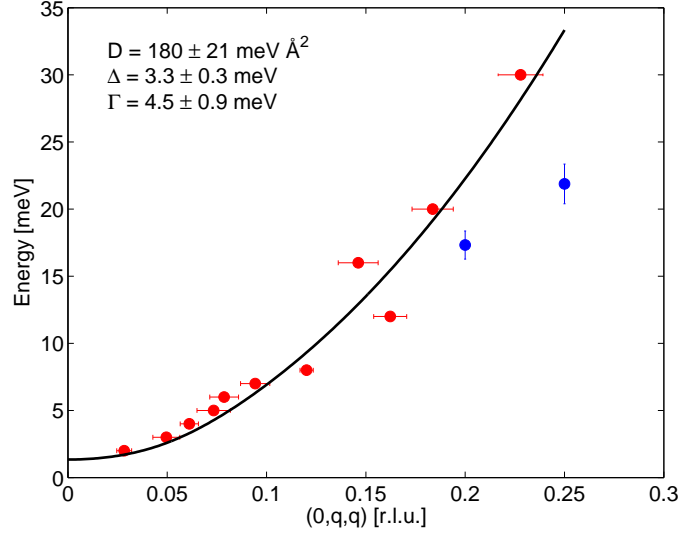


Figure 6.12: Damped harmonic oscillator fit to the low energy spin-waves, assuming a quadratic dispersion. The raw data have been fitted in this case.

The positions of the excitation peaks, determined by fitting to Lorentzians, were presented in figure 6.10. For the peaks below 7 meV these data were re-fitted to equation 6.7, and the results are shown in figure 6.12. The stiffness constant D_1 was found to be $180 \pm 20 \text{ meV } \text{\AA}^2$, the energy gap Δ_1 was $3.3 \pm 0.3 \text{ meV}$, and the damping constant Γ_1 was $4.5 \pm 0.9 \text{ meV}$. It appears from figure 6.12 that these parameters give a low energy dispersion curve that is slightly too low in energy, which at first glance is confusing. However recall that the points and errorbars on these plots were found by fitting the raw data to a Lorentzian line shape, whereas the low energy dispersion parameters were found by re-fitting the raw data with the damped harmonic oscillator function given by a combination of eq. 6.5 and eq. 6.6. The line shape given by this pair of functions is not the same Lorentzian, and it is this that results in the discrepancy between the points and the line in figure 6.12. To find an alternative set of parameters, one can fit the ‘processed’ data, i.e. by fitting a line to the points shown in figure 6.12, rather than fitting the raw data. In this case one sets $\frac{dI}{dq} = \frac{dI}{dE_0} \cdot \frac{dE_0}{dq} = 0$, which results in

$$E_{0\text{max}}^2 = \frac{2E^2 \mp \sqrt{4E^4 + (48\Gamma^2 E^2 + 12E^4)}}{6} \quad (6.8)$$

The resulting fit from equation 6.8 is shown in figure 6.13. The parameters in this case are $D_2 = 216 \pm 14 \text{ meV } \text{\AA}^2$, $\Delta_2 = 2.3 \pm 2.0 \text{ meV}$, and $\Gamma_2 = 2.7 \pm 5.3 \text{ meV}$, and more or less agree with the parameters found using the other fitting method.

These results can be compared to similar measurements in the CMR manganite $\text{La}_{0.8}\text{Sr}_{0.2}\text{MnO}_3$ [16] for which $D_{\text{LSMO}} \approx 150 \text{ meV } \text{\AA}^2$ and $\Delta_{\text{LSMO}} \leq 0.04 \text{ meV}$, so it appears the low energy spin-waves are stiffer in LSCO but that the energy gap is larger, although this latter quantity is not especially well constrained by the data presented here. The larger stiffness constant shows that in LSCO the ferromagnetic exchange between magnetic ions is stronger than in a similarly doped manganite compound.

For a nearest-neighbour interaction Heisenberg Hamiltonian, $D = 2SJ a^2$ (see section

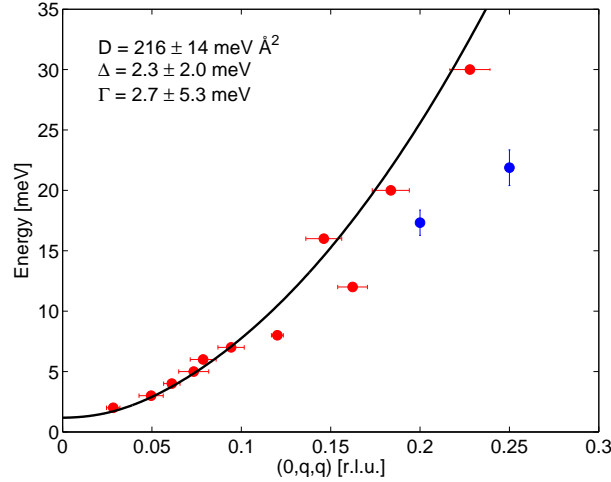


Figure 6.13: Damped harmonic oscillator fit to the low energy spin-waves, assuming a quadratic dispersion. The processed data have been fitted in this case.

1.3.1), where S is the spin quantum number of the system, J is the nearest neighbour exchange constant, and a is the lattice parameter. Although it is not clear whether only the Co^{4+} spins with $S = 1/2$ are ferromagnetically correlated, or whether the Co^{3+} spins with $S = 1$ or $S = 2$ are also correlated, it is possible nevertheless to write an ‘average’ Hamiltonian. In such a Hamiltonian we assume that $S = 1/2$ and then determine the exchange constants accordingly. If there is no clear way to separate the Co^{4+} and the Co^{3+} contributions to the magnetic scattering then this is the only sensible approach to take. Taking the first set of values for the spin-wave stiffness constant we find that $J_{\text{fit1}} = 12.3 \pm 1.5 \text{ meV}$. The same Heisenberg model also tells us that the band-width of the magnon spectrum is $8JS$ for dispersion from the $(0, 1, 1)$ wavevector parallel to $(0, 1, 1)$. This gives a band-width of 49.2 meV , i.e. the zone boundary magnon in such a model would have an energy of $52.5 \pm 6 \text{ meV}$. From the alternative fit we find $J_{\text{fit2}} = 14.8 \pm 1.0 \text{ meV}$, and a band-width of $61.5 \pm 2.8 \text{ meV}$.

It is clear from inspection of the data presented in figure 6.14, which shows energy scans near the Brillouin zone boundary, that this model does not provide a complete description of the physics of LSCoO , because there is no evidence of a signal near 50 meV in any of the energy scans shown. This leaves three possibilities; either the band-width of the magnons is greater than expected from the nearest-neighbour Heisenberg model; the band width is very much less than the expected value and is lower than the minimum energy of the scans shown; or the magnon signal becomes so weak as to be unobservable near the zone boundary due to some additional piece of physics.

Considering the first possibility, that the spin excitations at the zone boundary exist at an energy greater than $\sim 60 \text{ meV}$, it is hard to reconcile this possibility with the measurements of the low energy dispersion. The band width would reduce if higher order neighbour terms were to be introduced to the Heisenberg model, so the nearest-neighbour only bandwidth is an upper limit on the bandwidth in this type of model. The excellent agreement between the quadratic dispersion predicted in the Heisenberg model and the low energy measurements strongly suggests that such a model is appropriate to this system. So on this basis, an increase in the band width of the spin excitations beyond that expected from a nearest-neighbour Heisenberg model is ruled out.

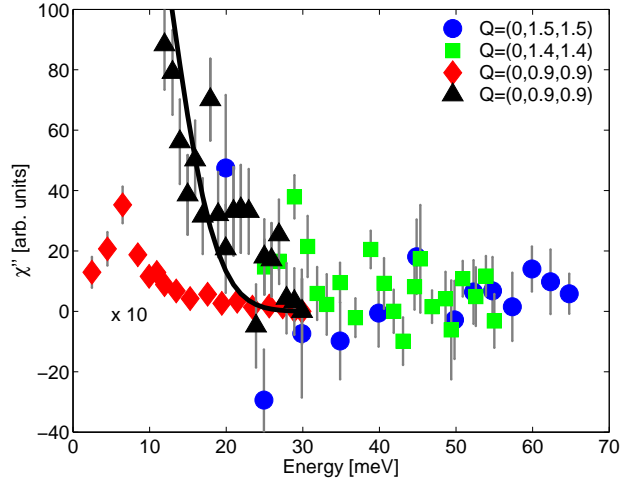


Figure 6.14: Fixed wavevector energy scans, comparing a scan at $(0, 0.9, 0.9)$ where there is a clear spin-wave peak, with scans at $(0, 1.4, 1.4)$ and $(0, 1.5, 1.5)$, where there is no apparent signal. The scan at $(0, 0.9, 0.9)$ is shown twice, black triangles and the black line show it to scale with a fit, whereas red diamonds show it reduced by a factor of 10.

In hole-doped manganites the second possibility, of a softening of the magnon modes at higher wavevectors, has previously been encountered [17, 18] and several authors have introduced longer ranged couplings to fit their data. It has been found that 2nd and 3rd nearest neighbour couplings seem not to be important, however 4th nearest neighbour couplings are. A Heisenberg model which includes nearest- and 4th-nearest neighbour interactions, for the case of scans along the $(0, q, q)$ direction, gives a dispersion relation of the form

$$E_0 = 2J_1[1 - \cos(2\pi q)] + 4J_4[1 - \cos^2(2\pi q)] \quad (6.9)$$

where J_1 is the nearest-neighbour exchange constant, and J_4 is the 4th nearest-neighbour exchange constant, and the $S = 1/2$ factor has been incorporated into the pre-factors of the two terms on the right hand side. Equation 6.9 can be calculated for small wavevectors using a Taylor expansion of the cosine terms. Doing this gives

$$E_0 = \Delta + (D_1 + D_4)q^2 \quad (6.10)$$

where $D_1 = 8J_1S\pi^2$ and $D_4 = 32J_4S\pi^2$. Notice that for this definition the D_n s are defined in units of meV r.l.u.^{-2} , unlike in equation 6.5. Converting the value of D found from fitting the processed data into these units, we get $D_{\text{fit2}}^{\text{r.l.u.}} = 584 \pm 38 \text{ meV r.l.u.}^{-2}$. The constraint $(D_1 + D_4) = 584$ means we can calculate what the full dispersion would look like for any given ratio of J_1 and J_4 . One limiting case is when $J_4 = 0$, i.e. nearest-neighbour interactions only, and another would be when $J_4 > J_1$. Specifically it is when the ratio $4J_4/J_1 \rightarrow \infty$. The expected dispersions are shown in figure 6.15 for the case $J_4 = 0$ and $4J_4/J_1 = 10$.

This figure shows that the addition of a 4th-nearest neighbour term results in softening of the magnon energy for larger wavevectors, and in fact the size of the softening compared to the nearest-neighbour only case is a measure of J_4 . It is clear from the data that in LSCO any magnon softening due to interactions of this type must be very small. Of course

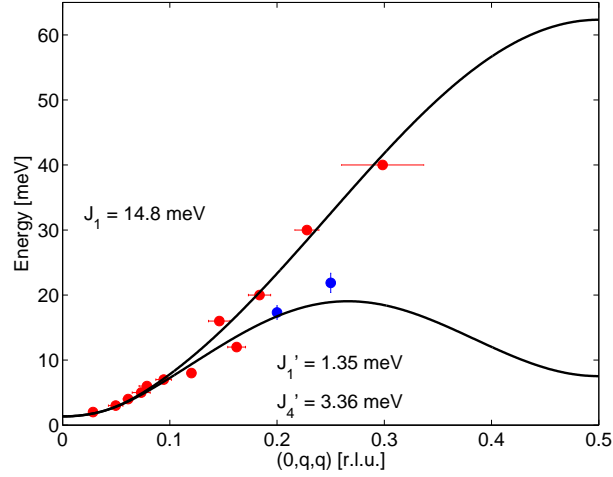


Figure 6.15: A comparison of the magnon dispersion with nearest-neighbour only terms (upper curve), and with $4J'_4/J'_1 = 10$ (lower curve), with identical spin-wave stiffness constants.

this mechanism for magnon softening does not of itself provide any explanation of why the width, Γ , increases so dramatically away from the magnetic zone centre. Indeed it would seem that this effect is the more significant one in LSCoO. It appears, therefore, that 4th nearest-neighbour interactions do not play a significant part in determining the magnetic excitation spectrum in LSCoO.

Indeed, as has been noted by Perring *et al* [22] for $\text{La}_{0.7}\text{Pb}_{0.3}\text{MnO}_3$, in a Heisenberg model with only nearest-neighbour interactions the Curie temperature T_C is related through mean-field theory to the exchange energy by

$$T_C = \frac{zJ_1S(S+1)}{3k_B} \quad (6.11)$$

where z is the number of nearest neighbours, and all the other symbols have their usual meanings. When this is corrected (reduced) for the effects of fluctuations [28] equation 6.11 is re-written as

$$T_C = \frac{J_1}{2k_B} [2.90S(S+1) - 0.36] \quad (6.12)$$

and using the value of J_1 obtained from the spin-wave stiffness, this gives an expected Curie temperature in LSCoO of 156 K, which is in excellent agreement with measurements of the susceptibility [5].

One possible cause of broadening and loss of intensity at higher wavevectors would be the presence of a continuum of Stoner excitations, which are typical in metallic ferromagnets and were described in section 1.3.2. A measurement of the Stoner continuum using polarised inelastic neutron scattering shows a continuum of states characterised by wavevector and energy where the scattering is weak and isotropic. Outside of this continuum, and just inside it, it is possible for spin-wave modes to be measured [29], so it would seem, at least qualitatively, that this effect may explain what has been observed here in LSCoO. A classic example of such a measurement is the paper by Mook and Nicklow [30], where the spin-waves

in iron are observed at low wavevector with high precision before the dispersion runs into the Stoner band and the intensity of the scattering becomes much weaker.

The precise details of the Stoner continuum are dependent on the band structure, which is parameterised by the effective mass of the charge carriers. Unfortunately neither of these are available in the literature, so a detailed calculation of where the boundaries of the Stoner continuum lie is not possible. However it is possible to determine experimentally whether or not the presence of Stoner excitations is the cause of the spin-wave broadening in LSCoO. The Stoner continuum is dependent on the Fermi energy (at zero temperature), which depends on the number of charge carriers, and how it compares to the splitting between spin up and spin down bands in a material. If a series of experiments similar to this one were performed where the charge concentration was varied (for $x \geq 0.18$ so that the materials studied would be in the ferromagnetic-metallic phase) it should be possible to determine whether the energy and wavevector at which spin-waves are broadened is dependent on doping.

Moussa *et al* [23] noted that in $\text{La}_{1-x}(\text{Ca}_{1-y}\text{Sr}_y)_x\text{MnO}_3$ the magnons are broadened in wavevector and energy an increasing amount as q increases, with the maximum broadening at the magnetic zone boundary. They explain this phenomenon by suggesting that there exist defects in the mean magnetic structure. For example, if there was only a nearest-neighbour coupling J_1 , but there was a random spatial distribution of this coupling about a mean value due to defects in the magnetic structure on a microscopic scale, then the magnons would be broadened and the effect of this broadening would be more apparent at higher wavevectors. An illustration of this is given in figure 6.16, which shows schematically what the magnetic scattering arising from such a dispersion would look like if the exchange parameter J_1 was given by a Gaussian distribution centred on a value of 12.3 meV with a FWHM of 5.6 meV. The colour map is such that the lighter parts of the plot correspond to higher intensity and the darker parts to lower intensity. This appears to capture qualitatively the observed broadening of the spin-waves in LSCoO.

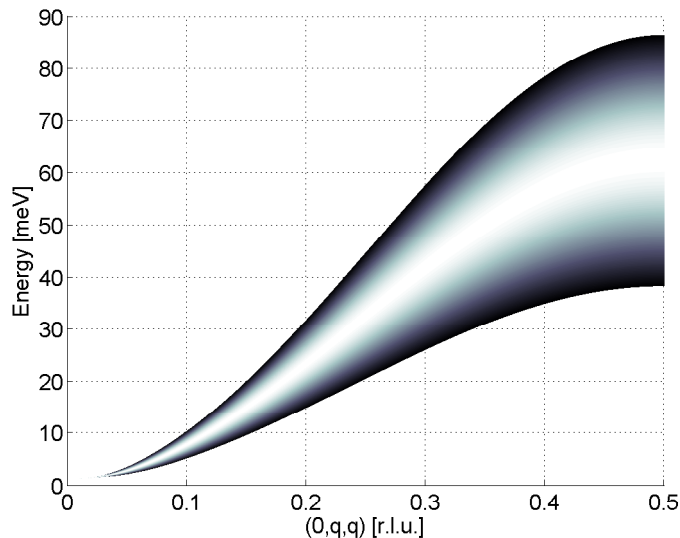


Figure 6.16: Broadening of the dispersion due to a Gaussian distribution of nearest-neighbour exchange parameters.

To test the appropriateness of this model one must examine the width in both wavevector and energy throughout the Brillouin zone. At low energies and wavevectors the width of

both Q -scans and E -scans will be limited in part by the resolution of the instrument, rather than the effects described above. However if the excitations become broader than this instrumental resolution then it should be possible to determine if the observed broadening is consistent with the model proposed.

It was found that the widths of the Q -scans at low energies were more or less constant, although the uncertainty on the fits means that small changes would not be possible to detect. However the low wavevector widths were much larger than what would be expected if they were limited by resolution only, so there must be an additional damping of the excitations. The width of the E -scans was shown in figure 6.11. This figure is re-plotted in figure 6.17 with a line drawn on to indicate the energy width that would be expected if the exchange parameter J_1 was randomly disordered such that its value followed a Gaussian distribution with $\text{FWHM} \sim 10 \text{ meV}$ (as above). At low wavevectors and energies the width would have to be limited by some other factor, and this is accounted for in the plot by adding a broadening Γ , as in equation 6.6, which occurs in addition. At higher wavevectors the width is then given by the width due to exchange disorder, whereas at lower wavevectors it is given by the finite Γ .

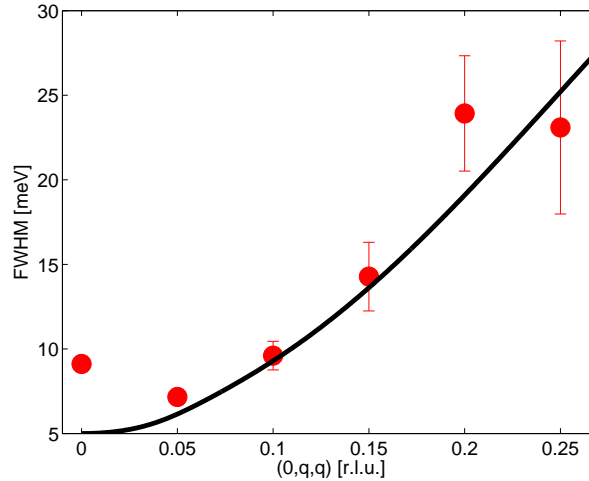


Figure 6.17: The expected width of the spin excitations if the exchange parameter has random disorder (black line), plotted over the real energy width of the spin excitations (filled red circles).

Note that because the plot of the energy widths contains only a few points it is not possible to find a fit using the model of a randomised exchange parameter because the fit would be under-constrained. Moreover it is not clear how the additional damping that is required to explain the width of the lower energy scans would arise. Finally the amount of disorder required to fit the data here is significantly larger than that found in $\text{La}_{1-x}(\text{Ca}_{1-y}\text{Sr}_y)_x\text{MnO}_3$, indeed it is hard to see how an amount of disorder as large as that required to fit the LSCO data would arise.

It was noted in section 6.1 that in $\text{La}_{1-x}\text{Ca}_x\text{MnO}_3$ (LCMO) standing spin-waves have been observed using neutron magnetic scattering [25] due to the existence of hole-rich and hole-poor magnetic clusters, the latter supporting the standing waves. The size of the clusters and their spacing was uniform in LCMO, enabling the nature of the exchange and the spin state of the cluster region to be determined accurately. Consider now a similar situation, but with a non-uniform cluster size. Standing spin-waves might still exist in these clusters,

either in the hole-rich or the hole-poor ones, however there would be an almost continuous range of energies allowed for these standing waves. If one were then to measure the neutron magnetic scattering from these standing waves, the modes (that are well defined in LCMO) would become broader in energy because of the variation in cluster size, resulting in lower neutron count rates and a much less well defined signal. If there was a significant range of cluster sizes then the standing wave modes may even become so broad as to coalesce to form almost a continuum of weak magnetic scattering. If such a scenario were to occur then, clearly, it might be a possible explanation for the measurements of LSCoO presented here. It is not, however, possible to verify this hypothesis from the data obtained in the experiments described here.

6.5 Conclusions

To conclude, it is clear from these measurements from the spin excitations that LSCoO with $x = 0.18$ is not a simple localised Heisenberg ferromagnet. The spin excitations along the $(0, 1, 1)$ -direction have been measured using a half-polarised neutron inelastic scattering technique. At low energies and wavevectors spin-waves were measured and their stiffness was found to be larger than in similarly doped manganites. At higher energies the spin excitations broaden significantly, and become too weak to measure near the Brillouin zone boundary.

There are several possible mechanisms which might explain this broadening and weakening. The first is that a continuum of Stoner excitations crosses the spin-wave dispersion, which would result in the magnetic excitations rapidly becoming isotropic and weak. Another possible explanation is that the nearest-neighbour Heisenberg exchange is randomly distributed about a mean value so that several different dispersion curves overlies each other to give an overall measured dispersion that is significantly broadened as the wavevector increases. The amount of disorder required to fit the data is, however, unrealistically large. Finally standing spin-wave modes may exist in ferromagnetic clusters with a range of sizes, giving rise to a broad continuum of magnetic scattering.

Future experiments on this material could take a number of directions. The ‘pure’ ferromagnetic phase ($x \gg 0.18$) could be investigated using polarised neutrons, and the dispersion obtained would help future characterisation of the excitations at lower doping fractions. Furthermore lower doping fractions ($x < 0.18$) could be investigated for the existence of optic spin-wave modes. Broadening possibly due to the existence of a Stoner continuum can be checked by measuring the scattering throughout the Brillouin zone for a range of dopings in the ferromagnetic metallic phase.

References

- [1] A. P. Ramirez, *J. Phys. Condensed Matter* **9**, 8171 (1997).
- [2] E. Dagotto, *Nanoscale Phase Separation and Colossal Magnetoresistance - The Physics of Manganites and Related Compounds*, Springer (2003).
- [3] M. N. Baibich, J. M. Broto, A. Fert, F. Nguyen Van Dau, F. Petroff, P. Eitenne, G. Creuzet, A. Friederich, and J. Chazelas, *Phys. Rev. Lett.* **61** 2472 (1988).
- [4] A. J. Millis, B. I. Shraiman, and R. Mueller, *Phys. Rev. Lett.* **77**, 175 (1996).
- [5] M. Kriener, C. Zobel, A. Reichl, J. Baier, M. Cwik, K. Berggold, H. Kierspel, O. Zabara, A. Freimuth, and T. Lorenz, *Phys. Rev. B* **69**, 094417 (2004).
- [6] J. Wu, H. Zheng, J. F. Mitchell, and C. Leighton, *Phys. Rev. B* **73**, 020404 (2006).
- [7] R. Caciuffo, D. Rinaldi, G. Barucca, J. Mira, J. Rivas, M.A. Señarís-Rodríguez, P. G. Radaelli, D. Fiorani, and J. B. Goodenough, *Phys. Rev. B* **59**, 1068 (1999).
- [8] J. Wu, and C. Leighton, *Phys. Rev. B* **67**, 174408 (2003).
- [9] S. J. Blundell, *Magnetism in Condensed Matter*, p.100, Oxford University Press (2001).
- [10] P. L. Kuhns, M. J. R. Hoch, W. G. Moulton, A. P. Reyes, J. Wu, and C. Leighton, *Phys. Rev. Lett.* **91**, 127202 (2003).
- [11] J. Wu, J. W. Lynn, C. J. Glinka, J. Burley, H. Zheng, J. F. Mitchell, and C. Leighton, *Phys. Rev. Lett.* **94**, 037201 (2005).
- [12] S. R. Giblin, I. Terry, D. Prabhakaran, A. T. Boothroyd, J. Wu, and C. Leighton, *Phys. Rev. B* **74**, 104411 (2006).
- [13] A. Podlesnyak, K. Conder, E. Pomjakushina, A. Mirmelstein, P. Allenspach, and D. I. Khomskii, *J. Mag. Mag. Mat.* **310**, 1552 (2007).
- [14] D. Phelan, D. Louca, S. Rosenkranz, S. -H. Lee, Y. Qiu, P. J. Chupas, R. Osborn, H. Zheng, J. F. Mitchell, J. R. D. Copley, J. L. Sarrao, and Y. Moritomo, *Phys. Rev. Lett.* **96**, 027201 (2006).
- [15] D. Phelan, D. Louca, K. Kawazama, S. -H. Lee, S. N. Ancona, S. Rosenkranz, Y. Motome, M. F. Hundley, J. F. Mitchell, and Y. Moritomo, *Phys. Rev. Lett.* **97**, 235501 (2006).

- [16] A. H. Moudden, L. Vasiliu-Doloc, L. Pinsard, A. Revcolevschi, *Physica B* **241-243**, 276 (1998).
- [17] F. Ye, P. Dai, J. A. Fernandez-Baca, H. Sha, J. W. Lynn, H. Kawano-Furukawa, Y. Tomioka, Y. Tokura, and J. Zhang, *Phys. Rev. Lett.* **96**, 047204 (2006).
- [18] P. Dai, H. -Y. Hwang, J. Zhang, J. A. Fernandez-Baca, S. -W. Cheong, C. Kloc, Y. Tomioka, and Y. Tokura, *Phys. Rev. B* **61**, 9553 (2000).
- [19] J. A. Fernandez-Baca, M. E. Hagen, P. Dai, F. Ye, J. Kulda, Y. Tomioka, and Y. Tokura, *Physica B* **385-386**, 66 (2006).
- [20] F. Ye, P. Dai, J. A. Fernandez-Baca, D. T. Adroja, T. G. Perring, Y. Tomioka, and Y. Tokura, *Phys. Rev. B* **75**, 144408 (2007).
- [21] L. Vasiliu-Doluc, J. W. Lynn, A. H. Moudden, A. M. de Leon-Guervara, and A. Revcolevschi, *Phys. Rev. B* **58**, 14913 (1998).
- [22] T. G. Perring, G. Aeppli, S. M. Hayden, S. A. Carter, J. P. Remeika, and S. -W. Cheong, *Phys. Rev. Lett.* **77**, 711 (1996).
- [23] F. Moussa, M. Hennion, P. Kober-Lehouelleur, D. Reznik, S. Petit, H. Moudden, A. Ivanov, Ya. M. Mukovskii, R. Privezentsev, and F. Albenque-Rullier, *Phys. Rev. B* **76**, 064403 (2007).
- [24] M. Hennion, F. Moussa, G. Biotteau, J. Rodriguez-Carvajal, L. Pinsard, and A. Revcolevschi, *Phys. Rev. B* **61** 9513 (2000).
- [25] M. Hennion, F. Moussa, P. Lehouelleur, F. Wang, A. Ivanov, Y. M. Mukovskii, and D. Shulyatev, *Phys. Rev. Lett.* **94**, 057006 (2005).
- [26] http://www.ill.fr/fileadmin/users_files/ILL_News/29/29_news4.htm
- [27] W. Marshall and S. W. Lovesey, *Theory of Thermal Neutron Scattering*, p.366, Clarendon Press (1971).
- [28] G. S. Rushbrooke, G. A. Baker, and P. J. Wood, *Phase Transitions and Critical Phenomena*, ed. C. Domb and M. S. Green, (Academic, New York, 1974).
- [29] J. B. Sokoloff, *Phys. Rev. B* **13**, 4172 (1976).
- [30] H. A. Mook, and R. M. Nicklow, *Phys. Rev. B* **7**, 336 (1973).

Chapter 7

X-ray Resonant Scattering Measurements of Multiferroic DyMn₂O₅

X-ray resonant scattering has been used to measure the magnetic order below 40 K in multiferroic DyMn₂O₅. The magnetic order has a complex behaviour. Several different ordering wavevectors, both incommensurate and commensurate, present themselves as the temperature is varied. In addition a non-magnetic signal at twice the wavevector of one of the commensurate signals is observed, the maximum intensity of which occurs at the same temperature as a local maximum in the ferroelectric polarisation. Some of the results, which bear resemblance to the behaviour of other members of the RMn_2O_5 family of multiferroic materials, may be explained by a theory based on so-called acentric spin-density waves.

7.1 Introduction

7.1.1 Bulk Properties

The RMn_2O_5 (R = rare earth) materials have played a major part in the recent upsurge of interest in multiferroics [1, 2], with their seemingly complex phase diagram providing a series of problems for physicists to solve. The bulk properties of the RMn_2O_5 (R = Tb, Ho, Er, Dy, ...) compounds have been studied in some detail and have many common features [1, 2, 3, 4, 5]. In zero applied magnetic field there exists a finite FE polarisation along the b -axis in the approximate temperature range $20 \leq T \leq 35$ K, which, with increasing temperature, increases rapidly at the lower end of the temperature range and decreases more gradually at the upper end. Such behaviour is present for all RMn_2O_5 compounds, however the magnitude of the polarisation is largest in DyMn₂O₅, and appears to be significantly weaker if R is a non-magnetic ion such as Y [5]. It would seem, therefore, that the presence of a magnetic rare-earth enhances the ferroelectric (FE) polarisation. Coexistent with the ferroelectric order a complicated series of magnetic orders present themselves, the nature of which will be described below. It is this coexistence that make the RMn_2O_5 compounds multiferroic.

The temperature dependence of the FE polarisation of DyMn₂O₅ is shown in Figure 7.1, reproduced from the paper of Higashiyama *et al.* [4]. It can be seen that the behaviour is

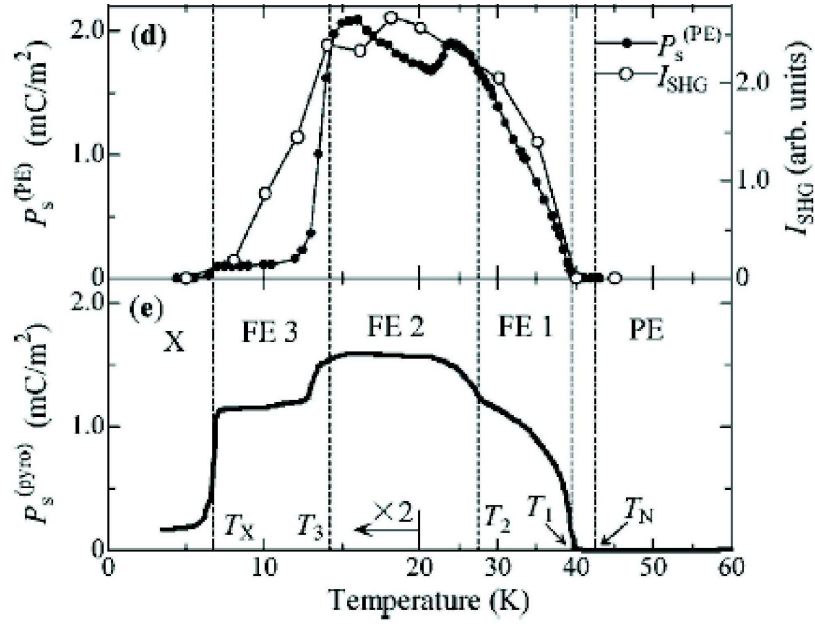


Figure 7.1: FE polarisation measured by Higashiyama *et al.* [4]. The upper figure shows remnant polarisation after the applied electric field has been cycled, analogous to a magnetic hysteresis loop. The lower figure shows the polarisation inferred from measurement of the pyroelectric current.

rather complicated. Features of particular note, from the upper pane, are

- The FE polarisation is small but non-negligible for $7 \leq T \leq 12\text{K}$,
- The sharp rise beginning at 12 K to a maximum at 15 K,
- A local maximum at about 25 K
- A steady reduction of FE polarisation with increasing temperature, reaching zero at about 39 K.

A strong hint towards the existence of coupling between the ferroelectric and magnetic orders is provided by the fact that the application of a magnetic field can affect the ferroelectric properties of the RMn_2O_5 compounds. In DyMn_2O_5 Higashiyama *et al* [4] showed that application of a magnetic field parallel to the a -axis can have a strong effect on the ferroelectric polarisation parallel to the b -axis. Above about 17 K application of a magnetic field up to 3 T has very little effect on the polarisation, however for $T \leq 17\text{K}$ an increase in field causes a steady increase in the magnitude of the polarisation. The general form of the polarisation as a function of temperature is unchanged for $H_a \leq 1\text{T}$ however the decrease in polarisation on cooling from about 14 K is less steep. This effect becomes even more marked for $1 < H_a < 2.5\text{T}$, with the polarisation becoming much larger at the lowest temperatures than in the zero field case. Eventually for $H_a \geq 2.5\text{T}$ the polarisation actually increases on cooling below 14 K and tends to saturate below about 7 K.

As well as the ferroelectric phase, other common features among RMn_2O_5 compounds are the existence of a magnetic transition from an ordered to a disordered state at $T_N \sim 40\text{K}$,

with a transition into a ferroelectric state just below T_N . At low temperatures, typically $T < 10$ K, the magnetic rare earth ions are observed to order antiferromagnetically. The precise details of these changes are different, depending on the choice of R . This may depend on the magnetic easy axis of the material, which is the a -axis for $R = \text{Tb}$, the b -axis for $R = \text{Dy}$ and Ho , and the c -axis for $R = \text{Er}$ and Tm . All of these transitions are accompanied by distinct anomalies in the specific heat.

DyMn₂O₅ crystallises in the orthorhombic space group $Pbam$ with the lattice parameters $a = 7.294 \text{ \AA}$, $b = 8.555 \text{ \AA}$ and $c = 5.688 \text{ \AA}$. The structure is such that interspersed between sheets of Dy³⁺ ions there are, in order along the c -axis, a Mn⁴⁺O₆ octahedron, a Mn³⁺O₅ bipyramid, followed by another Mn⁴⁺O₆ octahedron [6].

The crystal structure is shown in figure 7.2, with the polyhedra showing the DyO₈ environment. The Dy–O bond distances within each polyhedron are not all the same, however they are all within 10% of each other.

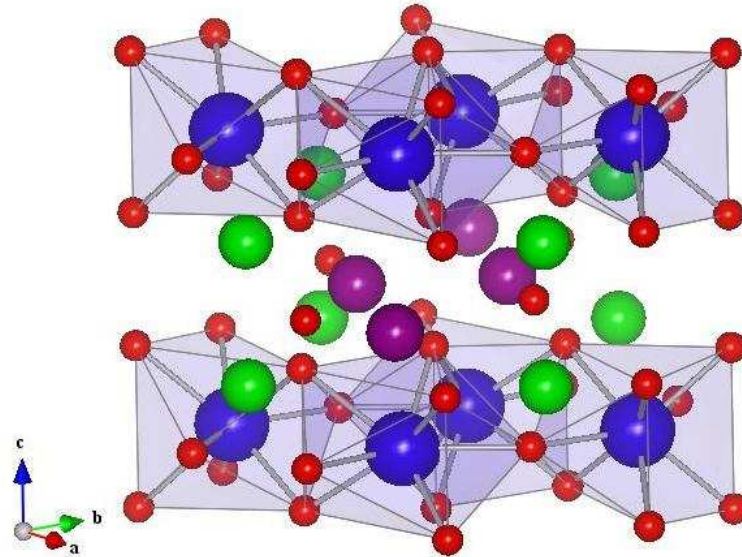
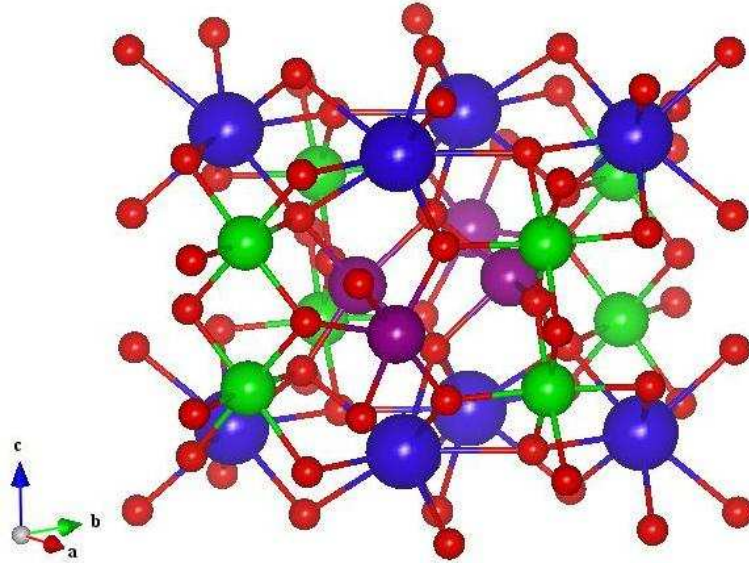
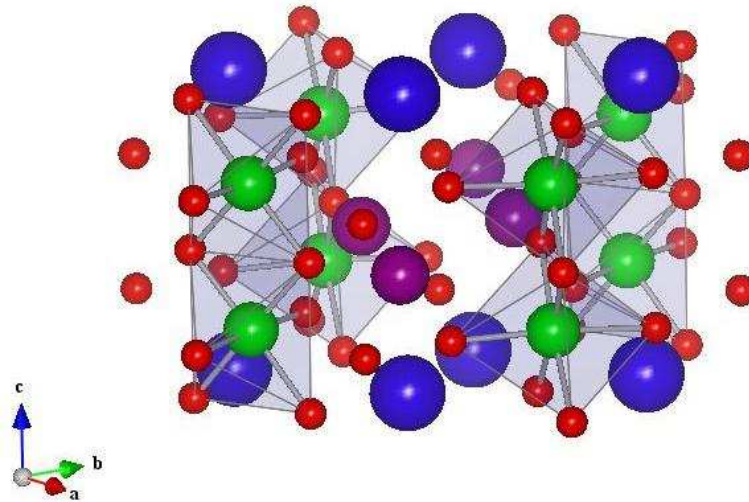


Figure 7.2: The unit cell of DyMn₂O₅, with Dy ions shown as blue spheres, Mn⁴⁺ ions shown as purple spheres, Mn³⁺ ions shown as green spheres, and O²⁻ ions shown as red spheres. The polyhedra show the DyO₈ neighbours.

Figure 7.3 shows schematically how the Dy–O bonds relate to the Mn–O bonds, with the colour half way along each bond showing the two ions that it connects. Although it is rather hard to see from the diagram, each Dy ion is connected via oxygen ions to 28 different Mn ions. The Dy–O–Mn bond angles range from 96.2° to 134.6°, so it is not clear from the GKA rules [7] whether the coupling between Dy and Mn ions would be ferromagnetic or antiferromagnetic. X-ray resonant magnetic scattering will be observed if there is a coherent magnetic polarisation of the Dy 5*d* states through coupling to the magnetically ordered Dy 4*f* or Mn 3*d* moments. Mn³⁺ is in the configuration $t_{2g}^3 e_g^1$, whereas the configuration of the 3*d* states in Mn⁴⁺ is t_{2g}^3 .

For completeness, figures 7.4 and 7.5 show the polyhedra that make up the Mn³⁺O₆ environment and the Mn⁴⁺O₅ environment respectively.

Figure 7.3: The DyMn_2O_5 unit cell showing Dy–O and Mn–O bonds.Figure 7.4: The DyMn_2O_5 unit cell showing Mn^{3+}O_6 octahedra

7.1.2 Previous Scattering Measurements

There have been several neutron scattering experiments conducted on DyMn_2O_5 [6, 8, 9]. These experiments have had some success in elucidating the crystallographic and magnetic structure of this material. It appears that there are three distinct magnetic phases present at various temperatures below T_N . Below $T \approx 8\text{ K}$ the Dy ions are modulated antiferromagnetically (AFM) along the a -axis, with wavevector $\mathbf{q}_{AFM}^{Dy} = (0.5, 0, 0)$, with their moments pointing along the b -axis. From base temperature up to T_N the Mn^{3+} and Mn^{4+} ions undergo several magnetic transitions between an incommensurate magnetic (ICM) phase and a commensurate magnetic (CM) phase. The propagation vectors of these phases will be denoted hereafter by \mathbf{q}_{ICM} and \mathbf{q}_{CM} respectively, where $\mathbf{q}_{ICM} = (0.5 \pm \delta, 0, 0.25 \pm \epsilon)$ and $\mathbf{q}_{CM} = (0.5, 0, 0.25)$. The existence of these phases has been shown in all the neutron scattering measurements, but the precise details of ordering wavevectors and their onset temperatures are not consistent between studies.

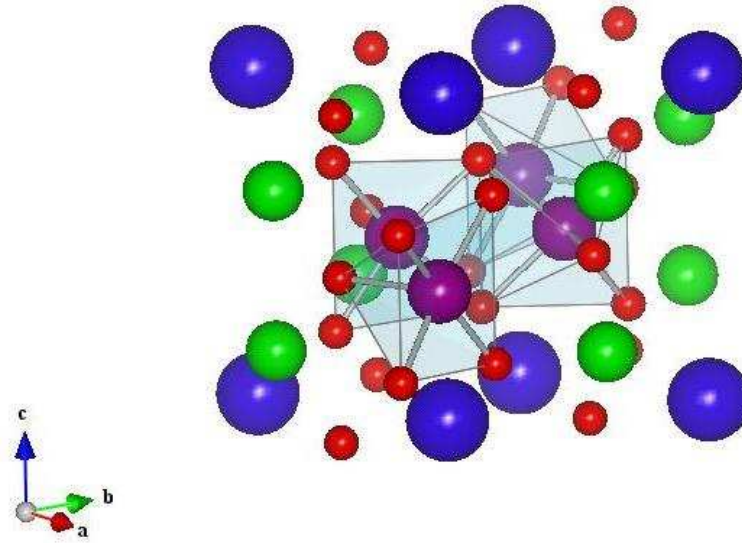


Figure 7.5: The DyMn₂O₅ unit cell showing Mn⁴⁺O₅ bi-pyramids

Wilkinson *et al.* [8] measured the magnetic structure at three temperatures (4.2 K, 18 K and 44 K) and found, coexisting with the AFM order of the Dy ions, an ICM structure with $\delta = 0$ but $\epsilon \neq 0$. The value of ϵ was found to vary slightly in the range $0 \leq \epsilon \leq 0.002$ for the three temperatures measured. This incommensurate order was attributed to the ordering of both sets of Mn ions. More recently, neutron powder diffraction measurements by Blake *et al.* [6] were able to resolve a magnetic structure with $\delta = 0.01$ and $\epsilon = 0$ below 32 K, which they did not observe to change on cooling until $T \leq 8$ K, whereupon it became much weaker and an AFM phase the same as that seen by Wilkinson *et al.* was found.

Subsequently, single crystal neutron diffraction measurements were made by Ratcliff *et al.* [9] over a temperature range $2 \text{ K} \leq T \leq 45 \text{ K}$. Like the other measurements they found an AFM phase below 8 K, but at higher temperatures they found a more complex behavior. Two different ICM phases were found for $8 \text{ K} \leq T \leq 18 \text{ K}$ characterised by the wavevector $\mathbf{q}_{ICM} = (0.5, 0, 0.25 + \epsilon_{1,2})$, where $\epsilon_{1,2}$ are two different incommensurabilities which vary in size between 0 and 0.02 and have opposite sign. For $18 \text{ K} \leq T \leq 33 \text{ K}$ one of the ICM peaks becomes CM whilst the other's intensity gradually decreases with increasing temperature. For $T > 33 \text{ K}$ there exists only the CM phase, and on warming this disappears by $\sim 40 \text{ K}$.

Up to now there have been no x-ray resonant scattering (XRS) studies of DyMn₂O₅, although there have been two XRS studies of the related compound TbMn₂O₅ [10, 11], both of which have concerned themselves with the ordering of the Mn sublattice by tuning the incident x-ray energy to one of the Mn absorption edges. For $10 \leq T \leq 41 \text{ K}$ a pair of ICM peaks at $(0.5 \pm \delta, 0, 0.25 + \epsilon)$ are observed, where δ decreases from about 0.012 at 10 K to 0.003 at 25 K, where it remains constant until 32 K above which it increases to about 0.012 at 41 K. The c -axis incommensurability, ϵ , gradually decreases from 0.06 at 10 K to 0.03 at 41 K. The intensity of the ICM peaks decreases steadily with increasing temperature. Above about 21 K a CM peak at $(0.5, 0, 0.25)$ appears, the intensity of which increases with increasing temperature up to about 30 K, and then decreases on further warming to 41 K. It is also noted that the $(3, 0, 0)$ Bragg peak, which is forbidden in the $Pbam$ space group that characterises the crystal structure of TbMn₂O₅, is observed to scale exactly as the FE polarisation squared. The $(3, 0, 0)$ Bragg peak would be allowed if the space group became

non-centrosymmetric, and lack of a center of inversion is required in all of the proposed explanations for the occurrence of FE polarisation in magnetically ordered materials.

In their neutron powder diffraction study Blake *et al* [6] considered the possibility that in the ferroelectric phase the symmetry of the crystal structure is lowered so that the space group of the material is $Pb2_1m$. Such a group would allow a change in the positions of the Mn³⁺ ions that might give rise to a ferroelectric polarisation along the b -axis. Table 7.1 shows the allowed reflections for the $Pbam$ and $Pb2_1m$ space groups. The $(3, 0, 0)$ reflection is still forbidden in the lower symmetry $Pb2_1m$ space group, however there are some extra allowed peaks – for example the $(1, 0, 4)$ peak is allowed in $Pb2_1m$ but is forbidden in $Pbam$, so if this peak were to be found in DyMn₂O₅ then the veracity of the existence of a lower crystal symmetry could be proven.

Space group	Allowed reflections
$Pbam$	$0kl : k = 2n$
	$h0l : h = 2n$
	$h00 : h = 2n$
	$0k0 : k = 2n$
	$hkl : h + k = 2n$
$Pb2_1m$	$h0l : l = 2n$
	$00l : l = 2n$

Table 7.1: Allowed reflections for $Pbam$ and $Pb2_1m$ space groups

There were several motivations for this XRS study of DyMn₂O₅. Firstly, XRS offers the possibility of probing the magnetic order on the Dy and Mn sites separately by using the resonant enhancement in the scattering when the x-ray energy is tuned to an atomic absorption edge. Neutron diffraction, by contrast, is sensitive only to the size of the overall magnetic moment and not to the atomic species to which it is attached. Secondly, XRS offers a high wavevector resolution, which makes it possible to measure changes in the magnetic ordering wavevector with very high accuracy. Thirdly, XRS is particularly useful for the case of DyMn₂O₅ because the neutron absorption cross section for ¹⁶⁴Dy is relatively large and this isotope makes up about 28% of naturally occurring Dy. Hence, it is difficult to obtain a good signal to background ratio in a neutron diffraction measurement on DyMn₂O₅. The advantages of XRS will therefore enable us in this study to clarify the existing data on DyMn₂O₅, and to provide a more detailed picture of the various ordering features of this important multiferroic material.

7.1.3 Analogies with TbMnO₃: X-ray Resonant Scattering

A recent extensive study of TbMnO₃ [12] using XRS has demonstrated additional types of measurements that are only possible with this technique, and it will be instructive to consider them here. TbMnO₃ possesses magnetic order with the wavevector $(0, q_{\text{Mn}}, 0)$, where $0.28 \leq q_{\text{Mn}} \leq 0.29$, and for $T \leq 28$ K it is non-collinear. The non-collinear magnetic order coexists with ferroelectric order, with the FE polarisation parallel to the c -axis in

zero applied magnetic field. Using XRS it was possible to show that this corresponds to a magnetic order on the Mn sites. Mannix *et al* [12] also showed, using resonant scattering at the Tb L₃ edge, that the Tb ions also order with this wavevector. Furthermore the behaviour of the intensity of the scattering with temperature using both Mn K edge and Tb L₃ edge resonances was the same, providing further proof that their physical origin is the same. Conversely it was found that at low temperatures ($T \leq 7$ K) there is a distinct ordering of the Tb ions, with wavevector $(0, q_{\text{Tb}}, 0)$ with $q_{\text{Tb}} = 0.42$, which is not reflected by the Mn ions. This Tb-only signal is, however, rather weak and is therefore probably due to an interaction with an energy scale similar to the mean field due to the surrounding ordered Mn ions.

The signal due to Mn ordering that is seen using the Tb L₃ resonance was polarisation-analysed in order to obtain more information about the physics giving rise to it. Using incident σ -polarised x-rays (see below) it was found that the magnetic signal scattered into both the π and σ polarisation states. The latter would only arise due to magnetic order that is non-dipolar in nature, demonstrating that the interaction between the Mn and Tb ions is far from straightforward. It was also possible to scan the azimuth (defined in section 2.2.3) in order to uncover the symmetry of the magnetic order. Dipolar magnetic order would give rise to an azimuth dependence of the scattered intensity that was proportional to $\cos^2(\phi)$, where ϕ is the azimuthal angle. In TbMnO₃ it was found that most of the azimuth scans of the magnetic scattering behaved in this way, however for Tb L₃ resonances at $(0, 3 \pm q_{\text{Mn}}, 0)$ a more complex behaviour was observed, which was attributed to interference between dipole and quadrupolar magnetic scattering channels caused by the existence of a toroidal magnetic order.

Although many of the measurements described above are specific to TbMnO₃ and are unlikely to be reproduced in DyMn₂O₅, they serve the purpose of demonstrating further the power of the XRS technique compared to bulk measurements, and the additional information that can be obtained by XRS compared to neutron scattering.

7.2 Experimental details

The single crystal sample was grown using the flux method [13]. The particular crystal used for these bulk measurements and scattering measurements was grown c.1972 by B.M.R. Wanklyn in Oxford. Because of the age of the sample careful characterisation of its bulk properties was required, and these measurements are presented in section 7.3. Preliminary x-ray measurements using a standard Laue camera showed that the lattice parameters and space group of the sample used were consistent with those expected from the literature.

The alignment of the crystal was determined using an x-ray Laue. After this the sample was cut and polished so that the $(0, 0, 1)$ direction was normal to the largest surface, from which x-rays could be easily scattered. Most of the synchrotron x-ray measurements were consequently made at wavevectors of the form $\mathbf{Q} = (0, 0, 4) \pm \mathbf{q}$.

Magnetometry measurements were performed using a Quantum Design SQUID magnetometer. The sample mounted using the second method described in section 2.3.1, and was additionally secured using a small amount of kapton tape. The crystal was oriented in this arrangement so that the b -axis was parallel to the applied field, i.e. vertical. The specific

heat measurements were performed in zero applied magnetic field using a Quantum Design PPMS, a description of which is given in section 2.3.2.

X-ray resonant scattering (XRS) and non-resonant x-ray scattering measurements were performed on the XMaS beamline at the European Synchrotron Radiation Facility (ESRF), Grenoble, France. The source of x-rays at XMaS is a bending magnet, so the light is linearly polarised in the horizontal plane. A vertical scattering geometry was used, shown in figure 2.8, so the incoming x-rays were σ -polarised. For the XRS measurements an incident energy of 7.795 keV, corresponding to the Dy L₃-edge (see below), was used. For non-resonant measurements an incident energy of 11.17 keV was used. For the XRS measurements at the Dy L₃-edge a Au(222) analyser crystal between the sample and detector was used in order to measure the σ' and π' polarised components in the scattered beam. The detector used for the scattering measurements was a Si drift diode, which can be set up to count only x-rays within a certain energy range in order to improve the signal to noise. Fluorescence measurements were performed on the sample in order to check the energy calibration of the x-ray beam relative to the known absorption edges of the atoms in the sample, and for these a NaI bicron detector was used.

The Dy L₃-edge, which involves virtual electronic transitions between the $2p$ and $5d$ states, was used for XRS measurements because the resonant enhancement of the magnetic scattering at this energy can be several orders of magnitude. This contrasts with the resonant enhancement of magnetic scattering at the Mn K-edge ($1s \rightarrow 4p$), which is only a factor of about 3. Furthermore, the spectrum of the bending magnet source at XMaS is such that the flux of x-rays with energies near the Dy L₃-edge is significantly higher than the flux of x-rays with energies near the Mn K-edge. Thus one would expect it to be possible to observe magnetic scattering arising from ordering on both the Mn and Dy sublattices by measuring the signal from the Dy sublattice alone, assuming that the magnetic polarisation of the $5d$ states of the Dy ions is caused by a combination of the local magnetic environment due to the Mn ions and the magnetisation of the Dy $4f$ electrons.

An energy of 11.17 keV was chosen for the non-resonant measurements for two reasons. First, at higher x-ray energies the penetration depth of the x-rays is larger, thus increasing the scattering volume and making the signal less surface sensitive. This means that any observed signal is both more intense and sharper in wavevector than it would be for lower energies. Second, this energy is sufficiently high that although the flux of x-rays from the bending magnet is still very high, the flux of higher harmonic x-rays is vastly smaller. This effectively eliminates the possibility of mistaking scattering at this energy with scattering resulting from second or third harmonic x-rays.

The sample was aligned using the $(0, 0, 4)$ Bragg peak, which is in the specular direction¹ and also happens to be one of the strongest. The additional, off-specular, reflection that was used to give a full alignment was the $(1, 0, 4)$ peak, which is in fact forbidden in the $Pbam$ space group but is allowed in the $Pb2_1m$ space group, as detailed in section 7.1.2. This peak was a factor of approximately 10000 weaker than the $(0, 0, 4)$ peak. Note that although the $(1, 0, 4)$ Bragg peak is allowed only in the $Pb2_1m$ space group and not in $Pbam$, and the $Pb2_1m$ space group has been associated with the existence of ferroelectricity, it was found not to vary with temperature, and is therefore not equivalent to the $(3, 0, 0)$ peak used in

¹Specular means perpendicular to the Miller planes which form the crystal's surface. The highest reflectivity is found for specular reflections.

x-ray studies of TbMn₂O₅ as a measure of the ferroelectric polarisation.

The sample was mounted on a four-circle diffractometer, although once the alignment had been established ϕ , the azimuthal angle, was fixed so that in fact the three angles that could be varied were θ , 2θ and χ . The scattering geometry used was such that for specular reflections the bc -plane was the scattering plane. The resonant magnetic scattering in the dipole channel was therefore sensitive to components of the magnetic order in the b and c directions. The sample was placed in an evacuated space enclosed by Be domes (Be is almost transparent to x-rays) and was mounted on a ‘cold finger’ which was cooled by a displax cryostat. The cooling was achieved using the Joule-Thomson effect on low pressure He gas that was pre-cooled using liquid nitrogen.

7.3 Results

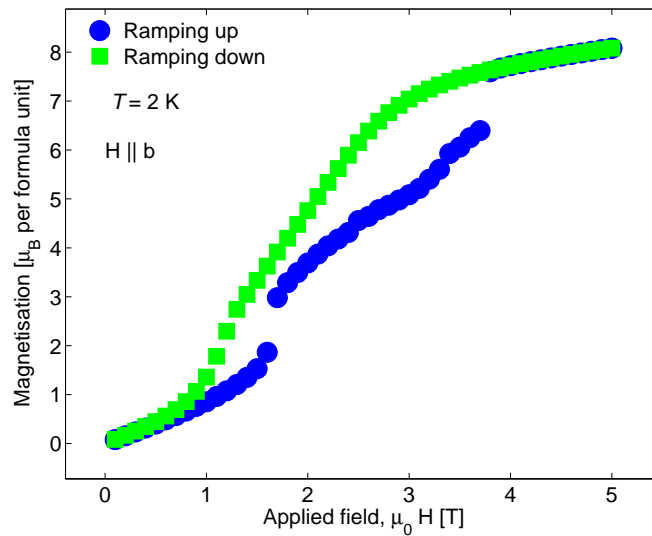


Figure 7.6: Measurement of the magnetisation at $T = 2$ K, with the applied magnetic field, which was parallel to the b -direction, being ramped up (blue circles) and ramped down (green squares). On ramping the field up there are jumps in the magnetisation at about 1.7 T and 3.7 T, however these transitions do not occur when the field is ramped down.

The magnetisation of the sample used for the XRS study is shown as a function of applied magnetic field at $T = 2$ K in figure 7.6. There is a clear hysteresis displayed between ramping the field up and ramping the field down, and there is a clear anomaly around 1.7 T, both of which are in agreement with the literature [2]. An additional effect not seen before is the jump in magnetisation around 3.7 T. Hur *et al* [2] show that when $\mathbf{H} \parallel \mathbf{b}$ there is a maximum in the dielectric constant between 3 T and 5 T when $T = 3$ K. However the changes in the dielectric constant are much greater when $\mathbf{H} \parallel \mathbf{a}$. The saturation moment of about $8\mu_B$ mole⁻¹ is about 75% of the expected moment of the free Dy³⁺ ion².

Scans of the temperature with fixed applied field, an example of which is shown in figure 7.7 where the field was applied along the b -direction, are not especially informative. This is

²Dy³⁺ has the $4f^9$ configuration, so according to Hund’s rules it has $L = 5$, $S = \frac{5}{2}$, and $J = \frac{15}{2}$, giving an effective moment of $10.63\mu_B$ per ion.

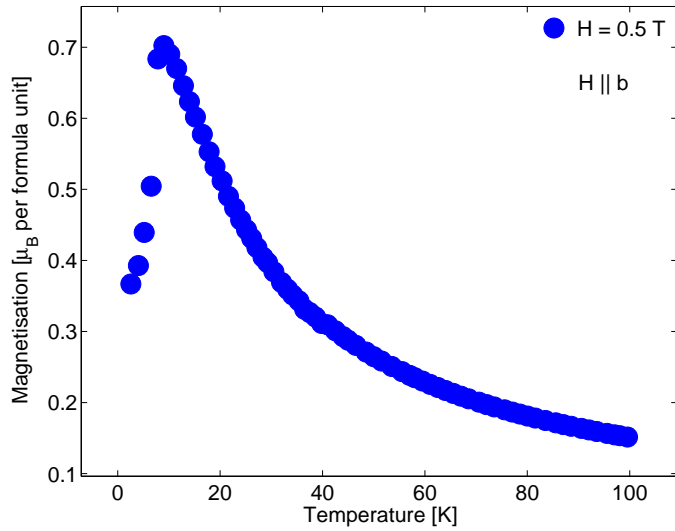


Figure 7.7: The magnetisation of DyMn_2O_5 as a function of temperature in an applied field of 0.5 T parallel to the b -direction.

because over the whole temperature range the signal from the Dy moments is much greater than any other contribution – at low temperatures there is an antiferromagnetic transition, at $T_N^{\text{Dy}} \approx 7\text{ K}$, and at higher temperatures there is a Curie-Weiss-like behaviour which swamps any signal from the Mn moments.

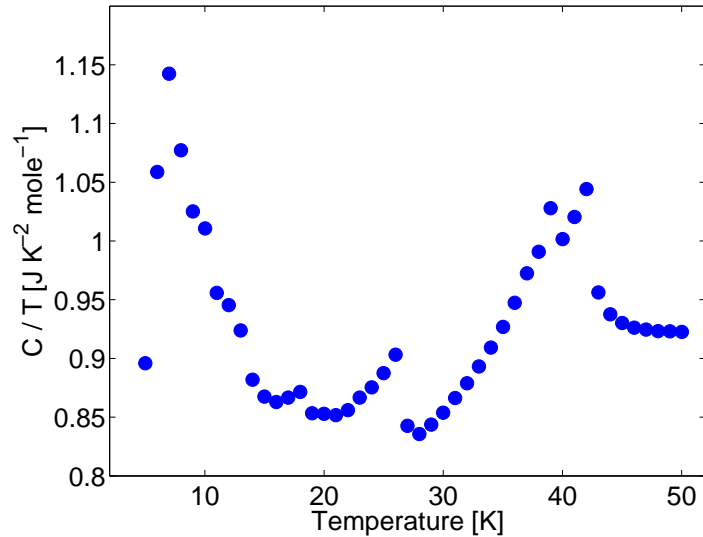


Figure 7.8: Measurement of the heat capacity of the crystal of DyMn_2O_5 used in the x-ray measurements. The temperatures at which there are anomalies agree with those measured previously [2, 4]. Note that the lattice heat capacity has not been subtracted from these data.

The heat capacity of the sample as a function of temperature is shown in figure 7.8. There are clear anomalies at $T = 7.2\text{ K}$, 13 K, 27 K, 39 K, and 42 K, which is in agreement with previous measurements of the heat capacity [4]. Some of these transitions may be compared to figure 7.1 and be seen to mark the onset of the various different ferroelectric phases, and also magnetic phases. The anomalies correspond to the Néel temperature of the

Dy moments, FE3, FE2, FE1, and the Néel temperature of the Mn moments respectively.

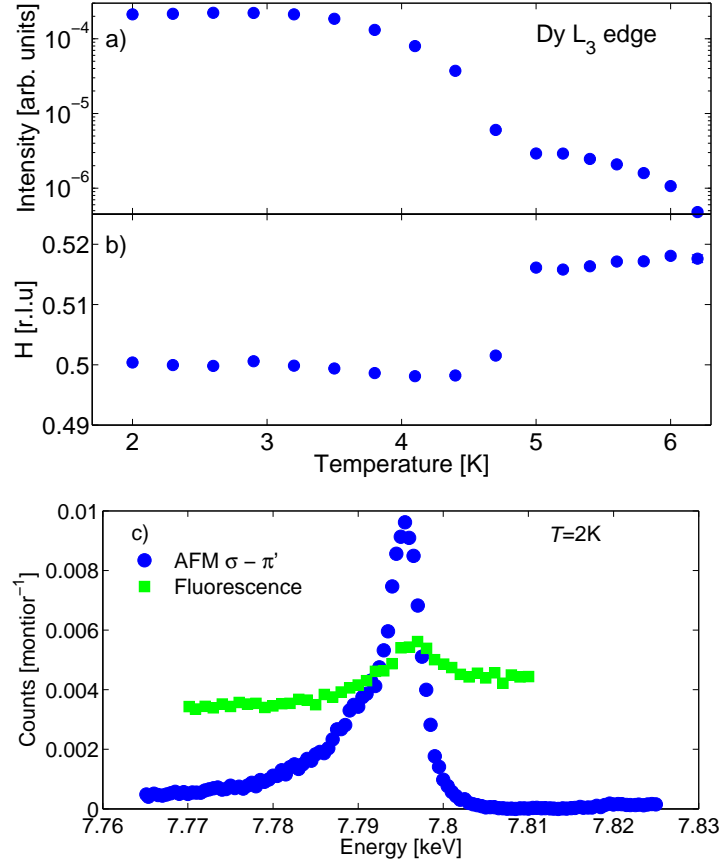


Figure 7.9: XRS from the AFM ordering of the Dy ions in DyMn_2O_5 with wavevector $\mathbf{q}_{AFM}^{Dy} = (0.5, 0, 0)$. (a) and (b) Results of fits to the peak in scans parallel to $(H, 0, 0)$ to a Gaussian lineshape. Notice that the intensity is plotted on a logarithmic scale, and that the incommensurate signal is two orders of magnitude weaker than the AFM signal. Above 6.2K the intensity became so weak as to be below the detection threshold of the apparatus. (c) Scans of the incident x-ray energy at fixed wavevector $\mathbf{q}_{AFM}^{Dy} = (0.5, 0, 0)$, showing a strong resonance at the Dy L_3 edge (blue circles) and the sample fluorescence (green squares, rescaled).

The first XRS measurements I shall describe were designed to confirm the existence of antiferromagnetic (AFM) order on the Dy ions at low temperatures, an effect which is seemingly ubiquitous in the $R\text{Mn}_2\text{O}_5$ compounds when R is magnetic. Figure 7.9(a) shows the integrated intensity and 7.9(b) shows position in reciprocal space of the scattering arising from the Dy AFM order. On warming, the intensity of the scattering decreases monotonically, as expected, until T_N^{Dy} is reached. However, between 4.5 K and 5 K the ordering wavevector of the Dy ions suddenly changes from $(0.5, 0, 0)$ to $(0.52, 0, 0)$. Such an effect has not previously been observed in neutron or x-ray scattering measurements on any of the $R\text{Mn}_2\text{O}_5$ compounds. Figure 7.9(c) shows a scan of the incident x-ray energy at the $(0.5, 0, 0)$ position at 2 K. There is a clear resonance at 7.795 keV, which corresponds to virtual transitions to the $5d$ states. The resonance peak is broadened on the left-hand side by about 10 eV, and the background level on the left-hand side is higher than that on the right-hand side. Such broadening is probably due to interference between resonant and non-resonant magnetic scattering [14]. Figure 7.9(c) also shows the sample fluorescence,

which has been re-scaled because a different detector (the NaI bicron, rather than the Si drift diode) was used to measure it.

These data show that the scattering due to AFM order disappears below the T_N^{Dy} indicated by heat capacity measurements shown in figure 7.6, even though the measurements were made using the same sample. There are two possible explanations for this. The first is that as the intensity of the scattered signal decreases the amplitude of the peak will become more comparable to the random fluctuations of the background scatter and the electronic noise intrinsic to the detector. At some point the peak will no longer have a greater statistical significance than these background fluctuations, and at this point the measurable intensity is effectively zero. This means that if the detector was yet more sensitive, and/or had a lower background, the peak might still be visible. Such an effect might account for a discrepancy of at most 1 K, so it does not account for the full difference between T_N^{Dy} deduced from the x-ray measurements and T_N^{Dy} deduced from the heat capacity measurements.

The second reason for the discrepancy between T_N^{Dy} from the x-ray measurements and the maximum of the heat capacity is to do with what each method is actually measuring. The x-ray diffraction only has a peak when the order has become sufficiently long-ranged that the peak is quite narrow and can be easily discerned above the background. The maximum in the heat capacity occurs discontinuously and this indicates that the phase transition of the Dy spins is second order and continuous. The spins are likely to order locally at first, before a global order rapidly condenses out of this local order. So the heat capacity anomaly occurs at the onset of local magnetic order, whereas the x-ray measurements will not show a peak until some kind of long-range magnetic order is achieved, which may well be at a temperature a degree or so lower.

Figure 7.10(a) shows the temperature dependence of the intensity, together with the temperature dependence of the Dy AFM order, and figs. 7.10(b) and (c) show the H - and L -components respectively of wavevector of the magnetic signal associated with the order on the Mn sublattice. The scattering arising from order on the Mn sublattice was measured at several ICM wavevectors of the form $\mathbf{Q} = (0, 0, 4) + \mathbf{q}_{ICM}$ where $\mathbf{q}_{ICM} = (\pm 0.5 \pm \delta, 0, \pm 0.25 \pm \epsilon)$. At low temperatures this ICM phase has non-zero δ and ϵ . Between $T = 2$ K and $T = 19$ K δ increases slightly from about -0.023 to -0.018 , and ϵ increases almost linearly from -0.015 to zero, then changes sign and increases further to 0.007 . The intensity of the scattering has a maximum at 5 K, the same temperature at which the Dy AFM order disappears. Above 5 K the intensity decreases steadily, and eventually falls below the detection threshold at $T = 19$ K.

Figure 7.10 also shows that for $T \geq 14$ K a CM phase appears, i.e. one for which $\mathbf{q}_{CM} = (0.5, 0, 0.25)$. The intensity of this signal grows upon warming, becoming stronger than the ICM signal by 15 K, where it also reaches a maximum. The maximum intensity of the CM signal is a factor of 5 weaker than the maximum intensity of the ICM signal. As temperature is increased above 15 K the intensity of the scattering gradually decreases, falling below the detection threshold for $T > 37$ K.

Signals were measured at the equivalent positions $\mathbf{q}_1 = (-0.5 + \delta, 0, 0.25 - \epsilon)$, $\mathbf{q}_2 = (-0.5 - \delta, 0, 0.25 - \epsilon)$ and $\mathbf{q}_3 = (-0.5 + \delta, 0, -0.25 + \epsilon)$ for several temperatures. Although the same behavior was observed at each position the absolute intensity of the signal was strongest at \mathbf{q}_2 , probably due to a certain amount of absorption of x-rays by the crystal in the other orientations. The intensity and wavevector at each temperature were determined by

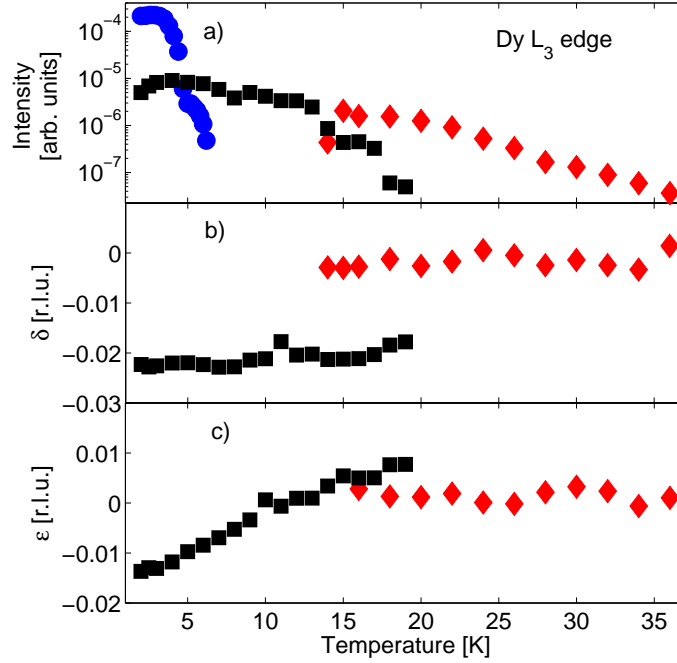


Figure 7.10: XRS data from DyMn₂O₅ at the wavevectors $\mathbf{q}_{AFM}^{Dy} = (0.5, 0, 0)$ (filled circles), $\mathbf{q}_{ICM} = (-0.5 + \delta, 0, 0.25 + \epsilon)$ (filled squares), and $\mathbf{q}_{CM} = (-0.5, 0, 0.25)$ (filled diamonds). Diffraction peaks were fitted to a Gaussian lineshape for scans parallel to $(H, 0, 0)$, and to a Lorentzian-squared for scans parallel to $(0, 0, L)$. (a) Shows the integrated intensity, which is the product of the Gaussian amplitude and width at each temperature. (b) and (c) show the H - and L -components of the ordering wavevector respectively. The error bars are smaller than the size of the points.

fitting the lineshape in scans parallel to $(H, 0, 0)$ to a Gaussian, and scans parallel to $(0, 0, L)$ to a Lorentzian-squared function. These functions were chosen on phenomenological grounds simply because they gave the best fit to the data. The maximum intensities of these signals were at least an order of magnitude smaller than the signal arising from the AFM order of the Dy ions. The intensity of the scattering arising from the Dy AFM order is shown on the same (logarithmic) scale in fig. 7.10 (a) to illustrate this.

Figure 7.11 shows scans of the incident x-ray energy through the Dy L₃-edge at the ICM wavevector $(0.5 + \delta, 0, 0.25 + \epsilon)$. The resonance has essentially the same profile as that shown in figure 7.9(c), for the same reasons. The existence of this resonance proves that the Dy 5*d* states are affected by the magnetic order of the surrounding Mn ions.

Figure 7.12 shows the temperature variation of the widths of the AFM, ICM and CM peaks for scans parallel to $(0, 0, L)$. The peaks were fitted to a Lorentzian-squared lineshape, and a moment analysis was also performed to find the width. Both procedures gave the same results. As the intensity of the peaks became weaker quite large variations in the width parameter were possible without increasing the value of the goodness of fit parameter χ^2 , thus giving rise to quite large error bars. The moment analysis was therefore used to provide a clearer picture of the change in width with temperature. It is clear that the correlation length, proportional to $(\text{width})^{-1}$, is shorter for the ICM order at low temperatures than for the Dy AFM and the CM order at higher temperatures. Indeed, the correlation length of the order on the electrons spins in the 5*d* states of the Dy ions, induced by the Mn sublattice

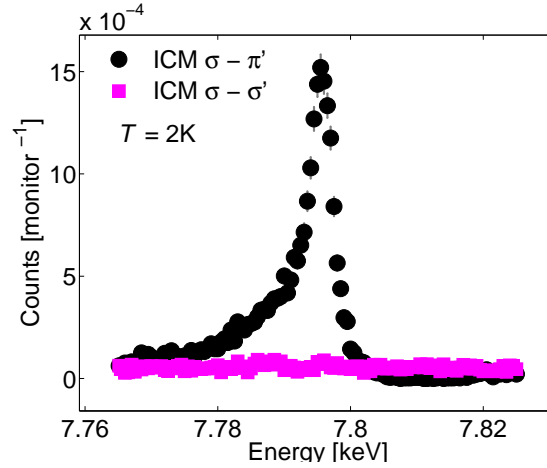


Figure 7.11: Scans of the incident x-ray energy for the ICM signal at $(0.5 + \delta, 0, 0.25 + \epsilon)$. The strong peaks in the $\sigma - \pi'$ channel, together with a lack of signal in the $\sigma - \sigma'$ channel, shows that the scattering is purely magnetic at this wavevector.

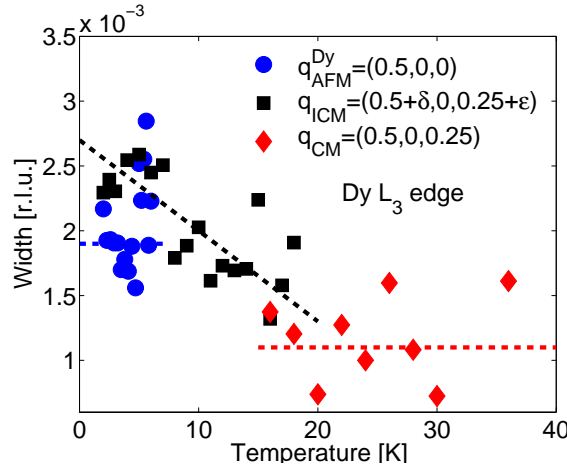


Figure 7.12: The widths (FWHM) of the peaks corresponding to the Dy AFM, ICM and CM order measured in scans parallel to $(0, 0, L)$. The widths were determined by moment analysis. The dashed lines are guides to the eye. Similar analysis of scans parallel to $(H, 0, 0)$ and $(0, K, 0)$ (not shown) shows no change in the width in these directions.

ordering, increases with increasing temperature, before becoming constant above about 20K.

Figure 7.13 shows the results of non-resonant x-ray scattering measurements made with an incident x-ray energy of 11.17 keV, plotting the intensity of the signal at $\mathbf{Q} = (0, 0, 4.5) = (0, 0, 4) + 2\mathbf{q}_{CM}$, versus temperature. At no temperature was a signal corresponding to $(0, 0, 4) \pm 2\mathbf{q}_{ICM}$ observed. The signal at $2\mathbf{q}_{CM}$ appears at $T = 15$ K and its intensity increases steadily with warming, reaching a maximum at 27 K. On further warming the intensity decreases until it becomes too weak to measure at $T > 38$ K. This measurement is in complete agreement with the x-ray scattering data of Higashiyama *et al.* [4] on the same material. Interestingly, the temperature at which this signal is a maximum is the same temperature at which there is a distinct anomaly in the heat capacity (see Figure 7.8), and at which the FE polarisation reaches a local maximum [4]. Since this peak occurs in a non-magnetic, non-resonant channel it must arise from Thomson scattering, i.e. scattering

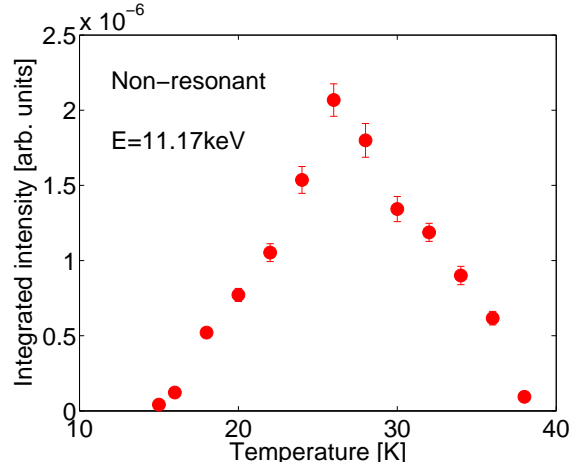


Figure 7.13: Temperature variation of the intensity of the signal at $\mathbf{q} = (0, 0, 0.5)$ measured with a non-resonant x-ray energy. The intensities were calculated from fits to a Gaussian for scans parallel to $(H, 0, 0)$. This scattering is structural in origin.

of the x-rays by the charge of the ions in the system, and therefore be structural in origin.

7.4 Discussion

XRS methods have been used to examine the magnetic ordering in DyMn₂O₅ by measuring the magnetism on the Dy ions induced by the magnetic environment of the surrounding Mn ions. Several observations have been made which go beyond previous neutron scattering studies of this compound. Specifically these are:

1. The existence of a purely commensurate magnetic order in the same temperature range as the largest FE polarisation³.
2. The existence of a structural distortion, characterised by $\mathbf{q} = (0, 0, 0.5)$, for $15 \text{ K} \leq T < 40 \text{ K}$, coexistent with the strongest FE polarisation.
3. The existence of magnetic interactions in the $5d$ states of the Dy ions induced by the magnetism of the surrounding Mn sublattice. This is an effect which is present for $T \leq T_N \approx 40 \text{ K}$, and not just below 8 K ($T \leq T_N^{Dy}$).
4. Changes in the H component of the wavevector of the ICM order for $2 \text{ K} \leq T \leq 19 \text{ K}$, and indeed non-zero incommensurability of this H component, as well as an incommensurate L component.

There have also been observed differences with XRS measurements on the related compound TbMn₂O₅:

³This apparently contradicts the neutron powder diffraction study of Blake *et al.* [6] in which the ordering wavevector was found to be incommensurate and temperature independent. Note however that the wavevector resolution of single crystal x-ray diffraction is in general much better than that of neutron powder diffraction. The data in Figs. 7.10(b) and 7.10(c) establish that the high temperature magnetic phase observed above $\sim 15 \text{ K}$ is commensurate to within an experimental uncertainty of ± 0.0015 in the H and L wavevector components.

1. No sign of a re-entrant ICM phase at higher temperatures.
2. The existence of an ICM phase with negative ϵ as well as positive ϵ , as opposed to the phase with only positive ϵ observed by Okamoto *et al.* [10].

In addition, this study goes beyond all previous scattering studies by measuring changes in the widths of the various peaks with temperature. Finally, the existence of a previously undetected magnetic ordering wavevector of $\mathbf{q} = (0.52, 0, 0)$ between 5 K and T_N^{Dy} was observed.

There are, of course, many similarities between the findings in this study and the findings of previous studies which used neutron scattering to examine DyMn₂O₅, or XRS to measure TbMn₂O₅:

1. The existence of two distinct phases below T_N , namely the ICM and CM phases.
2. Changes in the incommensurability of the ICM signal with changing temperature.
3. The existence of antiferromagnetic order on the Dy ions at low temperatures.

The change in wavevector of the AFM order from $(0.5, 0, 0)$ to $(0.52, 0, 0)$ shown in fig. 7.9, which has not been observed before in scattering measurements of other RMn_2O_5 compounds, might be explained as follows. The Dy $4f$ spins are coupled antiferromagnetically, and so the exchange Hamiltonian contains terms which are proportional to μ_{Dy}^2 , the square of the ordered Dy magnetic moments. With increasing temperature the ordered moment reduces, causing the exchange energy to decrease rapidly, as does the exchange interaction between the ordered $4f$ spins and the $5d$ states. As well as the Dy–Dy interaction the Dy $5d$ spin states and the Mn spins are also coupled. The Mn spins order at a much higher temperature so their average magnetic moment remains fairly constant at the low temperatures under consideration, so the exchange energy of the Dy–Mn coupled system will reduce much less. At low temperatures the Dy–Dy interaction dominates over the Dy–Mn coupling, but as temperature increases the two couplings eventually become similar in strength. This may allow the H -component of the Dy $5d$ magnetic order to become entrained to the ICM order of the Mn sublattice. Further support for such an interpretation is found from the widths of the peaks in scans parallel to $(0, 0, L)$ shown in Figure 7.12. The change of wavevector from $(0.5, 0, 0)$ to $(0.52, 0, 0)$ is accompanied by a sudden increase in the width to a value similar to that of the ICM phase. If indeed the competition between Dy–Dy AFM coupling and Dy–Mn ICM coupling causes the change in wavevector then one might expect the width of the peak at $(0.52, 0, 0)$ to be similar to that of the ICM peak at the same temperature.

To reiterate, the data presented here show that the Dy $5d$ bands show some magnetic order right up to the Néel temperature of the Mn sublattice. Since the measurements presented here show only the magnetic order on the Dy $5d$ states, assuming that above T_N^{Dy} the measurements reflect only the magnetic order of the Mn sublattice, then the changes in the width of the L -component of the ICM and CM peaks, shown in figure 7.12, must arise due to a change in correlation length of the Mn magnetic order. A possible explanation of the increased L width in the ICM phase compared to the CM phase is that the magnetic structure is broken up into locally commensurate domains between which there exist ‘slips’ which have the overall effect of making the magnetic structure incommensurate. Koo *et al.*

[11] suggest that in TbMn₂O₅ the ICM phase may be interpreted as CM spin modulations with domain walls, analogous to an effect observed in ErNi₂B₂C [15]. The measurements detailed above would appear to support such an interpretation, with domain walls parallel to the *ab*-plane.

The non-resonant scattering measured at $2\mathbf{q}_{CM} = (0, 0, 0.5)$, which is structural in origin, ties in with a model proposed to explain multiferroicity in TbMn₂O₅ [16] and later extended to describe YMn₂O₅ [17]. The *RMn₂O₅* materials are geometrically frustrated, with five different exchange interactions identified between the Mn ions, and it is clear a small distortion would lift the degeneracy. Analysis of the atomic displacement parameters [16] suggests that a canted antiferroelectric (CAF) structural phase may be the way in which this occurs. In this case the lattice distorts in the opposite sense in adjacent unit cells along the *c*-axis, but in the same sense along the *a*- and *b*-axes. In each unit cell the distortions along the *a*-axis of different ions are in different directions such that the FE polarisation along the *a*-axis is cancelled out, however this does not occur for the distortions along the *b*-axis, giving rise to the observed FE polarisation along the *b*-axis. A difficulty with this explanation of the occurrence of ferroelectricity in DyMn₂O₅, however, is that the amplitude of the scattering at $2\mathbf{q}_{CM}$ does not map on to the amplitude of the observed FE polarisation. The polarisation does have a local maximum at the same temperature at which the scattering at $2\mathbf{q}_{CM}$ is most intense, $T_{max} = 27$ K, but the onset of the largest polarisation is actually at about 17 K, and the signal at $2\mathbf{q}_{CM}$ is relatively weak at this temperature.

Several phenomenological theories have been proposed to explain the occurrence of multiferroicity [18, 19, 20, 21]. A successful approach for the *RMnO₃* compounds has been developed by Mostovoy [20], which was briefly discussed in section 1.2.5, as was the theory of Betouras *et al.* [21], which was designed specifically to account for the multiferroic properties of the *RMn₂O₅*-type compounds. The physical grounds for both theories are in essence the same, namely a consideration of magneto-electric coupling within a Ginzburg-Landau framework, with differences only in the precise details of the spatial variation of the magnetisation and FE polarisation. Betouras *et al.* require that the chiral magnetic structure is *acentric*, i.e. the spin density is not necessarily centred on a lattice site and has a non-zero phase, and that the polarisation and inverse ferroelectric susceptibility have small oscillatory parts in addition to a constant term. The result of this is that a spontaneous polarisation is only allowed for magnetic phases which are *commensurate* with a non-zero acentricity. The former of these two conditions suggests that this model can successfully describe the multiferroic behaviour of DyMn₂O₅, where the polarisation is much larger when the magnetic order is, as has been shown here, purely commensurate.

As mentioned in section 7.1.1, the magnitude of the FE polarisation in DyMn₂O₅ is the strongest of all the materials in the *RMn₂O₅* family. The results presented here show that there is a significant magnetic interaction in the Dy 5*d* bands, and it is possible that there is also an induced ordering of the partially occupied Dy 4*f* states. It has been found previously that the size of the ordered moment of the Dy ions in DyMn₂O₅ is larger than that of other rare earth ions in the *RMn₂O₅* series [6], which might partly explain why such a clear signal at the Dy L-edge resonance is observed here. The models used to explain multiferroic effects discussed above do not constrain the magneto-electric coupling to involve just the Mn ions, so in principle magnetic order of the Dy ions with the same wavevector as the magnetic order of the Mn ions could give rise to an ‘extra’ contribution to the FE polarisation through the same mechanism. If such coupling were proportional to the size of the rare-earth moment

then that might explain the existence of the strongest polarisation in DyMn_2O_5 and the weakest polarisation in YMn_2O_5 among the RMn_2O_5 materials.

7.5 Conclusions

In conclusion, the XRS measurements presented here have shown that the magnetic ordering in DyMn₂O₅ bears many similarities to that of other members of the *RMn₂O₅* family of materials previously studied. These measurements also show extra features not previously observed in neutron scattering measurements on DyMn₂O₅. Of particular note is the observation that the Dy *5d* bands are magnetically polarised right up to $T_N \sim 40$ K, the Néel temperature of the Mn ions. If the *4f* states are magnetised in a similar fashion there may be an enhancement of the ferroelectric polarisation in this material, given the large Dy magnetic moment. Such measurements demonstrate that x-ray resonant scattering is a powerful tool for studying materials in which there exists more than one magnetic ion, in particular allowing one to resonantly enhance the scattering from magnetic order on one sublattice which has been induced by the magnetisation of the other sublattice.

In the future one obvious experiment to do would be to measure the same diffraction peaks as was done here using soft resonant x-rays. With these the Mn *3d* states can be probed directly, so the measurements presented here of the ICM and CM states could be checked. Of particular interest would be the variation of the intensities of the different magnetically ordered states with temperature – specifically it would be interesting to see if the intensity of the CM order is maximal at 15 K when the FE polarisation is at a maximum. Furthermore the symmetry of the magnetic order in the ICM and CM states could be investigated using azimuth scans, allowing the symmetry of the order parameters to be investigated like they were in the XRS study of TbMnO₃ [12] which was discussed in section 7.1.3.

References

- [1] N. Hur, S. Park, P. A. Sharma, J. S. Ahn, S. Guha, and S. -W. Cheong, *Nature (London)* **429**, 392 (2004).
- [2] N. Hur, S. Park, P. A. Sharma, S. Guha, and S. -W. Cheong, *Phys. Rev. Lett.* **93**, 107207 (2004).
- [3] D. Higashiyama, S. Miyasaka, and Y. Tokura, *Phys. Rev. B* **72**, 064421 (2005).
- [4] D. Higashiyama, S. Miyasaka, N. Kida, T. Arima, and Y. Tokura, *Phys. Rev. B* **70**, 174405 (2004).
- [5] A. Inomata and K. Kohn, *J. Phys. Condensed Matter* **8**, 2673 (1996).
- [6] G. R. Blake, L. C. Chapon, P. G. Radaelli, S. Park, N. Hur, S. -W. Cheong, and J. Rodríguez-Carvajal, *Phys. Rev. B* **71**, 214402 (2005).
- [7] P. Baettig, C. Ederer, and N. Spaldin, *Phys. Rev. B* **72**, 214105 (2005).
- [8] C. Wilkinson, F. Sinclair, P. Bardner, J. B. Forsyth, and B. M. R. Wanklyn, *J. Phys. C* **14**, 1671 (1981).
- [9] W. Ratcliff III, V. Kiryukhin, M. Kenzelman, S.-H Lee, R. Erwin, J. Schefer, N. Hur, S. Park, and S. -W. Cheog, *Phys. Rev. B* **72**, 060407 (2005).
- [10] J. Okamoto, D. J. Huang, C. -Y. Mou, K. S. Chao, H. -J. Lin, S. Park, S. -W. Cheong, and C. T. Chen, *Phys. Rev. Lett.* **98**, 157202 (2007).
- [11] J. Koo, C. Song, S. Ji, J. -S. Lee, J. Park, T. -H. Jang, C. -H. Yang, J. -H. Park, Y. H. Jeong, K. -B. Lee, T. Y. Koo, Y. J. Park, J. -Y. Kim, D. Wermeille, A. I. Goldman, G. Srajer, S. Park, and S. -W. Cheong, *Phys. Rev. Lett.* **99**, 197601 (2007).
- [12] D. Mannix, D. F. McMorrow, R. A. Ewings, A. T. Boothroyd, D. Prabhakaran, Y. Joly, B. Janousova, C. Mazzoli, L. Paolasini, and S. B. Wilkins, *Phys. Rev. B* **76**, 184420 (2007).
- [13] B. M. R. Wanklyn, *J. Mater. Sci.* **7**, 813 (1972).
- [14] J. P. Hill, C. -C. Kao, and D. F. McMorrow, *Phys. Rev. B* **55**, 8662 (1997).
- [15] H. Kawano-Furukawa, H. Takeshita, M. Ochiai, T. Nagata, H. Yoshizawa, N. Furukawa, H. Takeya, and K. Kadowaki, *Phys. Rev. B* **65**, 180508 (2002).

- [16] L. C. Chapon, G. R. Blake, M. J. Gutmann, S. Park, N. Hur, P. G. Radaelli, and S. -W. Cheong, Phys. Rev. Lett. **93**, 177402 (2004).
- [17] L. C. Chapon, P. G. Radaelli, G. R. Blake, S. Park, and S. -W. Cheong, Phys. Rev. Lett. **96**, 097601 (2006).
- [18] H. Katsura, N. Nagaosa, and A. V. Balatsky, Phys. Rev. Lett. **95**, 057205 (2005).
- [19] M. Kenzelmann, A. B. Harris, S. Jonas, C. Broholm, J. Schefer, S. B. Kim, C. L. Zhang, S. -W. Cheong, O. P. Vajk, and J. W. Lynn, Phys. Rev. Lett. **95**, 087206 (2005).
- [20] M. Mostovoy, Phys. Rev. Lett. **96**, 067601 (2006).
- [21] J. J. Betouras, G. Giovannetti, and J. van den Brink, Phys. Rev. Lett. **98**, 257602 (2007).

Appendix A

Extra Terms in the Neutron Magnetic Scattering Cross-Section

In section 2.1.4, when considering the cross-section for polarised neutron magnetic diffraction, I neglected considerations of non-uniaxial changes in polarisation, which account for nuclear-magnetic interaction terms in the cross section. For a chiral magnetic structure these are important, as will be demonstrated below. A more detailed calculation may be found in the paper of Moon *et al* [1].

Put the magnetic amplitude $p = (\gamma r_0/2)gSF(\mathbf{Q})$ and write

$$\mathbf{A} = -p\mathbf{M}_\perp + B\mathbf{I}, \quad (\text{A.1})$$

where B is the spin-dependent nuclear scattering amplitude. We then define $\tilde{\mathbf{A}}$ and \tilde{b}_i as:

$$\tilde{\mathbf{A}} = \langle q' | \mathbf{A} | q \rangle, \quad (\text{A.2})$$

$$\tilde{b}_i = \langle q' | b_i | q \rangle. \quad (\text{A.3})$$

The neutron scattering cross-section is then given by

$$\frac{d^2\sigma}{d\Omega dE} = \sum_{qq'} P_q \frac{k'}{k} \left(\sum_{ij} e^{i\mathbf{Q}\cdot(\mathbf{r}_i - \mathbf{r}_j)} \left[\tilde{b}_i \tilde{b}_j + \tilde{\mathbf{A}}_i \cdot \tilde{\mathbf{A}}_j^* + \mathbf{P}_0 \cdot (\tilde{b}_i \tilde{\mathbf{A}}_j^* + \tilde{b}_j^* \tilde{\mathbf{A}}_i - i\tilde{\mathbf{A}}_i \times \tilde{\mathbf{A}}_j^*) \right] \right). \quad (\text{A.4})$$

Ignoring the effects of nuclear spins, i.e. put $\mathbf{A} = -p\mathbf{M}_\perp$, and also note that $\mathbf{P}_0 \times \mathbf{A}$ type terms rotate the polarisation through 90° and are therefore undetectable with a uniaxial polarising setup. We are then left with a cross-section which is proportional to a polarisation independent term

$$\tilde{\mathbf{M}}_{\perp i} \cdot \tilde{\mathbf{M}}_{\perp j}^*, \quad (\text{A.5})$$

and a polarisation dependent term

$$\mathbf{P}_0 \cdot (\tilde{\mathbf{M}}_{\perp i} \times \tilde{\mathbf{M}}_{\perp j}^*). \quad (\text{A.6})$$

References

- [1] R. M. Moon, T. Riste, and W. C. Koehler, Phys. Rev. **181**, 920 (1969).

Appendix B

Use of Pseudo-Cubic Notation for Rhombohedral Crystals

Although the crystallography of the cobaltites of the form $\text{La}_{1-x}\text{Sr}_x\text{CoO}_3$, which includes $x = 0$ and $x = 0.18$, is usually considered in terms of a cubic crystal structure, they are in fact rhombohedral with the space group $R\bar{3}c$. In some circumstances the difference between the rhombohedral crystal structure and the cubic structure is very small, and since the cubic notation is somewhat simpler it is more generally used by neutron and x-ray scatterers.

When one considers the rhombohedral unit cell, shown in figure B.1 in relation to the cubic unit cell one can see that it has a different periodicity. Indexing a cubic structure with rhombohedral co-ordinates in real space gives rise to the following conversion:

$$\begin{aligned}(100)_R &= (101)_C \\ (010)_R &= (110)_C \\ (001)_R &= (011)_C\end{aligned}\tag{B.1}$$

where the subscript R refers to the rhombohedral lattice and the subscript C refers to the cubic lattice. In reciprocal space, because the rhombohedral axes are non-orthogonal, this leads to

$$\begin{aligned}(100)_R^* &= \left(\frac{1}{2} \frac{\bar{1}}{2} \frac{1}{2}\right)_C^* \\ (010)_R^* &= \left(\frac{1}{2} \frac{1}{2} \frac{\bar{1}}{2}\right)_C^* \\ (001)_R^* &= \left(\frac{\bar{1}}{2} \frac{1}{2} \frac{1}{2}\right)_C^*\end{aligned}\tag{B.2}$$

It is immediately clear from this that one must be careful when using pseudo-cubic notation in a scattering experiment - there will be weak structural peaks at the cubic antiferromagnetic position $(1/2, 1/2, 1/2)$ which actually corresponds to the rhombohedral $(1, 1, 1)$ structural

position.

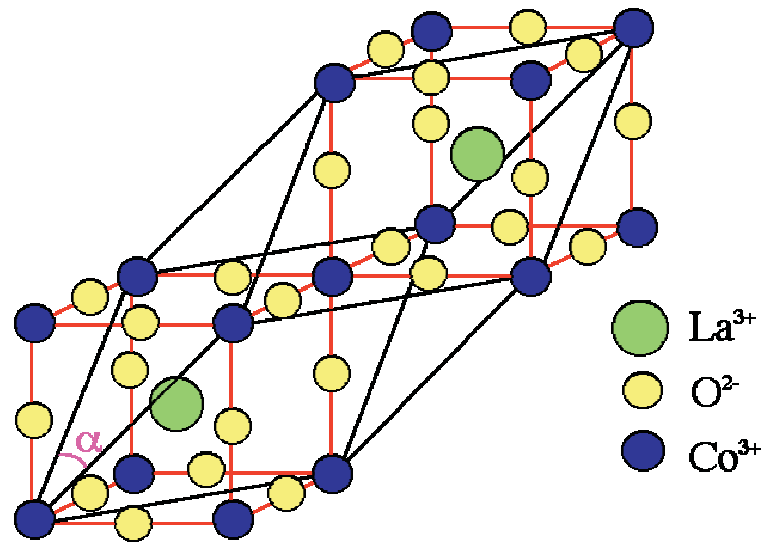


Figure B.1: The (non-primitive) unit cell of LaCoO₃, which is rhombohedral. Since the angle α is only slightly greater than 60° in this material the distortion away from cubic (for which $\alpha=60^\circ$) is also small.

Appendix C

LaCoO₃ Structure Factor Calculation

The structural form factor of LaCoO₃ can be approximately calculated as follows. Assume that the material really is cubic, rather than pseudo-cubic rhombohedral, in order to make the analysis easier. In the cubic unit cell there are eight Co³⁺ ions at each of the corners of the cell, the (0,0,0) positions. There is also a single La³⁺ ion at the ($\frac{1}{2}, \frac{1}{2}, \frac{1}{2}$) position, and there are four O²⁻ at each of the ($\frac{1}{2}, 0, 0$), ($0, \frac{1}{2}, 0$) and ($0, 0, \frac{1}{2}$).

Therefore the structure factor S_{hkl} is

$$S_{hkl} = b_{\text{Co}} + b_{\text{La}}e^{-i\pi(h+k+l)} + b_{\text{O}}(e^{-i\pi h} + e^{-i\pi k} + e^{-i\pi l}) \quad (\text{C.1})$$

where the b s are the nuclear scattering lengths for the different elements. Their values are $b_{\text{Co}} = 2.49$ fm, $b_{\text{La}} = 8.24$ fm and $b_{\text{O}} = 5.803$ fm. The scattered intensity I is proportional to the square of S_{hkl} .

The following rules for structural Bragg peak intensities follow:

$$(h,k,l) \text{ all even: } I \propto (b_{\text{Co}} - b_{\text{La}} - 3b_{\text{O}})^2 = 536.3 \quad (\text{C.2})$$

$$(h,k,l) \text{ all odd: } I \propto (b_{\text{Co}} + b_{\text{La}} + 3b_{\text{O}})^2 = 791.8 \quad (\text{C.3})$$

$$\text{One even index, two odd: } I \propto (b_{\text{Co}} + b_{\text{La}} - b_{\text{O}})^2 = 24.28 \quad (\text{C.4})$$

$$\text{One index odd, two even: } I \propto (b_{\text{Co}} - b_{\text{La}} + b_{\text{O}})^2 = 2.8 \times 10^{-3} \quad (\text{C.5})$$